Defining the Role of Metabolism in Prostate Epithelial Cell Fate and Response to Androgen Receptor Blockade

Giafaglione, Jenna M

2023

UNIVERSITY OF CALIFORNIA

Los Angeles

Defining the Role of Metabolism in Prostate Epithelial Cell Fate and Response to Androgen Receptor Blockade

A dissertation submitted in partial satisfaction of the requirements for the degree

Doctor of Philosophy in Molecular Biology

by

Jenna Marie Giafaglione

2023

ABSTRACT OF THE DISSERTATION

Defining the Role of Metabolism in Prostate Epithelial Cell Fate and Response to Androgen Receptor Blockade

by

Jenna Marie Giafaglione

Doctor of Philosophy in Molecular Biology

University of California, Los Angeles, 2023

Professor Paul C. Boutros, Co-Chair

Professor Andrew Goldstein, Co-Chair

Metabolic pathways coordinate a complex interplay between energy homeostasis, biosynthesis, signaling networks, and epigenetic processes. In many tissues, metabolism is involved in the regulation of cell fate. Furthermore, altered energy metabolism can often be leveraged to diagnose, monitor, and/or treat cancer. Lineage transitions play a pivotal role in prostate development, tumorigenesis, and treatment resistance. While the epigenome is a well-established regulator of prostate cell fate, how upstream metabolic signaling contributes to the maintenance of cell identity is poorly defined. In addition, inhibition of several metabolic pathways has been shown to antagonize the growth of prostate cancer cells. However, treatment-induced metabolic alterations and vulnerabilities have not been comprehensively elucidated. In this dissertation, I define the role of metabolism in prostate epithelial cell fate and response to therapy. In Chapter 2, I describe our refined approach to culture prostate organoids, which is used extensively in subsequent chapters. In Chapter 3, I establish pyruvate and lactate metabolism as key regulators of prostate epithelial lineage identity and response to treatment. Finally in Chapter 4, I define treatment-induced metabolic vulnerabilities in prostate cancer and identify molecular mechanisms that regulate the metabolic response to therapy. These findings yield new insights into how the modulation of metabolism can impact prostate cancer disease progression and treatment strategies.

The dissertation of Jenna Marie Giafaglione is approved.

Heather R. Christofk

Ajit S. Divakaruni

Brigitte N. Gomperts

Robert E. Reiter

Paul C. Boutros, Committee Co-Chair

Andrew Goldstein, Committee Co-Chair

University of California, Los Angeles

2023

This dissertation is dedicated to my grandfather, Bill Hurley, whose courageous battle with cancer originally led me on this path to pursue a career in biomedical research.

Table of Contents

List of Figures

Chapter 1: Introduction

Chapter 2: Evaluating the differentiation capacity of mouse prostate epithelial cells using organoid culture

Chapter 3: Prostate lineage-specific metabolism governs luminal differentiation and response to antiandrogen treatment

Chapter 4: MYC is a regulator of androgen receptor inhibition-induced metabolic requirements in prostate cancer

ACKNOWLEDGEMENTS

My passion for science began in ninth grade biology class when I became fascinated by the complexity of the cellular and molecular processes that enable humans to function, grow, and thrive. I would like to thank my high school biology teacher, Mr. Rob Zaccheo, for helping to ignite this passion and providing invaluable advice that I still carry with me today. I would also like to thank my high school physics and computer science teacher, Mr. Matthew Holm, for always challenging me to think critically and for his continued support and mentorship.

I would like to thank my undergraduate research advisor, Dr. Frédéric Chédin, for helping to cultivate my curiosity for biological research. My experience in his lab clarified my desire to pursue a graduate degree. I would also like to thank my graduate student mentors in the Chédin lab, Dr. Stella Hartono, Dr. John Smolka, Dr. Maika Malig, and Dr. Yoong Wearn Lim, for being patient when I was running my first PCR or loading my first Western blot. I would like to thank Kimberley Berg, a fellow undergraduate in the lab, for her camaraderie during late night study sessions. Furthermore, I would like to thank Adam Davis, my manager at Genentech, for providing me with the opportunity to experience the biotechnology industry during college. I would also like to thank Dr. Onn Brandman and all members of the Brandman lab for helping me further develop as a scientist during the year before I began graduate school.

I would like to thank all members of the Goldstein and Boutros labs, past and present, for their support and friendship. I would like to thank Dr. Takao Hashimoto, Dr. Preston Crowell, Matthew Bernard, Johnny Diaz, Nicholas Nunley, Jonathan Fox, Amelie Delcourt, Kylie Heering, Aishwarya Atmakuri, and Rachel Dove for creating a fun, collaborative, and intellectually stimulating environment that made me genuinely excited to come to lab every day.

I would like to extend a special thank you to Preston Crowell. What started as an instant connection over a passion for science quickly grew into a deep bond during board game nights, rounds of golf, dining experiences, and travels. I look forward to continuing to challenge, support, and celebrate each other during the next stage of our lives.

I would like to thank my thesis co-advisor and mentor, Dr. Andrew Goldstein. He taught me how to conduct rigorous scientific research and how to package data into a clear and compelling story. Throughout my graduate career, Andrew always seemed to know when I needed an extra push or additional guidance and when I needed space to carve my own path. He has been one of the most dedicated, supportive, and compassionate mentors I have ever encountered and will always be a role model for the type of mentor and scientist I strive to be. I would also like to thank my thesis co-advisor and mentor, Dr. Paul Boutros. His feedback and perspectives on how to lead a research group have contributed immensely to my growth as a scientist and person. I would like to thank my thesis committee, Dr. Heather Christofk, Dr. Ajit Divakaruni, Dr. Brigitte Gomperts, and Dr. Robert Reiter for their scientific feedback and support throughout my graduate career.

I would like to thank members of the BSCRC flow cytometry core, Felicia Codrea, Jessica Scholes, and Jeff Calimlim, as well as Johanna ten Hoeve-Scott from the UCLA Metabolomics Core. It would not have been possible to conduct our research without their help and guidance. I would also like to thank Dr. Bill Lowry, who provided invaluable advice and support throughout my graduate career, and Dr. Zoran Galic, whose humor and words of encouragement in the Terasaki hallway brightened my day-to-day life as a graduate student. In addition, I would like to thank all our collaborators, including Dr. Anthony Jones, Dr. Daniel Ha, and Marie Payne, for their contributions and helpful scientific discussions. I would also like to thank Ashley Straight, Stephanie Cuellar, and Helen Houldsworth for their help and support over the last five years.

Thank you to members of my cohort, including Ralph Crisostomo, Ian Ford, Kaiser Atai, and Mandy Cheng, for all the fun discussions during many happy hours.

I would like to thank my friends, Julia Holloway, Quincey Nguyen, Allison Poffenroth, Kara Brandt, Lindsey Gil, Darren Fang, Stephan Dodson, Barathan Jeevaretanam, Anthony Jones, and Eboni Martin, for always being there for me and enriching my life outside of the lab.

Finally, I would like to thank my family. Thank you to my aunts and uncles, Kristine and Perry Watts, Julie and Frank Nesci, and Lori and Frank Ybarra, and cousins, Colby, Austin, Anthony, Peyton, Sal, Alyssa, and Frankie, for sharing in some of my fondest childhood memories and celebrating milestones and achievements with me. Thank you to my parents, Jim and Sondra Giafaglione. They have shown me what it means to be hard-working, generous, kind, and resilient. I would not be able to pursue my personal and professional dreams without their unconditional love and support throughout every stage of my life. Thank you to my sisters, Krista and Alexa Giafaglione, for being my best friends. I'm extremely grateful to be able to celebrate our successes together and support each other through struggles. Thank you to Eddie Smith and CJ Peters for adding so much light to my life. Thank you to my grandparents, Jim and Kathy Giafaglione, for teaching me the importance of family. The countless holidays and celebrations they host and traditions they pass down create memories that I will cherish forever. Thank you to my late grandmother, Barbara Hurley. She was one of the most thoughtful, compassionate, and selfless people I have ever known. I am reminded of her often and miss her dearly. Thank you to my grandfather, Bill Hurley, for being the example for how I want to lead my life. His work ethic, morality, strength, and positive mindset in the face of hardship have always inspired me.

Chapter 2 was originally published in the *Journal of Visualized Experiments*. Crowell PD*, Giafaglione JM*, Hashimoto T, Diaz JA, Goldstein AS. Evaluating the differentiation capacity of

mouse prostate epithelial cells using organoid culture. *J. Vis. Exp.* (2019). PMID: 31814611. It is accessible with the DOI: 10.3791/60223. PDC and JMG are supported by the Ruth L. Kirschstein National Research Service Award GM007185. JAD is supported by the National Institute of General Medical Sciences of the National Institutes of Health (R25GM055052) awarded to T. Hasson and the Saul Martinez Scholarship. ASG is supported by the Spitzer Family Foundation Fund and the Gill Endowment. This work was supported by the American Cancer Society (RSG-17-068-01-TBG), Department of Defense (W81XWH-13-1-0470), Margaret E. Early Medical Research Trust, NIH/NCI (P50CA092131/UCLA SPORE in Prostate Cancer), Rose Hills Foundation, and support from UCLA's Jonsson Comprehensive Cancer Center, Broad Stem Cell Research Center, Clinical and Translational Science Institute, and Institute of Urologic Oncology.

Chapter 3 is currently in press at *Nature Cell Biology*. Giafaglione JM, Crowell PD, Delcourt AML, Hashimoto T, Ha SM, Atmakuri A, Nunley NM, Dang RMA, Tian M, Diaz JA, Tika E, Payne MC, Burkhart DL, Li D, Navone NM, Corey E, Nelson PS, Lin NYC, Blanpain C, Ellis L, Boutros PC, Goldstein AS. Prostate lineage-specific metabolism governs luminal differentiation and response to antiandrogen treatment. We thank Dr. Thomas Graeber, Dr. Daniel Braas, Dr. Johanna ten Hoeve-Scott, and the UCLA Metabolomics Core for guidance on metabolic profiling of small cell populations and metabolomics services. We thank Donghui Cheng for sorting of primary basal and luminal mouse prostate cells. We acknowledge the UCLA Technology Center for Genomics and Bioinformatics (TCGB) for assistance with RNA sequencing, the UCLA Quantitative & Computational Biosciences (QCB) Collaboratory for assistance with scRNA sequencing analysis, the UCLA Broad Stem Cell Research Center (BSCRC) for flow cytometry services, and Active Motif, Inc. for ATAC-sequencing services. We thank Dr. Bill Lowry and Dr. Jared Rutter for *Mpc1* floxed mouse prostate tissue. We thank Dr. Amina Zoubeidi for 16D cells and Dr. Robert Reiter for LAPC4 cells. The UCLA Integrated Molecular Technologies Core is supported by CURE/P30 DK041301. We acknowledge the support of the Hutton Family Foundation. J.M.G. and P.D.C.

acknowledge the support of the Ruth L. Kirschstein National Research Service Award GM007185 and the UCLA Eli and Edythe Broad Center of Regenerative Medicine and Stem Cell Research Training Program. P.D.C. is also supported by the NIH grants TL1 DK132768 and U2C DK129496. N.M.N. (Navone) is supported by NCI U01 CA224044-03. N.Y.C.L. is supported by a Young Investigator Award from the Prostate Cancer Foundation (Award ID #: 22YOUN28). P.S.N. is supported by NIH/NCI awards P50CA097186, R01CA234715, and R21CA277368. E.T. is supported by a Fonds de la Recherche Scientifique (FNRS-FRIA) fellowship. C.B. is supported by the WEL Research Institute, FNRS, TELEVIE, Fondation Contre le Cancer, ULB Foundation, EOS FNRS/FWO and the European Research Council. P.C.B. is supported by NIH grants P30CA016042, U2CCA271894 and U01CA214194 and by a Prostate Cancer Foundation Special Challenge Award to PCB (Award ID #: 20CHAS01) made possible by the generosity of Mr. Larry Ruvo. A.S.G. is supported by the National Cancer Institute of the National Institutes of Health under Award Number R01CA237191. The content is solely the responsibility of the authors and does not necessarily represent the official views of the National Institutes of Health. A.M.L.D. is supported by NCI/NIH supplement related to R01CA237191. A.S.G. is also supported by American Cancer Society award RSG-17-068-01-TBG, Department of Defense PCRP award HT94252310379, the UCLA Prostate Cancer Specialized Programs of Research Excellence (SPORE) NCI P50 CA092131, the UCLA Eli and Edythe Broad Center of Regenerative Medicine and Stem Cell Research Rose Hills Foundation Innovator Grant, the UCLA Jonsson Comprehensive Cancer Center and Eli and Edythe Broad Center of Regenerative Medicine and Stem Cell Research Ablon Scholars Program, the University of California Cancer Research Coordinating Committee Faculty Seed Grant, the National Center for Advancing Translational Sciences UCLA CTSI Grant UL1TR001881, STOP CANCER, and the UCLA Institute of Urologic Oncology. The funders had no role in study design, data collection and analysis, decision to publish or preparation of the manuscript.

Chapter 4 is currently in press at *Cell Reports*. Crowell PD, Giafaglione JM, Jones AE, Nunley NM, Hashimoto T, Delcourt AML, Petcherski A, Agrawal R, Bernard MJ, Diaz JA, Heering KY, Huang R, Low J, Matulionis N, Navone NM, Ye H, Zoubeidi A, Christofk HR, Rettig MB, Reiter RE, Haffner MC, Boutros PC, Shirihai OS, Divakaruni AS, Goldstein AS. MYC is a regulator of androgen receptor inhibition-induced metabolic requirements in prostate cancer. P.D.C. and J.M.G. acknowledge the support of the Ruth L. Kirschstein National Research Service Award GM007185 and the UCLA Eli and Edythe Broad Center of Regenerative Medicine and Stem Cell Research Training Program. P.D.C. is also supported by the NIH grants TL1 DK132768 and U2C DK129496. A.E.J. is supported by the UCLA Tumor Cell Biology Training Grant (NIH T32CA009056). A.S.G. is supported by the National Cancer Institute of the National Institutes of Health under Award Number R01CA237191. The content is solely the responsibility of the authors and does not necessarily represent the official views of the National Institutes of Health. A.M.L.D. is supported by NCI/NIH supplement related to R01CA237191. A.S.G. is also supported by American Cancer Society award RSG-17-068-01-TBG, the UCLA Eli and Edythe Broad Center of Regenerative Medicine and Stem Cell Research Rose Hills Foundation Innovator Grant, the UCLA Jonsson Comprehensive Cancer Center and Eli and Edythe Broad Center of Regenerative Medicine and Stem Cell Research Ablon Scholars Program, the National Center for Advancing Translational Sciences UCLA CTSI Grant UL1TR001881, STOP CANCER, and the UCLA Institute of Urologic Oncology. A.S.G., A.S.D., O.S.S., R.E.R, M.B.R., P.C.B are supported by the UCLA Prostate Cancer Specialized Programs of Research Excellence (SPORE) NCI P50 CA092131. M.C.H. is supported by the U.S. Department of Defense Prostate Cancer Research Program (W81XWH-20-1-0111, W81XWH-21-1-0229) and Grant 2021184 from the Doris Duke Charitable Foundation. N.M.N. (Navone) is supported by NCI U01 CA224044-03. We acknowledge the support of the Hutton Family Foundation. We thank UCLA Technology Center for Genomics & Bioinformatics, UCLA Metabolomics Center, UCLA MCDB/BSCRC Microscopy Core. The UCLA Integrated Technologies Core is supported by CURE/P30 DK041301.

VITA

EDUCATION

University of California, Davis, Davis, CA 2017
B.S. Genetics and Genomics, Minors: Computer Science, Education

PUBLICATIONS

Giafaglione JM, Crowell PD, Delcourt AML, Hashimoto T, Ha SM, Atmakuri A, Nunley NM, Dang RMA, Tian M, Diaz JA, Tika E, Payne MC, Burkhart DL, Li D, Navone NM, Corey E, Nelson PS, Lin NYC, Blanpain C, Ellis L, Boutros PC, Goldstein AS. Reciprocal regulation of metabolism and prostate epithelial lineage identity. *Nature Cell Biology* (*In press*).

Crowell PD, **Giafaglione JM**, Jones AE, Nunley NM, Hashimoto T, Delcourt AML, Petcherski A, Agrawal R, Bernard MJ, Diaz JA, Heering KY, Huang RR, Low JY, Matulionis N, Navone NM, Ye H, Zoubeidi A, Christofk HR, Rettig MB, Reiter RE, Haffner MC, Boutros PC, Shirihai OS, Divakaruni AS, Goldstein AS. MYC is a regulator of androgen receptor inhibition-induced metabolic requirements in prostate cancer. *Cell Reports* (2023). PMID: 37815914.

Huang R, **Giafaglione JM**, Hashimoto T, Zhang L, Yu W, Rao J, Russo JW, Balk SP, Nickols NG, Rettig MB, Goldstein AS, Ye H. Androgen drives expression of SARS-CoV-2 entry proteins in sinonasal tissue. *Journal of Clinical and Translational Pathology* (2023).

Freeland J, Crowell PD, **Giafaglione JM**, Boutros PC, Goldstein AS. Aging of the progenitor cells that initiate prostate cancer. *Cancer Letters* (2021). PMID: 34052326.

Crowell PD, **Giafaglione JM**, Hashimoto T, Goldstein AS. Distinct cell-types in the prostate share an aging signature suggestive of metabolic reprogramming. *American Journal of Clinical and Experimental Urology* (2020). PMID: 32929410.

Malig M*, Hartono SR*, **Giafaglione JM**, Sanz L, Chédin F. Ultra-Deep Coverage Single-Molecule R-loop Footprinting Reveals Principles of R-loop Formation. *Journal of Molecular Biology* (2020). PMID: 32105733.

Sitron CS*, Park JH*, **Giafaglione JM**, Brandman O. Aggregation of CAT tails blocks their degradation and causes proteotoxicity in S. cerevisiae. *PLoS One* (2020). PMID: 31945107.

Crowell PD*, **Giafaglione JM***, Hashimoto T, Diaz JA, Goldstein AS. Evaluating the differentiation capacity of mouse prostate epithelial cells using organoid culture. *J. Vis. Exp.* (2019). PMID: 31814611.

PRESENTATIONS

Giafaglione JM. (2023) Talk: Reciprocal regulation of metabolism and prostate epithelial lineage identity. Molecular, Cell, and Developmental Biology retreat. Santa Monica, CA.

Giafaglione JM. … Goldstein AS. (2023) Poster: Reciprocal regulation of metabolism and prostate epithelial lineage identity. UCLA Stem Cell Symposium. Los Angeles, CA.

Giafaglione JM. … Goldstein AS. (2022) Poster: Reciprocal regulation of metabolism and lineage identity in the benign prostate and prostate cancer. Metabolism in Health and Disease Conference. Cancun, MX.

Giafaglione JM. (2022) Talk: Reciprocal regulation of metabolism and prostate epithelial lineage identity. Jonsson Comprehensive Cancer Center Trainee Talk. Los Angeles, CA.

Giafaglione JM. … Goldstein AS. (2021) Poster: Reciprocal regulation of metabolism and lineage identity in the benign prostate and prostate cancer. Molecular, Cell, and Developmental Biology retreat. Santa Monica, CA. **Graduate Student Best Poster Award.**

Giafaglione JM. (2021) Talk: Reciprocal regulation of metabolism and lineage identity in the benign prostate and prostate cancer. SPORE Trainee Meeting. Los Angeles, CA.

Giafaglione JM. (2021) Talk: Metabolic modulation of cell fate to combat treatment-resistant prostate cancer. Molecular Biology Interdepartmental Doctoral Program Retreat. Los Angeles, CA.

Giafaglione JM. (2020) Talk: Identifying metabolic vulnerabilities to overcome antiandrogen therapy resistance in prostate cancer. UCLA Metabolism Interest Group. Los Angeles, CA.

Giafaglione JM. … Goldstein AS. (2019) Poster: Investigating the role of Rb family member Rbl2 in castration-resistant prostate cancer lineage plasticity. Society for Basic Urologic Research. New Orleans, LA.

Giafaglione JM. … Brandman O. (2017) Poster: Understanding the Factors that Influence Aggregation of CATylated Proteins. Stanford University Biochemistry Department Retreat. Palo Alto, CA.

Giafaglione JM. … Chedin F. (2016). Poster: Single Molecule Resolution Footprinting of R-loops in the Human Genome. UC Davis Undergraduate Research Conference. Davis, CA.

AWARDS AND HONORS

- Dissertation Year Fellowship, UCLA Graduate Division (2023)
- Whitcome Fellowship, UCLA (2023)
- Eli and Edythe BSCRC Training Program, UCLA (2021 – 2023)
- NIH Cell and Molecular Biology T32 Training Grant, UCLA (2019 – 2021)
- MCDB Retreat Graduate Student Best Poster Award, UCLA (2021)
- Graduate Dean’s Scholar, UCLA (2018 – Present)
- Genetics and Genomics Departmental Citation Award, UC Davis (2017)
- Genetics and Genomics Outstanding Performance Citation Award, UC Davis (2017)
- Phi Kappa Phi Honor Society (2016)
- Regents Scholar, UC Davis (2013 – 2017)

Chapter 1: Introduction

The prostate gland and prostate progenitor cells

The prostate is a walnut-sized gland in the male reproductive system that surrounds the urethra and is located between the base of the penis and the rectum (**Figure 1A**)[1]. The seminal fluid produced by the prostate is a critical component of semen, which nourishes and transports sperm during ejaculation[2]. The prostate gland contains ducts with an inner layer of epithelium composed of basal, luminal, and rare neuroendocrine cells (**Figure 1B**)[1]. The luminal cells have a secretory function and reside adjacent to the lumen of the gland. The basal cells line the basement membrane of the gland and are surrounded by the stroma, which contains fibroblasts and smooth muscle cells[1]. Lineage tracing studies have illustrated that prostate epithelial cells are predominantly self-sustained by distinct progenitors in the adult mouse under normal physiological conditions[3]. However, luminal differentiation from basal progenitors occurs during development[4, 5], tissue regeneration[6], inflammation[7, 8], and prostate cancer initiation[3, 9]. Furthermore, emerging data supports the existence of multipotent luminal progenitors as well as luminal-committed progenitors[10, 11].

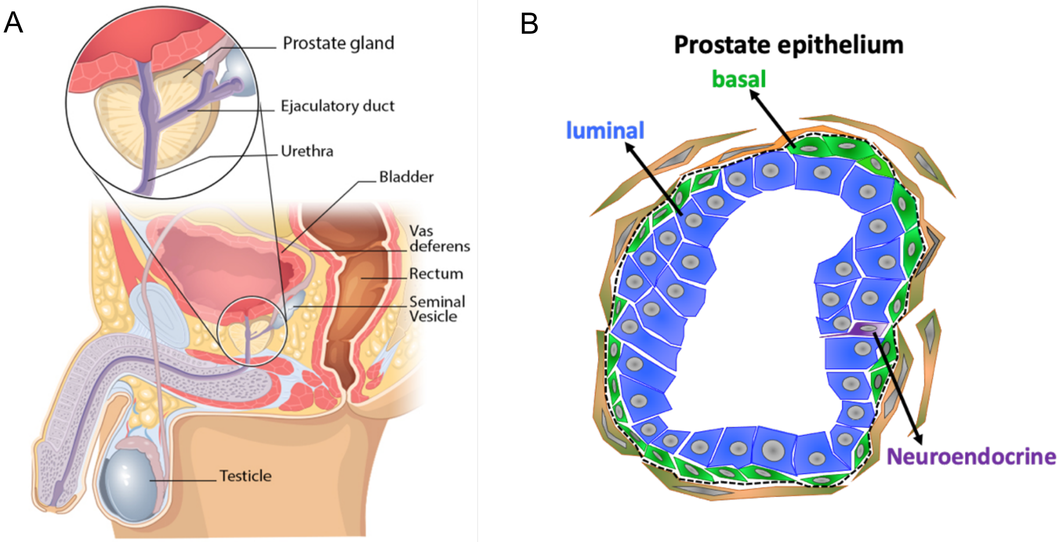

Figure 1. The prostate gland. A) Schematic of prostate within pelvic region. Figure from the Centers for Disease Control and Prevention. **B)** Cross section of prostate epithelium illustrating stromal cells (orange), basal cells (green), luminal cells (blue), and neuroendocrine cells (purple).

Cellular differentiation

Cellular differentiation is a process mediated by cell signaling and the epigenome that results in a stem or progenitor cell becoming a more specialized cell type. Differentiation can dramatically change a cell’s size, shape, metabolic activity, and functional abilities. Each cell type possesses a unique set of characteristics and functions that enables it to contribute to the overall functioning of the organism. Distinct cell types can be distinguished by their unique transcriptome and surface marker expression.

Ex vivo models to study prostate progenitor cells and prostate cancer

In vivo lineage tracing has been utilized to define the differentiation capacity of mouse prostate basal and luminal cells during development, tissue regeneration and transformation. In addition, genetically engineered mouse models (GEMMs) have been used to define the factors that regulate prostate cancer initiation and treatment resistance. However, the generation of *in vivo* lineage tracing models and GEMMs often requires extensive mouse breeding and can be cost- and time-prohibitive. In the prostate organoid assay, primary basal and luminal cells isolated from mice of any genetic background can generate prostate epithelium *ex vivo* in approximately a week[10–12]. Furthermore, cells can be genetically manipulated or treated with small molecules before or after plating into organoid culture. The organoid system enables the evaluation of cell-intrinsic and -extrinsic regulators of prostate differentiation and cancer progression in a cost and time efficient manner.

In Chapter 2, I describe our group’s effort to further optimize prostate organoid culture methods. Notable challenges associated with culturing prostate organoids include excluding two-dimensional (2D) colonies that form beneath the Matrigel matrix from analysis, maintaining the integrity of the Matrigel during media changes, and counting organoids accurately. Our approach entails coating plates with poly(2-hydroxyethyl methacrylate) (Poly-HEMA) to prevent the formation of 2D colonies. Furthermore, cells are plated into a Matrigel ring, rather than a Matrigel disc, which makes changing the media and counting organoids less challenging. We also describe our approaches to harvest organoids for collection of protein lysate and for whole-mount confocal microscopy. In Chapter 3, I use these methods extensively to define the metabolic regulation of cell fate in the prostate epithelium.

Interplay between metabolism, epigenetics, and cell fate

Metabolic pathways serve as regulators of cell fate, orchestrating a complex interplay between energy homeostasis, biosynthesis, signaling pathways, and epigenetics. Epigenetic marks have the capacity to integrate the expression state of chromatin with the metabolic state of the cell because most chromatin-modifying enzymes require intermediates of cellular metabolism as substrates or cofactors (**Figure 2**). *S*-adenosylmethionine (SAM) is generated from methionine and is a substrate for histone and DNA methylation, while α-ketoglutarate (αKG) is a required cofactor for jumonji histone demethylases[13, 14]. Furthermore, histone acetylation is dependent on acetyl-CoA, which can be generated by the metabolic enzymes ACLY, ACSS2, or PDHA1[15–17]. Through these and other mechanisms, metabolic signaling has been shown to influence cell fate, cell function, and the balance between stem cell self-renewal and differentiation. For example, hematopoietic stem cell function and leukemogenesis are limited by the accumulation of ascorbate, which regulates TET2, a dioxygenase that demethylates DNA[18]. Epidermal stem cells activate *de novo* serine synthesis in response to serine starvation, which stimulates αKG-dependent demethylases, activates differentiation programs, and antagonizes squamous cell carcinoma growth[19]. Proper hippocampal function is dependent on the metabolic enzyme ACSS2 associating with chromatin to increase local concentrations of acetyl-CoA to promote histone acetylation and transcription of neuronal genes[16]. While metabolic rewiring can modulate cell fate and function in a wide variety of tissue systems, the interplay between metabolic signaling and lineage identity in the prostate is poorly elucidated.

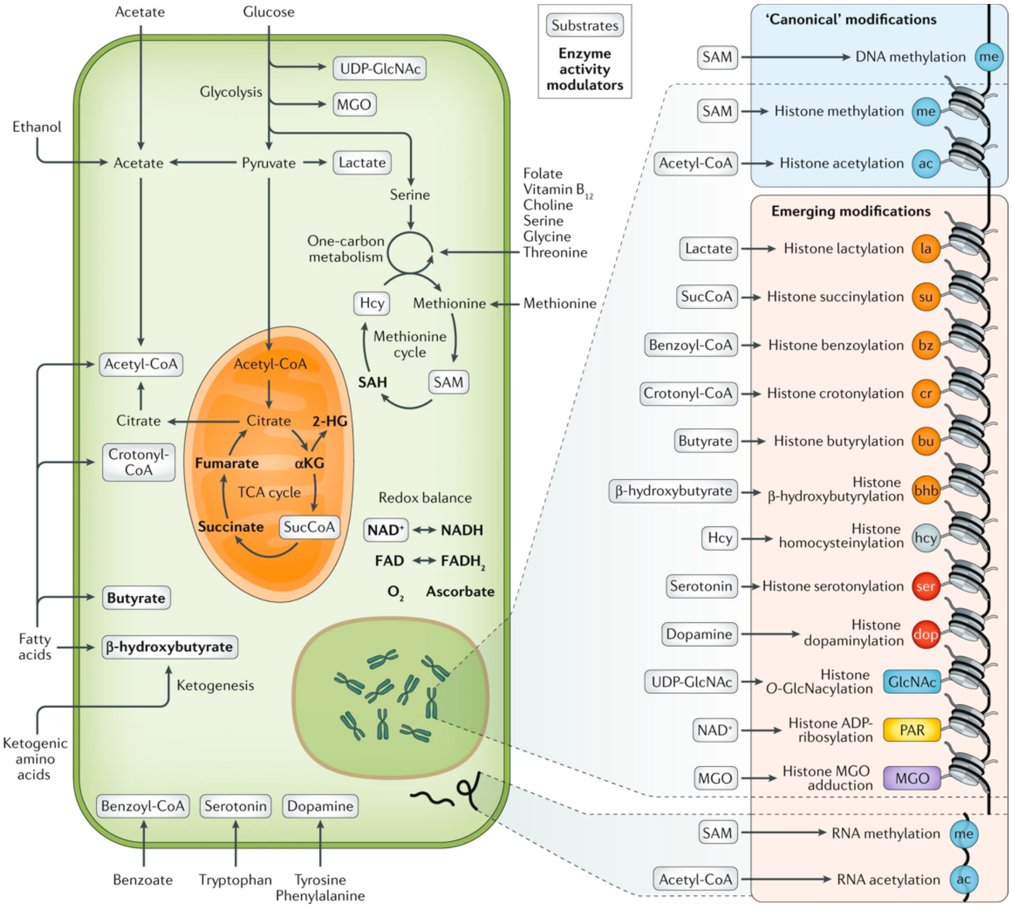

Figure 2. Metabolic pathways produce chromatin-modifying metabolites. Figure from Dai *et al.*, *Nature Reviews Genetics* (2020)[20]

Epigenetic changes have been implicated in the establishment and maintenance of prostate epithelial identity. For example, deacetylation of KLF5 induces excess basal to luminal differentiation[21], while de-repression of the histone methyltransferase *EZH2* facilitates loss of luminal identity and activation of pluripotency networks[22–24]. *FOXA1* is recurrently mutated in localized and metastatic prostate tumors[25], and these mutations alter chromatin accessibility to drive luminal, mesenchymal or neuroendocrine differentiation phenotypes[26, 27]. How upstream metabolic signaling contributes to the downstream epigenetic regulation of prostate lineage identity remains poorly understood. Understanding the molecular mechanisms that govern prostate cell fate is critical as lineage transitions are a central feature of prostate development[4, 5], tumorigenesis[3, 9], and treatment resistance[28, 29].

In Chapter 3, I describe our group's investigation of the metabolic regulation of cell fate in the prostate epithelium. We developed an approach to perform metabolic profiling and heavy isotope nutrient tracing on primary prostate epithelial cells. Using this approach, we discover that basal and luminal cells have distinct metabolic signatures and nutrient utilization patterns. We also demonstrate that basal to luminal differentiation is accompanied by increased pyruvate oxidation. The mitochondrial pyruvate carrier (MPC) and subsequent lactate accumulation emerged as regulators of prostate luminal identity. Inhibition of the MPC or supplementation with exogenous lactate reprogram the chromatin landscape of key lineage-specific transcription factors and modulate response to antiandrogen treatment. Our results indicate that prostate epithelial cells have lineage-rooted metabolic features and that modulation of metabolism can govern prostate lineage transitions through epigenetic mechanisms.

Prostate cancer initiation

Prostate cancer is the most frequently diagnosed cancer among men in the United States, with over 280,000 new cases expected in 2023[30]. The most well-established risk factors for prostate cancer include age, family history, genetics, and chronic inflammation. The probability of developing prostate cancer increases from about 1.9% in men 60-69 years old to 9% in men 70 and older[31]. Furthermore, men that have a first-degree relative with prostate cancer have an approximately 2.5-fold increased risk of being diagnosed with prostate cancer themselves[32]. Data from twin studies suggest that prostate cancer is one of the most genetically heritable cancers, with an estimated 58% of prostate cancers being driven by heritable genetic factors[33, 34]. Proliferative inflammatory atrophy (PIA), a precursor for prostate cancer, is characterized by an inflammation-associated luminal epithelial layer with an atrophic appearance and increased proliferative index[35]. A progenitor-enriched subpopulation of luminal cells, marked by low CD38 expression, resides adjacent to areas of inflammation and has been shown to be more susceptible to transformation[36]. These findings implicate chronic inflammation in prostate cancer initiation.

The majority of prostate cancers arise in the peripheral zone of the prostate[1]. Luminal cells were originally believed to be the cells of origin for prostate cancer based on the histological absence of basal cell markers. However, studies in the mouse prostate have demonstrated that both basal[37–39] and luminal[40–42] cells can serve as cells of origin for prostate cancer. In addition, basal cells isolated from benign human prostate can give rise to adenocarcinomas following oncogenic transformation[9, 43]. Despite arising from distinct cell types, both basal- and luminal-derived prostate tumors exhibit an adenocarcinoma luminal phenotype because basal to luminal differentiation proceeds prostate cancer initiation from basal cells[9, 43].

Normal prostate epithelium and primary prostate cancer metabolism

The metabolism of the normal prostate epithelium is regulated by androgen receptor (AR) signaling and characterized by an incomplete tricarboxylic acid (TCA) cycle. Zinc accumulates in the prostate epithelium and inhibits mitochondrial aconitase (ACO2), the enzyme that catalyzes the oxidation of citrate, to enable the secretion of citrate into the prostatic fluid[44]. Consequently, the prostate epithelium relies predominantly on glycolysis for ATP production, as it cannot produce reducing equivalents in the TCA cycle to power oxidative phosphorylation. Prostate cancer initiation is associated with metabolic reprogramming, which enables cells to consume citrate to fuel oxidative phosphorylation and lipogenesis (**Figure 3**)[45, 46]. Unlike most cancers, localized prostate cancers are not highly glycolytic and therefore cannot be reliably detected using the radiolabeled glucose analogue ^{18}F-fluorodeoxyglucose (FDG)[47].

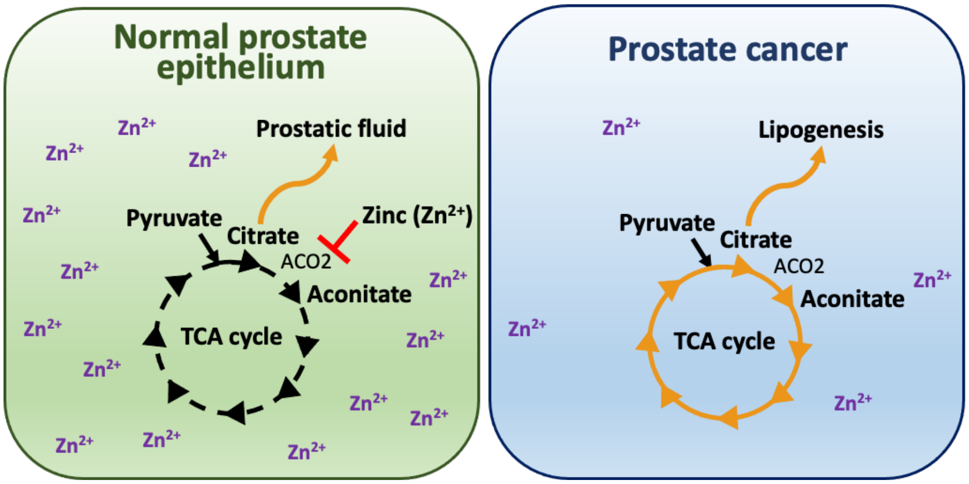

Figure 3. Metabolic rewiring of citrate metabolism during prostate cancer. Zinc accumulation in the normal prostate epithelium inhibits ACO2, which enables the secretion of citrate into the prostatic fluid. In prostate cancer, zinc accumulation is reduced, enabling citrate to fuel the TCA cycle and lipogenesis.

Prostate cancer treatment resistance

Prostate cancer is the leading cause of cancer-related death in non-smoking men[30]. In 2023, an estimated 34,700 men in the United States will die from prostate cancer[30]. Patients with localized or regional prostate cancer have a 5-year survival rate of greater than 99% and are typically treated with surgery and/or radiation[30]. On the other hand, patients with metastatic prostate cancers have a 5-year survival rate of only 32%[30].

AR is a nuclear steroid hormone receptor that functions as a transcription factor to regulate prostate development and prostate cell proliferation[48]. Therefore, patients with advanced tumors are treated with androgen deprivation therapy (ADT) to dampen AR activity[49]. However, ADT is typically palliative and prostate cancer cells often adapt to restore AR signaling even when androgen production is low, leading to recurrence as castration-resistant prostate cancer[49]. Mechanisms of aberrant AR activity include increased production of its ligand, dihydrotestosterone, AR mutation, AR amplification, and the expression of constitutively active

AR splice variants[48]. Castration-resistant tumors remain dependent on AR signaling and are treated with next-generation AR pathway inhibitors, such as Enzalutamide[50]. Prolonged AR pathway inhibition can drive the formation of AR-indifferent tumors with basal, small cell, and/or neuroendocrine features that are resistant to treatment (**Figure 4**)[23, 24, 28, 29, 51]. Consequently, patients diagnosed with this form of prostate cancer typically succumb to the disease within one year[52]. New approaches are needed to understand how prostate cancer cells respond to therapy in order to exploit treatment-induced vulnerabilities and prevent or delay disease progression.

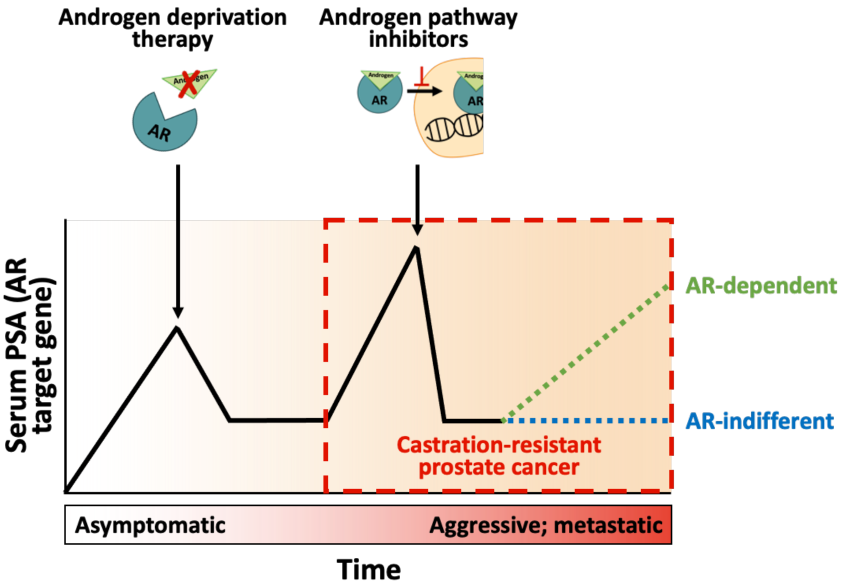

Figure 4. Prostate cancer progression. Prostate cancer that recurs after surgery or radiation is treated with androgen deprivation therapy (ADT). Prostate cancer that recurs after ADT is termed castration-resistant prostate cancer and is treated with androgen pathway inhibitors (APIs). Following treatment with APIs, patients can develop AR-dependent or AR-indifferent resistant disease.

Evolution of metabolic requirements and vulnerabilities during cancer progression

Metabolic reprogramming is a hallmark of malignancy[53]. In many cases, altered energy metabolism can be exploited to diagnose, monitor, and/or treat cancer. Importantly, metabolic requirements and vulnerabilities evolve as the disease progresses from premalignant lesions to locally invasive tumors to metastatic cancer. For example, several studies demonstrate that in order for a cancer to metastasize, cells must activate mechanisms to resist the oxidative stress induced by the harsh environment in the bloodstream[54, 55]. Furthermore, therapy resistant tumors develop dependence on metabolic pathways that are distinct from those required by primary treatment-naïve tumors. In pancreatic cancer, mutated KRAS promotes upregulation of NRF2, a master regulator of antioxidant metabolism, and contributes to resistance to chemotherapy[56]. Interestingly, glutaminase inhibitors re-sensitize chemoresistant pancreatic cancer cells to therapy[56]. Therefore, it is critical to understand how metabolic phenotypes evolve during cancer progression in order to identify metabolic vulnerabilities that can be exploited to treat patients.

Several studies demonstrate that metabolic pathways can be targeted to antagonize prostate cancer cell growth. For example, targeting lipogenesis via FASN inhibition, glutamine utilization via GLS inhibition, or mitochondrial pyruvate import via MPC inhibition impairs castration-resistant prostate cancer growth[57–59]. In addition, CAMKK2 inhibition impairs prostate cancer growth by disrupting anabolic metabolism[60, 61]. Unlike localized prostate cancer, metastatic neuroendocrine prostate cancer is highly glycolytic and can be detected by ^{18}F-FDG imaging, illustrating that metabolic reprogramming occurs during the transition from AR-dependent to AR-indifferent disease[62]. Inhibition of the mTORC1/ATF4/PHGDH axis or lactate export via MCT4 inhibition antagonize the growth of neuroendocrine prostate cancers[63, 64]. AR inhibition has been shown to increase reliance on electron transport chain complex I activity and glutaminase activity[65]; however, the mechanisms that govern AR inhibition-induced metabolic rewiring have not been clearly defined. Elucidating the molecular mechanisms that regulate how prostate cancer cells respond to AR-targeted therapies is critical in order to develop approaches to prevent or delay disease progression.

In Chapter 4, I describe our group's investigation into the regulation of treatment-induced metabolic phenotypes and vulnerabilities in prostate cancer. We use transcriptomics, metabolomics, and bioenergetics approaches to comprehensively characterize the effect of AR blockade on prostate cancer metabolism. The metabolic response to AR inhibition is defined by maintenance of oxidative phosphorylation and reduced glycolysis, resulting in increased reliance on oxidative mitochondrial metabolism. We establish DRP1 activity and MYC signaling as mediators of AR blockade-induced metabolic phenotypes. Rescuing DRP1 phosphorylation after AR inhibition restores mitochondrial fission, while rescuing MYC restores glycolytic activity and glutamine metabolism and reverses sensitivity to complex I inhibition. Our findings identify altered metabolic signaling as a mechanism through which prostate cancer cells survive AR blockade and highlight the potential of therapies that target metabolic vulnerabilities in AR-inhibited cells.

References

1. Ittmann, M. Anatomy and histology of the human and murine prostate. *Cold Spring Harbor Perspectives in Medicine*. **8** (5), doi: 10.1101/cshperspect.a030346 (2023).

2. Verze, P., Cai, T., Lorenzetti, S. The role of the prostate in male fertility, health and disease. *Nature Reviews Urology*. **13** (7), 379–386, doi: 10.1038/nrurol.2016.89 (2016).

3. Choi, N., Zhang, B., Zhang, L., *et al.* Adult murine prostate basal and luminal cells are self-sustained lineages that can both serve as targets for prostate cancer initiation. *Cancer Cell*. **21** (2), 253–265, doi: 10.1016/j.ccr.2012.01.005 (2012).

4. Ousset, M., Keymeulen, A. Van, Bouvencourt, G., *et al.* Multipotent and unipotent progenitors contribute to prostate postnatal development. *Nature Cell Biology*. **14** (11), doi: 10.1038/ncb2600 (2012).

5. Wang, J., Zhu, H.H., Chu, M., *et al.* Symmetrical and asymmetrical division analysis provides evidence for a hierarchy of prostate epithelial cell lineages. *Nature Communications*. **5** (4758), doi: 10.1038/ncomms5758 (2014).

6. Wang, Z.A., Mitrofanova, A., Bergren, S.K., *et al.* Lineage analysis of basal epithelial cells reveals their unexpected plasticity and supports a cell-of-origin model for prostate cancer heterogeneity. *Nature Cell Biology*. **15** (3), 274–283, doi: 10.1038/ncb2697 (2013).

7. Kwon, O., Zhang, B., Zhang, L., *et al.* High fat diet promotes prostatic basal-to-luminal differentiation and accelerates initiation of prostate epithelial hyperplasia originated from basal cells. *Stem Cell Research*. **16** (3), 682–691, doi: 10.1016/j.scr.2016.04.009 (2016).

8. Kwon, O., Zhang, L., Ittmann, M.M., *et al.* Prostatic inflammation enhances basal-to-luminal differentiation and accelerates initiation of prostate cancer with a basal cell origin. *PNAS*. **5** (111), doi: 10.1073/pnas.1318157111 (2013).

9. Stoyanova, T., Cooper, A.R., Drake, J.M., *et al.* Prostate cancer originating in basal cells progresses to adenocarcinoma propagated by luminal-like cells. *PNAS*. **110** (50), 20111–20116, doi: 10.1073/pnas.1320565110 (2013).

10. Agarwal, S., Hynes, P.G.G., Tillman, H.S.S., *et al.* Identification of Different Classes of Luminal Progenitor Cells within Prostate Tumors. *Cell Reports*. **13** (10), 2147–2158, doi: 10.1016/j.celrep.2015.10.077 (2015).

11. Karthaus, W.R., Iaquinta, P.J., Drost, J., *et al.* Identification of multipotent luminal progenitor cells in human prostate organoid cultures. *Cell*. **159** (1), 163–175, doi: 10.1016/j.cell.2014.08.017 (2014).

12. Drost, J., Karthaus, W.R., Gao, D., *et al.* Organoid culture systems for prostate epithelial and cancer tissue. *Nature Protocols*. **11** (2), 347–358, doi: 10.1038/nprot.2016.006 (2016).

13. Mentch, S.J., Mehrmohamadi, M., Huang, L., *et al.* Histone methylation dynamics and gene regulation occur through the sensing of one-carbon metabolism. *Celll Metabolism*. **22** (5), 861–873, doi: 10.1016/j.cmet.2015.08.024 (2015).

14. Carey, B.W., Finley, L.W.S., Cross, J.R., *et al.* Intracellular a-ketoglutarate maintains the pluripotency of embryonic stem cells. *Nature*. **518** (7539), 413–416, doi: 10.1038/nature13981 (2015).

15. Wellen, K.E., Hatzivassiliou, G., Sachdeva, U.M., *et al.* ATP-citrate lyase links cellular metabolism to histone acetylation. *Science*. **324** (5930), 1076–1081 (2009).

16. Mews, P., Donahue, G., Drake, A.M., *et al.* Acetyl-CoA synthetase regulates histone acetylation and hippocampal memory. *Nature*. **546** (7658), 381–386, doi: 10.1038/nature22405 (2017).

17. Nagaraj, R., Sharpley, M.S., Chi, F., *et al.* Nuclear localization of mitochondrial TCA cycle enzymes as a critical step in mammalian zygotic genome activation. *Cell*. **168** (1–2), 210-223.e11, doi: 10.1016/j.cell.2016.12.026 (2016).

18. Agathocleous, M., Meacham, C.E., Burgess, R.J., *et al.* Ascorbate regulates haematopoietic stem cell function and leukaemogenesis. *Nature*. **549** (7673), 476–481, doi: 10.1038/nature23876 (2017).

19. Baksh, S.C., Todorova, P.K., Gur-cohen, S., *et al.* Extracellular serine controls epidermal stem cell fate and tumour initiation. *Nature Cell Biology*. **22** (7), 779–790, doi: 10.1038/s41556-020-0525-9 (2020).

20. Dai, Z., Ramesh, V., Locasale, J.W. The evolving metabolic landscape of chromatin biology and epigenetics. *Nature Reviews Genetics*. **21** (12), 737–753, doi: 10.1038/s41576-020-0270-8 (2020).

21. Zhang, B., Ci, X., Tao, R., *et al.* Klf5 acetylation regulates luminal differentiation of basal progenitors in prostate development and regeneration. *Nature Communications*. **11** (1), doi: 10.1038/s41467-020-14737-8 (2020).

22. Ku, S.Y., Rosario, S., Wang, Y., *et al.* Rb1 and Trp53 cooperate to suppress prostate cancer lineage plasticity, metastasis, and antiandrogen resistance. *Science*. **355** (6320), 78–83, doi: 10.1126/science.aah4199 (2017).

23. Dardenne, E., Beltran, H., Benelli, M., *et al.* N-Myc induces an EZH2-mediated transcriptional program driving neuroendocrine prostate cancer. *Cancer Cell*. **30** (4), 563–577, doi: 10.1016/j.ccell.2016.09.005 (2016).

24. Berger, A., Beltran, H., Rickman, D.S., *et al.* N-Myc –mediated epigenetic reprogramming drives lineage plasticity in advanced prostate cancer. *Journal of Clinical Investigation*. **129** (9), 3924–3940, doi: 10.1172/JCI127961 (2019).

25. Fraser, M., Livingstone, J., Wrana, J.L., *et al.* Somatic driver mutation prevalence in 1844 prostate cancers identifies ZNRF3 loss as a predictor of metastatic relapse. *Nature Communications*. **12** (6248), 1–15, doi: 10.1038/s41467-021-26489-0 (2021).

26. Adams, E.J., Karthaus, W.R., Hoover, E., *et al.* FOXA1 mutations alter pioneering activity, differentiation and prostate cancer phenotypes. *Nature*. **571** (7765), doi: 10.1038/s41586-019-1318-9 (2019).

27. Parolia, A., Cieslik, M., Chu, S., *et al.* Distinct structural classes of activating FOXA1 alterations in advanced prostate cancer. *Nature*. **571** (7765), doi: 10.1038/s41586-019-1347-4 (2019).

28. Ku, S.Y., Rosario, S., Wang, Y., *et al.* Rb1 and Trp53 cooperate to suppress prostate cancer lineage plasticity, metastasis, and antiandrogen resistance. *Science*. **355** (6320), 78–83, doi: 10.1126/science.aah4199 (2017).

29. Beltran, H., Hruszkewycz, A., Scher, H.I., *et al.* The role of lineage plasticity in prostate cancer therapy resistance. *Clinical Cancer Research*. **25** (23), 6916–6924, doi: 10.1158/1078-0432.CCR-19-1423 (2019).

30. Siegel, R.L., Miller, K.D., Wagle, N.S., *et al.* Cancer statistics, 2023. *CA: A Cancer Journal for Clinicians*. **73**, 17–48, doi: 10.3322/caac.21763 (2023).

31. Bergengren, O., Pekala, K.R., Matsoukas, K., *et al.* 2022 update on prostate cancer epidemiology and risk factors — A systematic review. *European Urology*. **84** (2), 191–206, doi: 10.1016/j.eururo.2023.04.021 (2023).

32. Johns, L., Houlston, R. A systematic review and meta-analysis of familial prostate cancer risk. *BJU International*. **91** (9), 789–794, doi: 10.1046/j.1464-410X.2003.04232.x (2003).

33. Mucci, L.A., Hjelmborg, J.B., Harris, J.R., *et al.* Familial risk and heritability of cancer among twins in nordic countries. *JAMA*. **315** (1), 68–76, doi: 10.1001/jama.2015.17703 (2023).

34. Lichtenstein, P., Holm, N. V, Verkasalo, P.K., *et al.* Environmental and heritable factors in the causation of cancer - analyses of cohorts of twins from Sweden, Denmark, and Finland. *New England Journal of Medicine*. **343** (2), 78–85, doi: 10.1056/NEJM200007133430201 (2000).

35. De Marzo, A.M., Marchi, V.L., Epstein, J.I., *et al.* Proliferative inflammatory atrophy of the prostate: implications for prostatic carcinogenesis. *The American Journal of Pathology*. **155** (6), 1985–1992, doi: 10.1016/S0002-9440(10)65517-4 (1999).

36. Liu, X., Grogan, T.R., Hieronymus, H., *et al.* Low CD38 identifies progenitor-like inflammation-associated luminal cells that can initiate human prostate cancer and predict poor outcome. *Cell Reports*. **17** (10), 2596–2606, doi: 10.1016/j.celrep.2016.11.010 (2016).

37. Lawson, D.A., Zong, Y., Memarzadeh, S., *et al.* Basal epithelial stem cells are efficient targets for prostate cancer initiation. *PNAS*. **107** (6), 2610–2615, doi: 10.1073/pnas.0913873107 (2009).

38. Mulholland, D.J., Xin, L., Morim, A., *et al.* Lin− Sca-1+ CD49f high stem / progenitors are tumor-initiating cells in the Pten-null prostate cancer model. *Cancer Research*. **69** (22), 8555–8562, doi: 10.1158/0008-5472.CAN-08-4673 (2009).

39. Wang, S., Garcia, A.J., Wu, M., *et al.* Pten deletion leads to the expansion of a prostatic stem/progenitor cell subpopulation and tumor initiation. *PNAS*. **103** (5), 1480–1485, doi: 10.1073/pnas.0510652103 (2006).

40. Ma, X., Made, A.C.Z. Der, Autar, B., *et al.* Targeted biallelic inactivation of Pten in the mouse prostate leads to prostate cancer accompanied by increased epithelial cell proliferation but not by reduced apoptosis. *Cancer Research*. **65** (13), 5730–5739, doi: 10.1158/0008-5472.CAN-04-4519 (2005).

41. Wang, X., Julio, M.K., Economides, K.D., *et al.* A luminal epithelial stem cell that is a cell of origin for prostate cancer. *Nature*. **461** (7263), 495–500, doi: 10.1038/nature08361 (2009).

42. Iwata, T., Schultz, D., Hicks, J., *et al.* MYC Overexpression Induces Prostatic Intraepithelial Neoplasia and Loss of Nkx3.1 in Mouse Luminal Epithelial Cells. *PlOS One*. **5** (2), doi: 10.1371/journal.pone.0009427 (2010).

43. Goldstein, A.S., Huang, J., Guo, C., *et al.* Identification of a Cell of Origin for Human Prostate Cancer. *Science*. (July), 568–572 (2010).

44. Costello, L.C., Franklin, R.B. Aconitase activity, citrate oxidation, and zinc inhibition in rat ventral prostate. *Enzyme*. **26** (6), 281–287, doi: 10.1159/000459195 (1981).

45. Costello, L.C., Franklin, R.B. The clinical relevance of the metabolism of prostate cancer; zinc and tumor suppression: connecting the dots. *Molecular Cancer*. **5** (17), 1–13, doi: 10.1186/1476-4598-5-17 (2006).

46. Zadra, G., Photopoulos, C., Loda, M. The fat side of prostate cancer. *Molecular and Cell Biology of Lipids*. **1831** (10), 1518–1532, doi: 10.1016/j.bbalip.2013.03.010 (2013).

47. Liu, I.J., Zafar, M.B., Lai, Y., *et al.* Fluorodeoxyglucose positron emission tomography studies in diagnosis and staging of clinically organ-confined prostate cancer. *Urology*. **57** (1), 108–111, doi: 10.1016/s0090-4295(00)00896-7 (2001).

48. Hu, R., Denmeade, S.R., Luo, J. Molecular processes leading to aberrant androgen receptor signaling and castration resistance in prostate cancer. *Expert Rev Endocrinol Metab*. **5** (5), 753–764, doi: 10.1586/eem.10.49.Molecular (2011).

49. Sayegh, N., Swami, U., Agarwal, N. Recent Advances in the Management of Metastatic Prostate Cancer. *JCO Oncol Pract*. **18** (1), 45–55, doi: 10.1200/OP.21.00206 (2022).

50. Tran, C., Ouk, S., Clegg, N.J., *et al.* Development of a second-generation antiandrogen for treatment of advanced prostate cancer. *Science*. **324** (5928), 787–791, doi: 10.1126/science.1168175 (2009).

51. Davies, A.H., Beltran, H., Zoubeidi, A. Cellular plasticity and the neuroendocrine phenotype in prostate cancer. *Nature Reviews Urology*. **15** (5), 271–286, doi: 10.1038/nrurol.2018.22 (2018).

52. Beltran, H., Rickman, D.S., Park, K., *et al.* Molecular Characterization of Neuroendocrine Prostate Cancer and Identification of New Drug Targets. *Cancer Discovery*. **1** (6), 487–496, doi: 10.1158/2159-8290.cd-11-0130 (2011).

53. Hanahan, D., Weinberg, R.A. Hallmarks of cancer: the next generation. *Cell*. **144** (5), 646–674, doi: 10.1016/j.cell.2011.02.013 (2011).

54. Piskounova, E., Agathocleous, M., Murphy, M.M., *et al.* Oxidative stress inhibits distant metastasis by human melanoma cells. *Nature*. **527**, 186–191, doi: 10.1038/nature15726 (2015).

55. Tasdogan, A., Faubert, B., Ramesh, V., *et al.* Metabolic heterogeneity confers differences in melanoma metastatic potential. *Nature*. **577** (7788), 115–120, doi: 10.1038/s41586-019-1847-2 (2020).

56. Mukhopadhyay, S., Goswami, D., Adiseshaiah, P.P., *et al.* Undermining glutaminolysis bolsters chemotherapy while NRF2 promotes chemoresistance in KRAS-driven pancreatic cancers. *Cancer Research*. **80** (8), 1630–1643, doi: 10.1158/0008-5472.CAN-19-1363 (2020).

57. Zadra, G., Ribeiro, C.F., Chetta, P., *et al.* Inhibition of de novo lipogenesis targets androgen receptor signaling in castration-resistant prostate cancer. *PNAS*. **116** (2), 631–640, doi: 10.1073/pnas.1808834116 (2019).

58. Xu, L., Yin, Y., Li, Y., *et al.* A glutaminase isoform switch drives therapeutic resistance and disease progression of prostate cancer. *PNAS*. **118** (13), 1–11, doi: 10.1073/pnas.2012748118 (2021).

59. Bader, D.A., Hartig, S.M., Putluri, V., *et al.* Mitochondrial pyruvate import is a metabolic vulnerability in androgen recptor-driven prostate cancer. *Nature Metabolism*. **1** (1), 70–85, doi: 10.1038/s42255-018-0002-y (2019).

60. Massie, C.E., Lynch, A., Ramos-montoya, A., *et al.* The androgen receptor fuels prostate cancer by regulating central metabolism and biosynthesis. *EMBO*. **30** (13), 2719–2733, doi: 10.1038/emboj.2011.158 (2011).

61. Frigo, D.E., Howe, M.K., Wittmann, B.M., *et al.* CaM kinase kinase beta-mediated activation of the growth regulatory kinase AMPK is required for androgen-dependentmigration of prostate cancer cells. *Cancer Research*. **71** (2), 528–537, doi: 10.1158/0008-5472.CAN-10-2581 (2011).

62. Spratt, D.E., Gavane, S., Tarlinton, L., *et al.* Utility of FDG-PET in clinical neuroendocrine prostate cancer. *The Prostate*. **74**, 1153–1159, doi: 10.1002/pros.22831 (2014).

63. Reina-campos, M., Linares, J.F., Duran, A., *et al.* Increased serine and one-carbon pathway metabolism by PKC I / i deficiency promotes neuroendocrine prostate cancer. *Cancer Cell*. **35** (3), 385–400, doi: 10.1016/j.ccell.2019.01.018 (2019).

64. Choi, S.Y.C., Ettinger, S.L., Lin, D., *et al.* Targeting MCT4 to reduce lactic acid secretion and glycolysis for treatment of neuroendocrine prostate cancer. *Cancer Medicine*. **7** (7), 3385–3392, doi: 10.1002/cam4.1587 (2018).

65. Basu, H.S., Wilganowski, N., Robertson, S., *et al.* Prostate cancer cells survive anti-androgen and mitochondrial metabolic inhibitors by modulating glycolysis and mitochondrial metabolic activities. *The Prostate*. **81** (12), 799–811, doi: 10.1002/pros.24146 (2021).

66. Lukacs, R.U., Goldstein, A.S., Lawson, D.A., *et al.* Isolation, cultivation and

characterization of adult murine prostate stem cells. *Nature protocols*. **5** (4), 702–713, doi: 10.1038/nprot.2010.11 (2010).

67. Hoadley, K.A., Yau, C., Hinoue, T., *et al.* Cell-of-origin patterns dominate the molecular classification of 10,000 tumors from 33 types of cancer. *Cell*. **173** (2), 291–304, doi: 10.1016/j.cell.2018.03.022 (2018).

Chapter 2: Evaluating the differentiation capacity of mouse prostate epithelial cells using organoid culture

Title: Evaluating the Differentiation Capacity of Mouse Prostate Epithelial Cells Using Organoid Culture

Authors and affiliations
Preston D. Crowell[1]*, Jenna M. Giafaglione[1]*, Takao Hashimoto[2], Johnny A. Diaz[2], Andrew S. Goldstein[2-6]

[1]Molecular Biology Interdepartmental Program, University of California, Los Angeles, Los Angeles, CA, USA
[2]Department of Molecular, Cell, and Developmental Biology, University of California, Los Angeles, Los Angeles, CA, USA
[3]Department of Urology, David Geffen School of Medicine, University of California, Los Angeles, Los Angeles, CA, USA
[4]Eli and Edythe Broad Center of Regenerative Medicine and Stem Cell Research, University of California, Los Angeles, Los Angeles, CA, USA
[5]Jonsson Comprehensive Cancer Center, University of California, Los Angeles, Los Angeles, CA, USA
[6]Molecular Biology Institute, University of California, Los Angeles, Los Angeles, CA, USA
*These authors contributed equally

Corresponding author:
Andrew Goldstein
Email: agoldstein@mednet.ucla.edu

Keywords
organoid, prostate, epithelium, progenitor, basal, luminal, differentiation, mouse

Short abstract

Mouse prostate organoids represent a promising context to evaluate mechanisms that regulate differentiation. This paper describes an improved approach to establish prostate organoids, and introduces methods to (1) collect protein lysate from organoids, and (2) fix and stain organoids for whole-mount confocal microscopy.

Long abstract

The prostate epithelium is comprised predominantly of basal and luminal cells. *In vivo* lineage tracing has been utilized to define the differentiation capacity of mouse prostate basal and luminal cells during development, tissue-regeneration and transformation. However, evaluating cell-intrinsic and extrinsic regulators of prostate epithelial differentiation capacity using a lineage tracing approach often requires extensive breeding and can be cost-prohibitive. In the prostate

organoid assay, basal and luminal cells generate prostatic epithelium *ex vivo*. Importantly, primary epithelial cells can be isolated from mice of any genetic background or mice treated with any number of small molecules prior to, or after, plating into three-dimensional (3D) culture. Sufficient material for evaluation of differentiation capacity is generated after 7-10 days. Collection of basal-derived and luminal-derived organoids for (1) protein analysis by Western blot and (2) immunohistochemical analysis of intact organoids by whole-mount confocal microscopy enables researchers to evaluate the *ex vivo* differentiation capacity of prostate epithelial cells. When used in combination, these two approaches provide complementary information about the differentiation capacity of prostate basal and luminal cells in response to genetic or pharmacological manipulation.

Introduction

Basal and luminal cells comprise the majority of the prostate epithelium[1]. Lineage tracing studies have revealed that these cell types are predominantly self-sustained by distinct progenitors in the adult mouse[2]; however, luminal differentiation from basal progenitors has been observed in several contexts including development[3,4], tissue regeneration[5], inflammation[6,7] and prostate cancer initiation[2,8]. Furthermore, emerging data supports the existence of multipotent luminal progenitors as well as luminal-committed progenitors[9]. In metastatic prostate cancer, differentiation from an AR-dependent luminal lineage to an AR-indifferent lineage with basal and neuroendocrine features represents an increasingly appreciated mechanism of resistance to androgen pathway inhibitors[10–12]. Therefore, as differentiation is implicated in normal physiology, cancer initiation and resistance to therapy, elucidating key molecular regulators of prostate epithelial cell differentiation is critical.

The mouse prostate organoid model has emerged as an elegant *ex vivo* context to study prostate epithelial cell differentiation[9,13,14]. In this assay, individual epithelial cells are plated into a 3D matrix where they generate glandular structures containing both basal and luminal cells within 1 week. While existing approaches for plating cells into organoid culture can be used to efficiently generate organoids, these approaches require further optimization14. Notable challenges associated with culturing prostate organoids include (1) excluding two-dimensional (2D) colonies that form beneath the Matrigel (matrix gel) from analysis, (2) maintaining the integrity of the matrix gel during media changes, and (3) counting organoids accurately. This paper outlines an approach to generate organoids from epithelial cells isolated from mouse prostate. The approach described entails coating plates with poly(2-hydroxyethyl methacrylate) (Poly-HEMA) to prevent the occurrence of 2D colonies. Furthermore, cells are plated into a matrix gel ring, rather than a matrix gel disc, which makes changing the media and counting organoids less challenging. These techniques allow researchers to more easily investigate how genetic alterations or small molecules introduced prior to, or during, organoid formation alter key processes such as differentiation.

Harvesting of prostate organoids for Western blot or immunohistochemical analysis by whole-mount confocal microscopy can provide valuable mechanistic insight into differentiation[13], yet well-established protocols to prepare organoids for such techniques are lacking. This manuscript describes approaches to harvest organoids for (1) collection of protein lysate, or (2) fixation and staining for confocal microscopy. Importantly, the approach described for fixing and staining prostate organoids is considerably improved in relation to existing methods. While these rely on sectioning organoids[15], the method described in this manuscript utilizes intact organoids, which helps protect against organoid damage during sample preparation. When used in combination, Western blot and confocal microscopy can provide valuable insight into the molecular regulators of differentiation. Alternatively, these approaches can be used to model other processes such as development and transformation.

Protocol

All methods described here have been approved by the Institutional Review Board at the University of California, Los Angeles.

NOTE: A schematic illustrating the approaches described in the paper is provided in **Figure 1**.

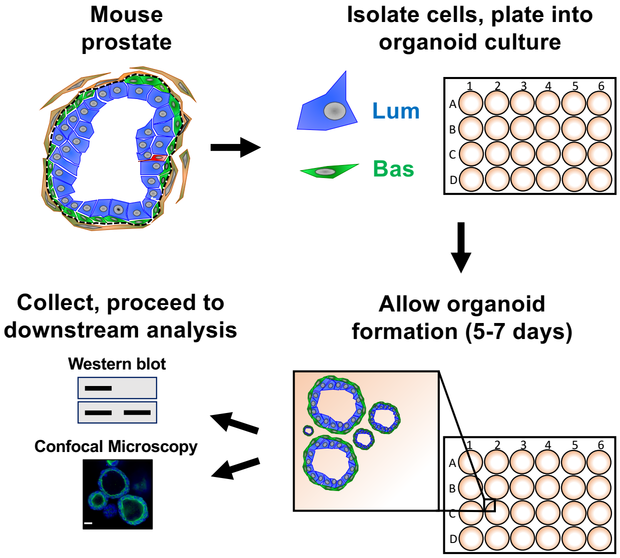

Figure 1. Schematic illustrating workflow to generate prostate organoids for collection and analysis. Total mouse prostate is dissociated and basal and luminal prostate epithelial cells are isolated by fluorescence-activated cell sorting via established protocols[36, 66]. Basal or luminal cells suspended in a mixture of mouse organoid media and matrix gel are plated into matrix gel rings. After 5 to 7 days of culture, organoids are harvested for analysis by Western blot or confocal microscopy.

1. Isolating mouse basal and luminal prostate epithelial cells using Fluorescence-Activated Cell Sorting (FACS) TIMING: 30 min

NOTE: Perform steps 1.3-1.5 in the dark.

1.1. After dissociating cells from total mouse prostate as described in Lawson *et al.*[16], transfer the cells to FACS tubes and resuspend 0.1-5 × 106 cells in 100 µL of dissociation media (**Table 1**).

1.2. Add the appropriate volume of the following directly-conjugated primary antibodies: CD45, CD31, Ter-119, EpCAM and CD49f.

1.3. Incubate on ice, protected from light, for 20 min.

NOTE: It is recommended to utilize 10% of the total dissociated cells for unstained and single-stained controls. These controls are necessary to set the correct compensation and voltage for sorting.

1.4. Quench antibody cocktail by adding 1 mL of dissociation media to each sample. Pellet the cells by centrifugation at 800 x g for 5 min at (room temperature) RT and remove the supernatant by aspirating.

1.5. Resuspend the cells in appropriate volume (250 µL per 1 × 106 cells) of dissociation media containing 1 µg/mL 4’,6-diamidino-2-phenylindole (DAPI). Proceed to FACS. Flow cytometry plots demonstrating isolation of mouse basal and luminal prostate epithelial cells are illustrated in **Figure 2**.

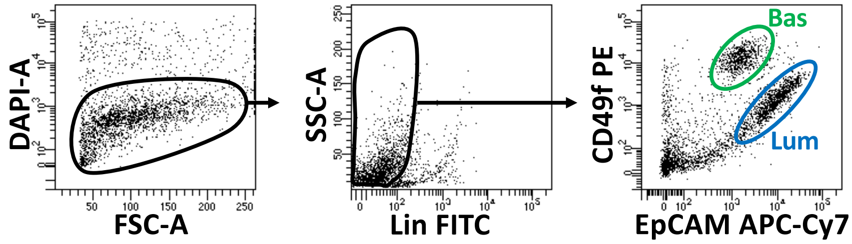

Figure 2. Isolation of mouse basal and luminal prostate epithelial cells using Fluorescence-Activated Cell Sorting (FACS). Dissociated cells from mouse prostate are stained with DAPI, to distinguish live from dead cells, and surface antibodies, to distinguish basal from luminal cells, prior to FACS. Left: Gated on DAPI- cells. FSC-A: forward-scatter. Center: Gated on Lin- cells (CD45^{low}, CD31^{low}, Ter119^{low}). SSC-A: side-scatter. Right: Basal cells (Bas) (EpCAM^{high}, CD49f^{high}), Luminal cells (Lum) (EpCAM^{high}, CD49f^{mid}).

2. Plating sorted prostate epithelial cells into primary mouse organoid culture - TIMING: 2-3 h (excluding Poly-HEMA-coated plate preparation)

NOTE: Plates are coated with Poly-HEMA to prevent 2D colony formation on the surface of the well beneath the matrix gel. Prepare Poly-HEMA-coated plates 1 day prior to plating sorted basal or luminal prostate epithelial cells into mouse organoid culture. Thaw 1 mL aliquots of reduced growth factor matrix gel, hereafter referred to as matrix gel, on ice 2 h prior to step 2.1. Y-27632 (ROCK inhibitor) should be added to mouse organoid media immediately prior to step 2.1. Perform steps 2.1-2.8 on ice.

2.1. Pellet the cells in 5 mL round-bottom tubes by centrifugation at 800 x g for 5 min at 4 °C and aspirate the supernatant.

2.2. Wash the cell pellet in 500 µL of mouse organoid media (**Table 2**)[14].

2.3. Pellet the cells by centrifugation at 800 x g for 5 min at 4 °C and aspirate the supernatant.

2.4. Resuspend in mouse organoid media at a cell density of 1000 cells/µL.

2.5. To prepare master mixes, mix epithelial cells suspended in mouse organoid media with matrix gel to generate a final mixture that contains 25% cells/media and 75% matrix gel. Basal cells are typically plated at a concentration of 100-2,000 cells/80 µL, whereas luminal cells are typically plated at a concentration of 2,000-10,000 cells/80 µL. The density of cells plated varies depending upon the day of anticipated material collection, and the desired downstream application.

NOTE: Chill appropriately sized tube(s) for expected master mix volume 5 min prior to master mix preparation. To ensure the matrix gel does not harden while handling, it is critical to chill the pipette tip by pipetting the matrix gel 3-4 times prior to transferring it to a new tube.

2.6. Add 80 µL of the matrix gel/cell mixture per well of a 24-well plate. Pipetting a droplet onto the lower half of the wall of the well, while avoiding direct contact with the Poly-HEMA coating is recommended. After adding the matrix gel, swirl the plate to allow the matrix gel/cell mixture to form a ring around the rim of the well.

2.7. Place the 24-well plate into a 37 °C 5% CO2 incubator right-side up for 10 min to allow the matrix gel to partially harden.

NOTE: Begin warming mouse organoid media at 37 °C immediately after placing the 24-well plate in the incubator.

2.8. After incubating for 10 min, flip the 24-well plate upside-down and incubate for an additional 50 min to allow the matrix gel to completely harden.

2.9. Add 350 µL of pre-warmed mouse organoid media dropwise to the center of each well.

NOTE: To maintain the integrity of the matrix gel, it is critical to avoid the matrix gel ring while adding media.

2.10. After adding the media, return the 24-well plate to the 37 °C 5% CO2 incubator.

3. Replenishing mouse organoid media - TIMING: 10-15 min per 24-well plate

NOTE: Existing media should be replaced with fresh media every 48 h. Before each media change, pre-warm mouse organoid media. It is not necessary to add ROCK inhibitor to the media used for replenishing.

3.1. Tilt the 24-well plate at a 45° angle and gently remove existing media from the center of each well using a p1000 pipette, while avoiding the matrix gel ring.

3.2. Add 350 µL of pre-warmed mouse organoid media as in step 2.8. It is recommended to add a larger volume of media (up to 1 mL) to organoids cultured for longer than 5 days in order to prevent rapid depletion of key nutrients and growth factors.

4. Extracting protein lysate from prostate organoids for Western blot analysis - TIMING: 2.5-4 h

NOTE: Prior to collecting organoids for protein lysate extraction, prepare and pre-warm dispase-containing media (**Table 1**).

4.1. Remove the media from each well as in step 3.1.

4.2. To collect organoids, repeatedly blast the matrix gel by pipetting 1 mL of dispase-containing media directly onto the matrix gel ring until the entire ring is dislodged, and transfer to a 1.5 mL microcentrifuge tube.

NOTE: It is critical to avoid direct contact with the Poly-HEMA-coated wells. Direct contact may cause contamination of the collected material with Poly-HEMA, which could negatively impact cell survival.

4.3. Place the 1.5 mL microcentrifuge tube(s) into a 37 °C 5% CO2 incubator for 30 min to 1 h to allow complete digestion of the matrix gel by dispase.

4.4. Pellet organoids by centrifugation at 800 x g for 5 min at RT and remove the supernatant using a micropipette.

4.5. Add phosphate-buffered saline (PBS) to the organoid pellet and resuspend by gently flicking.

NOTE: Failure to sufficiently resuspend the organoid pellet may result in the contamination of organoid material with residual dispase or matrix gel.

4.6. Pellet the organoids by centrifugation at 800 x g for 5 min at RT and remove the supernatant using a micropipette.

4.7. Fast freeze the organoid pellets by placing each tube into a solution containing dry ice and methanol. Store the tube(s) until future use at -80 °C. Alternatively, extract protein lysate immediately following step 4.6.

4.8. Resuspend the organoid pellets in 100 µL of protein lysis buffer (**Table 1**) per 10 µL of packed cell volume. Flick to resuspend.

NOTE: If resuming after fast-freezing, ensure protein lysis buffer is thawed prior to removing samples from -80 °C, as lysis buffer must be added to samples immediately in order to prevent phosphatase and protease activity.

4.9. Incubate the samples in protein lysis buffer on ice for at least 45 min.

NOTE: It is recommended to sonicate prior to incubation on ice to increase the efficiency of nuclear protein recovery; however, sonication is not required. If sonication is not performed, proceed to step 4.10.

4.9.1. To sonicate, submerge tubes in wet ice and gently apply the tip of the sonic dismembrator to the outside of the microcentrifuge tube. Sonicate for 40 s at 20 kHz.

4.10. Proceed to Western blot following established protocols.

5. Fixing and staining prostate organoids for immunohistochemical analysis by whole-mount confocal microscopy

5.1. Collecting prostate organoids from 24-well plates - TIMING: 45 min-1 h

NOTE: When collecting prostate organoids to process for confocal microscopy, it is critical to handle them with care in order to maintain their structure. The collection protocol below is designed to reduce disruption of organoid structure during isolation.

5.1.1. Remove the media from each well as in step 3.1.

5.1.2. Digest the matrix gel by incubating with 500 µL of dispase-containing media (**Table 1**) for 30 min in a 37 °C 5% CO2 incubator.

5.1.3. Collect digested organoid suspension in a microcentrifuge tube and pellet the organoids by centrifugation at 800 x g for 3 min at RT. Remove the supernatant.

5.2. Whole-mount immunofluorescent staining of prostate organoids - TIMING: 3-4 days (1-5 h(s)/day)

5.2.1. Add 500 µL of 4% paraformaldehyde in PBS and incubate for 2 h at RT with gentle shaking.

5.2.2. Pellet the organoids by centrifugation at 800 x g for 3 min at RT, remove the supernatant, and wash the pellet with 1 mL of PBS for 15 min with gentle shaking.

5.2.3. Wash the pellet as in step 5.2.2 for additional two times.

5.2.4. Pellet the organoids by centrifugation at 800 x g for 3 min at RT and remove the supernatant. Add 1 µg/mL DAPI in blocking solution (**Table 1**). Incubate for 2 h at RT or alternatively overnight at 4 °C with gentle shaking.

5.2.5. Pellet the organoids by centrifugation at 800 x g for 3 min at RT and remove the supernatant. Add primary antibody (rabbit-anti-p63, mouse-anti-cytokeratin 8) in blocking solution and incubate overnight at 4 °C with gentle shaking.

5.2.6. Pellet the organoids by centrifugation at 800 x g for 3 min at RT and remove the supernatant. Wash the pellet with 1 mL of PBS for 15 min with gentle shaking.

5.2.7. Wash the pellet as in step 5.2.6 for additional two times.

5.2.8. Pellet the organoids by centrifugation at 800 x g for 3 min at RT and remove the supernatant. Add secondary antibody (Goat anti-rabbit IgG-Alexa Fluor 594, Goat anti-mouse IgG-Alexa Fluor 488) in blocking solution and incubate overnight at 4 °C with gentle shaking.

5.2.9. Pellet the organoids by centrifugation at 800 x g for 3 min at RT, remove the supernatant, and wash the pellet with 1 mL of PBS for 15 min with gentle shaking.

5.2.10. Wash the pellet as in step 5.2.9 for additional two times.

6. Tissue clearing and mounting of the stained prostate organoids for whole-mount confocal microscopy - TIMING: 7 h

6.1.1. Pellet the organoids by centrifugation at 800 x g for 3 min at RT and remove the supernatant.

6.1.2. Add 1 mL of 30% sucrose in PBS with 1% Triton X-100 and incubate for 2 h at RT with gentle shaking.

6.1.3. Pellet the organoids by centrifugation at 800 x g for 3 min at RT and remove the supernatant.

6.1.4. Add 1 mL of 45% sucrose in PBS with 1% Triton X-100 and incubate for 2 h at RT with gentle shaking.

6.1.5. Pellet the organoids by centrifugation at 800 x g for 3 min at RT and remove the supernatant.

6.1.6. Add 1 mL of 60% sucrose in PBS with 1% Triton X-100 and incubate for 2 h at RT with gentle shaking.

6.1.7. Pellet the organoids by centrifugation at 800 x g for 3 min at RT and remove 95% of the supernatant.

NOTE: The pellet becomes looser as the concentration of sucrose becomes higher. Observing the DAPI-stained organoids under the UV light to confirm that they were not lost during removal of the supernatant is recommended.

6.1.8. Transfer a 10-20 µL droplet of the remaining suspension to a chambered coverslip and proceed to confocal microscopy.

NOTE: Coverslip fragments can be placed on either side of the droplet to be used as spacers. These prevent organoids from collapsing when a coverslip is placed over the droplet.

Representative results

Prostate epithelial cells are plated into mouse organoid culture where they form organoids, which are harvested prior to preparation for downstream analysis (**Figure 1**).

Basal and luminal epithelial cells are isolated using FACS. After excluding DAPI+ cells and depleting Lin+ cells (CD45, CD31, Ter119), basal and luminal cells are distinguished based on differential expression of EpCAM and CD49f (**Figure 2**). The approach described to plate prostate basal and luminal cells into organoid culture entails: (1) plating cells into matrix gel rings, and (2) coating wells with Poly-HEMA. Plating into rings has been previously described in Agarwal *et al.*[9] Utilizing this approach (**Figure 3A**) allows researchers to more easily avoid the matrix gel while replenishing the media (Step 3), and more easily count organoids by following the circumference of the well. Coating wells with Poly-HEMA has been shown to prevent 2D colony formation in retinal organoids[17]; however, this approach has not been utilized in the prostate organoid model. Importantly, coating wells with Poly-HEMA (**Table 3**) eliminates the occurrence of 2D colonies without interfering with organoid formation (**Figure 3B**). These modifications expand the capabilities of the prostate organoid assay.

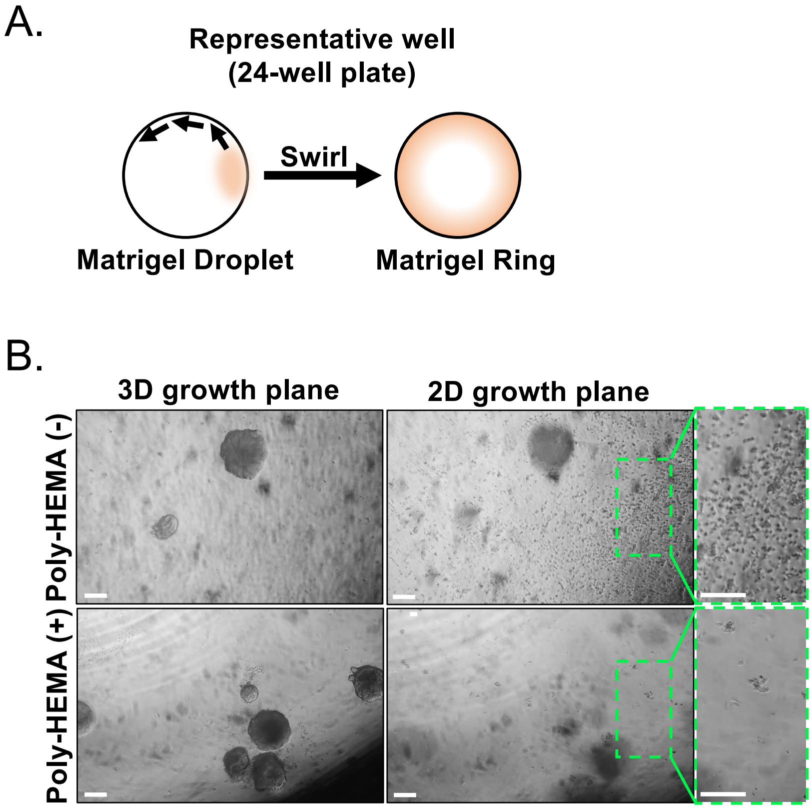

Figure 3. Establishment of mouse prostate organoids. (A) Schematic illustrating approach to generate a matrix gel ring in a well of a 24-well plate. **(B)** Representative phase contrast images of organoids (3D growth plane) and two-dimensional colonies (2D growth plane) formed 7 days after plating prostate epithelial cells into un-coated (Poly-HEMA (-)), or coated (Poly-HEMA (+)) 24-well plates. Boxed regions within 2D growth plane are magnified on the right. Scale bars, 200 µm*.*

Basal and luminal cells form organoids with distinct morphologies (**Figure 4A**). While most basal-derived organoids are similar in size (100-300 µm diameter) after 7 days in culture, luminal-derived organoids exhibit significant heterogeneity (30-450 µm diameter). Furthermore, most basal-derived organoids contain lumens surrounded by multi-layered epithelium (**Figure 4A, top**), whereas luminal-derived organoids range in morphology from hollow, with single-layered epithelium to solid, with multi-layered cords of cells that do not canalize (**Figure 4A, bottom**). The approaches described above to prepare organoids for downstream analysis (Steps 4, 5), were used to investigate whether these phenotypic differences are reflective of differences in lineage marker expression. Western blot analysis revealed that basal and luminal-derived organoids retain features associated with basal and luminal primary cells. Basal-derived organoids express higher levels of the basal marker cytokeratin 5 (K5), whereas luminal-derived organoids express higher levels of the luminal marker cytokeratin 8 (K8) (**Figure 4B**). Both basal and luminal markers were detected in basal and luminal-derived organoids in the bulk population, perhaps suggestive of differentiation (**Figure 4B**).

We sought to characterize lineage marker expression in basal-derived organoids and determine whether morphologically distinct luminal-derived organoids exhibit differences in marker expression by staining intact organoids and performing confocal microscopy (**Figure 4C**). Basal-derived organoids contained multi-layered epithelium with outer layers expressing high levels of the basal marker p63 and moderate levels of the luminal marker K8 (p63hi, K8mid), and inner layers without detectable levels of p63 and high levels of K8 (p63lo, K8hi) (**Figure 4D, top**). While all cells in single-layered luminal-derived organoids stained positively for K8, only select cells contained nuclear p63 (**Figure 4D, bottom**). These data validate the approaches to harvest and prepare organoids for analysis by Western blot or confocal microscopy and thereby expand the capability of the organoid assay to study key cellular processes, including differentiation.

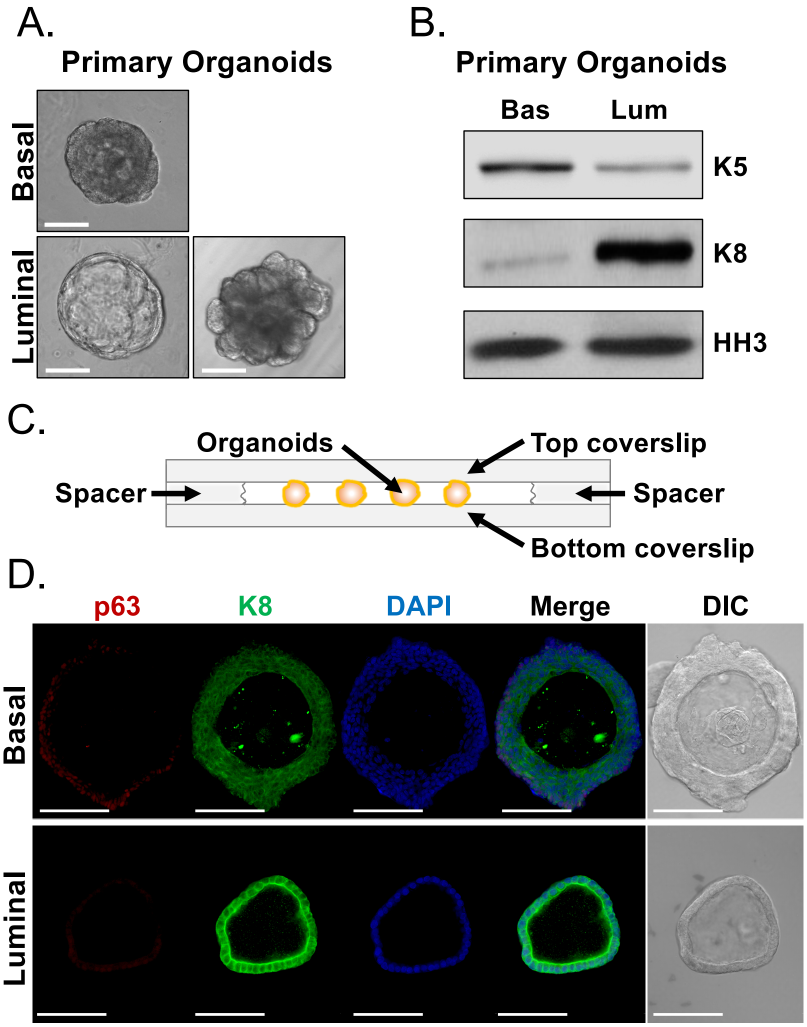

Figure 4. Analysis of lineage marker expression in prostate organoids by Western blot and whole-mount confocal microscopy. (A) Representative phase contrast images of basal-derived (top), and luminal-derived (bottom) organoids after 7 days of culture. Scale bar, 100 μm. **(B)** Western blot analysis of basal-derived (Bas) and luminal-derived (Lum) organoids after 5 days of culture. Staining for the basal marker, cytokeratin 5 (K5), and the luminal marker, cytokeratin 8 (K8), and a loading control, histone H3 (HH3). **(C)** Schematic illustrating chambered coverslip with spacers. **(D)** Representative differential interference contrast (DIC) and immunofluorescent images of basal-derived (top) and luminal-derived (bottom) organoids after 7 days of culture. Staining for p63 (red), K8 (green) and DAPI (blue) individually and merged. Scale bars, 100 μm.

Discussion

Prostate epithelial cell differentiation has been implicated in both normal prostate biology[2–7] and disease biology[8,10–12]; however, the master regulators of this process remain undefined. Identifying key regulators of prostate epithelial cell differentiation has been difficult in part due to the absence of well-established contexts to model it. While 2D monolayer culture can be used to model differentiation[11,12], this context fails to recapitulate the complex prostate microenvironment. Furthermore, *in vivo* contexts to model differentiation do not lend themselves to mechanistic studies, as they are challenging to manipulate. Therefore, the identification of an easy to manipulate, yet physiologically-relevant context, to study differentiation is critical.

The prostate organoid model represents an elegant *ex vivo* context where basal to luminal differentiation is reported to occur. Methods to establish prostate organoids are well established[14]; however, further optimization of these methods is necessary. Furthermore, approaches to harvest and prepare prostate organoids for analysis are not clearly described. This paper describes an approach to plate prostate epithelial cells isolated from mouse prostate into organoid culture. This approach allows researchers to (1) prevent the occurrence of 2D colonies during organoid formation, (2) reduce the risk of disruption to the matrix gel during media replenishment, and (3) count organoids more effectively. In addition, this manuscript outlines approaches to harvest organoids for preparation for Western blot analysis, or whole-mount confocal microscopy. Importantly, the approach utilized to prepare organoids for confocal microscopy maintains the intact structure of organoids through its duration, which reduces organoid damage prior to image acquisition. Altogether, the approaches described expand the capabilities of the prostate organoid assay.

Notably, the organoid-forming capacity of basal and luminal cells can be altered both by methods used to isolate the respective populations, and by culture conditions. The organoid culture conditions used in this assay were first described by Karthaus *et al.*[13] Whereas Karthaus *et al.* have reported that basal cells have a higher organoid forming capacity (15%) than luminal cells (1%)[13], Chua *et al.*, using distinct isolation methods and culture conditions, have reported that luminal cells (0.2-0.3%) have a higher organoid-forming capacity than basal cells (.03%)[20]. Overall, methods described by Karthaus *et al.* lead to higher organoid-forming rates for both basal and luminal cells, likely reflecting differences in the approach used to isolate basal and luminal cells[13], as opposed to culture conditions that bias against organoid formation from luminal cells. It remains unclear whether the protocol described in this manuscript favors luminal organoid formation from multipotent luminal progenitors, or committed-luminal progenitors[9]. Though timely and cost-prohibitive, *in vivo* lineage tracing studies can be used to validate progenitor features associated with distinct prostate epithelial lineages elucidated in the organoid assay.

Processes such as development, differentiation and transformation are not only relevant to prostate biology, but also relevant to the biology of other tissues including the brain, lung, intestine, pancreas and liver. The methods described facilitate the utilization of the organoid model to study these processes in not only the prostate, but also a wide range of tissues.

Tables

Recipes	
Dispase-containing media	1 mg dispase per ml advanced DMEM F12, 10 µM ROCK inhibitor. Filter sterilize using 0.22 µm filter.
Dissociation media	RPMI-1640 + 10% FBS + 1% Penicillin-Streptomycin. Filter sterilize using 0.22 µm filter.
Protein lysis buffer	RIPA buffer + phosphatase inhibitors + protease inhibitors
Blocking solution	10% FBS in PBS with 0.2% Triton X-100

Table 1. Instructions for the preparation of key solutions.

Component	Concentration
B-27	50x
GlutaMAX	100x
N-acetyl-L-cysteine	1.25 mM
Normocin	50 µg/mL
Recombinant Human EGF, Animal-Free	50 ng/mL
Recombinant Human Noggin	100 ng/mL
R-spondin 1-conditioned media	10% conditioned media
A83-01	200 nM
DHT	1 nM
Y-27632 dihydrochloride (ROCK inhibitor)	10 µM
Advanced DMEM/F-12	Base media
R-spondin 1-conditioned media is generated as described in Drost, *et al*[13]. After addition of all components, filter sterilize mouse organoid media using 0.22 µm filter. ROCK inhibitor is only added during establishment of culture and passaging of organoids.	

Table 2. Instructions for the preparation of mouse organoid media.

Protocol for preparing Poly-HEMA-coated plates	
1	Add 0.25 g Poly-HEMA to 50 ml 98% EtOH. Dissolve Poly-HEMA at 37 °C on a shaker. This process takes **at least 4 hr**.
2	Filter sterilize Poly-HEMA using 0.22 µm filter.
3	Add 200 µl of Poly-HEMA solution per well of a 24-well plate(s).
4	Remove lid(s) from 24-well plate(s) after adding Poly-HEMA and allow solution to evaporate overnight.
5	Wash each well twice with PBS and ensure wells are completely dry prior to storage after final wash. NOTE: Disrupting the Poly-HEMA coating during washing could contribute to 2-dimensional growth upon plating epithelial cells into organoid culture. To prevent damage to Poly-HEMA-coated wells, avoid direct contact with the pipette tip while washing. The integrity of the Poly-HEMA-coated wells will remain intact unless the Poly-HEMA is scraped off by the pipette tip.
6	Poly-HEMA-coated plates can be stored at 4 °C for up to two weeks. **NOTE:** Wrapping plates in parafilm prior to storage will reduce the risk of contamination.

Table 3. Protocol for preparation of Poly-HEMA-coated plates.

Acknowledgements

PDC and JMG are supported by the Ruth L. Kirschstein National Research Service Award GM007185. JAD is supported by the National Institute of General Medical Sciences of the National Institutes of Health (R25GM055052) awarded to T. Hasson and the Saul Martinez Scholarship. ASG is supported by the Spitzer Family Foundation Fund and the Gill Endowment.

This work was supported by the American Cancer Society (RSG-17-068-01-TBG), Department of Defense (W81XWH-13-1-0470), Margaret E. Early Medical Research Trust, NIH/NCI (P50CA092131/UCLA SPORE in Prostate Cancer), Rose Hills Foundation, and support from UCLA's Jonsson Comprehensive Cancer Center, Broad Stem Cell Research Center, Clinical and Translational Science Institute, and Institute of Urologic Oncology.

Disclosures

The authors have nothing to disclose.

References

1. Kwon, O.J., Xin, L. Prostate epithelial stem and progenitor cells. American Journal of Clinical and Experimental Urology. 2 (3), 209–218, (2014).

2. Choi, N., Zhang, B., Zhang, L., Ittmann, M., Xin, L. Adult Murine Prostate Basal and Luminal Cells Are Self-Sustained Lineages that Can Both Serve as Targets for Prostate Cancer Initiation. Cancer Cell. 21 (2), 253–265, (2012).

3. Ousset, M., Van Keymeulen, A., et al. Multipotent and unipotent progenitors contribute to prostate postnatal development. Nature Cell Biology. 14 (11), 1131–1138, (2012).

4. Wang, J., et al. Symmetrical and asymmetrical division analysis provides evidence for a hierarchy of prostate epithelial cell lineages. Nature Communications. 5, 1–13, (2014).

5. Wang, Z.A., Mitrofanova, A., et al. Lineage analysis of basal epithelial cells reveals their unexpected plasticity and supports a cell-of-origin model for prostate cancer heterogeneity. Nature Cell Biology. 15, (3), 274–283, (2013).

6. Kwon, O.J., Zhang, B., Zhang, L., Xin, L. High fat diet promotes prostatic basal-to-luminal differentiation and accelerates initiation of prostate epithelial hyperplasia originated from basal cells. Stem Cell Research. 16 (3), 682–691, (2016).

7. Kwon O.J., Zhang L, Ittmann, M.M., Xin L. Prostatic inflammation enhances basal-to-luminal differentiation and accelerates initiation of prostate cancer with a basal cell origin. Proceedings of the National Academy of Sciences. 192 (3), 997–999, (2014).

8. Stoyanova, T., et al. Prostate cancer originating in basal cells progresses to adenocarcinoma propagated by luminal-like cells. Proceedings of the National Academy of Sciences. 110 (50), 20111–20116, (2013).

9. Agarwal, S., Hynes, P.G., et al. Identification of Different Classes of Luminal Progenitor Cells within Prostate Tumors. Cell Reports. 13 (10), 2147–2158, (2015).

10. Ku, S.Y., et al. Rb1 and Trp53 cooperate to suppress prostate cancer lineage plasticity, metastasis, and antiandrogen resistance. Science. 355 (6320), 78–83, (2017).

11. Mu, P., et al. SOX2 promotes lineage plasticity and antiandrogen resistance in TP53- and RB1-deficient prostate cancer. Science. 355 (6320), 84–88, (2017).

12. Bishop, J.L., et al. The Master Neural Transcription Factor BRN2 Is an Androgen Receptor–Suppressed Driver of Neuroendocrine Differentiation in Prostate Cancer. Cancer Discovery. 7 (1), 54–71, (2016).

13. Karthaus, W.R., et al. Identification of multipotent luminal progenitor cells in human prostate organoid cultures. Cell. 159 (1), 163–175, (2014).

14. Drost, J., Karthaus, W.R., et al. Organoid culture systems for prostate epithelial and cancer tissue. Nature Protocols. 11 (2), 347–358, (2016).

15. McCray, T., Richards, Z., Marsili, J., Prins, G.S., Nonn, L. Handling and Assessment of

Human Primary Prostate Organoid Culture. Journal of Visualized Experiments. (143), doi:10.3791/59051 (2019).

16. Lawson, D.A, Xin, L., Lukacs, R.U., Cheng, D. & Witte, O.N. Isolation and functional characterization of murine prostate stem cells. Proceedings of the National Academy of Sciences of the United States of America. 104 (1), 181–186, (2007).

17. Chen, H.Y., Kaya, K.D., Dong, L. & Swaroop, A. Three-dimensional retinal organoids from mouse pluripotent stem cells mimic in vivo development with enhanced stratification and rod photoreceptor differentiation. Molecular vision. 22, 1077–1094, (2016).

18. Liu, X., et al. Low CD38 Identifies Progenitor-like Inflammation-Associated Luminal Cells that Can Initiate Human Prostate Cancer and Predict Poor Outcome. Cell Reports. 17 (10), 2596–2606, (2016).

19. Lukacs, R.U., Goldstein, A.S., Lawson, D.A., Cheng, D., Witte, O.N. Isolation, cultivation and characterization of adult murine prostate stem cells. Nature protocols. 5 (4), 702–713, (2010).

20. Chua, C. W., Shibata, M., et al. Single luminal epithelial progenitors can generate prostate organoids in culture. Nature Cell Biology. 16 (10), 951–961, (2014).

Chapter 3: Prostate lineage-specific metabolism governs luminal differentiation and response to antiandrogen treatment

Title: Prostate lineage-specific metabolism governs luminal differentiation and response to antiandrogen treatment

Author list: Jenna M. Giafaglione[1], Preston D. Crowell[1], Amelie M.L. Delcourt[2], Takao Hashimoto[2], Sung Min Ha[3], Aishwarya Atmakuri[2], Nicholas M. Nunley[2,4], Rachel M.A. Dang[5], Mao Tian[5], Johnny A. Diaz[2], Elisavet Tika[6], Marie C. Payne[7], Deborah L. Burkhart[8], Dapei Li[9], Nora M. Navone[10], Eva Corey[11], Peter S. Nelson[9], Neil Y.C. Lin[7,12,13], Cedric Blanpain[6], Leigh Ellis[14,15,16,17], Paul C. Boutros[4,5,18,19,20,21,22], Andrew S. Goldstein[2,4,5,22,23,*]

Affiliations:
[1]Molecular Biology Interdepartmental Program, University of California, Los Angeles, Los Angeles, CA 90095, USA
[2]Department of Molecular, Cell, and Developmental Biology, University of California, Los Angeles, Los Angeles, CA 90095, USA
[3]Department of Integrative Biology and Physiology, University of California, Los Angeles, Los Angeles, CA 90095, USA
[4]Department of Urology, David Geffen School of Medicine, University of California, Los Angeles, Los Angeles, CA 90095, US
[5]Jonsson Comprehensive Cancer Center, University of California, Los Angeles, Los Angeles, CA 90095, USA
[6]Laboratory of Stem Cells and Cancer, WEL Research Institute, Université Libre de Bruxelles (ULB), Brussels 1070, Belgium
[7]Department of Mechanical & Aerospace Engineering, University of California, Los Angeles, Los Angeles, CA 90095, USA
[8]Department of Cancer Biology, Dana-Farber Cancer Institute, Boston, MA 02215, USA
[9]Fred Hutchinson Cancer Center, Seattle, WA, 98109, USA
[10]Department of GU Medical Oncology, MD Anderson Cancer Center, Houston, TX 77030, USA
[11]University of Washington, Seattle, WA, 98195, USA
[12]Department of Bioengineering, University of California, Los Angeles, Los Angeles, CA 90095, USA
[13]Institute for Quantitative and Computational Biosciences, University of California, Los Angeles, Los Angeles, CA 90095, USA
[14]Department of Medicine, Cedars-Sinai Medical Center, Los Angeles, CA 90048, USA
[15]Cedars-Sinai Samuel Oschin Comprehensive Cancer Institute, Los Angeles, CA 90048, USA
[16]Department of Biomedical Sciences, Cedars-Sinai Medical Center, Los Angeles, CA 90048, USA
[17]Center for Bioinformatics and Functional Genomics, Cedars-Sinai Medical Center, Los Angeles, CA 90048, USA
[18]Department of Human Genetics, University of California, Los Angeles, Los Angeles, CA 90095, USA
[19]Department of Medical Biophysics, University of Toronto, Toronto, Ontario, Canada
[20]Vector Institute, Toronto, Ontario, Canada
[21]Institute for Precision Health, University of California, Los Angeles, Los Angeles, CA 90095, USA
[22]Eli and Edythe Broad Stem Cell Research Center, University of California, Los Angeles, Los Angeles, CA, USA
[23]Molecular Biology Institute, University of California, Los Angeles, Los Angeles, CA 90095, USA
*Correspondence: agoldstein@mednet.ucla.edu

Lead Contact: Andrew S. Goldstein, agoldstein@mednet.ucla.edu

Abstract

Lineage transitions are a central feature of prostate development, tumourigenesis and treatment resistance. While epigenetic changes are well-known to drive prostate lineage transitions, it remains unclear how upstream metabolic signaling contributes to the regulation of prostate epithelial identity. To fill this gap, we developed an approach to perform metabolomics on primary prostate epithelial cells. Using this approach, we discovered that the basal and luminal cells of the prostate exhibit distinct metabolomes and nutrient utilization patterns. Furthermore, basal to luminal differentiation is accompanied by increased pyruvate oxidation. We establish the mitochondrial pyruvate carrier (MPC) and subsequent lactate accumulation as regulators of prostate luminal identity. Inhibition of the MPC or supplementation with exogenous lactate results in large-scale chromatin remodeling, influencing both lineage-specific transcription factors and response to antiandrogen treatment. These results establish reciprocal regulation of metabolism and prostate epithelial lineage identity.

Main text

Introduction

Prostate epithelium contains basal and luminal cells as well as rare neuroendocrine cells[1]. Adult mouse prostate basal and luminal cells are predominantly self-sustained under physiological conditions[2]. Luminal differentiation from basal progenitors occurs during development[3, 4], tissue regeneration[5], inflammation[6] and prostate cancer initiation[2, 7]. Epigenetic changes facilitate the establishment and maintenance of prostate epithelial identity[8,9,10,11]. How upstream signaling contributes to the downstream epigenetic regulation of prostate lineage identity remains poorly understood. Metabolism is a key upstream regulator of the epigenome. Most chromatin-modifying enzymes require intermediates of cellular metabolism as substrates or cofactors[12,13]. While metabolic rewiring can modulate differentiation in a wide variety of tissue systems[14,15,16], the interplay between metabolic signaling and lineage identity in the prostate remains to be elucidated.

To fill this gap, we sought to understand prostate epithelial cell type-specific metabolic features. We developed an approach to perform metabolic profiling and heavy isotope nutrient tracing on primary prostate epithelial cells, finding that basal and luminal cells have distinct metabolic signatures. We demonstrate that basal to luminal differentiation is associated with increased pyruvate oxidation. Pharmacological inhibition of mitochondrial pyruvate transport, or genetic deletion of *Mpc1*, antagonizes luminal features. Both lactate supplementation and inhibition of lactate efflux block luminal differentiation, suggesting that intracellular lactate accumulation mediates the effect on lineage identity. Inhibition of the MPC and supplementation with exogenous lactate reprogram the chromatin landscape of key lineage-specific transcription factors and modulate response to antiandrogen treatment. Our results indicate that prostate epithelial cells have lineage-rooted metabolic features and that modulation of metabolism can govern prostate lineage transitions through epigenetic mechanisms.

Results

Basal and luminal cells have distinct metabolic features

We first sought to investigate the relationship between prostate epithelial cell type and metabolic identity. We analyzed adult murine prostates using fluorescence-activated cell sorting (FACS) to isolate primary basal (EpCAM$^+$ CD49f^{high}) and luminal (EpCAM$^+$ CD49f^{low}) cells (**Extended Data Figure 1a**). We first interrogated prior RNA sequencing results[17] and then performed metabolic profiling and glucose tracing (**Figure 1a**). Transcriptional analysis of canonical lineage markers validated isolation of epithelial cell populations (**Extended Data Figure 1b**). Gene set enrichment analysis (GSEA) demonstrated appropriate enrichment of the Smith *et al.*[18] basal and luminal signatures (**Extended Data Figures 1c-d**, **Supplementary Table 1**). Of the 30 pathways most statistically enriched in differentially abundant genes, 12 were metabolism-related (**Extended Data Figure 1e**, **Supplementary Table 2**). We performed GSEA on all Hallmark, Reactome and KEGG metabolism gene sets and identified enrichment of MYC targets in basal cells and enrichment of pyruvate metabolism and oxidative phosphorylation in luminal cells (**Figure 1b**, **Supplementary Table 3**). We also found that basal cells exhibit elevated RNA and protein abundance of several glycolytic enzymes and transporters, while luminal cells exhibit elevated levels of many key TCA cycle enzymes (**Figure 1c, Extended Data Figure 1f**). Analysis of mouse prostate single cell RNA sequencing data[19, 20] corroborated differential expression of metabolic enzymes in distinct epithelial subsets (**Extended Data Figures 2a-b**).

After identifying candidate cell type-specific metabolic features, we established an approach that enabled us to perform metabolic characterization of distinct prostate epithelial cell types using metabolic profiling and nutrient tracing. Primary cells isolated by FACS were cultured overnight to enhance cell attachment and enable equilibration prior to metabolite extraction. AnnexinV and 7-AAD analysis illustrated that adherent basal and luminal cells both exhibit greater than 80% viability after overnight culture (**Extended Data Figure 2c**), validating that metabolomics was performed on healthy cell populations. Basal cells have elevated levels of key glycolytic metabolites including PEP, 3PG and F6P, while luminal cells have elevated levels of TCA cycle intermediates including isocitrate, aKG and succinate (**Figure 1d, Supplementary Table 4**). [U-^{13}C]glucose tracing revealed a significant reduction in incorporation of glucose-derived carbon from citrate to aconitate specifically in luminal cells, but not in basal cells (**Figure 1e, Supplementary Table 4**). This metabolic wiring may enable luminal cells to secrete high levels of citrate found in seminal fluid[21] or to utilize citrate for lipid synthesis. Consistent with this hypothesis, we observed increased RNA abundance of genes involved in *de novo* lipogenesis in luminal cells relative to basal cells (**Figure 1f**). Previous studies have reported that zinc accumulation in the prostate epithelium inhibits aconitase activity to prevent citrate oxidation and promote citrate secretion[22]. We evaluated expression of zinc transporters and found that several are elevated in luminal cells relative to basal cells (**Figure 1g**). [U-^{13}C]glucose tracer analysis also illustrated that basal cells preferentially generate M2 citrate through pyruvate dehydrogenase (PDH) activity (**Figure 1h, Supplementary Table 4**), while luminal cells preferentially generate M3 citrate through pyruvate carboxylase (PCX) activity (**Figure 1i, Supplementary Table 4**). These data indicate that basal and luminal cells have both distinct metabolite abundance profiles and nutrient utilization patterns.

We next asked whether cell type-specific metabolic features are conserved across species. We utilized a dataset of RNA sequencing of benign prostatic basal and luminal epithelial populations from three human prostates[23]. All glycolytic enzymes and transporters evaluated, except *HK2*, were enriched in basal cells, while many TCA cycle enzymes were enriched in luminal cells (**Figure 1j**). Our data provide the most comprehensive evidence to date that distinct prostate epithelial cell types contain unique metabolic features.

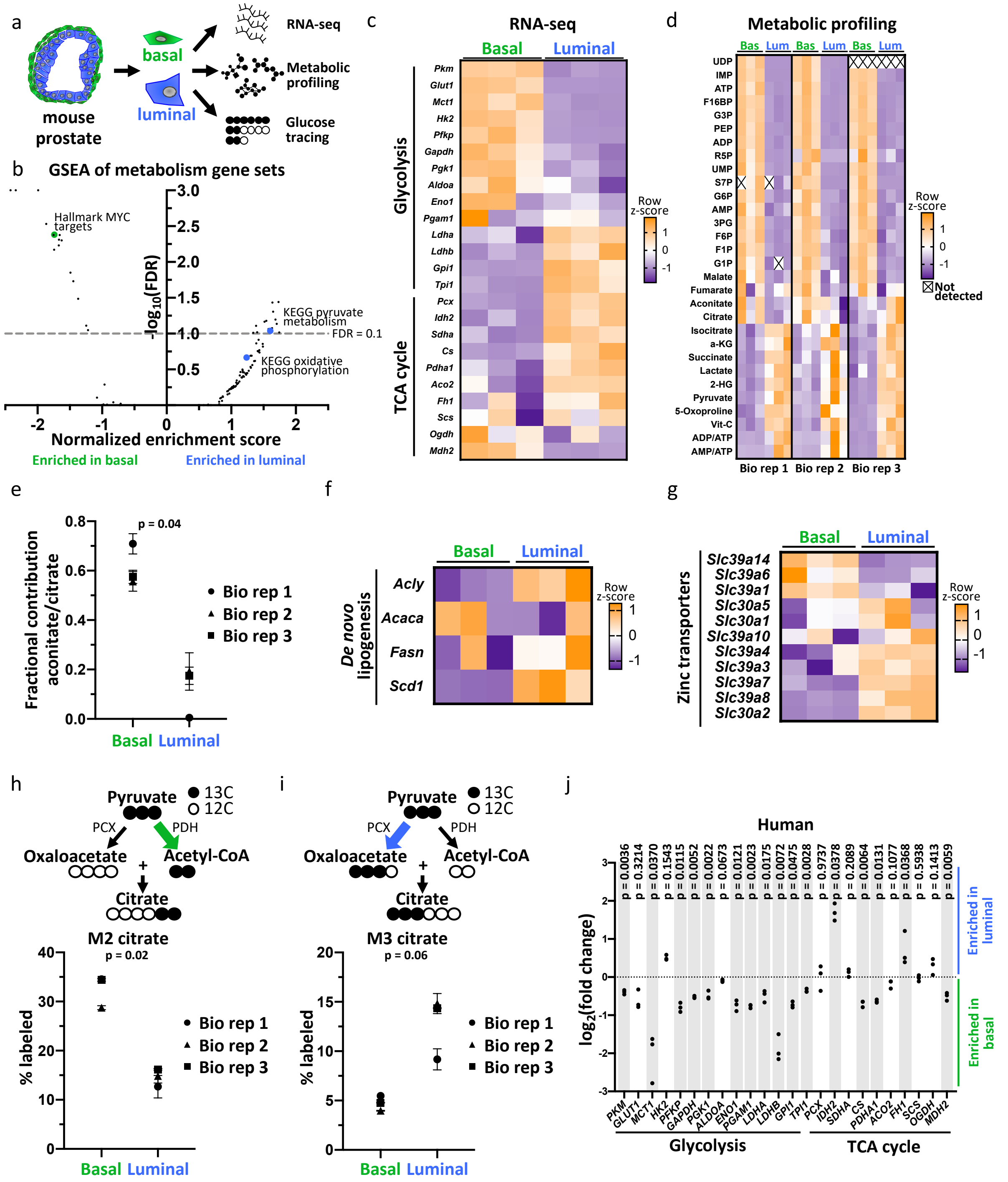

Figure 1. Primary basal and luminal prostate cells have distinct metabolic features
(a) Schematic of RNA sequencing, metabolic profiling and glucose tracing performed on primary basal and luminal cells isolated from mouse prostate. (b) Gene set enrichment analysis of all KEGG, Hallmark, and Reactome metabolism gene sets in basal and luminal cells. (c) Heatmap of glycolytic and TCA cycle enzymes from RNA sequencing of three biological replicates of basal and luminal cells. (d) Heatmap of metabolite abundance in primary basal and luminal mouse prostate cells with three technical replicates for each of the three biological replicates. (e)

Aconitate to citrate fractional contribution ratio in primary basal and luminal mouse prostate cells fed [U-^{13}C]glucose tracer for 16 hours. (f-g) Heatmaps of genes involved in *de novo* lipogenesis (f) and zinc transport (g) from RNA sequencing of primary basal and luminal mouse prostate cells. (h-i) Percent M2 citrate (h) and percent M3 citrate (i) from [U-^{13}C]glucose in basal and luminal cells (n=3 technical replicates for each of the 3 biological replicates). (j) Fold change in glycolytic and TCA cycle enzymes from RNA sequencing of basal and luminal cells from three human prostates. Shaded gray rectangles indicate genes that have statistically significant ($p < 0.05$) differential abundance. For all panels, data are shown as mean ± SEM. p-values were calculated using a paired two-tailed t-test.

Increased pyruvate oxidation with luminal differentiation

We next sought to investigate whether there is *in vivo* evidence of metabolic reprogramming during basal to luminal differentiation. We took advantage of the spatial restriction of multipotent basal cells at the distal region (tip – 100 μm) of the developing prostate at postnatal day (P)10[24] (**Figure 2a**). Comparing RNA expression in multipotent basal cells and basal-derived luminal cells isolated by FACS, we found 15 of the 30 most enriched pathways identified by KEGG pathway analysis are metabolism-related (**Extended Data Figure 3a, Supplementary Table 5**). GSEA revealed negative enrichment of genes in KEGG oxidative phosphorylation in multipotent basal cells relative to basal-derived luminal cells (**Figure 2b**).

Features of basal to luminal differentiation have been reported in prostate organoid culture; however, the induction kinetics of luminal marker expression were previously poorly defined[25]. Western blot analysis revealed that basal-derived organoids initially express high levels of the basal marker Trp63 (p63) but low levels of the luminal marker cytokeratin 8 (KRT8) (**Figure 2c-d**). By day five in *ex vivo* culture, KRT8 is elevated and p63 is reduced (**Figure 2d**). Using intracellular flow cytometry, we established that there is gradual upregulation of KRT8 that continues between days six and nine (**Extended Figure 3b**).

We performed metabolic profiling and [U-^{13}C]glucose tracer analysis three, five and seven days after plating into organoid culture. Principal component analysis of both metabolic profiling data and glucose tracer analysis data illustrate that each timepoint clusters independently (**Extended Data Figure 3c**, **Figure 2e**). Heatmap visualization also demonstrates that primary basal-derived organoids have differences in their metabolite abundance profiles at each time point (**Extended Data Figure 3d, Supplementary Table 4**). Incorporation of glucose-derived carbon into glycolytic metabolites does not significantly change from day three to seven (**Figure 2f, Supplementary Table 4**). In contrast, fractional contribution to TCA cycle intermediates increases significantly as basal-derived organoids acquire luminal features (**Figure 2g, Extended Data Figure 3e, Supplementary Table 4**). Both fractional contribution to nucleotide intermediates and expression of the proliferation marker PCNA decrease between days five and seven (**Figure 2h**, **Extended Data Figure 3f, Supplementary Table 4**). These data suggest that increased pyruvate oxidation is unlikely to be driven predominantly by organoid growth, but rather represents a shift in metabolism with luminal differentiation. Collectively, our data indicate basal to luminal differentiation is associated with metabolic rewiring, which includes a shift towards increased glucose oxidation.

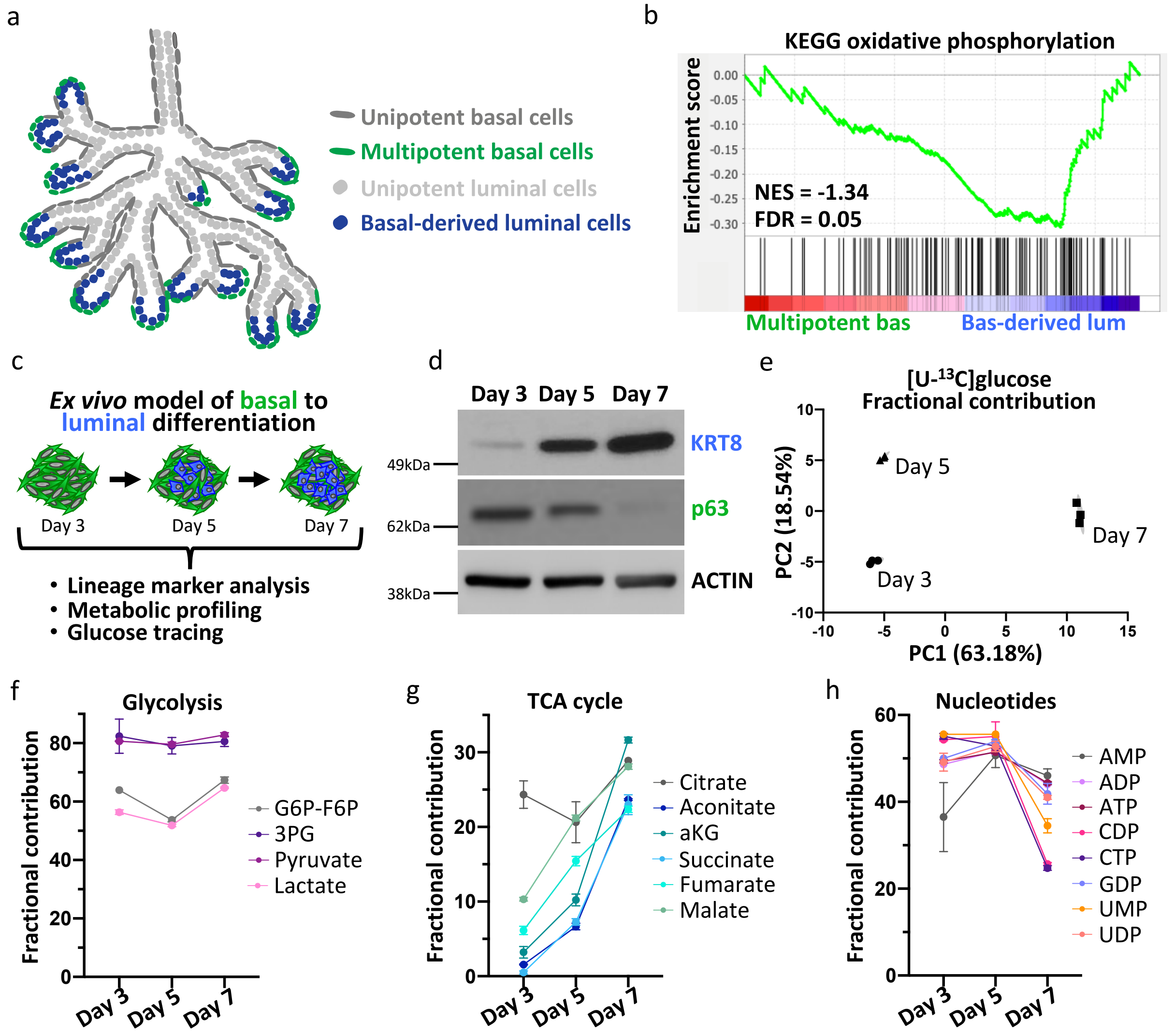

Figure 2. Basal to luminal differentiation is accompanied by increased pyruvate oxidation (a) Schematic of *in vivo* model of basal to luminal differentiation in P10-P12 murine prostate. (b) Gene set enrichment analysis showing enrichment of KEGG oxidative phosphorylation in basal-derived luminal cells relative to multipotent basal cells *in vivo*. (c) Schematic of lineage marker analysis, metabolic profiling and glucose tracing performed on primary basal-derived mouse organoids three, five and seven days after plating into organoid culture. (d) Western blot analysis of the luminal marker cytokeratin 8 (KRT8) and the basal marker p63 in basal-derived organoids. (e) Principal component analysis of fractional contribution from [U-^{13}C]glucose metabolic tracing data of basal-derived organoids with three technical replicates per timepoint. Organoids were cultured with [U-^{13}C]glucose 48 hours prior to harvesting metabolites at each timepoint. (f-h) Fractional contribution from [U-^{13}C]glucose to glycolytic (f), TCA cycle (g) and nucleotide intermediates (h) in basal-derived organoids with three technical replicates per timepoint. For all panels, data are shown as mean ± SEM.

The mitochondrial pyruvate carrier regulates cell fate

The mitochondrial pyruvate carrier (MPC) transports pyruvate from the cytosol to the mitochondria, where it can be oxidized to fuel the TCA cycle[26]. As basal to luminal differentiation is associated with increased pyruvate oxidation, we investigated the effects of inhibiting the MPC with the small molecule MPC inhibitor UK5099. [U-^{13}C]glucose tracer analysis confirmed that UK5099 significantly reduces incorporation of glucose-derived carbon into TCA cycle intermediates in mouse basal-derived organoids, consistent with its on-target effect (**Figure 3a, Supplementary Table 4**). UK5099 does not significantly influence organoid-formation rate (**Figure 3b**) or organoid size (**Figure 3c**) of basal-derived organoids.

Western blot analysis and immunofluorescence illustrate that UK5099 treatment reduces the expression of KRT8 and increases the expression of p63 (**Figure 3d-e**). We evaluated KRT8 expression at single-cell resolution using intracellular flow cytometry and found downregulation of KRT8 with UK5099 treatment (**Figures 3f-g**). UK5099 treatment reduces KRT8 protein abundance in a dose-dependent manner without altering the rate of organoid formation (**Extended Data Figures 4a-b**). UK5099 does not modulate the organoid-forming rate (**Extended Data Figure 4c**) or the expression of proliferation and death markers (**Extended Data Figure 4d**) in luminal-derived organoids, and thus does not appear to be toxic to them. These data indicate that MPC inhibition is antagonizing luminal differentiation rather than selectively killing cells with a luminal identity.

To complement small molecule-mediated MPC inhibition, we used a genetics approach to block pyruvate oxidation. [U-^{13}C]glucose tracer analysis revealed that *Mpc1*-KO basal-derived organoids have reduced incorporation of glucose-derived carbon into TCA cycle intermediates (**Figure 3h, Supplementary Table 4**). We also performed correlation analysis on [U-^{13}C]glucose fractional contribution data from 10μM UK5099-treated and *Mpc1*-KO organoids, which illustrates that MPC inhibition and *Mpc1* knockout have a similar effect on glucose utilization (**Extended Data Figure 4e**). Western blot analysis demonstrated that *Mpc1*-KO, as observed with UK5099, reduces luminal lineage markers (**Figure 3i**). RNA sequencing and GSEA revealed negative enrichment of the luminal signature and positive enrichment of the basal signature in UK5099-treated (**Extended Data Figure 4f-g**) and *Mpc1*-KO organoids (**Figure 3j**, **Extended Data Figure 4h**) relative to control organoids.

To further evaluate the role of MPC inhibition in governing prostate lineage identity, we performed single-cell RNA sequencing (scRNA-seq) on basal-derived organoids that were passaged weekly for one month (quaternary organoids). Only 1% of cells in primary basal-derived organoids are *Epcam*$^-$*Krt8*$^-$ (**Figure 3k, Extended Data Figure 5a**). In contrast, quaternary organoids that are maintained in 3D culture for one month display features of epithelial-mesenchymal transition (EMT), illustrated by an increase in the percentage of *Epcam*$^-$*Krt8*$^-$ cells (**Figure 3k, Extended Data Figure 5a**). To understand how MPC inhibition alters lineage identity in a context with greater cellular heterogeneity, we performed scRNA-seq on quaternary organoids treated with vehicle or UK5099 for three days. Clustering analysis and annotation of canonical lineage marker expression were used to classify cells into six different cell types (**Figures 3l-m**, **Extended Data Figure 5b**). The percentage of cells in the phenotypic luminal population (*Krt8*$^+$ *Krt18*$^+$ *Krt5*$^-$ *Trp63*$^-$) decreases with MPC inhibition, while the percentage of cells in the EMT-like population (*Epcam*$^-$ *Cdh1*$^-$ *Vim*$^+$) increases with MPC inhibition (**Figure 3n**). UK5099 treatment significantly altered gene expression of cells in the luminal population, reducing luminal marker expression while increasing expression of basal markers, glycolytic enzymes and inflammatory signaling genes (**Extended Data Figure 5c**). Apoptosis analysis illustrates that UK5099 treatment of quaternary organoids does not increase the percentage of AnnexinV$^+$ cells (**Extended Data Figure 5d-e**), suggesting that MPC inhibition alters lineage identity rather than selects against specific phenotypic populations. Taken together, these data illustrate that modulating metabolism can alter prostate epithelial identity and that the MPC is a key regulator of lineage identity in benign prostate epithelial cells.

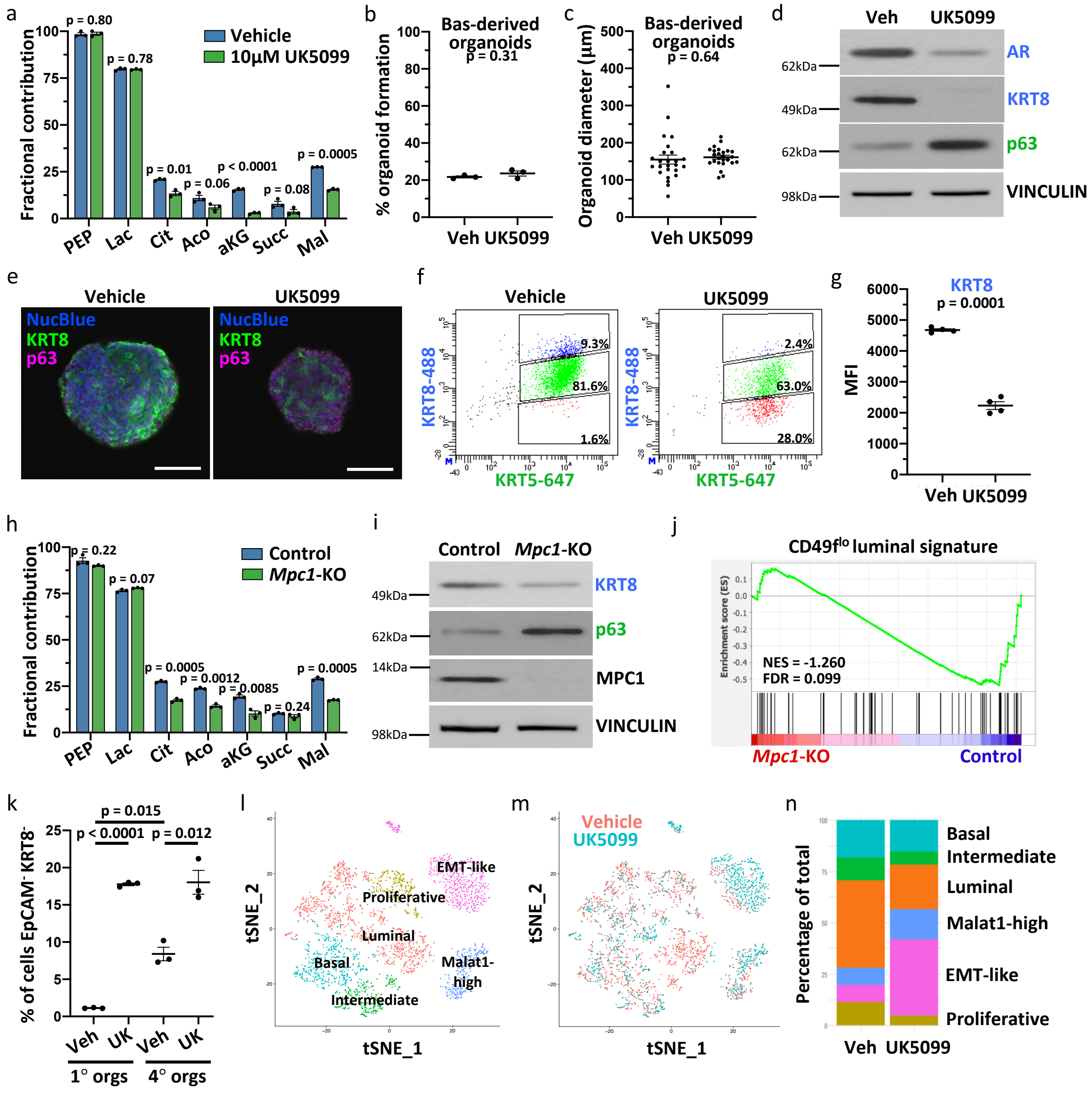

Figure 3. Inhibition or knockout of the mitochondrial pyruvate carrier prevents basal to luminal differentiation

(a) [U-^{13}C]glucose tracer analysis of vehicle- and 10μM UK5099-treated basal-derived organoids seven days after plating (n=3 independent biological replicates) Data are shown as mean ± SEM. (b-c) Percent organoid formation (n=3 independent biological replicates) (b) and organoid diameter (n=25 independent biological samples) (c) of vehicle- and 10μM UK5099-treated basal-derived organoids seven days after plating. (d) Western blot analysis of luminal markers androgen receptor (AR) and cytokeratin 8 (KRT8) and basal marker p63 in vehicle- and 10μM UK5099-treated basal-derived organoids seven days after plating. (e) Immunofluorescence of luminal marker KRT8 and basal marker p63 in representative vehicle- and 10μM UK5099-treated basal-derived organoids seven days after plating. Scale bars, 100μm. (f) Intracellular flow cytometry of KRT8 and basal marker cytokeratin 5 (KRT5) in vehicle- and 10μM UK5099-treated basal-derived organoids seven days after plating. (g) Quantification of mean fluorescence intensity (MFI) of KRT8 from panel e (n=4 independent biological replicates). (h) [U-^{13}C]glucose tracer analysis of control and *Mpc1* knockout basal-derived organoids (n=3 independent biological replicates). Data are shown as mean ± SEM. (i) Western blot analysis of basal and luminal markers in control and *Mpc1* knockout basal-derived organoids. (j) GSEA showing negative enrichment of CD49f^{low} luminal signature[18] in *Mpc1* knockout relative to control basal-derived organoids. (k) Flow cytometry quantification of percentage of EpCAM^{-}KRT8^{-} cells in vehicle- and 10μM UK5099-treated primary and quaternary basal-derived organoids (n=3 independent biological replicates). (l) tSNE plot of scRNA-seq data on quaternary prostate organoids illustrating distinct cell populations. (m) tSNE plot of vehicle- and 10μM UK5099-treated cells from scRNA-seq data. (n) Quantification of percentage of vehicle- and 10μM UK5099-treated cells in each cluster from scRNA-seq data. For all panels, error bars represent SEM. p-values were calculated using an unpaired two-tailed t-test with Welch's correction.

MPC is a regulator of lineage identity in prostate cancer

Loss of tumour suppressor genes *Pten* and *Rb1* are common in prostate cancer[10], and genetically engineered mouse models of *Pten* loss and combined *Pten*;*Rb1* loss recapitulate key features of prostate adenocarcinoma[27]. Western blot analysis validated tumour suppressor loss in *Pten* single knockout (SKO) and *Pten*;*Rb1* double knockout (DKO) basal-derived organoids (**Extended Data Figure 6a**). Both SKO and DKO organoids had significantly larger diameters than benign control organoids (**Extended Data Figure 6b**), consistent with a transformed phenotype. RNA sequencing data from Ku *et al.*[27] illustrate that SKO and DKO mouse prostates have increased expression of canonical luminal markers whereas only DKO prostates have increased expression of neuroendocrine markers relative to wildtype prostates (**Extended Data Figure 6c**). We found that both SKO and DKO organoids retain the lineage features of their respective primary tissues (**Extended Data Figure 6d**). UK5099 treatment of SKO and DKO organoids reduces the expression of luminal markers KRT8 and KRT18 (**Figure 4a**). RNA sequencing analysis confirmed reduced expression of canonical luminal markers and increased basal marker expression in UK5099-treated DKO organoids (**Figure 4b**). We discovered that UK5099 treatment reduces expression of canonical luminal markers and increases expression of stem-like and neuroendocrine markers in several human prostate cancer models, including 16D cells, LuCaP35 cells, LAPC4 cells and MDA PCa 183-A patient-derived xenograft (PDX) organoids (**Extended Data Figures 6e-h**). We also discovered that MPC inhibition antagonizes luminal lineage identity in subcutaneous 16D tumours *in vivo* (**Extended Data Figure 6i-j**). Collectively, these data establish the MPC as a regulator of lineage identity in transformed mouse prostate organoids and human prostate cancer models.

Next, we investigated the relationship between MPC expression and lineage identity in prostate cancer patient samples. Correlation analysis of RNA sequencing of 499 primary prostate carcinomas from The Cancer Genome Atlas (TCGA)[28] revealed that abundance of *MPC1* and *MPC2* RNA are positively correlated with RNA abundance of the luminal markers *KRT8* and *KRT18* (**Extended Data Figures 6k-n**). Furthermore, we calculated luminal signature scores using the Second Military Medical University (SMMU) dataset[29], which contains RNA sequencing of treatment-naïve adenocarcinoma prostate tumours, and the Beltran *et al.* dataset[30], which contains metastatic castration-resistant adenocarcinoma and neuroendocrine prostate tumours. Abundance of *MPC1* and *MPC2* transcripts are positively correlated with luminal signature score in both datasets (**Figures 4c-f**). Furthermore, *MPC1* RNA abundance is not significantly different in adenocarcinoma compared to neuroendocrine prostate cancer samples in the Beltran *et al.* dataset (**Figure 4g**). However, *MPC2* RNA abundance is significantly decreased in neuroendocrine tumours compared to adenocarcinoma tumours (**Figure 4h**). Similarly, in the Nguyen *et al.* dataset[31], *MPC2* is decreased in neuroendocrine compared to adenocarcinoma PDX models (**Figures 4i-j**). Importantly, since the MPC complex functions as a heterodimer, loss of MPC2 would yield the complex non-functional[32]. These data illustrate that MPC RNA abundance positively correlates with luminal lineage identity across disease states.

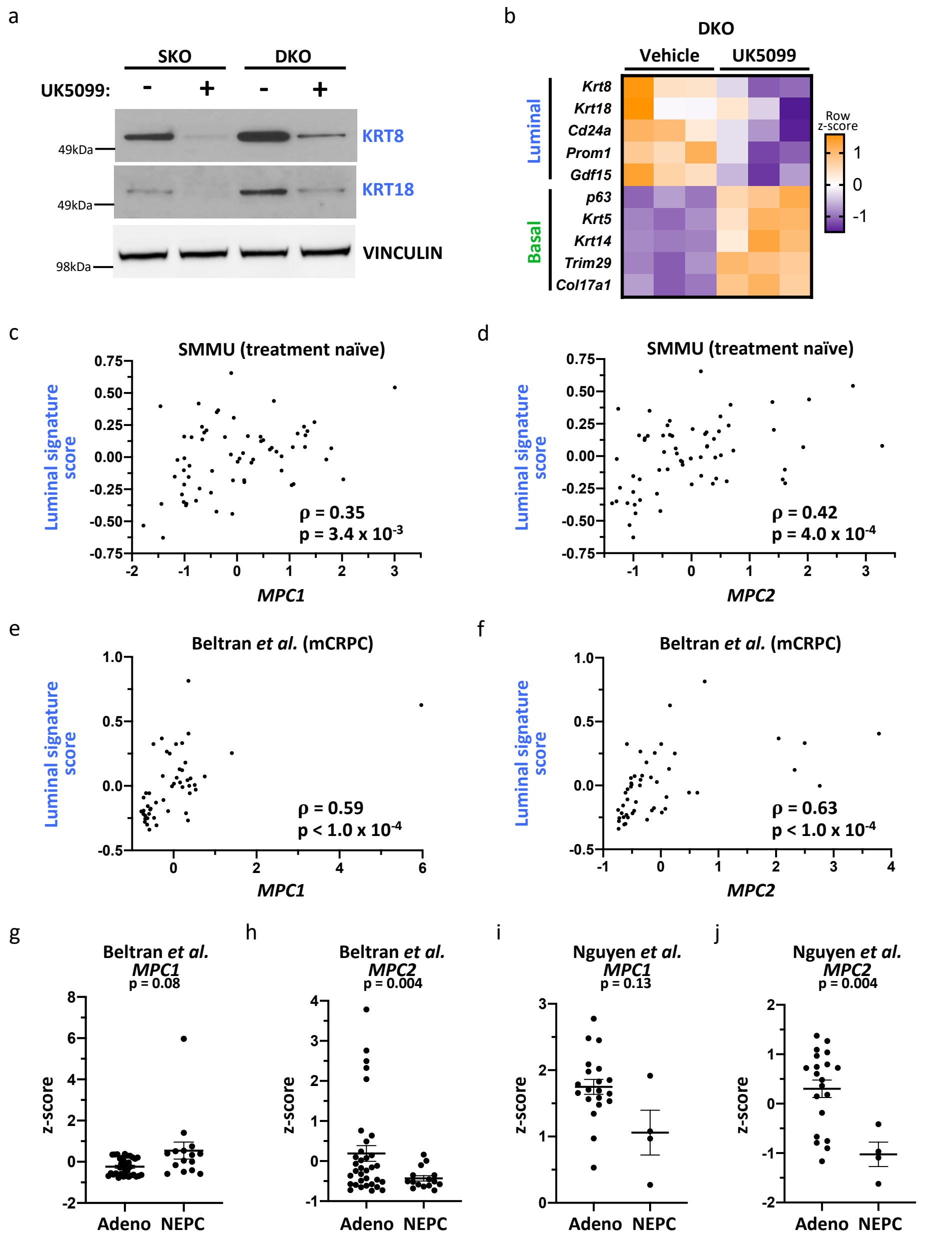

Figure 4. MPC is a regulator of luminal lineage identity in prostate cancer
(a) Western blot analysis of luminal markers KRT8 and KRT18 in single knockout (SKO) and double knockout (DKO) mouse prostate organoids treated with vehicle or 10µM UK5099 for five days. (b) Heatmap of canonical basal and luminal markers from RNA sequencing of vehicle- and 10µM UK5099-treated DKO organoids. (c-d) Correlation analysis of luminal signature score and *MPC1* (c) or *MPC2* (d) z-scores in treatment naïve prostate cancer samples from the Second Military Medical University (SMMU) dataset[29]. (e-f) Correlation analysis of luminal signature score and *MPC1* (e) or *MPC2* (f) z-scores in metastatic castration-resistant prostate cancer samples from the Beltran *et al.* dataset[30]. (g-h) RNA abundance of *MPC1* (g) or *MPC2* (h) in adenocarcinoma (adeno) or neuroendocrine prostate cancer (NEPC) samples from the Beltran *et al.* dataset[30]. (i-j) RNA abundance of *MPC1* (i) or *MPC2* (j) in adeno or NEPC samples from the Nguyen *et al.* patient-derived xenograft dataset[31]. Correlation analysis was performed using

Spearman's correlation with a two-tailed p-value. For all panels, error bars represent SEM. p-values in (g-j) were calculated using an unpaired two-tailed t-test with Welch's correction.

Lactate accumulation results in chromatin remodeling

We next sought to elucidate the mechanism by which MPC inhibition antagonizes luminal lineage identity. We hypothesized that MPC inhibition may result in lactate accumulation due to increased availability of pyruvate in the cytosol. Metabolic footprinting and metabolic profiling revealed that both extracellular and intracellular lactate abundance are increased with UK5099 treatment (**Figure 5a**, **Extended Data Figure 7a, Supplementary Table 4**). Therefore, we asked if lactate supplementation would be sufficient to reduce luminal features in basal-derived prostate organoids. We first validated that 20mM sodium lactate supplementation increased extracellular and intracellular lactate abundance (**Extended Data Figures 7b-c, Supplementary Table 4**). Lactate supplementation reduces the protein abundance of KRT8 and increases the protein abundance of p63 (**Figure 5b**). To uncouple the effect of extracellular and intracellular lactate accumulation, we used a monocarboxylate transporter 1 (MCT1) inhibitor, AZD3965. As expected, AZD3965 treatment reduces extracellular lactate abundance and results in intracellular lactate accumulation (**Extended Data Figures 7d-e, Supplementary Table 4**). Western blot analysis revealed that AZD3965 treatment reduces luminal features (**Extended Data Figure 7f**), suggesting that intracellular lactate accumulation drives the effect on lineage identity.

To understand how prostate organoid cells are utilizing supplemented lactate, we performed heavy isotope nutrient tracing on organoids cultured with 20mM [U-^{13}C]lactate. Heavy isotope carbons were detected in metabolites representing various pathways including choline metabolism, pyrimidine synthesis and glutathione metabolism (**Extended Data Figure 7g, Supplementary Table 4**). Supplemented lactate fuels the TCA cycle through conversion to pyruvate and entry into the mitochondria (**Extended Data Figure 7h, Supplementary Table 4**). Since MPC inhibition and lactate supplementation antagonize luminal identity but have largely opposing effects on metabolism, we hypothesized that the mechanism may be epigenetic in nature. Lactate has been reported to inhibit histone deacetylase (HDAC) activity[33]. We validated the on-target effect of two HDAC inhibitors, Trichostatin A (TSA) and sodium butyrate (**Extended Data Figure 7i**) and found that inhibition of HDAC activity antagonizes luminal identity and enhances basal features in prostate organoids (**Figures 5c-d**).

To determine if HDAC inhibition and MPC inhibition have similar effects on gene expression, we performed RNA sequencing on primary mouse prostate organoids treated with vehicle, UK5099, sodium butyrate, or UK5099 and sodium butyrate in combination (**Extended Data Figure 8a**). Using two-factor, two-level general linear models, we identified genes influenced by each treatment alone and evaluated potential synergy between them. Significantly more genes were influenced by sodium butyrate than UK5099 (1,120 *vs.* 674), and there were few interactions, mostly of small effect-size (**Extended Data Figure 8b**) and reflecting saturation effects rather than synergy (**Extended Data Figure 8c**). We found that 60% of genes affected by UK5099 were also affected by sodium butyrate (**Extended Data Figure 8d**) and with very similar effect-sizes (**Figure 5e**). The 25 genes most associated with basal phenotypes and the 25 most associated with luminal phenotypes strongly distinguished the groups, with basal genes like *p63* and *Krt5* being upregulated after both treatments (**Extended Data Figure 8e**). Genes upregulated by either treatment were preferentially involved in development and differentiation (**Extended Data Figures 8f,h-i**) while those downregulated tended be involved in immune pathways (**Extended Data Figure 8g**). Taken together, these data suggest that MPC inhibition and the subsequent accumulation of lactate may modulate lineage identity through alterations to histone acetylation. Therefore, we performed assay for transposase-accessible chromatin using sequencing (ATAC-seq) on organoids treated with UK5099 or lactate to elucidate how these metabolic manipulations alter chromatin accessibility. We identified 1,712 genes with increased accessibility and 766 genes with decreased accessibility in UK5099-treated organoids (**Figure 5f**, **Supplementary**

Table 6). Lactate-supplemented organoids contain 1,147 hyper-accessible genes and 336 hypo-accessible genes (**Figure 5g**, **Supplementary Table 7**). The global increase in chromatin accessibility observed with UK5099 treatment and lactate supplementation is consistent with the phenotype being mediated by inhibition of HDAC activity.

To identify potential regulators of the shift in lineage identity following lactate accumulation, we performed HOMER transcription factor motif analysis on differentially accessible regions in organoids treated with UK5099 or supplemented with lactate. Of the 47 transcription factor motifs significantly less accessible after lactate supplementation, 44 were also significantly less accessible with UK5099 treatment (**Extended Data Figures 9a-c**, **Supplementary Table 8**). HOXB13, a master regulator of prostate luminal identity[34], is one of the most significantly less accessible binding motifs in both UK5099-treated and lactate-supplemented organoids (**Supplementary Table 8**). Furthermore, we found that the promoter of the luminal marker *Prom1* is hypo-accessible in both UK5099-treated and lactate-supplemented organoids (**Extended Data Figure 9d**). We also identified transcription factor binding motifs in regions that become hyper-accessible after UK5099 treatment and lactate supplementation (**Figures 5h-i**). We found that 36 of the 40 transcription factor motifs significantly more accessible with lactate supplementation are also significantly more accessible with UK5099 treatment (**Figure 5j**, **Supplementary Table 9**). One such motif is p63, a master regulator of basal identity[35]. The *p63* promoter itself is also significantly more accessible in organoids treated with UK5099 and exogenous lactate (**Figure 5k**). From RNA sequencing data, we generated a set of 2,000 genes that are most significantly enriched in primary mouse prostate basal cells relative to luminal cells (**Supplementary Table 10**). We found that 1,507 of the 2,000 basal cell-enriched genes are more accessible in both UK5099-treated and lactate-supplemented prostate organoids (**Figure 5l**). Collectively, these data suggest that MPC inhibition and lactate supplementation facilitate large-scale chromatin remodeling of key lineage-specific transcription factors and genes.

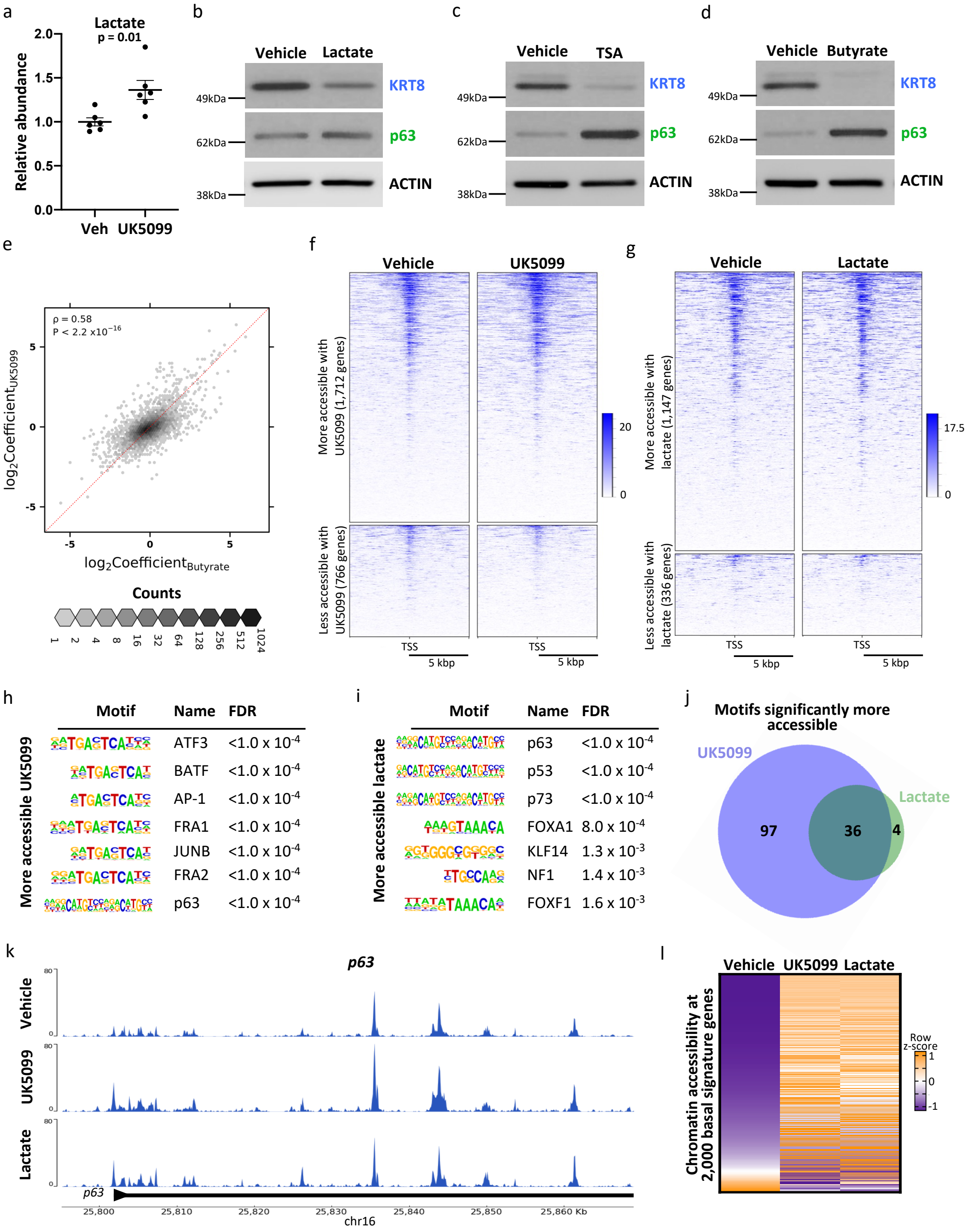

h

Motif	Name	FDR
	ATF3	$<1.0 \times 10^{-4}$
	BATF	$<1.0 \times 10^{-4}$
	AP-1	$<1.0 \times 10^{-4}$
	FRA1	$<1.0 \times 10^{-4}$
	JUNB	$<1.0 \times 10^{-4}$
	FRA2	$<1.0 \times 10^{-4}$
	p63	$<1.0 \times 10^{-4}$

i

Motif	Name	FDR
	p63	$<1.0 \times 10^{-4}$
	p53	$<1.0 \times 10^{-4}$
	p73	$<1.0 \times 10^{-4}$
	FOXA1	8.0×10^{-4}
	KLF14	1.3×10^{-3}
	NF1	1.4×10^{-3}
	FOXF1	1.6×10^{-3}

Figure 5. Intracellular lactate accumulation results in large-scale chromatin remodeling of key lineage-specific transcription factors

(a) Extracellular lactate abundance in primary basal-derived mouse organoids treated with vehicle or 10μM UK5099 for seven days (n=6 independent biological replicates). Error bars represent SEM. p-value was calculated using an unpaired two-tailed t-test with Welch's correction. (b-d) Western blot analysis of the luminal marker KRT8 and the basal marker p63 in basal-derived organoids treated with vehicle or 20mM sodium lactate (b), 10nM TSA (c), or 1mM sodium butyrate (d) for seven days. (e) Spearman's correlation between $\log_2$Coefficients of UK5099 and Butyrate effects for each gene ($r = 0.58$, p-value $< 2.2 \times 10^{-16}$). Each hexagonal bin represents a region of the plot with the color denoting the number of genes that fall within that region. The red dotted line represents x = y. (f) Heatmap of 1,712 hyper-accessible genes and 766 hypo-accessible genes (fold change ≥ 1.5 or fold change ≤ 0.5) in basal-derived mouse organoids treated with vehicle or 10μM UK5099 for seven days. (g) Heatmap of 1,147 hyper-accessible genes and 336 hypo-accessible genes (fold change ≥ 1.5 or fold change ≤ 0.5) in basal-derived mouse organoids treated with vehicle or 20mM sodium lactate for seven days. (h-i) Seven most significantly enriched transcription factor binding motifs in more accessible regions in organoids treated with 10μM UK5099 (h) or 20mM sodium lactate (i). The false discovery rate (FDR) was controlled using the Benjamini-Hochberg method. (j) Venn diagram depicting overlap in significantly enriched transcription factor binding motifs in more accessible regions in UK5099-treated and lactate-supplemented organoids. (k) Browser track depicting ATAC-seq peaks in *p63* gene in vehicle-treated, UK5099-treated, and lactate-supplemented organoids. (l) Heatmap of chromatin accessibility of 2,000 basal signature genes in vehicle-treated, UK5099-treated, and lactate-supplemented organoids.

Lactate metabolism modulation alters antiandrogen response

Given that plasticity from a luminal lineage to a cell state with stem-like, basal and/or neuroendocrine features is associated with resistance to androgen pathway inhibitors[27], we evaluated whether MPC expression is also associated with response to therapy. We used the Tewari *et al.* dataset[36], which contains RNA sequencing of pre-treatment localized prostate cancer biopsies from 43 patients enrolled in neoadjuvant trials of androgen pathway inhibition, and the Alumkal *et al.* dataset[37], which contains RNA sequencing of metastatic castration-resistant prostate cancer biopsies from 25 patients enrolled in a clinical trial of androgen pathway inhibition. Exceptional responders (ER) to therapy exhibit increased RNA abundance of *KRT8* and *KRT18* relative to non-responders to therapy (**Extended Data Figures 10a-b**), consistent with exceptional responders to therapy having tumours with luminal features. ERs exhibit increased RNA abundance of both *MPC1* and *MPC2* relative to non-responders (**Figures 6a-d**). Taken together, these data illustrate that high MPC RNA abundance is positively correlated with increased luminal features and better response to androgen pathway inhibition.

Since lactate accumulation antagonizes luminal lineage identity, we hypothesized that metabolic manipulations that increase lactate abundance would lead to increased resistance to the antiandrogen Enzalutamide. We first confirmed that MPC inhibition or lactate supplementation does not alter proliferation or apoptosis in the castration-resistant 16D prostate cancer cell line. (**Extended Data Figures 10c-f**). We discovered that vehicle-treated cells exhibit sensitivity to Enzalutamide, but pretreatment with UK5099 significantly reduces Enzalutamide sensitivity (**Extended Data Figure 10g**). Furthermore, the reduction in proliferation and increase in apoptosis induced by Enzalutamide is dampened with lactate accumulation (**Extended Data Figures 10h-i**). In organoids derived from the castration-resistant MDA PCa 203-A PDX model (**Figure 6e**), treatment with UK5099 and lactate reduce AR signaling, increase expression of neuroendocrine-like markers (**Extended Data Figure 10j**) and reduce Enzalutamide sensitivity (**Figure 6f**). These data suggest that increasing intracellular lactate abundance can modulate response to antiandrogen treatment.

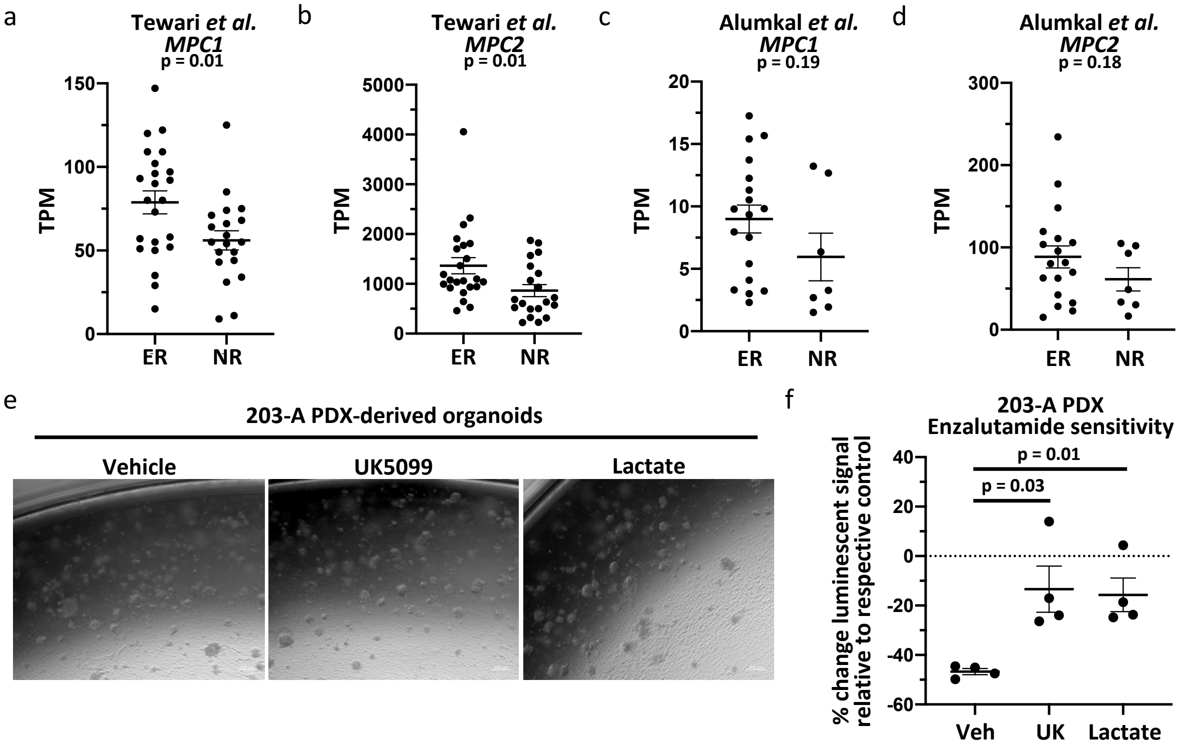

Figure 6. Modulation of lactate metabolism alters antiandrogen response in prostate cancer

(a-b) RNA abundance of *MPC1* (a) or *MPC2* (b) in non-responders (NR) or exceptional responders (ER) from the Tewari *et al.* dataset[36], which contains RNA sequencing of pre-treatment localized prostate cancer biopsies from 43 patients enrolled in neoadjuvant trials of androgen pathway inhibition. (c-d) mRNA abundance of *MPC1* (c) or *MPC2* (d) in non-responders (NR) or exceptional responders (ER) from the Alumkal *et al.*dataset[37], which contains RNA sequencing of metastatic castration-resistant prostate cancer biopsies from 25 patients enrolled in neoadjuvant trials of androgen pathway inhibition. (e) Representative phase contrast images of MDA PCa 203-A PDX-derived organoids treated with vehicle, 10µM UK5099, or 20mM sodium lactate for seven days. (f) Percent change in luminescence signal with 10µM Enzalutamide treatment from CellTiter-Glo assay in castration-resistant MDA PCa 203-A PDX-derived organoids treated with vehicle, 10µM UK5099, or 20mM sodium lactate for seven days before beginning 10µM Enzalutamide treatment (n=4 independent biological replicates). For all panels, error bars represent SEM. p-values were calculated using an unpaired two-tailed t-test with Welch’s correction.

Discussion

Recent work has implicated the epigenome in the establishment and maintenance of prostate epithelial cell fate[8–11, 27]. Metabolism is a key upstream regulator of the epigenome[13–16]; however, the interplay between metabolic signaling and lineage identity in the prostate was previously poorly understood. Previous studies have demonstrated that modulation of pyruvate and lactate metabolism mediates differentiation phenotypes through a metabolic-epigenetic axis[38,39]. We discovered that both MPC inhibition and exogenous lactate supplementation promote increased chromatin accessibility and global chromatin remodeling of lineage-specific transcription factors in prostate epithelial cells (**Figure 5**). We also illustrated that inhibition of HDAC activity antagonizes luminal identity (**Figure 5**). Future experiments will be necessary to elucidate which specific epigenetic modifications are responsible for antagonizing luminal differentiation.

At diagnosis, most prostate tumours rely on androgen receptor (AR) signaling to promote proliferation[40]. As a result, therapies targeting the AR signaling axis are initially effective and extend patient survival[41]. The loss of luminal identity is associated with resistance to AR inhibition[27, 42]. We established that MPC inhibition and intracellular lactate accumulation antagonize luminal differentiation (**Figures 3-5**). It remains unclear whether metabolic regulation of lineage identity can be exploited to promote the reacquisition of luminal features and restore sensitivity to AR inhibition in prostate cancer.

Low oxygen, or hypoxia, is a common feature of prostate tumours and is associated with poor outcome[43]. Furthermore, lactate accumulation in prostate tumours increases with Gleason grade[44]. Hypoxia has also been shown to induce prostate cancer plasticity and neuroendocrine differentiation[45]. Under hypoxic conditions, cellular metabolism is rewired towards a glycolytic program with increased lactate production[46]. Therefore, our work may provide insight into one potential mechanism by which hypoxia and lactate accumulation could promote lineage plasticity.

Distinct cancer types have differing dependencies on the MPC and glycolytic metabolism[47,48]. In prostate cancer, high MPC activity is required for lipogenesis and oxidative phosphorylation, while MPC inactivation suppresses tumour growth[49]. Furthermore, disrupting lactate-dependent lipid rewiring in prostate cancer cells reduces growth and metastasis[50]. Our data suggest MPC inhibition and lactate accumulation may make prostate tumours more resistant to AR inhibition (**Figure 6**). It will be critical to consider how targeting metabolic enzymes and transporters may influence prostate cancer plasticity and response to therapy.

Acknowledgements

We thank Dr. Thomas Graeber, Dr. Daniel Braas, Dr. Johanna ten Hoeve-Scott, and the UCLA Metabolomics Core for guidance on metabolic profiling of small cell populations and metabolomics services. We thank Donghui Cheng for sorting of primary basal and luminal mouse prostate cells. We acknowledge the UCLA Technology Center for Genomics and Bioinformatics (TCGB) for assistance with RNA sequencing, the UCLA Quantitative & Computational Biosciences (QCB) Collaboratory for assistance with scRNA sequencing analysis, the UCLA Broad Stem Cell Research Center (BSCRC) for flow cytometry services, and Active Motif, Inc. for ATAC-sequencing services. We thank Dr. Bill Lowry and Dr. Jared Rutter for *Mpc1* floxed mouse prostate tissue. We thank Dr. Amina Zoubeidi for 16D cells and Dr. Robert Reiter for LAPC4 cells. The UCLA Integrated Molecular Technologies Core is supported by CURE/P30 DK041301. We acknowledge the support of the Hutton Family Foundation. J.M.G. and P.D.C. acknowledge the support of the Ruth L. Kirschstein National Research Service Award GM007185 and the UCLA Eli and Edythe Broad Center of Regenerative Medicine and Stem Cell Research Training Program. P.D.C. is also supported by the NIH grants TL1 DK132768 and U2C DK129496. N.M.N. (Navone) is supported by NCI U01 CA224044-03. N.Y.C.L. is supported by a Young Investigator Award from the Prostate Cancer Foundation (Award ID #: 22YOUN28). P.S.N. is supported by NIH/NCI awards P50CA097186, R01CA234715, and R21CA277368. E.T. is supported by a Fonds de la Recherche Scientifique (FNRS-FRIA) fellowship. C.B. is supported by the WEL Research Institute, FNRS, TELEVIE, Fondation Contre le Cancer, ULB Foundation, EOS FNRS/FWO and the European Research Council. P.C.B. is supported by NIH grants P30CA016042, U2CCA271894 and U01CA214194 and by a Prostate Cancer Foundation Special Challenge Award to PCB (Award ID #: 20CHAS01) made possible by the generosity of Mr. Larry Ruvo. A.S.G. is supported by the National Cancer Institute of the National Institutes of Health under Award Number R01CA237191. The content is solely the responsibility of the authors and does not necessarily represent the official views of the National Institutes of Health. A.M.L.D. is supported by NCI/NIH supplement related to R01CA237191. A.S.G. is also supported by American Cancer Society award RSG-17-068-01-TBG, Department of Defense PCRP award HT94252310379, the UCLA Prostate Cancer Specialized Programs of Research Excellence (SPORE) NCI P50 CA092131, the UCLA Eli and Edythe Broad Center of Regenerative Medicine and Stem Cell Research Rose Hills Foundation Innovator Grant, the UCLA Jonsson Comprehensive Cancer Center and Eli and Edythe Broad Center of Regenerative Medicine and Stem Cell Research Ablon Scholars Program, the University of California Cancer Research Coordinating Committee Faculty Seed Grant, the National Center for Advancing Translational Sciences UCLA CTSI Grant UL1TR001881, STOP CANCER, and the UCLA Institute of Urologic Oncology. The funders had no role in study design, data collection and analysis, decision to publish or preparation of the manuscript.

Author contributions statement

J.M.G., P.D.C., A.M.L.D., T.H., A.A., and J.A.D. conducted the experiments. J.M.G., P.D.C., and A.S.G. designed the experiments. S.M.H. performed single cell RNA sequencing analysis and wrote the related methods section. N.M.N. (Nunley) performed the principal component analysis and wrote the related methods section. R.M.A.D. and M.T. performed UK5099/butyrate RNA sequencing analysis and wrote the related methods section. E.T. and C.B. performed *in vivo* basal to luminal differentiation RNA sequencing and wrote the related methods section. M.C.P. performed organoid immunofluorescence. D.L.B. and L.E. provided *Pten*$^{fl/fl}$ and *Pten*$^{fl/fl}$;*Rb1*$^{fl/fl}$ mouse prostates. D.L., E.C., and P.S.N. provided LuCaP35 cells. N.M.N. (Navone) provided PDX models. J.M.G., P.C.B., and A.S.G. wrote and edited the manuscript. N.Y.C.L., P.C.B., and A.S.G. supervised experiments. A.S.G. procured funding. All authors edited and approved the final version of the manuscript.

Competing interests statement

P.C.B. sits on the Scientific Advisory Boards of Sage Bionetworks, BioSymetrics Inc. and Intersect Diagnostics Inc. E.C. obtains funding from Genentech, Sanofi, AbbVie, Astra Zeneca, Foghorn Pharmaceuticals, Kronos Bio, MacroGenics, Janssen Research, Bayer Pharmaceuticals, Forma Pharmaceuticals, Gilead, Zenith Epigenetics and is a consultant of DotQuant. P.S.N. has received consulting fees from Janssen, Merck, Bristol Myers Squib, Venable Fitzpatrick, and received research funding from Janssen for work unrelated to the present study. All other authors declare no competing interests.

References

1. Abate-Shen, C., Shen, M.M. Molecular genetics of prostate cancer. *Genes and Development*. **14** (732), 2410–2434, doi: 10.1101/gad.819500.2410 (2000).

2. Choi, N., Zhang, B., Zhang, L., *et al.* Adult murine prostate basal and luminal cells are self-sustained lineages that can both serve as targets for prostate cancer initiation. *Cancer Cell*. **21** (2), 253–265, doi: 10.1016/j.ccr.2012.01.005 (2012).

3. Ousset, M., Keymeulen, A. Van, Bouvencourt, G., *et al.* Multipotent and unipotent progenitors contribute to prostate postnatal development. *Nature Cell Biology*. **14** (11), doi: 10.1038/ncb2600 (2012).

4. Wang, J., Zhu, H.H., Chu, M., *et al.* Symmetrical and asymmetrical division analysis provides evidence for a hierarchy of prostate epithelial cell lineages. *Nature Communications*. **5** (4758), doi: 10.1038/ncomms5758 (2014).

5. Toivanen, R., Mohan, A., Shen, M.M. Basal progenitors contribute to repair of the prostate epithelium following induced luminal anoikis. *Stem Cell Reports*. **6** (5), 660–667, doi: 10.1016/j.stemcr.2016.03.007 (2016).

6. Kwon, O., Zhang, L., Ittmann, M.M., *et al.* Prostatic inflammation enhances basal-to-luminal differentiation and accelerates initiation of prostate cancer with a basal cell origin. *PNAS*. **5** (111), doi: 10.1073/pnas.1318157111 (2013).

7. Stoyanova, T., Cooper, A.R., Drake, J.M., *et al.* Prostate cancer originating in basal cells progresses to adenocarcinoma propagated by luminal-like cells. *PNAS*. **110** (50), 20111–20116, doi: 10.1073/pnas.1320565110 (2013).

8. Zhang, B., Ci, X., Tao, R., *et al.* Klf5 acetylation regulates luminal differentiation of basal progenitors in prostate development and regeneration. *Nature Communications*. **11** (1), doi: 10.1038/s41467-020-14737-8 (2020).

9. Dardenne, E., Beltran, H., Benelli, M., *et al.* N-Myc induces an EZH2-mediated transcriptional program driving neuroendocrine prostate cancer. *Cancer Cell*. **30** (4), 563–577, doi: 10.1016/j.ccell.2016.09.005 (2016).

10. Fraser, M., Livingstone, J., Wrana, J.L., *et al.* Somatic driver mutation prevalence in 1844 prostate cancers identifies ZNRF3 loss as a predictor of metastatic relapse. *Nature Communications*. **12** (6248), 1–15, doi: 10.1038/s41467-021-26489-0 (2021).

11. Parolia, A., Cieslik, M., Chu, S., *et al.* Distinct structural classes of activating FOXA1 alterations in advanced prostate cancer. *Nature*. **571** (7765), doi: 10.1038/s41586-019-1347-4 (2019).

12. Lu, C., Thompson, C.B. Metabolic regulation of epigenetics. *Cell Metabolism*. **16** (1), 9–17, doi: 10.1016/j.cmet.2012.06.001 (2012).

13. Morrish, F., Noonan, J., Perez-olsen, C., *et al.* Myc-dependent mitochondrial generation of acetyl-CoA contributes to fatty acid biosynthesis and histone ccetylation during cell cycle entry. *Journal of Biological Chemistry*. **285** (47), 36267–36274, doi: 10.1074/jbc.M110.141606 (2010).

14. Agathocleous, M., Meacham, C.E., Burgess, R.J., *et al.* Ascorbate regulates haematopoietic stem cell function and leukaemogenesis. *Nature*. **549** (7673), 476–481, doi: 10.1038/nature23876 (2017).

15. Baksh, S.C., Todorova, P.K., Gur-cohen, S., *et al.* Extracellular serine controls epidermal stem cell fate and tumour initiation. *Nature Cell Biology*. **22** (7), 779–790, doi: 10.1038/s41556-020-0525-9 (2020).

16. Mews, P., Donahue, G., Drake, A.M., *et al.* Acetyl-CoA synthetase regulates histone acetylation and hippocampal memory. *Nature*. **546** (7658), 381–386, doi: 10.1038/nature22405 (2017).

17. Crowell, P.D., Fox, J.J., Hashimoto, T., *et al.* Expansion of luminal progenitor cells in the aging mouse and human prostate. *Cell Reports*. **28** (6), 1499–1510, doi: 10.1016/j.celrep.2019.07.007 (2019).

18. Smith, B.A., Sokolov, A., Uzunangelov, V., *et al.* A basal stem cell signature identifies aggressive prostate cancer phenotypes. *PNAS*. **112** (47), doi: 10.1073/pnas.1518007112 (2015).

19. Karthaus, W.R., Hofree, M., Choi, D., *et al.* Regenerative potential of prostate luminal cells revealed by single-cell analysis. *Science*. **368** (6490), 497–505 (2020).

20. Crowley, L., Cambuli, F., Aparicio, L., *et al.* A single-cell atlas of the mouse and human prostate reveals heterogeneity and conservation of epithelial progenitors. *eLife*. **9**, 1–24 (2020).

21. Mann, T., Lutwak-Mann, C. *Male reproductive function and semen*. Springer-Verlag. (1981).

22. Costello, L.C., Liu, Y., Franklin, R.B., *et al.* Zinc inhibition of mitochondrial aconitase and its importance in citrate metabolism of prostate epithelial cells. *Journal of Biological Chemistry*. **272** (46), 28875–28881, doi: 10.1074/jbc.272.46.28875 (1997).

23. Zhang, D., Park, D., Zhong, Y., *et al.* Stem cell and neurogenic gene-expression profiles link prostate basal cells to aggressive prostate cancer. *Nature Communications*. **7** (10798), doi: 10.1038/ncomms10798 (2016).

24. Tika, E., Ousset, M., Dannau, A., *et al.* Spatiotemporal regulation of multipotency during prostate development. *Development*. **146** (20), doi: 10.1242/dev.180224 (2019).

25. Karthaus, W.R., Iaquinta, P.J., Drost, J., *et al.* Identification of multipotent luminal progenitor cells in human prostate organoid cultures. *Cell*. **159** (1), 163–175, doi: 10.1016/j.cell.2014.08.017 (2014).

26. Bricker, D.K., Taylor, E.B., Schell, J.C., *et al.* A mitochondrial pyruvate carrier required for pyruvate uptake in yeast, Drosophila, and humans. *Science*. **337** (6090), 96–101, doi: 10.1126/science.1218099 (2012).

27. Ku, S.Y., Rosario, S., Wang, Y., *et al.* Rb1 and Trp53 cooperate to suppress prostate cancer lineage plasticity, metastasis, and antiandrogen resistance. *Science*. **355** (6320), 78–83,

doi: 10.1126/science.aah4199 (2017).

28. Hoadley, K.A., Yau, C., Hinoue, T., *et al.* Cell-of-origin patterns dominate the molecular classification of 10,000 tumors from 33 types of cancer. *Cell*. **173** (2), 291–304, doi: 10.1016/j.cell.2018.03.022 (2018).

29. Ren, S. Whole-genome and Transcriptome Sequencing of Prostate Cancer Identify New Genetic Alterations Driving Disease Progressione. *European Urology*. **73** (3), doi: 10.1016/j.eururo.2017.08.027 (2018).

30. Beltran, H., Prandi, D., Mosquera, J.M., *et al.* Divergent clonal evolution of castration-resistant neuroendocrine prostate cancer. *Nature Medicine*. **22** (3), 298–305, doi: 10.1038/nm.4045 (2016).

31. Nguyen, H.M., Vessella, R.L., Morrissey, C., *et al.* LuCaP prostate cancer patient-derived xenografts reflect the molecular heterogeneity of advanced disease and serve as models for evaluating cancer therapeutics. *The Prostate*. **671** (6), 654–671, doi: 10.1002/pros.23313 (2017).

32. Lee, J., Jin, Z., Lee, D., *et al.* Characteristic analysis of homo- and heterodimeric complexes of human mitochondrial pyruvate carrier related to metabolic diseases. *International Journal of Molecular Sciences*. **21** (9) (2020).

33. Latham, T., Mackay, L., Sproul, D., *et al.* Lactate, a product of glycolytic metabolism, inhibits histone deacetylase activity and promotes changes in gene expression. *Nucleic Acids Research*. **40** (11), 4794–4803, doi: 10.1093/nar/gks066 (2012).

34. Mcmullin, R.P., Mutton, L.N., Bieberich, C.J. Hoxb13 regulatory elements mediate transgene expression during prostate organogenesis and carcinogenesis. *Developmental Dynamics*. **238** (3), 664–672, doi: 10.1002/dvdy.21870 (2009).

35. Signoretti, S., Waltregny, D., Dilks, J., *et al.* p63 is a prostate basal cell marker and is required for prostate development. *American Journal of Pathology*. **157** (6), 1769–1775 (2000).

36. Tewari, A.K., Cheung, A.T.M., Crowdis, J., *et al.* Molecular features of exceptional response to neoadjuvant anti-androgen therapy in high-risk localized prostate cancer. *Cell Reports*. **36** (10), doi: 10.1016/j.celrep.2021.109665 (2021).

37. Alumkal, J.J., Sun, D., Lu, E., *et al.* Transcriptional profiling identifies an androgen receptor activity-low , stemness program associated with enzalutamide resistance. *PNAS*. **22** (117), 12315–12323, doi: 10.1073/pnas.1922207117 (2020).

38. Wenes, M., Jaccard, A., Wyss, T., *et al.* The mitochondrial pyruvate carrier regulates memory T cell differentiation and antitumor function. *Cell Metabolism*. **34** (5), 731–746, doi: 10.1016/j.cmet.2022.03.013 (2022).

39. Feng, Q., Liu, Z., Yu, X., *et al.* Lactate increases stemness of CD8+ T cells to augment anti-tumor immunity. *Nature Communications*. **13** (4981), doi: 10.1038/s41467-022-32521-8 (2022).

40. Dai, C., Heemers, H., Sharifi, N. Androgen signaling in prostate cancer. *Cold Spring Harbor Perspectives in Medicine*. **7** (9) (2017).

41. Chen, Y., Sawyers, C.L., Scher, H.I. Targeting the androgen receptor pathway in prostate cancer. *Current Opinion in Pharmacology*. **8** (4), doi: 10.1016/j.coph.2008.07.005 (2008).

42. Beltran, H., Hruszkewycz, A., Scher, H.I., *et al.* The role of lineage plasticity in prostate cancer therapy resistance. *Clinical Cancer Research*. **25** (23), 6916–6924, doi: 10.1158/1078-0432.CCR-19-1423 (2019).

43. Bhandari, V., Hoey, C., Liu, L.Y., *et al.* Molecular landmarks of tumor hypoxia across cancer types. *Nature Genetics*. **51** (2), 308–318, doi: 10.1038/s41588-018-0318-2 (2019).

44. Granlund, K.L., Tee, S., Vargas, H.A., *et al.* Hyperpolarized MRI of human prostate cancer reveals increased lactate with tumor grade driven by monocarboxylate transporter 1. *Cell Metabolism*. **31** (1), 105–114, doi: 10.1016/j.cmet.2019.08.024 (2020).

45. Guo, H., Ci, X., Ahmed, M., *et al.* ONECUT2 is a driver of neuroendocrine prostate cancer. *Nature Communications*. **10** (1) (2019).

46. Denko, N.C. Hypoxia, HIF and glucose metabolism in the solid tumour. *Nature Reviews Cancer*. **8** (9), 705–713 (2008).

47. Bensard, C.L., Wisidagama, D.R., Olson, K.A., *et al.* Regulation of tumor initiation by the mitochondrial pyruvate carrier. *Cell Metabolism*. **31** (2), 284–300, doi: 10.1016/j.cmet.2019.11.002 (2020).

48. Tompkins, S.C., Sheldon, R.D., Rauckhorst, A.J., *et al.* Disrupting mitochondrial pyruvate uptake directs glutamine into the TCA cycle away from glutathione synthesis and impairs hepatocellular tumorigenesis. *Cell Reports*. **28** (10), 2608–2619, doi: 10.1016/j.celrep.2019.07.098 (2019).

49. Bader, D.A., Hartig, S.M., Putluri, V., *et al.* Mitochondrial pyruvate import is a metabolic vulnerability in androgen recptor-driven prostate cancer. *Nature Metabolism*. **1** (1), 70–85, doi: 10.1038/s42255-018-0002-y (2019).

50. Ippolito, L., Comito, G., Parri, M., *et al.* Lactate rewires lipid metabolism and sustains a metabolic–epigenetic axis in prostate cancer. *Cancer Research*. **82** (7), 1267–1282, doi: 10.1158/0008-5472.CAN-21-0914 (2022).

Methods

All experiments, including animal studies, were conducted in compliance with federal and state government guidelines and followed approved protocols by the Institutional Biosafety Committee and the Institutional Animal Care and Use Committee at the University of California, Los Angeles.

Animal work

All mice are housed under 12 h:12 h light–dark cycle, with room temperature maintained at 73°F and relative humidity level of 30-70%. Mouse cages include clean bedding and enrichment materials consistent with Institutional Animal Care and Use Committee regulations. According to the Animal Research Committee policy on humane treatment and endpoints, mice must be sacrificed if tumors become ulcerated, necrotic, and/or impair normal function. All experiments were terminated before tumors reached this stage.

For experiments described below, animals were housed under the care of the Division of Laboratory Animal Medicine at the University of California, Los Angeles, using protocols approved by the Animal Research Committee (ARC #2017-020). Prostates from three- to six-month-old immunocompetent male C57BL/6J mice from Jackson Laboratories were used for primary basal and luminal cell experiments. *Mpc1* floxed male mice were of mixed C57Bl/6N and C57Bl/6J genetic background[51]. For *in vivo* UK5099 experiments, twelve million 16D cells were subcutaneously implanted with 100 µl Matrigel (Corning) into the right flank of NOD-scid-IL2Rg^{null} male mice through a 25 gauge needle under inhalation anesthesia with 2-3% isoflurane. The mice were fed with either control chow or chow containing 0.08 mg/kg UK5099 (OpenStandard Diet with 15 kcal% Fat with Blue Dye Irradiated (10 to 20 kGy), Research Diets Inc.) until tumours were formed and harvested. Patient-derived xenograft (PDX) MDA PCa 203-A and MDA PCa 183-A tumours were obtained from MD Anderson Cancer Center[52]. Both 203-A and 183-A PDX models were derived from 58-year-old males. When these PDX models were originally generated, written informed consent was obtained from patients before sample acquisition, and all samples were processed according to a protocol approved by the Institutional Review Board of the University of Texas MD Anderson Cancer Center. The studies were conducted in accordance with the Belmont Report and the US Common Rule. Patients were not compensated, and they cannot be identified from data provided in this manuscript. A tumour tissue piece of 50 to 200 mg was implanted in the right flank of NOD-scid-IL2Rγ^{null} mice subcutaneously through a 5 mm skin incision under inhalation anesthesia with 2-3% isoflurane. After closing the wound with a surgical clip, 100 mL of Matrigel (Corning 354234) was injected at the implantation site. Carprofen was administered subcutaneously at a dose of 5 mg/kg after surgery. The surgical clip was removed 1 to 2 weeks later. When the tumour was grown larger than 500 mm^3, the mouse was euthanized and the tumour was excised, trimmed, and either processed for the experiments, re-implanted, or cryopreserved. Cryopreservation of the tissue was done in the media with 50% fetal bovine serum, 40% Dulbecco's Modified Eagle Medium, and 10% dimethyl sulfoxide.

The experiments described below were conducted in compliance with European guidelines regarding animal research and ethical protocols (under protocol numbers 671N and 673N) were approved by the local ethical committee for animal welfare (CEBEA). All animals were housed under standard laboratory conditions in a certified animal facility receiving food and water ad libitum. Prostates used for isolation of multipotent basal cells and basal-derived luminal cells were collected from CD1 mice purchased from the Jackson Laboratory. The experimental mice used were males of mixed background and at P10-P12 age.

Pten floxed and *Pten*;*Rb1* floxed three-month-old male mice were of mixed C57BL/6:129/Sv:FVB genetic background[27] and housed at Harvard Medical School under IACUC approved protocols.

Mouse prostate dissociation to single cells

Using a razor blade, individual mouse prostates were mechanically dissociated in dissociation media comprised of RPMI 1640 (Gibco) containing 10% fetal bovine serum (Corning), 1x penicillin-streptomycin (Gibco), 1 mg/mL collagenase type I (Gibco), 1 mg/mL dispase (Gibco), 0.1 mg/mL deoxyribonuclease (Gibco), and 10µM of the p160ROCK inhibitor Y-27632 dihydrochloride (Tocris Bioscience). When chunks were no longer visible, the samples were incubated at 37°C on a nutating platform for 1.5 hours in 10 mL of dissociation media. After centrifugation at 800g for 5 minutes, the pellet was washed with 1x phosphate buffered saline (PBS). The cell pellet was resuspended in 2.7 mL of 0.05% Trypsin-EDTA (Gibco) and incubated at 37°C for 5 minutes. Trypsin was inactivated with 300 mL of dissociation media. Cells were further dissociated by pipetting with a P-1000 pipette and an 18G syringe. Cells were passed through a 100µm cell strainer (Corning).

Staining and sorting cells from mouse prostate for isolation of primary basal and luminal cells

Dissociated cells were stained with directly conjugated primary antibodies: rat anti-CD49f-PE (BioLegend 313612, 1:100), rat anti-CD326 (EpCAM)-APC (BioLegend 324207, 1:100), rat anti-CD31-FITC (BioLegend 102405, 1:100), rat anti-CD45-FITC (BioLegend 103108, 1:100), rat anti-Ter119-FITC (BioLegend 116205, 1:100) and rat anti-ESAM-FITC (BioLegend 136205, 1:100) for 20 minutes on ice. Cells were stained in media containing RPMI 1640 (Gibco), 10% FBS (Corning), 1x penicillin-streptomycin (Gibco), and 10µM of the p160ROCK inhibitor Y-27632 dihydrochloride (Tocris Bioscience). Sorting was performed on a BD FACS Aria II (BD Biosciences).

Bulk RNA sequencing

These methods apply to Figure 1b-c, Figure 1f-g, Extended Data Figure 1b-e, Figure 3j, Extended Data Figure 4f-h, Figure 4b, Extended Data Figure 6d, Extended Data Figure 8. RNA was extracted from the cells using the RNeasy Mini Kit (QIAGEN) following the manufacturer's instruction. Libraries for RNA-seq were prepared with KAPA Stranded mRNA-Seq Kit (Roche). The workflow consists of mRNA enrichment, cDNA generation, and end repair to generate blunt ends, A-tailing, adaptor ligation and PCR amplification. Different adaptors were used for multiplexing samples in one lane. Sequencing was performed on Illumina HiSeq 3000 for single-end 1x50 run (Figure 1b-c, Extended Data Figure 1b-e, Extended Data Figure 2d-e, Figure 3j, Extended Data Figure 4f-h, Figure 4b, Extended Data Figure 6d) and paired-end 2x50 run (Extended Data Figure 8).

Bulk RNA sequencing analysis

These methods apply to Figure 1b-c, Figure 1f-g, Extended Data Figure 1b-e, Figure 3j, Extended Data Figure 4f-h, Figure 4b, and Extended Data Figure 6d. Sequencing quality metrics were generated during sequencing runs using Illumina Sequencing Analysis Viewer (SAV). Demultiplexing was performed with Illumina Bcl2fastq (v2.19.1.403) software. The reads were mapped by STAR 2.7.9a[53] and read counts per gene were quantified using the mouse Ensembl GRCm39.105 GTF file. In Partek Flow v7.0, read counts were normalized by CPM 1.0×10^{-4}. All results of differential expression analysis utilized the statistical analysis tool, DESeq2 (v1.40.2)[54]. KEGG pathway analysis was performed using DAVID Bioinformatics[55, 56]. GSEA was performed as described previously using GSEA_4.0.3 software[57, 58].

Significance testing of RNA sequencing of UK5099- and sodium butyrate-treated organoids

These methods apply to Extended Data Figure 8. To measure the RNA abundance, RNA-seq reads were trimmed using fastp (v0.20.1)[59] with default parameters, then mapped to the mouse Ensembl GRCm38-EBI102 using STAR (v2.7.10a)[53]. STAR alignment was carried out using default settings with an additional argument to include the minimum length of 10 bp for chimeric junction segment. Aligned reads were quantified using rsem-calculate-expression program (v1.3.3)[60] for TPM calculation with default settings. We also performed read level quality control metrics using FastQC (v0.11.8).

To test the combination effect of UK5099 and Butyrate, we constructed the following two-factor, two-level linear model:

$$Y \sim \alpha_0 + \alpha_1 \cdot UK5099 + \alpha_2 \cdot Butyrate + \alpha_3 \cdot UK5099{:}Butyrate$$

Here, *Y* refers to the abundance level of a gene, which is $\log_2$ transformation of TPM values; α_0 refers to the basal abundance level of that gene; *UK5099* indicates “UK5099-dependent, Butyrate-independent” abundance changes; *Butyrate* indicates “Butyrate-dependent, UK5099-independent” abundance changes; *UK5099-Butyrate* captures “UK5099-dependent, Butyrate-dependent” abundance changes.

We used R package limma (v3.17)[61] in R (v4.2.2) to fit each gene in the RNA sequencing to the model. The model was adjusted using empirical Bayes moderation for standard error, and the false discovery rate (FDR) was controlled using the Benjamini-Hochberg method[62]. Genes exhibiting significant changes were identified based on the adjusted p-value < 0.01 and $|\log_2(\text{Coefficient})| > 1$ threshold. Venn diagrams representing the overall and directional effects were generated using the VennDiagram package in R (v1.7.3)[63]. The hierarchical clustering heatmap of gene TPM was constructed using R package BoutrosLab.plotting.general (v7.0.8)[64].

Functional Enrichment Analysis

These methods apply to Extended Data Figure 8. For genes with differential mRNA abundance calculated based on the coefficient from the general linear model, we ranked the genes according to their $\log_2$(Coefficient) from high to low. Gene set enrichment analysis was then performed using the R package clusterProfiler (v3.17)[65]. Gene ontology enrichment analysis was conducted for both up-regulated genes ($\log_2$(Coefficient) > 1, $-\log_{10}$(FDR) > 1) and down-regulated genes ($\log_2$(Coefficient) < -1, $-\log_{10}$(FDR) > 1) using R package clusterProfiler (v3.17). The results of both GSEA and GO enrichment analyses were visualized using the BoutrosLab.plotting.general (v7.0.8)[64].

Single cell RNA sequencing (scRNA-seq)

Basal cells were isolated from *Pten*$^{fl/fl}$;*Rb1*$^{fl/fl}$ mouse prostates and infected with FU-CRW (RFP) lentivirus. Lentiviral spinfections were done by culturing the cells with virus in 200 µL RPMI 1640 (Gibco) containing 10% fetal bovine serum (Corning), 1x penicillin-streptomycin (Gibco), and 10µM of the p160ROCK inhibitor Y-27632 dihydrochloride (Tocris Bioscience) (RPMI 10% FBS 1% P/S +RI) plus 8 µg/mL polybrene for 30 minutes at 37°C then spinning at 300g for 90 minutes. After spinfection, growth factor reduced Matrigel (Corning) was added to the cell suspension at a final concentration of 75% before plating into rings in 24-well plates. Organoids were cultured as previously described[66] and passaged every 7-10 days. After >4 passages, organoids were treated with vehicle (DMSO) or 10µM UK5099 for 3 days. Organoids were removed from Matrigel by incubating in Advanced DMEM/F-12 (Gibco) containing 1 mg/mL dispase (Gibco) and 10µM of the p160ROCK inhibitor Y-27632 dihydrochloride (Tocris Biosciences) for 1 hour at 37°C. After centrifugation at 800g for 5 minutes, the pellet was washed with 1x phosphate buffered saline

(PBS, Gibco). Organoids were resuspended in 800 µL 0.05% Trypsin-EDTA (Gibco) and incubated at 37°C for 5 minutes. The Trypsin was quenched with 200 µL RPMI 10% FBS 1% P/S + ROCK inhibitor and organoids were pipetted up and down ten times to dissociate to single cells and passed through a 100µm cell strainer (Corning). Samples were counted using Countess II Automated Cell Counter (Thermo Fisher Scientific) and hemocytometer for cell concentration and viability using Trypan Blue stain 0.4% (Invitrogen). Cells were loaded to form GEMs and barcode individual cells. GEMs were treated according to manufacturer's instructions. Single cell gene expression libraries were created using Chromium Next GEM Single Cell 3' (v3.1 Chemistry) (10x Genomics), Chromium Next GEM Chip G Single Cell Kit (10x Genomics), and Single Index Kit T Set A (10x Genomics) according to the manufacturer's instructions. Paired-end sequencing was done using Illumina Novaseq 6000 at a sequencing depth of 492,915,641 and 555,876,242 read pairs for vehicle and UK5099 samples, respectively, with read length of 151 for both read 1 and read 2, and with an 8 bp index read for multiplexing. Basecalling was done using Illumina Casava (v1.7) software. CellRanger (v5.1) count was used to create an RNA abundance matrix with --expect-cells=1000 and Mus musculus (mm10) from Ensembl database as a reference genome[67]. RNA abundance matrices from vehicle- and UK5099-treated samples were loaded into the Seurat (v3.2.2) R package[68]. DoubletDcon (v1.1.2) was used to remove potential doublets[69]. Additionally, cells were filtered based on the number of genes (≥250), unique molecular identifiers (UMIs; ≥500) and percent of mitochondrial genes (<20%). After quality control, $\log_2$ normalization was performed within each sample using *NormalizeData* function with default parameters. The top 2,000 variable genes were selected using *FindVariableFeatures*. The two samples were integrated together with *FindIntegrationAnchors* and *IntegrateData* functions which incorporate canonical correlation analysis to align cells with similar transcriptomic patterns across samples. Principal component analysis (PCA) was performed after the integration. The top 20 PCs were used to construct the k-nearest neighbor graph, followed by Louvain algorithm to cluster cells based on similar gene expression patterns. Cell clusters were visualized using t-distributed stochastic neighbor embedding (tSNE). After, markers for each cluster were determined using FindAllMarkers with average $\log_2$ fold change > 0.25 and minimum percent difference > 0.25. Cell types were determined by comparing canonical markers with cluster-specific markers. After cell type identification, cell type proportions were calculated with the number of cells in each cell type divided by the total number of cells in each sample. To see the effect of UK5099 in the luminal cluster, *DotPlot* in Seurat was used to visualize the expression of luminal markers, basal markers, glycolytic enzymes, lipid metabolism genes, and inflammatory signaling genes.

Cell lysis and Western blot

Primary basal and luminal cells were sorted and immediately lysed in RIPA buffer (50mM Tris-HCl pH 8.0, 150mM NaCl, 1% NP-40, 0.5% Sodium Deoxycholate, 0.1% SDS, Fisher Scientific) containing a cOmplete protease inhibitor cocktail tablet (Roche) and Halt Phosphatase Inhibitor (Fisher Scientific). Organoids were removed from Matrigel by incubating in Advanced DMEM/F-12 (Gibco) containing 1 mg/mL dispase (Gibco) and 10μM of the p160ROCK inhibitor Y-27632 dihydrochloride (Tocris Biosciences) for 1 hour at 37°C. After centrifugation at 800g for 5 minutes, the pellet was washed with 1x phosphate buffered saline (PBS) and immediately lysed in RIPA buffer containing a cOmplete protease inhibitor cocktail tablet and Halt Phosphatase inhibitor. For tumour lysis, tumour tissue was added to a bead tube (Fisher, 15-340-153) containing 1 mL RIPA buffer containing a cOmplete protease inhibitor cocktail tablet and Halt Phosphatase inhibitor on ice. Samples were homogenized for 1 minute at max speed twice on a bead homogenizer (Fisher). Bead tubes were spun at 17000g at 4°C for 10 minutes. The supernatant was transferred to an Eppendorf tube and spun at 17000g at 4°C for 10 minutes. Each sample was sonicated for 40 seconds at 20kHz with a sonic dismembrator (Fisher Scientific) to improve membranous and nuclear protein yield. Samples were run on NuPAGE 4–12% Bis-Tris Gel (Invitrogen) and transferred onto PVDF membranes (Millipore Sigma). Total protein was visualized using SYPRO

RUBY protein blot stain (Fisher Scientific) and membranes were blocked in PBS + 0.1% Tween-20 (Fisher Scientific) + 5% milk (Fisher Scientific). Proteins were probed with primary antibodies followed by chromophore-conjugated anti-mouse (Invitrogen A21235, 1:1000) or anti-rabbit secondary antibodies (Invitrogen A21244, 1:1000) or HRP-conjugated anti-mouse (Thermo 31430, 1:10000) or anti-rabbit secondary antibodies (Thermo 31463, 1:10000) and detected by florescence or HRP chemiluminescence respectively. Primary antibodies used were anti-Cytokeratin 5 (Biolegend 905504, 1:3000), anti-Probasin (Santa Cruz sc-393830, 1:1000), anti-Glut1 (Abcam ab115730, 1:10,000), anti-Glut3 (Abcam ab191071, 1:1000), anti-Hexokinase 2 (Cell Signaling 28675, 1:1000), anti- Phosphofructokinase (Abcam ab204131, 1:5000), anti-Pyruvate carboxylase (Abcam ab128952, 1:1000), anti- Pyruvate dehydrogenase E1 component subunit alpha (Proteintech 18068-1-AP, 1:1000), anti-Aconitase 2 (Abcam ab110321, 1:1000), anti-Histone H3 (Cell Signaling 9717S, 1:1000), anti-Cytokeratin 8 (Biolegend 904804, 1:1000), anti-p63 (Biolegend 619002, 1:1000), anti-beta Actin (Fisher MA1-140, 1:15000), anti-Proliferating cell nuclear antigen (Fisher 13-3900, 1:1000), anti-Androgen receptor (Abcam ab133273, 1:1000), anti-Mitochondrial pyruvate carrier 1 (Cell Signaling 14462, 1:1000), anti-Ki-67 (Abcam ab15580, 1:1000), anti-cleaved caspase-3 (Cell Signaling 9661L, 1:500), anti-Cytokeratin 18 (Fisher MA5-12104, 1:100), anti-Vinculin (Abcam Ab129002, 1:1000), anti-Phosphatase and tensin homolog (Cell Signaling 9559, 1:1000), anti-Retinoblastoma protein 1 (Abcam ab181616, 1:1000), anti-Acetyl-histone H3 (Lys9) (Cell Signaling 9649, 1:1000), anti-Pan-acetyl histone H3 (Active Motif 61637, 1:1000), anti-Histone H4 (Abcam ab10158, 1:1000), anti-Pan-acetyl histone H4 (Abcam ab177790, 1:1000), anti-prostate-specific antigen (Cell Signaling 5877, 1:1000), anti-neuron-specific enolase (Proteintech 66150-1-Ig, 1:3000), anti-synaptophysin (Cell Signaling 5461, 1:1000), anti-Sox2 (Cell Signaling 14962, 1:1000).

Apoptosis assay

Cell culture media and wash media were collected and pooled with quenched trypsin-containing media containing cells and apoptosis analysis was performed using an apoptosis detection kit (BioLegend, 640922) according to manufacturer instructions. Flow cytometry was performed to quantify the percentage of annexin V^-, 7-AAD^- cells.

Primary cell metabolic profiling and nutrient tracing

12-well plates were coated with a 1/80 dilution of growth factor reduced Matrigel (Corning) in RPMI-1640 (Gibco) to enhance cell attachment. The 1/80 Matrigel coating was aspirated before primary basal and luminal cells were seeded at a density of 200,000 cells/well and 140,000 cells/well respectively. Cells were cultured overnight in mouse organoid media[66] containing [U-^{13}C]glucose (Cambridge Isotope Laboratories). Prior to metabolite extraction, tracer-containing media was aspirated and cells were washed with cold 150mM ammonium acetate pH 7.3. Metabolite extractions were performed by adding 500 µL cold 80% methanol to each well and removing cells using a cell scrapper. The cell suspension was transferred to an Eppendorf tube and 10 µL 1mM norvaline (Sigma) was added as an internal standard. Each sample was vortexed for 30 seconds and centrifuged at 17000g for 5 minutes at 1°C. 420 µL of the supernatant was transferred to an ABC vial (Fisher Scientific) and evaporated using an EZ-2Elite evaporator (Genevac). Samples were stored at -80°C prior to analysis.

The LC separation utilizing an Ion Chromatography System (ICS) 5000 (Thermo Scientific) was performed on a Dionex IonPac AS11-HC-4µm anion exchange column. The gradient was 5-95 mM KOH over 13 minutes, followed by 5 minutes at 95mM, before re-equilibration to 5mM. Other LC parameters: flow rate 350 µl/min, column temperature 35°C, injection volume 5 µL. The Q Exactive mass spectrometer (Thermo Scientific) was operated in negative ion mode for detection of metabolites using a resolution of 70,000 at m/z 200 and a scan range of 70-900 m/z. Data were extracted using Tracefinder 3.1 (Thermo Scientific). Metabolites were identified based on accurate mass (±5 ppm) and previously established retention times of pure standards.

Normalization was performed by resuspending the cell pellet in 300 µL lysis solution (0.1M NaCl, 20mM Tris-HCl, 0.1% SDS, 5mM EDTA in distilled water). Samples were syringed with a 25G needle to reduce viscosity and 50 µL of each sample was transferred to a 96-well black wall clear bottom tissue culture plate (Corning). 50 µL lysis solution was added to one well for a blank reading. 100 µL of 5 µg/mL Hoechst 33342 (Invitrogen) in distilled water was added to each well and 96-well plates were incubated for 30 minutes in the dark at 37°C before measurement of DNA-based florescence using a Tecan Infinite M1000 plate reader with 355nm excitation and 465nm emission. The blank reading was subtracted from each absorbance value to calculate relative cell amount.

In vivo **basal to luminal differentiation RNA sequencing**

Cell preparation from postnatal prostates

Prostate tissue of mice at P10-P12 was microdissected under a stereoscope to separate the different lobes. The ventral lobe was used to further separate (by cutting) the tips from the main ducts. The ventral lobes of 20 mice at P10-P12 were used. Tissues were collected in 24-well plates and chopped. Minced tissues were digested in 5 mg/mL Collagenase Type I (Sigma-Aldrich, diluted in HBSS) for 2 hours at 37°C under agitation. Physical dissociation using a P1000 pipette was performed every 20 minutes throughout the enzymatic digestion. Collagenase activity was blocked by adding EDTA (5 mM) for 2 minutes, followed by 0.25% trypsin-EDTA for 5 minutes. Cells were rinsed in HBSS supplemented with 10% FBS and the cell suspensions were filtered through a 70µm cell strainers (BD Bioscience), followed by two successive washes in HBSS supplemented with 2% FBS.

Cell labelling, flow cytometry and sorting from postnatal prostates

Samples were incubated in 200 µL PBS supplemented with 2% FBS with fluorochrome-conjugated antibodies for 30 minutes on ice protected from light, with shaking every 10 minutes. Antibodies were washed with 2% FBS/PBS and cells were resuspended in 2.5 mg/mL DAPI (Invitrogen, D1306) before analysis. The following antibodies were used: PE-conjugated anti-CD45 (rat, clone 30-F11, dilution 1:100, BD Biosciences Cat#553081), PE-conjugated anti-CD31 (rat, clone MEC 13.3, dilution 1:100, BD Biosciences Cat#553373), PE-conjugated anti-CD140a (rat, clone APA5, dilution 1:100, BD Biosciences Cat#624049), APC-conjugated anti-CD49f (rat, clone GoH3, dilution 1:100, eBioscience Cat#17-0495), APC-Cy7-conjugated anti-EpCAM (rat, clone G8.8, dilution 1:100, BioLegend Cat#118218). Living cells were selected by forward and side scatter, doublets discriminating and DAPI dye exclusion. CD45+, CD31+ and CD140a+ cells were excluded (Lin+) before analysis of the epithelial basal (EpCam^{high}/CD49f^{high}) and luminal (EpCam^{high}/CD49f^{low}) cells. Fluorescence-activated cell sorting and analysis were performed using FACSAria and LSRFortessa, using FACSDiva software (BD Bioscience). Sorted cells were collected in lysis buffer for RNA extraction (RLT buffer, QIAGEN). The following samples were collected in replicates from P10-P12 prostates: 1702 basal cells and 1626 luminal cells from the tips.

RNA extraction and RNA sequencing

These methods apply to Figure 2b and Extended Data Figure 3a. RNA extraction from FACS isolated cells was performed using RNeasy micro kit (QIAGEN) according to the manufacturer´s recommendations. Prior to sequencing the quality of RNA was evaluated by Bioanalyzer 2100 (Agilent). Indexed cDNA libraries were obtained using the Ovation Solo RNA-seq Systems (NuGen) following manufacturer’s recommendations. The multiplexed libraries (11 pM/18 pM) were loaded on flow cells and sequences were produced using a NovaSeq 6000 S2 Reagent Kit (200 cycles from Novaseq 6000 System, Illumina) on a NovaSeq 6000 System (Illumina). Reads were mapped against the mouse reference genome (Grcm38/mm10) using STAR software to generate read alignments for each sample. Annotations for Mus_musculus.GRCm38.87.gtf were obtained from ftp.Ensembl.org. After transcripts assembling, gene level counts were obtained using HTseq and normalized to 20 millions of aligned reads. Genes with individual sample expression levels lower than 10 and replicate average abundance levels lower than 20 were filtered out. The fold changes of average gene abundance for the replicates were used to calculate the level of differential gene abundance between different cell populations. Genes with a fold change greater or equal to 2 were considered as up-regulated and those with a fold change lower or equal to 0.5 were considered down-regulated.

Organoid culture of primary basal- and luminal-derived mouse organoids

Basal cells were plated at a density of 1000 cells/well and luminal cells were plated at a density of 20,000 cells/well. Growth factor reduced Matrigel (Corning) was added to the cell suspension at a final concentration of 75% before plating into rings in 24-well plates.

Viral vectors

A Cre recombinase cassette was inserted into a red fluorescent protein-expressing FU-CRW lentivirus vector[70] by restriction digestion and ligation at the EcoRI site to make FU-Cre-CRW. Insertion of the Cre cassette was confirmed by DNA sequencing. Concentrated viral preps of FU-Cre-CRW and FU-CRW were made by the UCLA Vector Core facility and the Cre recombinase activity was validated by infecting HEK 293T cells transduced with a Cre-reporter plasmid (Addgene #62732)[71].

Generation of *Mpc1*-KO, *Pten* single knockout (SKO) and *Pten*;*Rb1* double knockout (DKO) organoids

Basal cells were isolated from *Mpc1*$^{fl/fl}$, *Pten*$^{fl/fl}$, and *Pten*$^{fl/fl}$;*Rb1*$^{fl/fl}$ mouse prostates and infected with RFP (FU-CRW) or Cre-RFP (FU-Cre-CRW) lentivirus. Lentiviral spinfections were done by culturing the cells with virus in 200 µL RPMI 1640 (Gibco) containing 10% fetal bovine serum (Corning), 1x penicillin-streptomycin (Gibco), and 10µM of the p160ROCK inhibitor Y-27632 dihydrochloride (Tocris Bioscience) (RPMI 10% FBS 1% P/S +RI) plus 8 µg/mL polybrene for 30 minutes at 37°C then spinning at 300g for 90 minutes. After spinfection, growth factor reduced Matrigel (Corning) was added to the cell suspension at a final concentration of 75% before plating into rings in 24-well plates. After one week of culture, organoids were dissociated to single cells. Organoids were removed from Matrigel by incubating in Advanced DMEM/F-12 (Gibco) containing 1 mg/mL dispase (Gibco) and 10µM of the p160ROCK inhibitor Y-27632 dihydrochloride (Tocris Biosciences) for 1 hour at 37°C. After centrifugation at 800g for 5 minutes, the pellet was washed with 1x phosphate buffered saline (PBS). Organoids were resuspended in 800 µL 0.05% Trypsin-EDTA (Gibco) and incubated at 37°C for 5 minutes. The Trypsin was quenched with 200 µL RPMI 10% FBS 1% P/S + ROCK inhibitor and organoids were pipetted up and down ten times to dissociate to single cells and passed through a 100µm cell strainer (Corning). After centrifugation at 800g for 5 minutes, the pellet was washed with 1x phosphate buffered saline (PBS) and resuspended in RPMI 10% FBS 1% P/S +RI. RFP-positive cells were isolated by FACS. All prostate organoids were cultured based on established protocols[66, 72]. Single organoids were imaged on a light microscope and organoid diameter was measured as a readout of organoid size.

Organoid metabolic profiling and nutrient tracing

For glucose tracer analysis experiments, 17.5mM [U-^{13}C]glucose (Cambridge Isotope Laboratories) was added to glucose-free SILAC Advanced DMEM/F-12 Flex Media (Fisher

Scientific). Arginine, lysine and alanine were also added back to the SILAC base media at the same concentrations found in Advanced DMEM/F-12 (Fisher Scientific). Organoids were grown in mouse organoid media made with the SILAC base media. For lactate tracer analysis experiments, organoids were cultured with 20mM [U-^{13}C]Lactate (Cambridge Isotope Laboratories, CLM-1579-0.5) for 24 hours prior to metabolite extraction. To extract metabolites, tracer-containing media was aspirated. Organoids were repeatedly blasted with cold 150mM ammonium acetate pH 7.3 using a P-1000 pipette until the Matrigel ring was dislodged. The suspension was transferred to an Eppendorf tube and centrifuged at 800g for 5 minutes at 1°C. The supernatant was aspirated and 500μL cold 80% methanol was added to the organoid pellet. 10μL 1mM norvaline (Sigma) was added as an internal standard. Each sample was vortexed for 30 seconds and centrifuged at 17000g for 5 minutes at 1°C. 420μL of the supernatant was transferred to an ABC vial (Fisher Scientific) and evaporated using an EZ-2Elite evaporator (Genevac). Samples were stored at -80°C prior to analysis.

Dried metabolites were resuspended in 50% ACN:water and 1/10th was loaded onto a Luna 3um NH2 100A (150 × 2.0 mm) column (Phenomenex). The chromatographic separation was performed on a Vanquish Flex (Thermo Scientific) with mobile phases A (5 mM NH4AcO pH 9.9) and B (ACN) and a flow rate of 200 μL/minute. A linear gradient from 15% A to 95% A over 18 minutes was followed by 9 minutes isocratic flow at 95% A and reequilibration to 15% A. Metabolites were detection with a Thermo Scientific Q Exactive mass spectrometer run with polarity switching (+3.5 kV/− 3.5 kV) in full scan mode with an m/z range of 70-975 and 70.000 resolution. TraceFinder 4.1 (Thermo Scientific) was used to quantify the targeted metabolites by area under the curve using expected retention time and accurate mass measurements (<5 ppm). For labeled datasets, relative amounts of metabolites were calculated by summing up the values for all isotopologues of a given metabolite. Metabolite Isotopologue Distributions were corrected for natural C13 abundance.

Normalization was performed by resuspending the cell pellet in 300 µL lysis solution (0.1M NaCl, 20mM Tris-HCl, 0.1% SDS, 5mM EDTA, 500 µg/mL Proteinase K (Fisher Scientific) in distilled water). Samples were syringed with a 25G needle to reduce viscosity and 50 µL of each sample was transferred to a 96-well black wall clear bottom tissue culture plate (Corning). 50 µL lysis solution was added to one well for a blank reading. 100 µL of 5 µg/mL Hoechst 33342 (Invitrogen) in distilled water was added to each well and 96-well plates were incubated for 30 minutes in the dark at 37°C before measurement of DNA-based florescence using a Tecan Infinite M1000 plate reader with 355nm excitation and 465nm emission. The blank reading was subtracted from each absorbance value to calculate relative cell amount.

Principal component analysis

Principal component analysis (PCA) was performed using metabolite abundance and fractional contribution data in the Python programming language (v3.9.12). Data was processed using the NumPy (v1.22.4), pandas (v1.4.2), and scikit-learn (v1.0.2) libraries and visualized using the Matplotlib library (v3.5.1). Feature scaling was done along the metabolite dimension using the StandardScaler class from scikit-learn which employs z-score normalization. 95% confidence ellipses were generated with a script provided by Matplotlib.

Intracellular flow cytometry

Organoids were removed from Matrigel by incubating in Advanced DMEM/F-12 (Gibco) containing 1 mg/mL dispase (Gibco) and 10µM of the p160ROCK inhibitor Y-27632 dihydrochloride (Tocris Biosciences) for 1 hour at 37°C. After centrifugation at 800g for 5 minutes, the pellet was washed with 1x phosphate buffered saline (PBS). Organoids were resuspended in 800 µL 0.05% Trypsin-EDTA (Gibco) and incubated at 37°C for 5 minutes. The Trypsin was quenched with 200 µL RPMI 10% FBS 1% P/S + ROCK inhibitor and organoids were pipetted up and down ten times to dissociate to single cells and passed through a 100µm cell strainer

(Corning). Dissociated cells from mouse prostate organoids were washed with PBS and fixed in 1mL of 2% paraformaldehyde made from 16% paraformaldehyde (Electron Microscopy Sciences) in PBS for 15 minutes on ice. For experiments including EpCAM surface staining, cells were stained with EpCAM-APC/Cy7 (BioLegend 118218, 1:100) in RPMI 10% FBS 1% P/S + ROCK inhibitor for 15 minutes prior to fixation. Cells were then washed with PBS and permeabilized in 1 mL of permeabilization buffer (0.1% Saponin (Sigma-Aldrich), 5% FBS (Corning) in PBS) for 15 minutes at room temperature in the dark. Cells were resuspended in 100 mL of permeabilization buffer and stained with rabbit anti-cytokeratin 5-Alexa Fluor 647 (Abcam Ab193895, 1:100) and rabbit anti-cytokeratin 8-Alexa Fluor 488 (Abcam Ab192467, 1:100) for 20 minutes at room temperature in the dark. Cells were washed with permeabilization buffer and resuspended in PBS for analysis on a BD FACS Canto (BD Biosciences).

Organoid immunofluorescence

Organoids were removed from Matrigel by incubating in Advanced DMEM/F-12 (Gibco) containing 1 mg/mL dispase (Gibco) and 10μM of the p160ROCK inhibitor Y-27632 dihydrochloride (Tocris Biosciences) for 1 hour at 37°C. After centrifugation at 800g for 5 minutes, the pellet was washed with 1x phosphate buffered saline (PBS) three times. Organoids were then fixed in 4% paraformaldehyde (PFA) in PBS for 15 minutes. After fixation, organoids were washed with PBS three times. Organoids were then blocked in 2% donkey serum in 0.25% Triton X-100 for 1 hour. Organoids were washed once with PBS and stained with anti-Cytokeratin 8 (Biolegend 904804, 1:500) antibody and anti-p63 (Biolegend 619002, 1:500) antibody in 0.5% BSA 0.25% Triton X-100 at 4°C overnight. Organoids were then washed with PBS three times, with the last wash lasting six hours. Secondary antibody staining was performed overnight at 4°C using goat anti-rabbit IgG-AlexaFluor647 (ThermoFisher **21245,** 1:1000) and goat anti-mouse IgG-AlexaFluor488 (ThermoFisher **11001**, 1:1000) in 0.5% BSA 0.25% Triton X-100 with one drop of NucBlue. Organoids were washed with PBS three times and placed in PBS + 0.1% Tween-20 until imaging on a Nikon Ti-E Fluorescence Motorized DIC Microscope (Nikon) with RCM1 confocal box (Confocal.nl) using Nikon NIS Elements Imaging Software and Nikon CFI Apo LWD Lambda S 20XC WI objective, material number MRD77200.

Cell lines

Cell lines were routinely tested for mycoplasma and authentication by short tandem repeat analysis (Laragen). Tissue culture plates were coated with 0.01% (v/v) Poly-L-Lysine (Sigma, P4832) diluted 1/20 in distilled water and washed with PBS to enhance cell attachment. 16D cells were received from Dr. Amina Zoubeidi and cultured in RPMI base media (Gibco) + 10% FBS (v/v) + 100 units/mL penicillin, and 100µg/mL streptomycin. LuCaP35 cells were received from Dr. Eva Corey and Dr. Peter Nelson and cultured in DMEM base media (Gibco, 11965-092) + 10% FBS (v/v) + 100 units/mL penicillin, 100µg/mL streptomycin, and 1x GlutaMAX. LAPC4 cells were received from Dr. Rob Reiter and cultured in IMDM (Gibco, 31980-030) + 5% FBS (v/v) + 100 units/mL penicillin, and 100µg/mL streptomycin. UK5099 treatment was performed by adding 10µM or 30µM UK5099 (Sigma, PZ0160) every 48 hours.

Histone extractions

Histone extractions were performed using a histone extraction kit (Abcam, Ab113476) according to manufacturer instructions.

Assay for transposase-accessible chromatin using sequencing (ATAC-seq)

Cells were harvested and frozen in culture media containing FBS and 5% DMSO. Cryopreserved cells were sent to Active Motif to perform the ATAC-seq assay. The cells were then thawed in a 37°C water bath, pelleted, washed with cold PBS, and tagmented as previously described[73], with some modifications[74]. Briefly, cell pellets were resuspended in lysis buffer, pelleted, and tagmented using the enzyme and buffer provided in the Nextera Library Prep Kit (Illumina).

Tagmented DNA was then purified using the MinElute PCR purification kit (Qiagen), amplified with 10 cycles of PCR, and purified using Agencourt AMPure SPRI beads (Beckman Coulter). Resulting material was quantified using the KAPA Library Quantification Kit for Illumina platforms (KAPA Biosystems) and sequenced with PE42 sequencing on the NovaSeq 6000 sequencer (Illumina). Reads were aligned using the BWA algorithm (v0.7.12; mem mode; default settings). Duplicate reads were removed, only reads mapping as matched pairs and only uniquely mapped reads (mapping quality ≥ 1) were used for further analysis. Alignments were extended *in silico* at their 3'-ends to a length of 200 bp and assigned to bins 32 nucleotides in size along the genome. The resulting histograms (genomic "signal maps") were stored in bigWig files. Peaks were identified using the MACS 2.1.0 algorithm at a cutoff of p-value 1×10^{-7}, without control file, and with the –nomodel option. Peaks that were on the ENCODE blacklist of known false ChIP-Seq peaks were removed. Signal maps and peak locations were used as input data to Active Motif's proprietary analysis program, which creates Excel tables containing detailed information on sample comparison, peak metrics, peak locations and gene annotations. For differential analysis, reads were counted in all merged peak regions (using Subread), and the replicates for each condition were compared using DESeq2 (v1.24.0)[54].

HOMER transcription factor motif analysis

Identification of sites with differential ATAC-Seq signal

After identifying merged regions as part of the standard analysis pipeline, the DESeq2 software was ran on the unnormalized BAM files (without duplicates). In brief, the DESeq2 software generates normalized counts specifically for the merged regions, and the shrunken $\log_2$ fold-change and adjusted p-values for each merged region are calculated. For the subsequent steps of the analysis, we consider any region as differential if the adjusted p-value is less than 0.1.

HOMER-based motif analysis

BED files listing the significantly increased (“DESeq2_Up_difpeaks.bed”) and decreased (“DESeq2_Down_difpeaks.bed”) regions are generated for each comparison. Each BED file was then sorted by the shrunken $\log_2$ fold change and the 2500 regions with the largest absolute fold changes were selected. We then performed HOMER motif analysis (findMotifsGenome.pl) on the 200 bp sequence centered around the midpoint of the differential region (+100 bp, -100 bp). During this analysis, common repeats are masked as this can affect the discovery of *de novo* motifs. The analysis identifies motifs that are enriched across all sequences, individual peak regions are not annotated with specific motifs.

Patient-derived xenograft Enzalutamide sensitivity assay

Using a razor blade, MDA PCa 203-A PDX and MDA PCa 183-A PDX tumours were mechanically dissociated in dissociation media comprised of RPMI 1640 (Gibco) containing 10% fetal bovine serum (Corning), 1x penicillin-streptomycin (Gibco), 1 mg/mL collagenase type I (Gibco), 1 mg/mL dispase (Gibco), 0.1 mg/mL deoxyribonuclease (Gibco), and 10μM of the p160ROCK inhibitor Y-27632 dihydrochloride (Tocris Bioscience). When large chunks were no longer visible, the samples were incubated at 37°C on a nutating platform for 15 minutes in 20 mL of dissociation media. After centrifugation at 800g for 5 minutes, the pellet was washed with 1x phosphate buffered saline (PBS, Gibco). The cell pellet was resuspended in Advanced DMEM/F-12 and passed through a 100μm cell strainer (Corning). After centrifugation at 800g for 5 minutes, the pellet was resuspended in human organoid media and plated in 75% growth factor reduced Matrigel (Corning) based on established protocols[66]. After seven days of culture with either vehicle, 10μM UK5099 (Sigma, PZ0160), or 20mM sodium lactate (Sigma, L7022-5G), organoids were removed from Matrigel by incubating in Advanced DMEM/F-12 containing 1 mg/mL dispase and 10μM of the p160ROCK inhibitor Y-27632 dihydrochloride for 1 hour at 37°C. After centrifugation at 800g for 5 minutes, the pellet was washed with 1x phosphate buffered saline.

Organoids were then plated into rings in a 96-well black-wall clear-bottom plate (Fisher, 07-200-588) in 75% growth factor reduced Matrigel with or without 10µM Enzalutamide (Selleck Chemicals, S1250). After five days of culture, a CellTiter-Glo assay (Promega, G7571) was performed according to manufacturer instructions and relative luminescence signal was quantified on a Tecan Infinite M1000 plate reader.

Cell line Enzalutamide sensitivity assays

After seven days of culture with either vehicle, 10µM UK5099 (Sigma, PZ0160), 30µM UK5099, or 20mM sodium lactate (Sigma, L7022-5G), cells were plated into a 96-well black-wall clear-bottom plate (Fisher, 07-200-588) with or without 10µM Enzalutamide (Selleck Chemicals, S1250). The 96-well plate was coated with 0.01% (v/v) Poly-L-Lysine (Sigma, P4832) diluted 1/20 in distilled water and washed with PBS prior to plating cells to enhance cell attachment. After two days of culture, a CellTiter-Glo assay (Promega, G7571) was performed according to manufacturer instructions and relative luminescence signal was quantified on a Tecan Infinite M1000 plate reader. For the EdU cell cycle assay, cells were seeded at 30 percent confluence and cultured in 6-well dishes for 72 hours prior to cell cycle analysis. Media changes were performed 48 hours after plating. After 72 hours of culture, cell cycle analysis was performed using a 5-ethynyl-2'-deoxyuridine-based (EdU) kit (Thermo Fisher Scientific, C10635) according to the specified protocol. EdU labeling was performed for 2 hours. For experiments that contained small molecule inhibitors, fresh inhibitor(s) were adding during each media change. Flow cytometry analysis identified the percentage of EdU-positive.

Statistics and Reproducibility

Prism v8.3.0 (GraphPad) was used to generate graphs and perform statistical analyses. All *in vitro* experiments shown were repeated at least three times with similar results obtained, and representative data are shown unless otherwise indicated. No statistical method was used to predetermine sample size but our sample sizes are similar to those reported in previous publications[21]. Data distribution was assumed to be normal but this was not formally tested. No data were excluded from the analyses. Data collection and analysis were not performed blind to the conditions of the experiments. For animal experiments, mice were randomly divided into cages. For *in vitro* experiments, samples were not randomized as this was not relevant for the individual assays.

Data availability

Bulk RNA-seq, scRNA-seq and ATAC-seq data that support the findings of this study have been deposited in the Gene Expression Omnibus (GEO) under accession codes GSE221023, GSE222786, GSE236573, GSE206555 and GSE221442. Previously published RNA-seq data that were re-analyzed here are available under accession codes GSE122367 and GSE67070. The SMMU, Beltran *et al.*, and TCGA datasets were accessed on cBioPortal (https://www.cbioportal.org/). Ensembl database were accessed from http://useast.ensembl.org/Mus_musculus/Info/Index. An interactive scRNA-seq tSNE plot is available at: https://singlecell.broadinstitute.org/single_cell/study/SCP1234/prostate-organoid-vehicle-uk5099. All other data supporting the findings of this study are available from the corresponding author on reasonable request.

Code availability

The code used to generate the PCA plots can be accessed at https://github.com/Nick-Nunley/Metabolism-and-lineage-PCA.git.

Methods-only references

51. Gray, L.R., Sultana, M.R., Rauckhorst, A.J., *et al.* Hepatic mitochondrial pyruvate carrier 1 is required for efficient regulation of gluconeogenesis and whole-body glucose homeostasis. *Cell Metabolism*. **22** (4), 669–681, doi: 10.1016/j.cmet.2015.07.027 (2015).

52. Navone, N.M., Weerden, W.M. Van, Vessella, R.L., *et al.* Movember GAP1 PDX project : An international collection of serially transplantable prostate cancer patient-derived xenograft (PDX) models. *The Prostate*. **78** (16), 1262–1282, doi: 10.1002/pros.23701 (2018).

53. Dobin, A., Davis, C.A., Schlesinger, F., *et al.* STAR: ultrafast universal RNA-seq aligner. *Bioin*. **29** (1), 15–21, doi: 10.1093/bioinformatics/bts635 (2013).

54. Love, M.I., Huber, W., Anders, S. Moderated estimation of fold change and dispersion for RNA-seq data with DESeq2. *Genome Biology*. **15** (550), 1–21, doi: 10.1186/s13059-014-0550-8 (2014).

55. Huang, D.W., Sherman, B.T., Lempicki, R.A. Systematic and integrative analysis of large gene lists using DAVID bioinformatics resources. *Nature Protocols*. **4** (1), 44–57, doi: 10.1038/nprot.2008.211 (2009).

56. Huang, D.W., Sherman, B.T., Lempicki, R.A. Bioinformatics enrichment tools: paths toward the comprehensive functional analysis of large gene lists. *Nucleic Acids Research*. **37** (1), 1–13, doi: 10.1093/nar/gkn923 (2009).

57. Subramanian, A., Tamayo, P., Mootha, V.K., *et al.* Gene set enrichment analysis: A knowledge-based approach for interpreting genome-wide. *PNAS*. **102** (43), 15545–15550, doi: 10.1073/pnas.0506580102 (2005).

58. Mootha, V.K., Lindgren, C.M., Eriksson, K., *et al.* PGC-1α-responsive genes involved in oxidative phosphorylation are coordinately downregulated in human diabetes. *Nature Genetics*. **34** (3), 267–273 (2003).

59. Chen, S., Zhou, Y., Chen, Y., *et al.* fastp: an ultra-fast all-in-one FASTQ preprocessor. *Bioinformatics*. **34** (17), 884–890, doi: 10.1093/bioinformatics/bty560 (2018).

60. Li, B., Dewey, C.N. RSEM: accurate transcript quantification from RNA-Seq data with or without a reference genome. *BMC Bioinformatics*. **12** (323) (2011).

61. Ritchie, M.E., Phipson, B., Wu, D., *et al.* limma powers differential expression analyses for RNA-sequencing and microarray studies. *Nucleic Acids Research*. **43** (7), doi: 10.1093/nar/gkv007 (2015).

62. Efron, B., Tibshirani, R. Empirical bayes methods and false discovery rates for microarrays. *Genetic Epidemiology*. **23** (1), 70–86, doi: 10.1002/gepi.01124 (2002).

63. Chen, H., Boutros, P.C. VennDiagram: a package for the generation of highly-customizable Venn and Euler diagrams in R. *BMC Bioinformatics*. **12** (35) (2011).

64. P’ng, C., Green, J., Chong, L.C., *et al.* BPG: Seamless , automated and interactive visualization of scientific data. *BMC Bioinformatics*. **20** (1), 1–5, doi: 10.1186/s12859-019-2610-2 (2019).

65. Wu, T., Hu, E., Xu, S., *et al.* clusterProfiler 4. 0: A universal enrichment tool for interpreting omics data. *The Innovation*. **2** (3), doi: 10.1016/j.xinn.2021.100141 (2021).

66. Drost, J., Karthaus, W.R., Gao, D., *et al.* Organoid culture systems for prostate epithelial and cancer tissue. *Nature Protocols*. **11** (2), 347–358, doi: 10.1038/nprot.2016.006 (2016).

67. Yates, A.D., Achuthan, P., Akanni, W., *et al.* Ensembl 2020. *Nucleic Acids Research*. **8** (48), 682–688, doi: 10.1093/nar/gkz966 (2020).

68. Stuart, T., Butler, A., Hoffman, P., *et al.* Comprehensive integration of single-cell data. *Cell*. **177** (7), 1888–1902, doi: 10.1016/j.cell.2019.05.031 (2019).

69. DePasquale, E.A., Schnell, D.J., Camp, P.-J. Van, *et al.* DoubletDecon: Deconvoluting doublets from single-cell RNA-sequencing data. *Cell Reports*. **5** (6), 1718–1727, doi: 10.1016/j.celrep.2019.09.082 (2019).

70. Liu, X., Grogan, T.R., Hieronymus, H., *et al.* Low CD38 identifies progenitor-like inflammation-associated luminal cells that can initiate human prostate cancer and predict poor outcome. *Cell Reports*. **17** (10), 2596–2606, doi: 10.1016/j.celrep.2016.11.010 (2016).

71. D’Astolfo, D.S., Pagliero, R.J., Pras, A., *et al.* Efficient intracellular delivery of native proteins. *Cell*. **161** (3), 674–690, doi: 10.1016/j.cell.2015.03.028 (2015).

72. Crowell, P.D., Giafaglione, J.M., Hashimoto, T., *et al.* Evaluating the differentiation capacity of mouse prostate epithelial cells using organoid culture. *Journal of Visualized Experiments*. **153**, 1–9, doi: 10.3791/60223 (2019).

73. Buenrostro, J.D., Giresi, P.G., Zaba, L.C., *et al.* Transposition of native chromatin for fast and sensitive epigenomic profiling of open chromatin, DNA-binding proteins and nucleosome position. *Nature Methods*. **10** (12), doi: 10.1038/nmeth.2688 (2013).

74. Corces, M.R., Trevino, A.E., Hamilton, E.G., *et al.* An improved ATAC-seq protocol reduces background and enables interrogation of frozen tissues. *Nature Methods*. **14** (10), doi: 10.1038/nmeth.4396 (2017).

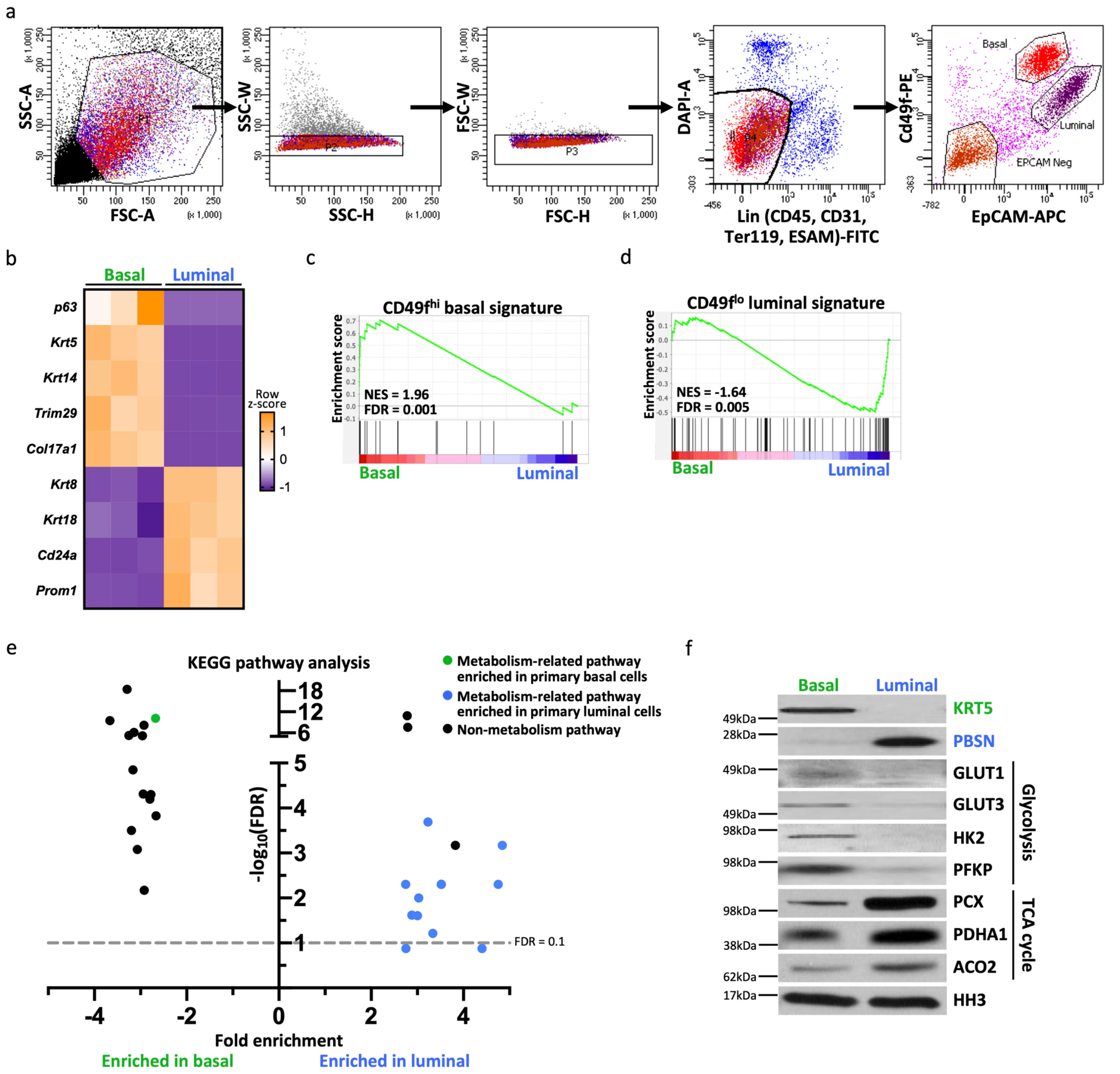

Extended Data Figure 1. (a) Gating scheme for isolating primary basal and luminal cells from mouse prostate. (b) Heatmap of select canonical basal and luminal markers from RNA sequencing of primary basal and luminal mouse prostate cells with three biological replicates. (c) Gene set enrichment analysis (GSEA) showing positive enrichment of CD49f^{high} signature in basal cells relative to luminal cells. (d) GSEA showing positive enrichment of CD49f^{low} signature[18] in luminal cells relative to basal cells. (e) 30 pathways most enriched in differentially abundant genes ($\log_2$(fold change) ≥ 1, FDR < 0.2) in basal and luminal cells identified by KEGG pathway analysis. Metabolism-related pathways highlighted in green (basal-enriched) and blue (luminal-enriched). (f) Western blot analysis of select glycolytic and TCA cycle enzymes in basal and luminal cells.

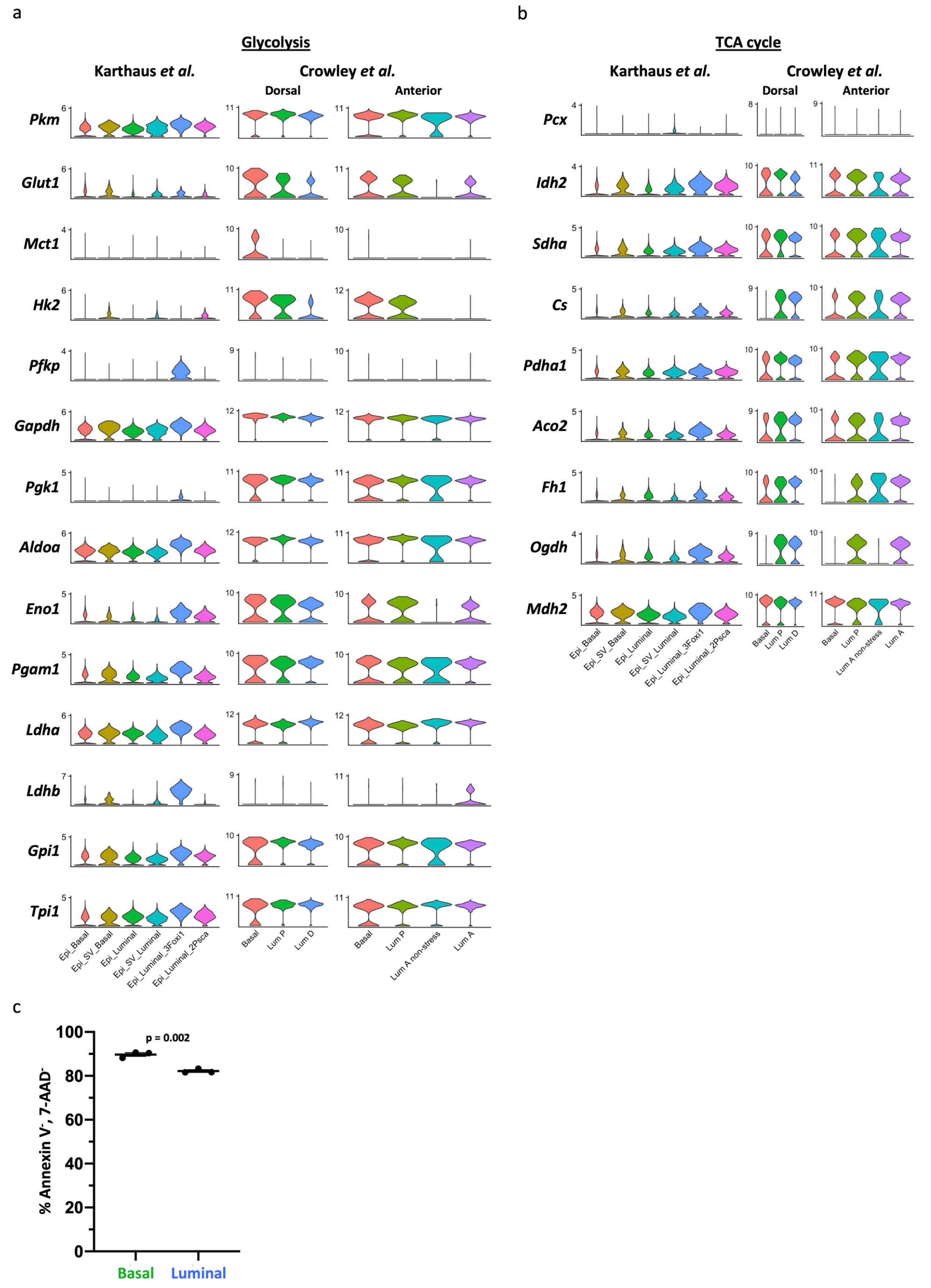

Extended Data Figure 2. (a-b) Analysis of glycolytic (a) and TCA cycle (b) enzymes in Karthaus *et al.*[25] and Crowley *et al.*[20] mouse single cell RNA sequencing data. (c) Percentage of Annexin V$^-$, 7-AAD$^-$ primary basal and luminal cells after overnight culture (n=3 independent biological replicates). Error bars represent SEM. p-values were calculated using an unpaired two-tailed t-test with Welch's correction.

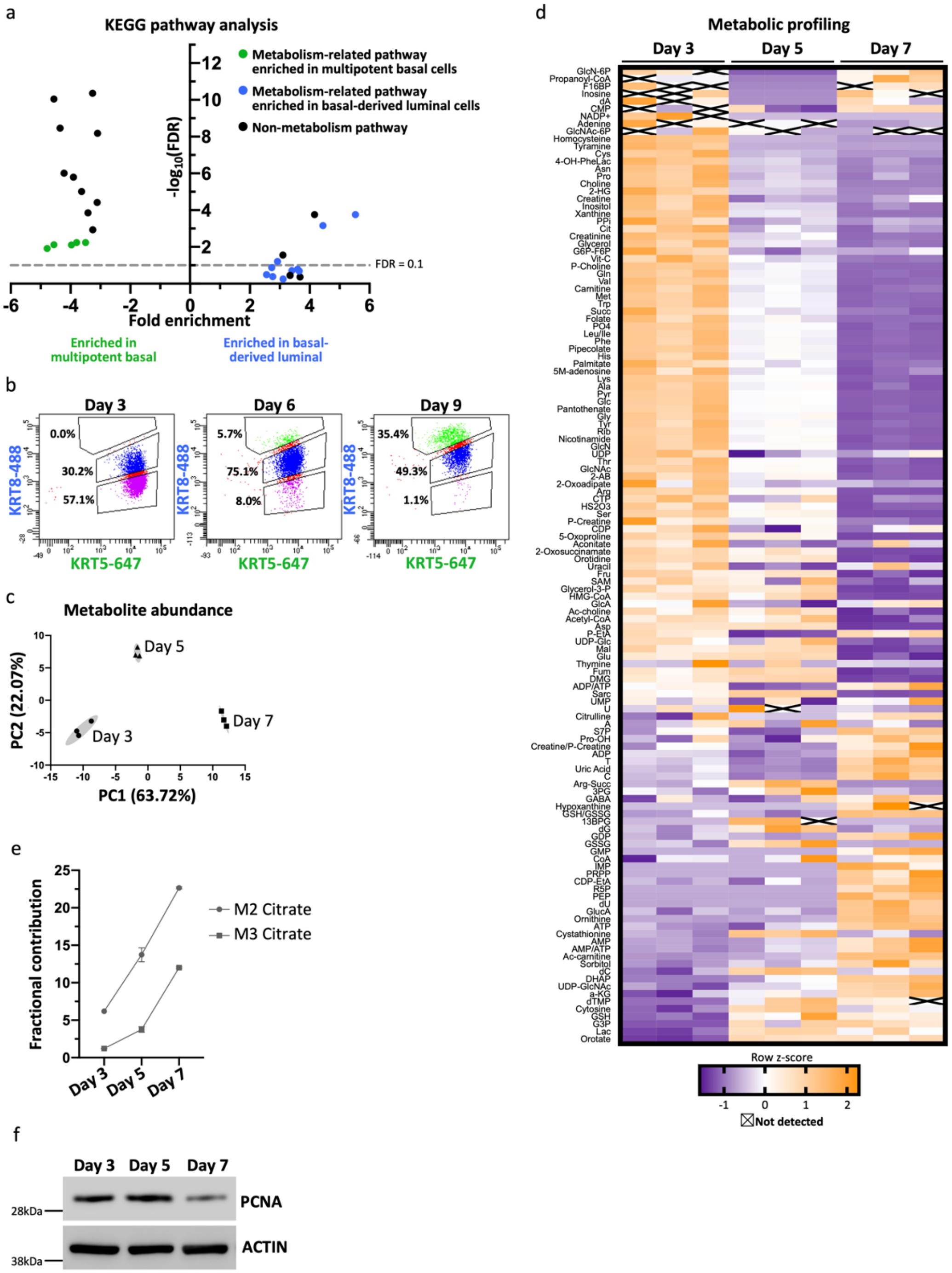

Extended Data Figure 3. (a) 30 pathways most enriched in differentially abundant genes (log$_2$(fold change) ≥ 1) in multipotent basal cells and basal-derived luminal cells identified by KEGG pathway analysis. Metabolism-related pathways highlighted in green (enriched in multipotent basal-enriched) and blue (enriched in basal-derived luminal-enriched). (b) Intracellular flow cytometry analysis of the basal marker cytokeratin 5 (KRT5) and the luminal marker cytokeratin 8 (KRT8) in primary basal-derived mouse organoids three, six and nine days after plating into organoid culture. (c) Principal component analysis of metabolic profiling data for basal-derived organoids with three technical replicates per timepoint. (d) Heatmap of metabolite abundance in primary basal-derived mouse organoids (n=3 independent biological replicates per timepoint). (e) Fractional contribution from [U-^{13}C]glucose to M2 and M3 citrate in basal-derived organoids (n=3 independent biological replicates per timepoint). Error bars represent SEM. (f) Western blot analysis of proliferation marker PCNA in basal-derived organoids.

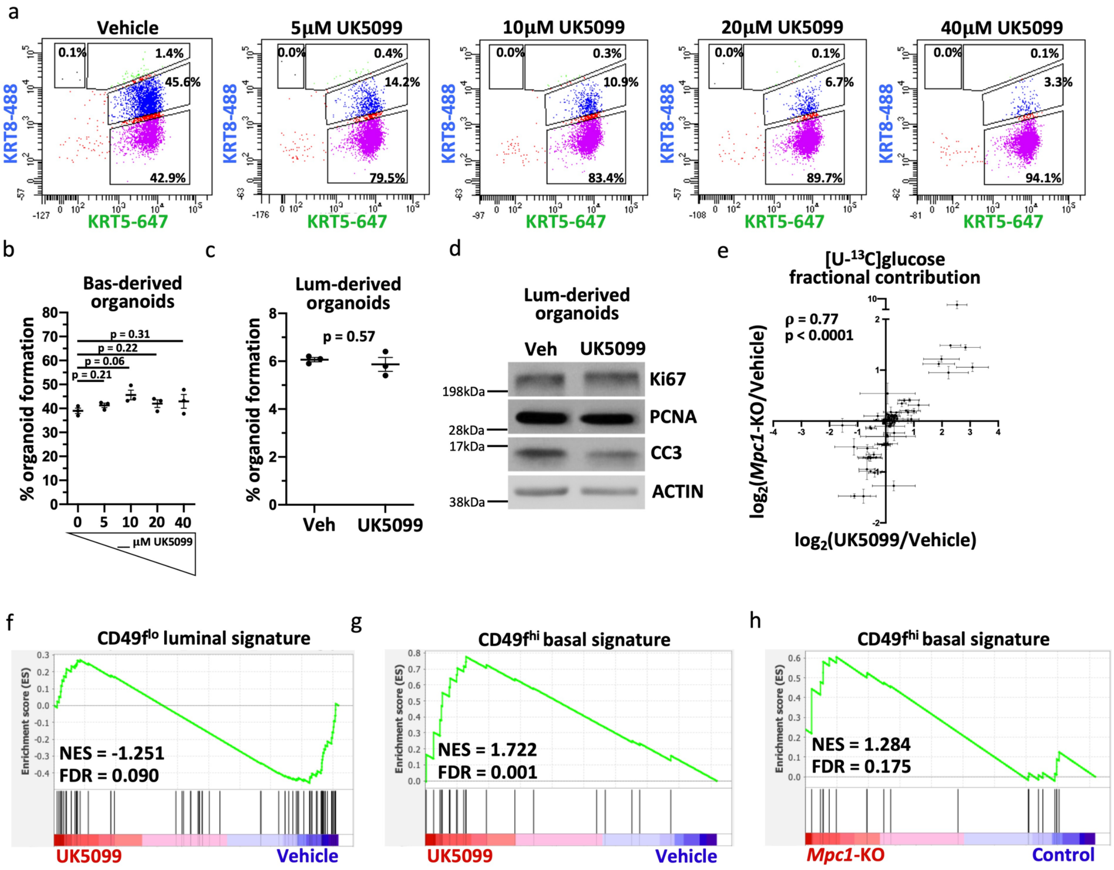

Extended Data Figure 4. (a) Intracellular flow cytometry of KRT8 and KRT5 in basal-derived organoids treated with 0-40μM UK5099 for seven days. (b) Percent organoid formation of basal-derived organoids treated with 0-40μM UK5099 (n=3 independent biological replicates). (c) Percent organoid formation of vehicle- and 10μM UK5099-treated luminal-derived organoids (n=3 independent biological replicates). (d) Western blot analysis of proliferation markers (Ki67 and PCNA) and apoptosis marker (CC3, cleaved caspase-3) in vehicle- and 10μM UK5099-treated luminal-derived organoids seven days after plating. (e) Correlation analysis of [U-^{13}C]glucose fractional contribution comparing *Mpc1*-KO and 10μM UK5099-treated basal-derived organoids (n=3 independent biological replicates). (f) GSEA showing negative enrichment of CD49f^{low} luminal signature[18] in 10μM UK5099-treated relative to vehicle-treated basal-derived organoids. (g) GSEA showing enrichment of CD49f^{high} basal signature[18] in vehicle-treated relative to 10μM UK5099-treated basal-derived organoids. (h) GSEA showing enrichment of CD49f^{high} basal signature[18] in control relative to *Mpc1* knockout basal-derived organoids. For all panels, error bars represent SEM. p-values were calculated using an unpaired two-tailed t-test with Welch's correction. Correlation analysis was performed using Spearman's correlation.

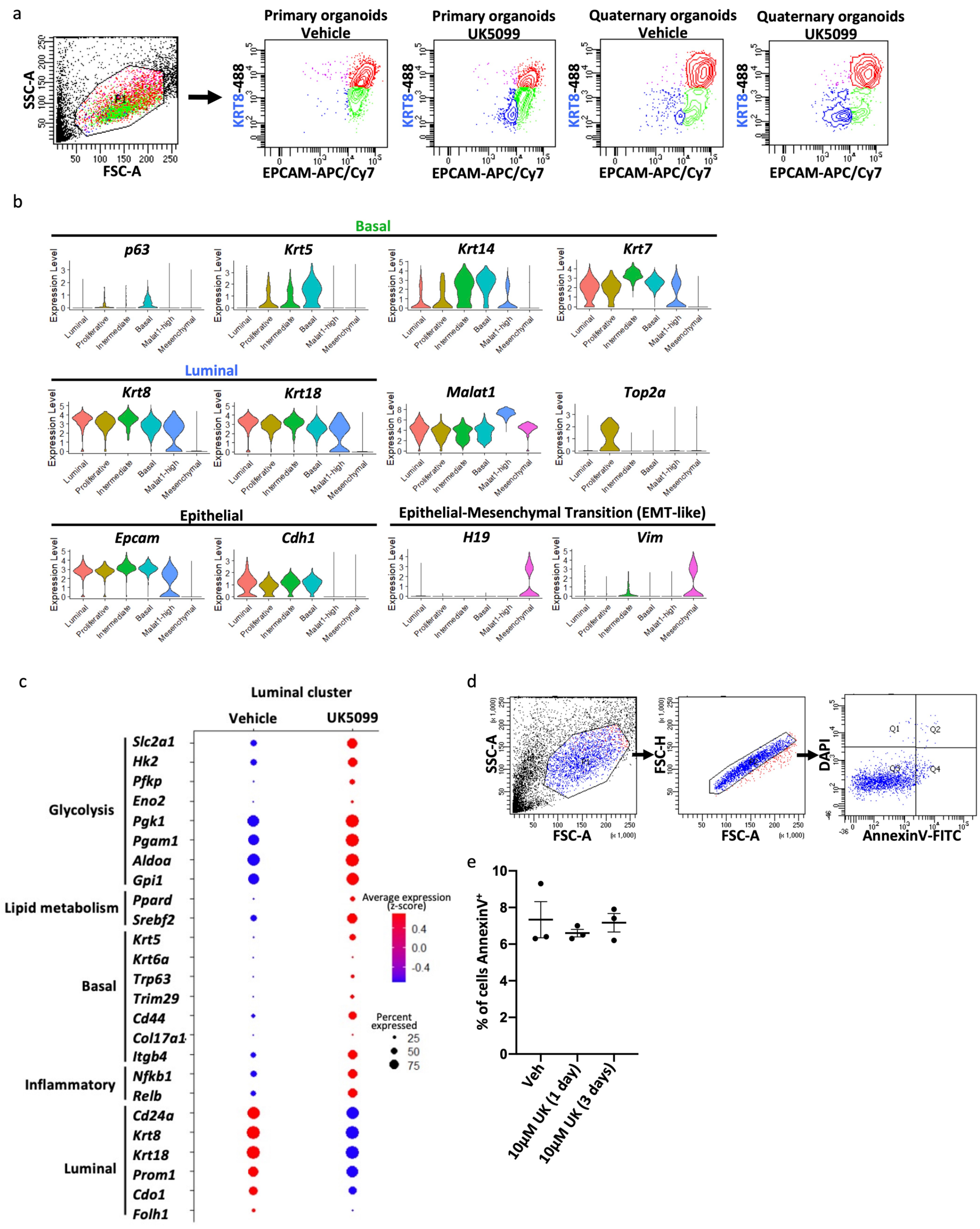

Extended Data Figure 5. (a) Representative flow cytometry plots illustrating EPCAM$^+$ KRT8$^+$ (red), EPCAM$^+$ KRT8$^-$ (green), and EPCAM$^-$ KRT8$^-$ (blue) populations in primary and quaternary organoids. (b) Expression level (log$_2$(read count)) of canonical basal, luminal, epithelial and epithelial-mesenchymal transition (EMT-like) markers in distinct cell populations from scRNA-seq data to validate cluster identification. (c) Dot plot of glycolytic enzymes, lipid metabolism genes, canonical basal markers, inflammatory genes and canonical luminal markers with vehicle or UK5099 treatment within the phenotypic luminal cluster. (d) Flow cytometry gating scheme for apoptosis analysis in panel (e). (e) Quantification of percent of AnnexinV$^+$ cells in quaternary organoids treated with vehicle, 10µM UK5099 for one day, or 10µM UK5099 for three days (n=3 independent biological replicates). Error bars in represent SEM.

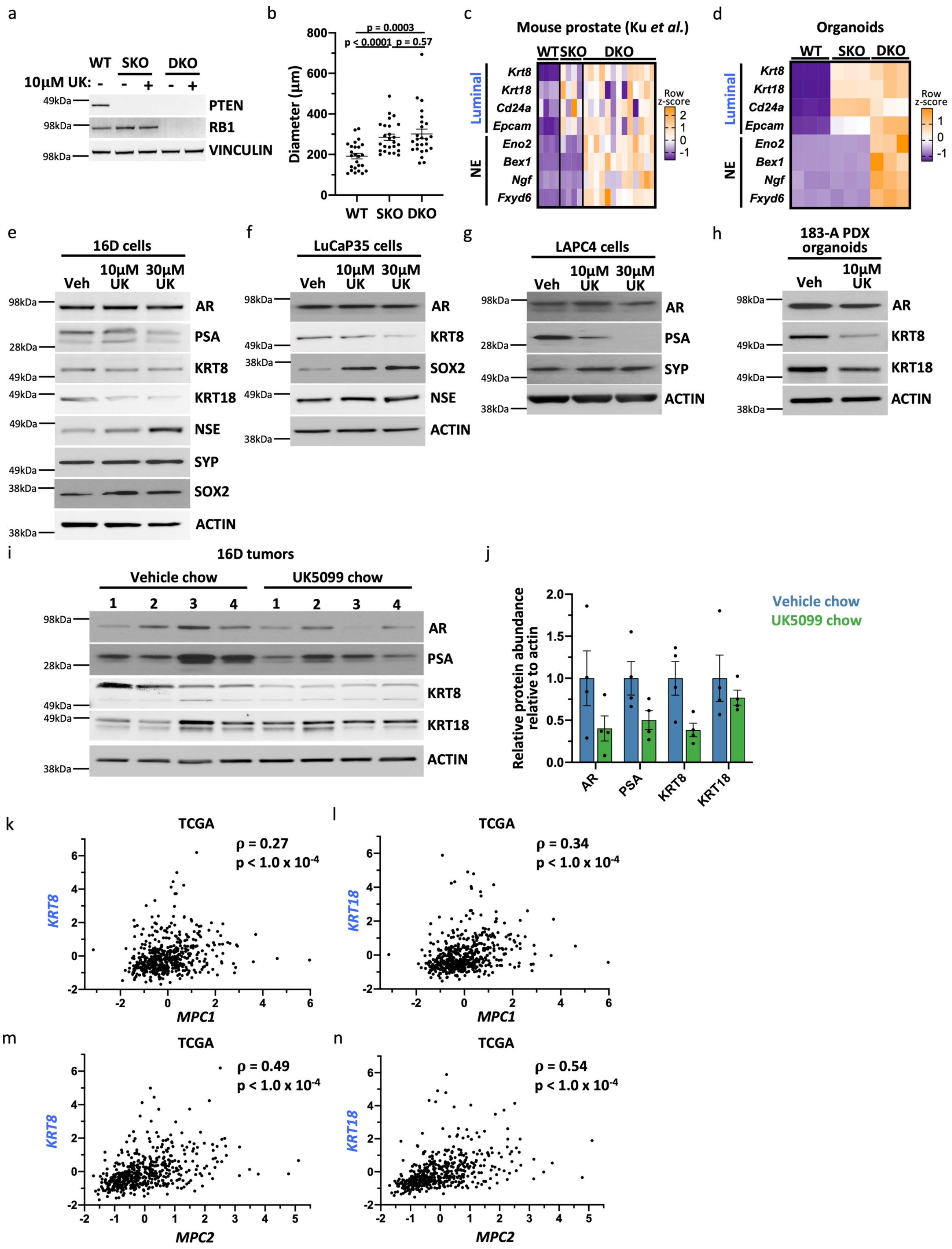

Extended Data Figure 6. (a) Western blot validation of knockout of *Pten* in single knockout (SKO) and double knockout (DKO) mouse prostate organoids and validation of knockout of *Rb1* in DKO organoids. (b) Organoid diameter (micrometers) of wildtype (WT), SKO and DKO organoids (n=25 independent biological samples). Error bars represent SEM. (c) Heatmap of canonical luminal and neuroendocrine markers in WT, SKO and DKO mouse prostates from RNA sequencing data published in Ku *et al.*[22] (d) Heatmap of canonical luminal and neuroendocrine markers in WT, SKO and DKO mouse organoids from RNA sequencing data. (e-i) Western blot analysis of lineage markers AR, PSA, KRT8, KRT18, NSE, SYP, and SOX2 in human 16D cell line (e), LuCaP35 cell line (f), LAPC4 cell line (g), 183-A PDX organoids (h), and 16D subcutaneous tumours (i). (j) Quantification of Western blot in panel I (n=4 independent tumors). Data are shown as mean ± SEM. (k-l) Correlation analysis of z-score expression of the luminal marker *KRT8* (k) or *KRT18* (l) with *MPC1* in 499 primary prostate carcinomas from The Cancer Genome Atlas (TCGA)[67]. (m-n) Correlation analysis of z-score expression of the luminal marker *KRT8* (m) or *KRT18* (n) with *MPC2* in 499 primary prostate carcinomas from TCGA[67]. Correlation analysis was performed using Spearman's correlation with a two-tailed p-value. p-values in (b) were calculated using an unpaired two-tailed t-test with Welch's correction.

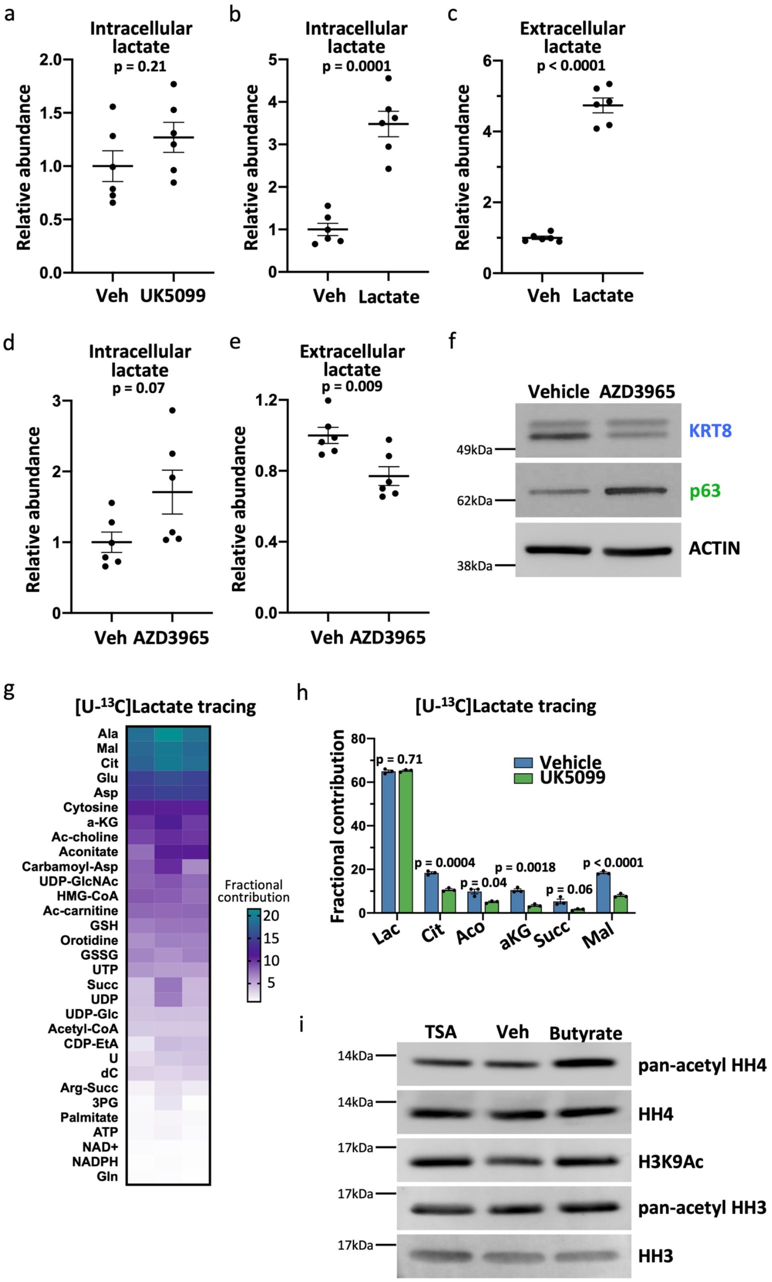

Extended Data Figure 7. (a-b) Intracellular lactate abundance in primary basal-derived mouse organoids treated with vehicle or 10μM UK5099 (a) or 20mM sodium lactate (b) for seven days (n=6 independent biological replicates). (c) Extracellular lactate abundance in organoids treated with vehicle or 20mM sodium lactate (n=6 independent biological replicates). (d-e) Intracellular (d) and extracellular (e) lactate abundance in organoids treated with vehicle or 10μM AZD3965 (n=6 independent biological replicates). Error bars in panels (a-e) represent SEM. (f) Western blot analysis of the luminal marker KRT8 and the basal marker p63 in basal-derived organoids treated with vehicle or 10μM AZD3965 for seven days. (g) Heatmap of fractional contribution of [U-^{13}C]lactate tracing data from organoids treated with 20mM sodium lactate for six days followed by treatment with 20mM [U-^{13}C]lactate for 24 hours. (h) Fractional contribution from [U-^{13}C]lactate to TCA cycle intermediates in organoids treated with 20mM sodium lactate for six days followed by treatment with 20mM [U-^{13}C]lactate and vehicle or 10µM UK5099 for 24 hours (n=3 independent biological replicates). Data are shown as mean ± SEM. p-values were calculated using an unpaired two-tailed t-test with Welch's correction. (i) Western blot analysis of pan-acetyl histone H4 (pan-acetyl HH4), total histone H4 (HH4), H3K9Ac, pan-acetyl histone H3 (pan-acetyl HH3) and total histone H3 (HH3) in histone extracts from basal-derived organoids treated with vehicle, 1mM sodium butyrate or 10nM TSA for seven days.

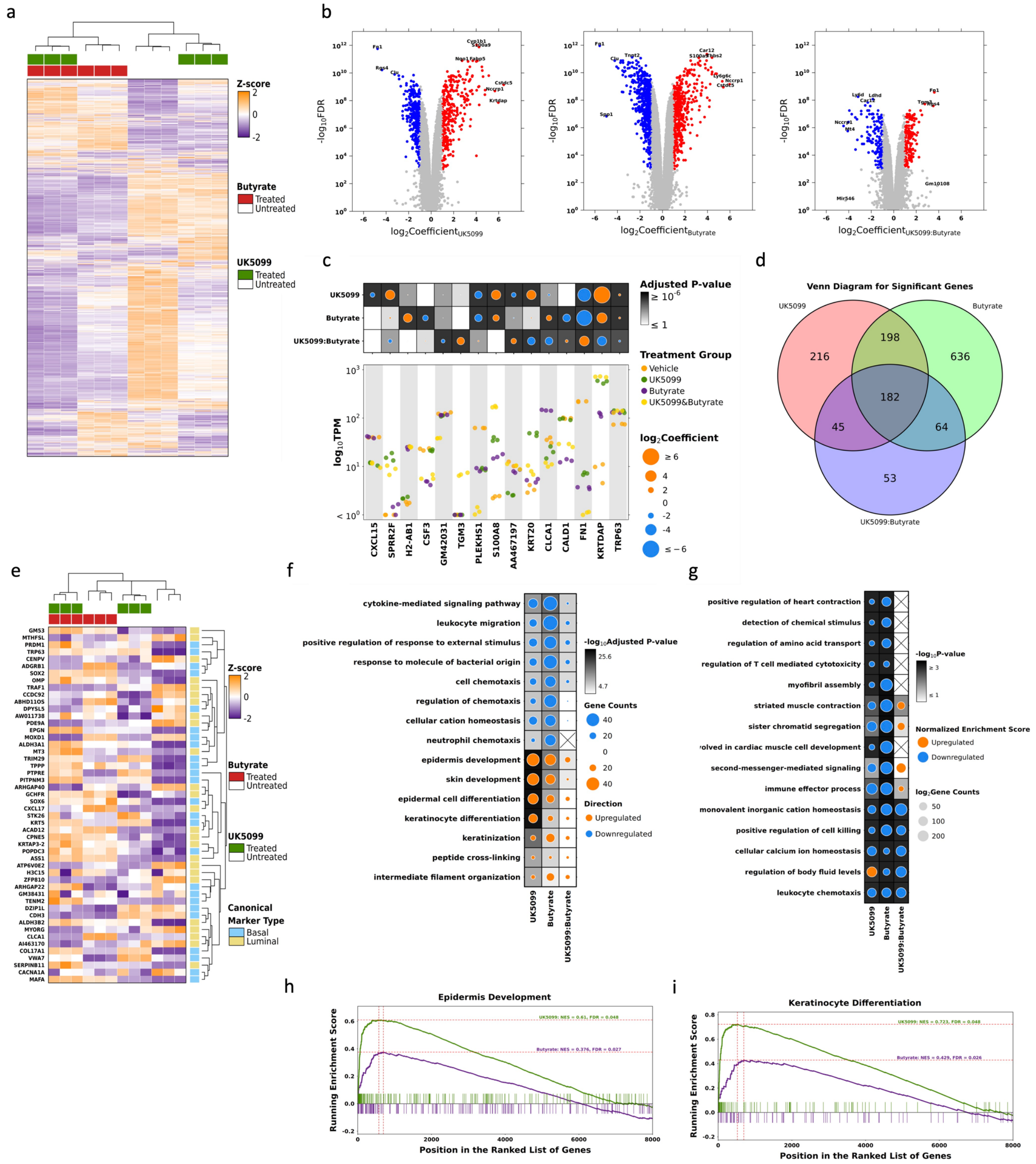

Extended Data Figure 8. (a) The distribution of gene abundance (n = 13687) among 12 samples. The primary heatmap color represents the Z-score normalized TPM value of each gene. Missing values were omitted. Hierarchical clustering has been applied to both samples (columns) and genes (rows). The top covariate heatmap indicates the treatment status of each sample. (b) Genes with significant differential RNA abundance were identified based on coefficient and adjusted p-value values ($|\log_2(\text{Coefficient})| > 1$, adjusted p-value < 0.01). Genes with downregulated RNA abundance are denoted by blue dots, while genes with upregulated RNA abundance are represented by red dots. Grey dots represent genes without a significant difference. Labeled genes have either the least adjusted p-values or the greatest $|\log_2(\text{Coefficient})|$ values. (c) Significant genes (adjusted p-value < 0.01) were selected to show univariate effects under different treatments. The primary strip plot shows raw TPM distribution among selected genes with dot colors indicating treatment types. The dotmap above presents the effect sizes and significance of each gene under different treatments. The dot size represents $\log_2$Coefficient values, while background color is indicative of the adjusted p-value. (d) The Venn diagram illustrates the overlap between effects, as reflected by the number of significant genes (n = 1,394; $|\log_2(\text{Coefficient})| > 1$, adjusted p-value < 0.01). The model was adjusted using empirical Bayes moderation for standard error, and the false discovery rate (FDR) was controlled using the Benjamini-Hochberg method. (e) The distribution of top basal and luminal gene abundance (n = 50) among 12 samples. The color in the primary heatmap signifies the Z-score normalized TPM value for each gene. Missing values were omitted. Hierarchical clustering has been applied to both samples (columns) and genes (rows). The top covariate heatmap indicates the treatment status for each sample, while the right covariate heatmap identifies the canonical marker type for each gene. (f) Top 15 enriched gene ontology terms in UK5099, Butyrate, and UK5099:Butyrate effects. The direction of regulation is calculated by the normalized enrichment score and is denoted by different colors: orange indicates upregulation, while blue represents downregulation. The dot size corresponds to the number of genes enriched in each gene set, while the background shading indicates the $-\log_{10}$adjusted p-value. (g) Top 15 enriched GSEA gene sets in UK5099, Butyrate, and UK5099:Butyrate effects. The direction of regulation is calculated by the normalized enrichment score (NES) and denoted by different colors: orange (upregulation), and blue (downregulation). The dot size corresponds to the number of genes enriched in each gene set, while the background shading indicates the $-\log_{10}$p-value. (h) Epidermis development gene set enrichment results. Genes were ranked from high to low based on $\log_2$Coefficient of UK5099 or Butyrate effect in the general linear model. (i) Keratinocyte differentiation gene set enrichment results. Genes were ranked from high to low based on $\log_2$Coefficient of UK5099 or Butyrate effect in the general linear model.

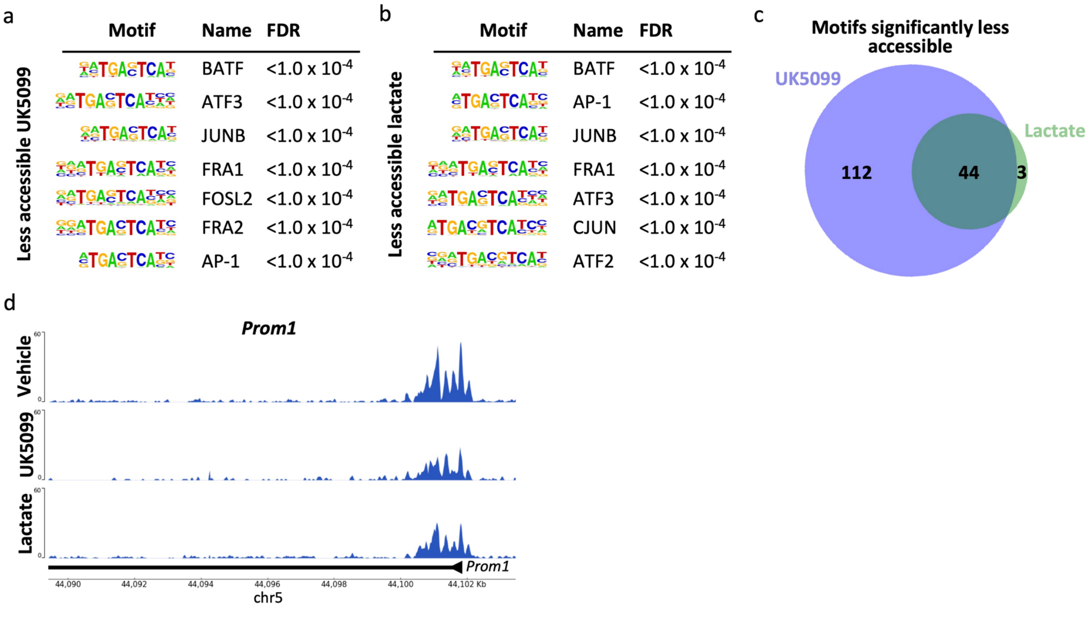

Extended Data Figure 9. (a-b) Seven most significantly enriched transcription factor binding motifs in less accessible regions in organoids treated with 10μM UK5099 (a) or 20mM sodium lactate (b). The false discovery rate (FDR) was controlled using the Benjamini-Hochberg method. (c) Venn diagram depicting overlap in significantly enriched transcription factor binding motifs in less accessible regions in UK5099-treated and lactate-supplemented organoids. (d) Browser track depicting ATAC-seq peaks in *Prom1* gene in vehicle-treated, UK5099-treated, and lactate-supplemented organoids.

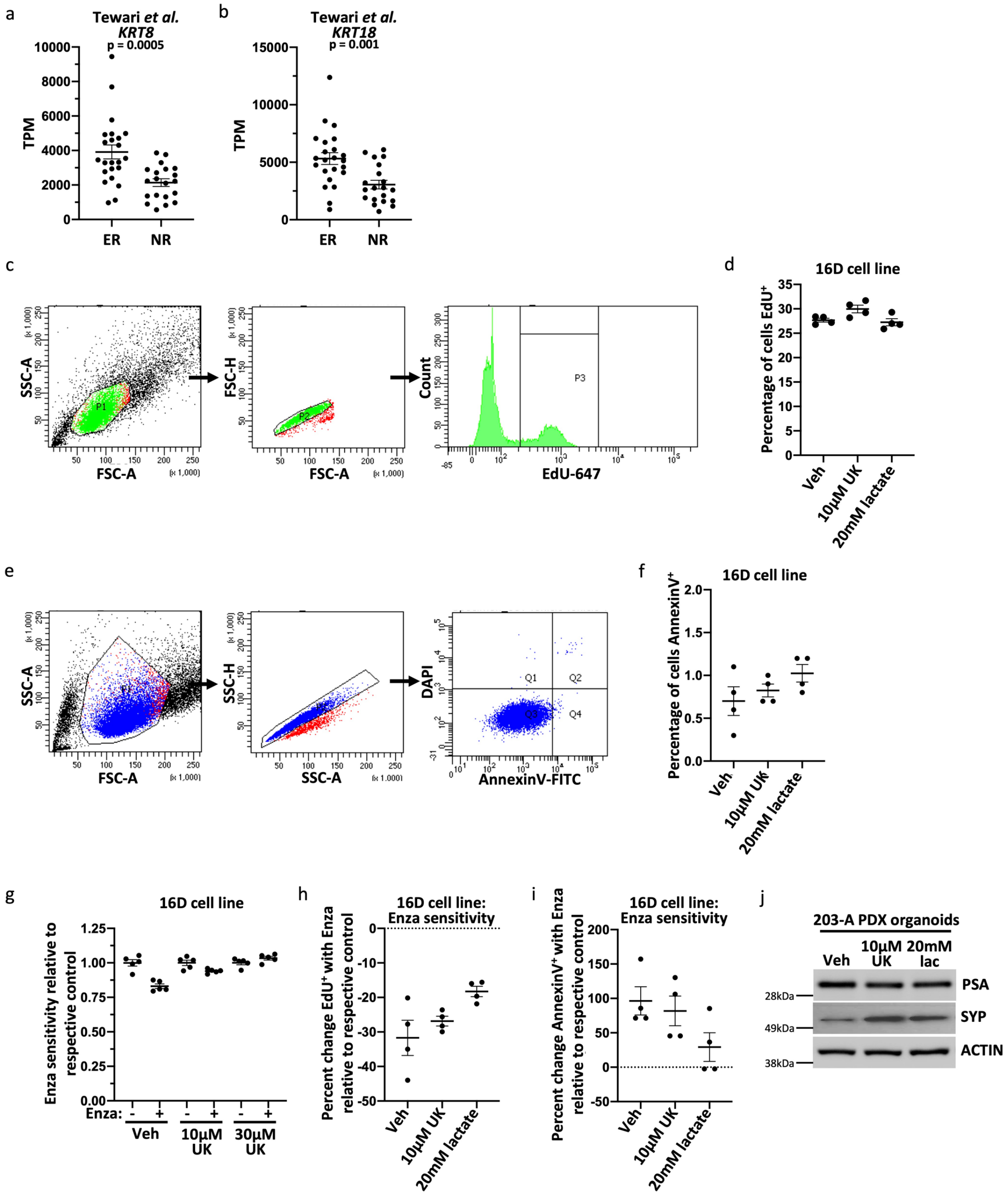

Extended Data Figure 10. (a-b) Seven most significantly enriched transcription factor binding motifs in less accessible regions in organoids treated with 10μM UK5099 (a) or 20mM sodium lactate (b). The false discovery rate (FDR) was controlled using the Benjamini-Hochberg method. (c) Venn diagram depicting overlap in significantly enriched transcription factor binding motifs in less accessible regions in UK5099-treated and lactate-supplemented organoids. (d) Browser track depicting ATAC-seq peaks in *Prom1* gene in vehicle-treated, UK5099-treated, and lactate-supplemented organoids.

Chapter 4: MYC is a regulator of androgen receptor inhibition-induced metabolic requirements in prostate cancer

Cell Reports

Article

MYC is a regulator of androgen receptor inhibition-induced metabolic requirements in prostate cancer

Graphical abstract

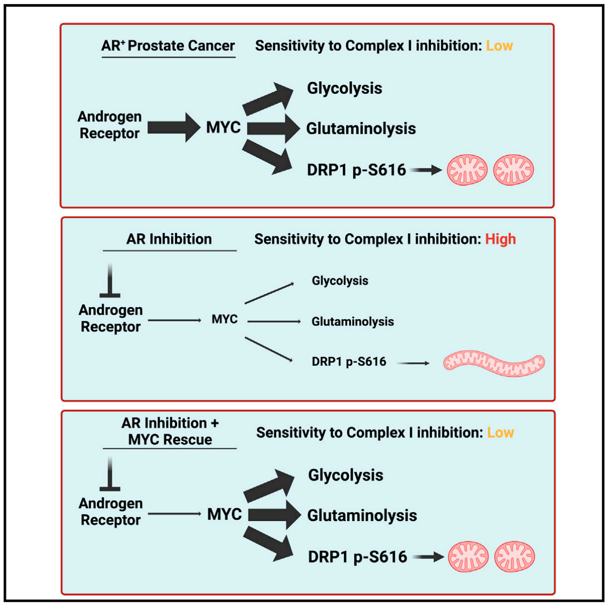

Highlights

- AR inhibition reduces DRP1 S616 phosphorylation, causing mitochondrial elongation
- MYC regulates AR inhibition-induced reduction in glycolysis and glutaminolysis
- MYC regulates AR inhibition-induced reliance on mitochondrial oxidative metabolism

Authors

Preston D. Crowell, Jenna M. Giafaglione, Anthony E. Jones, ..., Orian S. Shirihai, Ajit S. Divakaruni, Andrew S. Goldstein

Correspondence

agoldstein@mednet.ucla.edu

In brief

Resistance to androgen receptor (AR) inhibition is a major cause of prostate cancer-associated lethality. Crowell et al. comprehensively characterize the metabolic response to AR inhibition using transcriptomics, metabolomics, and bioenergetics. MYC activity and DRP1 phosphorylation regulate treatment-induced metabolic phenotypes and vulnerabilities, including sensitivity to complex I inhibition.

Crowell et al., 2023, Cell Reports *42*, 113221
October 31, 2023 © 2023 The Author(s).
https://doi.org/10.1016/j.celrep.2023.113221

Cell Reports

CellPress
OPEN ACCESS

Article

MYC is a regulator of androgen receptor inhibition-induced metabolic requirements in prostate cancer

Preston D. Crowell,[1] Jenna M. Giafaglione,[1] Anthony E. Jones,[2] Nicholas M. Nunley,[3] Takao Hashimoto,[3]
Amelie M.L. Delcourt,[3] Anton Petcherski,[4] Raag Agrawal,[5,6,7] Matthew J. Bernard,[1] Johnny A. Diaz,[3] Kylie Y. Heering,[3]
Rong Rong Huang,[8] Jin-Yih Low,[9] Nedas Matulionis,[10] Nora M. Navone,[11] Huihui Ye,[8] Amina Zoubeidi,[12,13]
Heather R. Christofk,[5,10,14] Matthew B. Rettig,[6] Robert E. Reiter,[6] Michael C. Haffner,[15,16] Paul C. Boutros,[5,6,7,17]
Orian S. Shirihai,[2,4,18] Ajit S. Divakaruni,[2] and Andrew S. Goldstein[3,5,6,14,19,20,*]

[1]Molecular Biology Interdepartmental Program, University of California, Los Angeles, Los Angeles, CA 90095, USA
[2]Department of Molecular and Medical Pharmacology, University of California, Los Angeles, Los Angeles, CA 90095, USA
[3]Department of Molecular, Cell, and Developmental Biology, University of California, Los Angeles, Los Angeles, CA 90095, USA
[4]Division of Endocrinology, Department of Medicine, David Geffen School of Medicine, University of California, Los Angeles, Los Angeles, CA 90095, USA
[5]Jonsson Comprehensive Cancer Center, University of California, Los Angeles, Los Angeles, CA 90095, USA
[6]Department of Urology, David Geffen School of Medicine, University of California, Los Angeles, Los Angeles, CA 90095, USA
[7]Department of Human Genetics, University of California, Los Angeles, Los Angeles, CA 90095, USA
[8]Department of Pathology & Laboratory Medicine, University of California, Los Angeles, Los Angeles, CA 90095, USA
[9]Division of Human Biology, Fred Hutchinson Cancer Research Center, Seattle, WA 98109, USA
[10]Department of Biological Chemistry, David Geffen School of Medicine, University of California, Los Angeles, Los Angeles, CA 90095, USA
[11]Department of GU Medical Oncology, MD Anderson Cancer Center, Houston, TX 77030, USA
[12]Department of Urologic Sciences, University of British Columbia, Vancouver, BC, Canada
[13]Vancouver Prostate Centre, Vancouver, BC, Canada
[14]Eli and Edythe Broad Stem Cell Research Center, University of California, Los Angeles, Los Angeles, CA 90095, USA
[15]Divisions of Human Biology and Clinical Research, Fred Hutchinson Cancer Research Center, Seattle, WA 98109, USA
[16]Department of Laboratory Medicine and Pathology, University of Washington, Seattle, WA 98195, USA
[17]Institute for Precision Health, University of California, Los Angeles, Los Angeles, CA 90095, USA
[18]Department of Clinical Biochemistry, School of Medicine, Ben Gurion University of The Negev, Beer-Sheva, Israel
[19]Molecular Biology Institute, University of California, Los Angeles, Los Angeles, CA 90095, USA
[20]Lead contact
*Correspondence: agoldstein@mednet.ucla.edu
https://doi.org/10.1016/j.celrep.2023.113221

SUMMARY

Advanced prostate cancers are treated with therapies targeting the androgen receptor (AR) signaling pathway. While many tumors initially respond to AR inhibition, nearly all develop resistance. It is critical to understand how prostate tumor cells respond to AR inhibition in order to exploit therapy-induced phenotypes prior to the outgrowth of treatment-resistant disease. Here, we comprehensively characterize the effects of AR blockade on prostate cancer metabolism using transcriptomics, metabolomics, and bioenergetics approaches. The metabolic response to AR inhibition is defined by reduced glycolysis, robust elongation of mitochondria, and increased reliance on mitochondrial oxidative metabolism. We establish DRP1 activity and MYC signaling as mediators of AR-blockade-induced metabolic phenotypes. Rescuing DRP1 phosphorylation after AR inhibition restores mitochondrial fission, while rescuing MYC restores glycolytic activity and prevents sensitivity to complex I inhibition. Our study provides insight into the regulation of treatment-induced metabolic phenotypes and vulnerabilities in prostate cancer.

INTRODUCTION

Prostate cancer is the leading cause of cancer-related death in non-smoking males in the United States.[1] Prostate cancer progression from localized to advanced metastatic disease is driven by aberrant androgen receptor (AR) activity. Therefore, patients with metastatic prostate cancer are treated with androgen deprivation therapy (ADT) to dampen AR activity.[2] While many advanced tumors initially respond to ADT, nearly all tumors recur as castration-resistant prostate cancer (CRPC).[3] CRPC is treated with AR pathway inhibitors (ARPIs), including enzalutamide,[4] because AR activation remains critical for tumor cell growth and survival. Enzalutamide treatment induces significant declines in prostate-specific antigen (PSA) levels and radiographic responses

Cell Reports 42, 113221, October 31, 2023

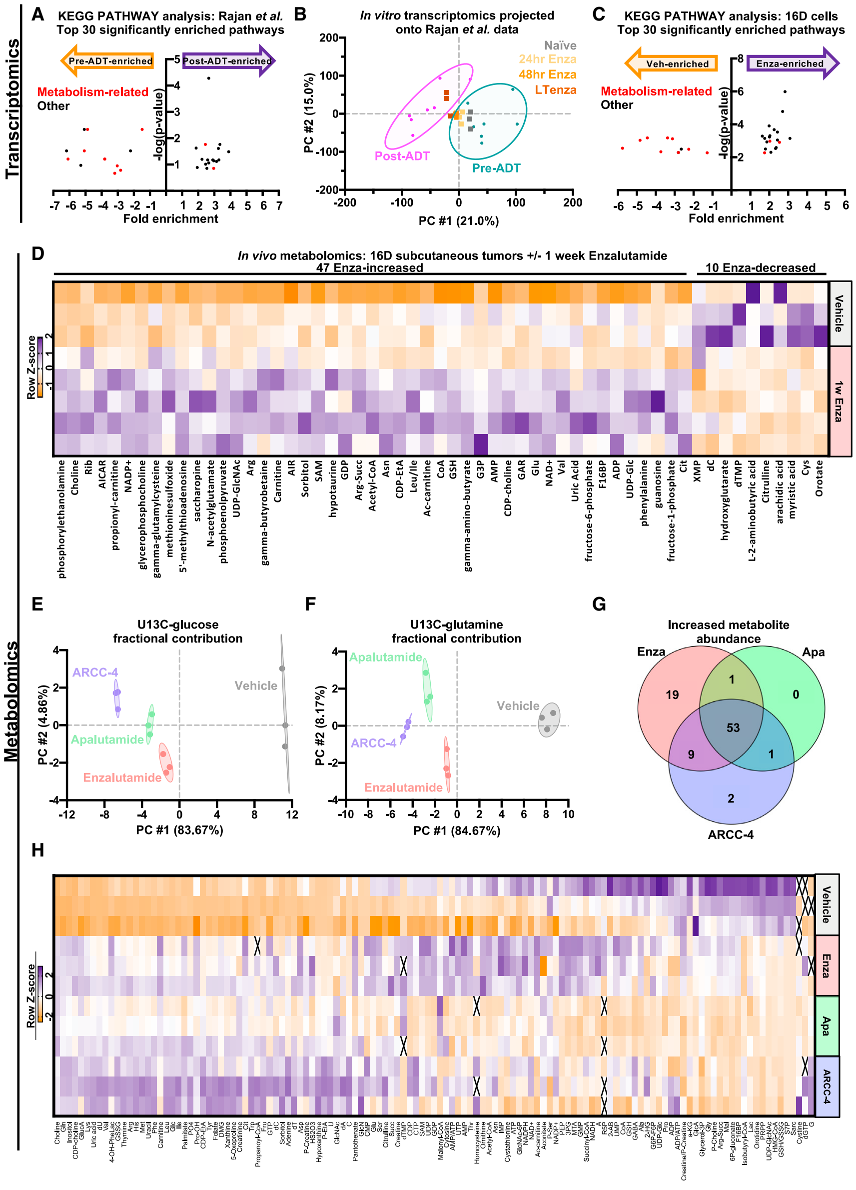

Figure 1. Transcriptomic and metabolic profiling identifies AR-inhibition-induced metabolic reprogramming

(A) Top 30 significantly enriched pathways identified by KEGG pathway analysis on differentially expressed (fold change ≥2, false discovery rate [FDR] <0.2) Rajan et al.[18] pre-androgen deprivation therapy (Pre-ADT) and post-androgen deprivation therapy (Post-ADT) genes. Metabolism-related pathways are highlighted in red. Also see Table S1.

(legend continued on next page)

in the majority of CRPC patients.[5,6] Unfortunately, prolonged ARPI treatment invariably results in disease progression, which is ultimately lethal.[7] New approaches are needed to understand how prostate cancer cells initially respond to AR-targeted therapies prior to relapse in order to exploit treatment-induced vulnerabilities and prevent or delay disease progression.

Metabolic requirements and vulnerabilities evolve during cancer progression,[8] and several studies suggest that metabolic pathways can be targeted in prostate cancer to impair tumor growth.[9–16] Short-term AR blockade (24–96 h) increases reliance on electron transport chain complex I activity and glutaminase activity.[17] However, the mechanisms that govern AR-inhibition-induced metabolic rewiring have not been clearly defined. In this study, we comprehensively characterize how prostate cancer cells that survive AR blockade reprogram their metabolism. We use *in vitro* and *in vivo* models as well as clinical datasets to demonstrate that cells surviving AR blockade maintain oxidative phosphorylation and exhibit reduced glycolysis, resulting in increased reliance on oxidative mitochondrial metabolism. We establish phosphorylation of DRP1-S616 as a key regulator of altered mitochondrial dynamics following AR blockade. Furthermore, MYC signaling is reduced following AR blockade, and overexpression of MYC restores glycolytic activity and glutamine metabolism. Finally, rescuing MYC is sufficient to reverse sensitivity to complex I inhibitors after AR inhibition. Taken together, our data suggest that AR blockade reprograms cellular metabolism and increases dependence on oxidative mitochondrial metabolism through reduced MYC.

RESULTS

Transcriptomic and metabolomic profiling reveals AR-inhibition-induced metabolic reprogramming

To gain insight into how prostate cancer cells survive AR inhibition, we evaluated which pathways are altered after clinical AR blockade using the dataset of Rajan et al.,[18] which contains transcriptomics data from seven patient tumors collected prior to and after ADT. Ten of the top 30 significantly altered pathways were metabolism related (Figure 1A; Table S1). To model transcriptional responses to AR inhibition in a system that is better suited to broad metabolic characterization, we treated the 16D CRPC cell line[19] with 10 μM enzalutamide for 48 h, termed STenza (short term), or up to 2 months, termed LTenza (long-term enzalutamide treatment). Both STenza and LTenza 16D cells contained increased expression of genes upregulated post-ADT in the Rajan et al.[18] clinical dataset, with LTenza cells containing the highest expression of such genes (Figure S1A). Principal-component projection analysis revealed that naive (vehicle-treated) 16D cells cluster with pre-ADT clinical samples, whereas LTenza 16D cells cluster with post-ADT samples from the Rajan et al. dataset[18] (Figure 1B). Gene set enrichment analysis (GSEA) identified negative enrichment of Hallmark_androgen_response genes in LTenza 16D cells (Figure S1B), validating AR inhibition. Furthermore, cell-cycle analysis illustrated that LTenza 16D cells are still sensitive to enzalutamide treatment (Figure S1C). KEGG pathway analysis on the differentially expressed genes (Figure S1D) identified 12 metabolism-related pathways among the top 30 significantly altered pathways (Figure 1C; Table S2). Taken together, these data provide strong evidence that (1) AR inhibition modulates metabolic gene expression and (2) enzalutamide treatment of 16D cells models transcriptional responses to clinical AR blockade.

Having identified transcriptional evidence of AR blockade-induced metabolic reprogramming, we asked whether enzalutamide treatment of 16D cells alters the metabolome. NOD SCID IL2Rγ^{null} (NSG) mice bearing subcutaneous 16D tumors were treated with vehicle or enzalutamide for 10 days prior to tumor harvest, metabolite extraction, and metabolic profiling. Enzalutamide-treated tumors exhibited reduced protein expression of PSA, an AR target, and increased expression of NSE, which is repressed by AR, confirming AR inhibition *in vivo* (Figure S1E). Metabolomic profiling of vehicle- and enzalutamide-treated tumors identified 47 enzalutamide-increased and 10 enzalutamide-decreased metabolites (Figure 1D). After performing metabolic profiling on *in vitro* naive and LTenza 16D cells, we found that metabolic profiles were grouped based on treatment, as naive 16D cells clustered with vehicle-treated 16D tumors, whereas LTenza 16D cells clustered with enzalutamide-treated 16D tumors (Figure S1F). In addition, we observed a higher abundance of *in vivo* enzalutamide-enriched metabolites in LTenza 16D cells compared with naive 16D cells (Figure S1G).

To identify metabolic pathways commonly altered *in vivo* and *in vitro*, we performed metabolite set enrichment analysis (MSEA) on the enzalutamide-increased metabolites from each dataset. Among the commonly enriched KEGG pathways were terms related to purine, lipid, and glutamine metabolism (Figure S1H). We explored how enzalutamide treatment alters lipid metabolism and found that there is a significant reduction in lipid droplet content within 96 h of beginning enzalutamide treatment (Figures S1I–S1K). Furthermore, lipid droplets begin to accumulate upon removal of enzalutamide (Figure S1L).

To evaluate how various methods of AR inhibition alter metabolism, we performed [U-^{13}C]glucose tracing, [U-^{13}C]glutamine tracing, and metabolic profiling on 16D cells treated with two

(B) Naive, 24 h enzalutamide-treated (Enza), 48 h Enza, and LTenza 16D transcriptomics data projected onto principal-component analysis (PCA) plot of pre-ADT and post-ADT samples from Rajan et al.[18] data.

(C) Top 30 significantly enriched pathways identified by KEGG pathway analysis on differentially expressed genes (fold change ≥2, FDR <0.05) in naive and LTenza 16D cells. Metabolism-related pathways are highlighted in red. Also see Table S2.

(D) Heatmap of differentially abundant metabolites (fold change ≥1.25, FDR <0.2) in 1 week enzalutamide-treated 16D tumors compared with vehicle-treated 16D tumors.

(E and F) PCA of [U-^{13}C]glucose (E) or [U-^{13}C]glutamine (F) fractional contribution data from 16D cells treated with vehicle, 10 μM enzalutamide, 10 μM apalutamide, or 0.5 μM ARCC-4 for 9 days prior to addition of [U-^{13}C]glucose or [U-^{13}C]glutamine for 24 h.

(G) Venn diagram illustrating overlap in metabolites with increased abundance (fold change ≥1.5) in enzalutamide-, apalutamide-, or ARCC-4-treated 16D cells relative to vehicle-treated 16D cells.

(H) Heatmap of metabolite abundances in 16D cells treated with vehicle, 10 μM enzalutamide, 10 μM apalutamide, or 0.5 μM ARCC-4 for 9 days.

ARPIs (10 μM enzalutamide and 10 μM apalutamide) and an AR degrader (0.5 μM ARCC-4). Cells treated with enzalutamide or apalutamide exhibit decreased expression of PSA, while cells treated with ARCC-4 have decreased expression of AR and PSA (Figure S1M). Principal-component analysis of fractional contribution illustrates that enzalutamide, apalutamide, and ARCC-4 similarly alter glucose and glutamine utilization (Figures 1E and 1F). Furthermore, changes to metabolite abundance were highly consistent across treatments (Figures 1G, 1H, and S1N). MSEA revealed that commonly enriched pathways include aminoacyl-tRNA biosynthesis, pyrimidine/purine metabolism, and valine/leucine/isoleucine synthesis (Figure S1O). Collectively, these data demonstrate that enzalutamide, apalutamide, and ARCC-4 have consistent effects on the metabolome.

AR blockade maintains oxidative phosphorylation and reduces glycolysis

Having identified AR-inhibition-induced changes to the metabolome, we explored whether enzalutamide treatment alters bioenergetics by measuring oxygen consumption rate (OCR) and extracellular acidification rate (ECAR) in naive and enzalutamide-maintained 16D cells[20,21] (Figures 2A and 2B). Although enzalutamide treatment did not significantly alter ATP-linked respiration (Figures 2A and 2C), carbonyl cyanide 4-(trifluoromethoxy) phenylhydrazone (FCCP)-stimulated respiration was increased in enzalutamide-treated cells (Figures 2A and 2D), demonstrating an enhanced maximal capacity for oxidative mitochondrial metabolism. We then transformed OCR and ECAR into rates of mitochondrial and glycolytic ATP production to quantify the redistribution between oxidative phosphorylation and glycolysis.[22] The mitochondrial ATP production rate was not altered in enzalutamide-treated 16D cells (Figures 2A and 2E), whereas the glycolytic ATP production rate was reduced (Figures 2B and 2F). As such, the total ATP production rate in enzalutamide-treated 16D cells was reduced (Figure 2G), and oxidative phosphorylation comprised a greater percentage of the overall ATP supply (Figure 2H). Consistent with dampened glycolysis, lower steady-state lactate was observed in enzalutamide-treated 16D cells (Figure 2I). Our data support a model whereby AR inhibition leads to reduced glycolysis but maintenance of oxidative mitochondrial metabolism.

AR inhibition enhances sensitivity to complex I inhibitors

As enzalutamide-treated 16D cells generate a greater proportion of ATP from oxidative mitochondrial metabolism, we hypothesized that these cells may be increasingly sensitive to inhibition of oxidative phosphorylation. To test our hypothesis, we cultured naive and enzalutamide-treated 16D cells with the highly specific complex I inhibitor IACS-010759[23] (IACS). Respirometry and [U-^{13}C]glucose tracer analyses were performed to validate the on-target effects of IACS. IACS reduced the ATP-linked respiration of naive and enzalutamide-treated 16D cells by roughly 95% (Figure 3A) and significantly reduced M+2 labeling of tricarboxylic acid (TCA) cycle intermediates by [U-^{13}C]glucose in both groups (Figures S2A and S2B). Increased M+3-labeled lactate was observed in both naive and enzalutamide-treated 16D cells after IACS treatment, indicating that both cell types compensate for reduced complex I activity by increasing glycolysis (Figure S2C). Respirometry revealed that, while both naive and enzalutamide-treated 16D cells increase glycolytic ATP production in response to IACS, naive cells contain a 2-fold higher IACS-induced glycolytic ATP production rate compared with enzalutamide-treated 16D cells (Figure S2D). Accordingly, IACS treatment reduced the total ATP production of naive cells by just 12% compared with a 29% reduction of total ATP production in enzalutamide-treated 16D cells (Figure S2E).

We performed cell-cycle analysis (Figure S2F) to determine the effects of IACS on proliferation. Whereas IACS treatment did not reduce the proliferation of naive cells, IACS reduced the proliferation of enzalutamide-treated 16D cells by roughly 35% in just 72 h (Figure 3B). IACS treatment significantly increased apoptosis in enzalutamide-treated cells after 72 h (Figure 3C). Furthermore, 16D cells treated with apalutamide or ARCC-4 also exhibited enhanced sensitivity to IACS (Figure 3D). Since AR blockade increases sensitivity to complex I inhibition, we wondered if IACS treatment of naive 16D cells might increase enzalutamide sensitivity. IACS pre-treatment significantly enhanced enzalutamide sensitivity, effectively doubling the growth inhibition caused by enzalutamide (Figure S2G).

The clinically viable drug metformin, which has complex I inhibitor activity *in vitro*,[24] reduced ATP-linked respiration in metformin-treated 16D cells (Figure S2H). Unlike IACS, metformin alone was sufficient to impair the proliferation of naive 16D cells (Figure S2I). Reduced proliferation in metformin-treated 16D cells was likely caused by known off-target effects,[24] as IACS treatment reduced ATP-linked respiration by greater than 95% without altering EdU labeling. Consistent with IACS pre-treatment increasing responsiveness to AR inhibition, metformin pre-treatment significantly enhanced the sensitivity of naive 16D cells to enzalutamide (Figure S2J).

To better understand the interaction between AR inhibition and complex I inhibition across various disease states, we explored whether metformin similarly enhances the sensitivity of LNCaP cells to deprivation of the AR ligand dihydrotestosterone (DHT). We first confirmed that LNCaP cells grown without DHT transcriptionally resemble patient tumors post-ADT[18] (Figures S3A–S3C). Consistent with our findings in the 16D model, metformin treatment reduced the growth of LNCaP cells and significantly increased DHT deprivation sensitivity, from roughly 45% to greater than 85% (Figures S3D and S3E).

After showing that various complex I inhibitors can synergize with AR blockade *in vitro*, we explored whether enzalutamide treatment of mice bearing patient-derived xenograft (PDX) tumors enhances IACS sensitivity. We utilized an AR-positive PDX model originating from a patient with localized CRPC, termed MDA-PCa 180-30.[25] Week-long enzalutamide-treated 180-30 PDX tumors exhibited reduced protein expression of PSA (Figures S3F and S3G). After treatment with vehicle or enzalutamide *in vivo*, we evaluated the effect of enzalutamide on proliferation and response to complex I inhibition. Cell-cycle analysis after *ex vivo* culture of tumor tissue under prostate organoid conditions confirmed reduced proliferation in enzalutamide-treated 180-30 PDX tumors (Figure S3H). Analysis of IACS sensitivity revealed that enzalutamide-treated samples accounted for four of the five most IACS-sensitive samples

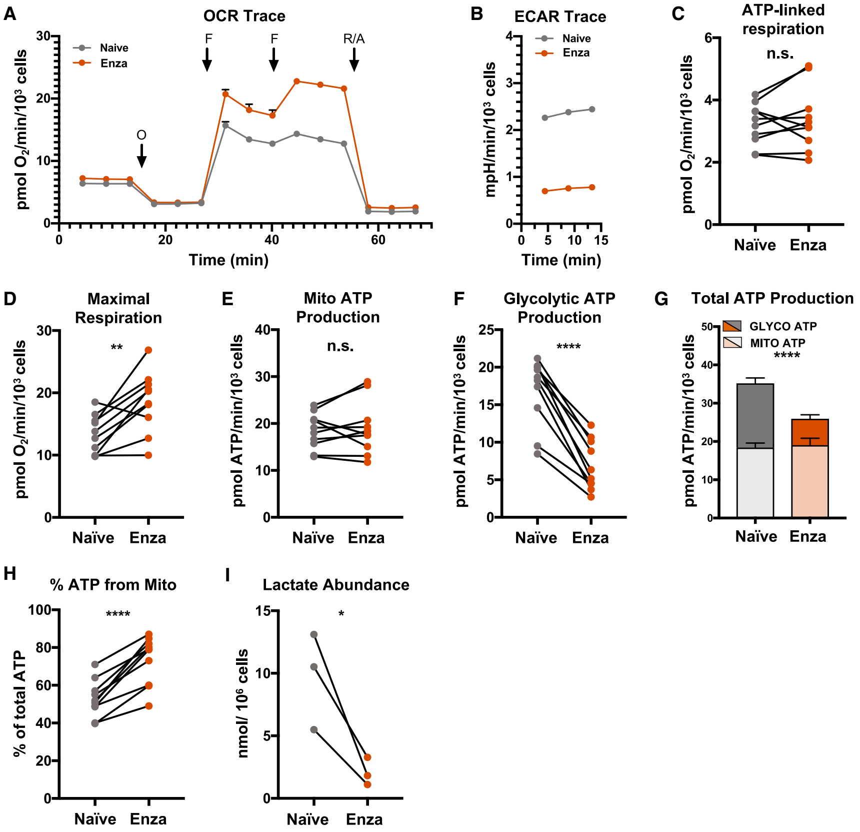

Figure 2. AR blockade maintains oxidative mitochondrial metabolism and reduces glycolysis

(A and B) Representative kinetic trace plots of the oxygen consumption rate (OCR) (A) and extracellular acidification rate (ECAR) (B) of naive and LTenza 16D cells. Treatments with oligomycin (O), FCCP (F), and rotenone and antimycin A (R/A) are indicated with arrows. Data represent the mean ± SEM.

(C and D) ATP-linked respiration (C) and maximal respiration (D) of naive and LTenza 16D cells from 10 biological replicate experiments.

(E and F) Mitochondrial (Mito) ATP production (E) and glycolytic ATP production (F) of naive and LTenza 16D cells from 10 biological replicate experiments.

(G) Total ATP production as the sum of mitochondrial ATP production (Mito ATP) and glycolytic ATP production (Glyco ATP) of naive and LTenza 16D cells from 10 biological replicate experiments. Statistics refer to comparison of total ATP levels. Data represent the mean + SEM.

(H) Percentage of total ATP production from mitochondrial ATP production (% ATP from Mito) of naive and LTenza 16D cells from 10 biological replicate experiments.

(I) Lactate abundance in naive and LTenza 16D cells from three biological replicate experiments. The p values were calculated from a ratio paired t test; $^{*}p < 0.05$, $^{**}p < 0.01$, $^{****}p < 0.0001$; n.s., not significant, $p \geq 0.05$.

(Figure 3E). Furthermore, whereas IACS did not alter the growth of vehicle-treated tumor cells in a statistically significant manner (Figure 3F), IACS significantly reduced proliferation of enzalutamide-treated cells (Figure 3G). In addition, we used the MDA-PCa 173-2 PDX model, which originated from a patient with localized treatment-naïve prostate cancer, to determine if complex I inhibition further decreases the growth of castrated tumors *in vivo*. Ki67 staining of tumor sections revealed that, while IACS treatment decreases the growth of 173-2 PDX tumors in intact mice, the combination of castration and IACS treatment almost completely abolishes proliferation (Figures 3H and 3I). The 173-2 PDX tumors grown in intact mice exhibited a 53% reduction in proliferation in response to IACS, whereas 173-2 PDX tumors grown in castrated mice exhibited an 80% reduction in proliferation in response to IACS (Figure S3I). Collectively, these data suggest that AR inhibition and complex I inhibition can cooperate to decrease growth across disease states.

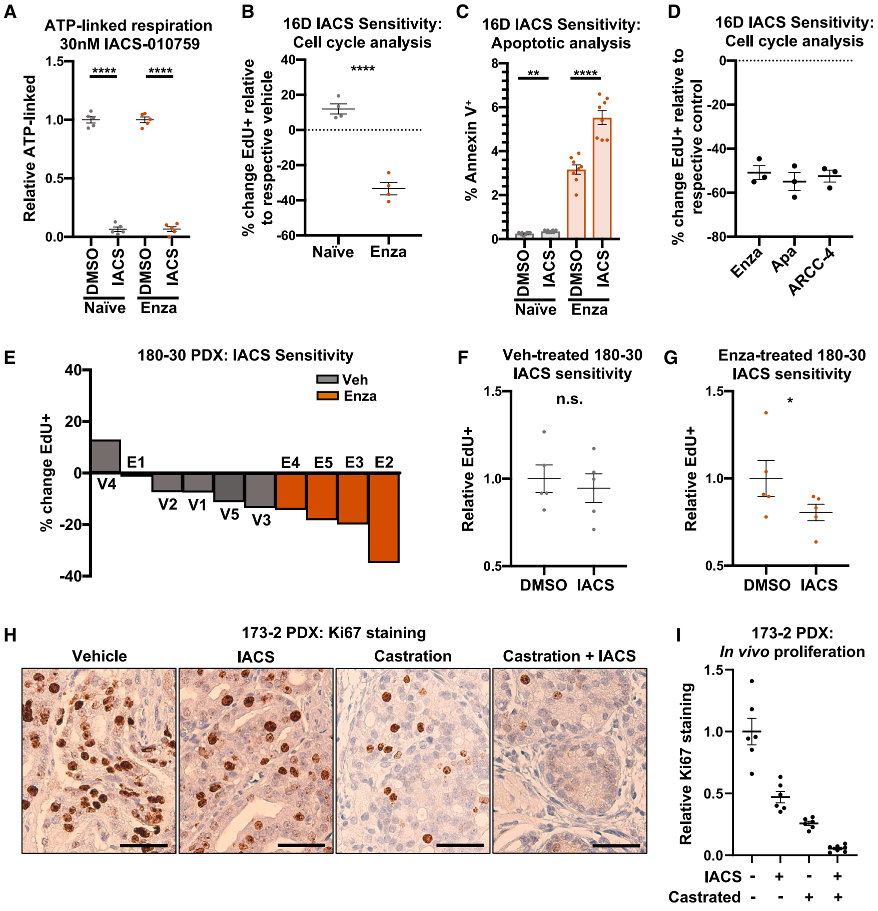

Figure 3. AR blockade enhances sensitivity to complex I inhibition

(A) ATP-linked respiration of naive and LTenza 16D cells treated with vehicle (DMSO) or 30 nM IACS-010759 (IACS) for 24 h. Data represent the mean ± SEM of five technical replicates.

(B) Cell-cycle analysis to quantify the relative sensitivity of naive and LTenza 16D cells to 30 nM IACS. Data represent the mean ± SEM of four technical replicates from a representative experiment (n = 3).

(C) Apoptosis analysis to identify the percentage of Annexin V-positive cells (% Annexin V^+) in naive and LTenza 16D cells treated with DMSO or 30 nM IACS for 48 h. Data represent the mean ± SEM of eight technical replicates.

(D) Cell-cycle analysis to quantify the relative sensitivity of 16D cells treated with 10 μM enzalutamide, 10 μM apalutamide, or 0.1 μM ARCC-4 to 30 nM IACS. Data represent the mean ± SEM of three technical replicates.

(E) Waterfall plot indicating the *ex vivo* sensitivity of 180-30 PDX tumor tissue from vehicle- and 1 week Enza-treated tumors to 30 nM IACS. Data represent the percentage change in EdU positivity (% change EdU^+) relative to the respective vehicle.

(F and G) Cell-cycle analysis of the sensitivity of vehicle-treated (F) or Enza-treated (G) 180-30 PDX tumor tissue to *ex vivo* culture ±30 nM IACS. Data represent the mean ± SEM of five tumor samples per treatment group.

(H) Immunohistochemical analysis of representative 173-2 PDX tumors grown in intact or castrated mice and treated with or without 7.5 mg/kg/day IACS for 5 days stained for Ki67. Scale bars, 50 μm.

(I) Quantification of Ki67 staining area from six representative images of 173-2 PDX tumors grown in intact or castrated mice and treated with or without 7.5 mg/kg/day IACS for 5 days. The p values were calculated from an unpaired t test with Welch's correction (A–D) and a ratio-paired t test (F and G); *$p < 0.05$, **$p < 0.01$, ****$p < 0.0001$; n.s., not significant, $p \geq 0.05$.

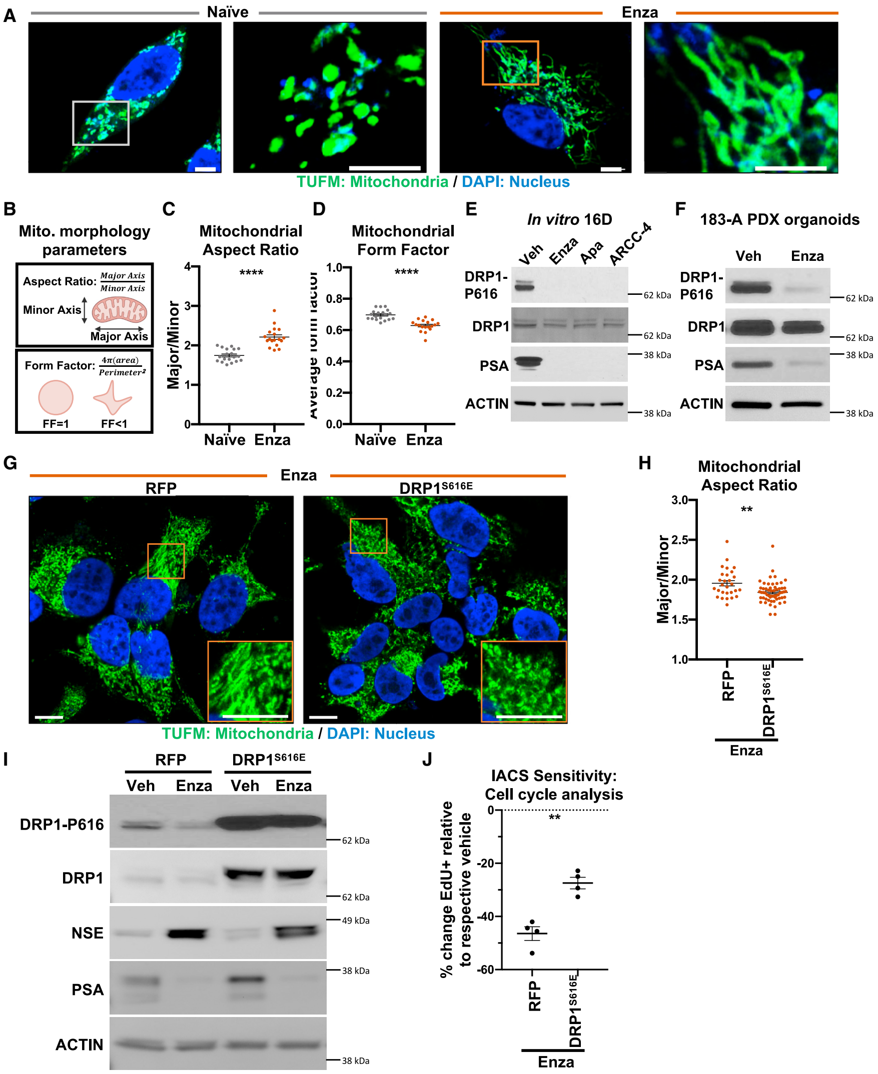

Figure 4. AR blockade elongates mitochondria via reduced DRP1 activity

(A) Representative immunofluorescence images of naive and LTenza 16D cells stained for TUFM (green) and DAPI (blue). Scale bars, 5 µm.

(B) Schematic illustrating calculation of aspect ratio and form factor.

(C and D) Quantification of mitochondrial aspect ratio (C) and mitochondrial form factor (D) from TUFM stains from 20 images per treatment group. Data represent the mean ± SEM.

(E and F) Western blots detecting DRP1 phosphorylation at S616 (DRP1-P616), DRP1, PSA, and actin (loading control) in 16D cells treated with vehicle, 10 µM enzalutamide, 10 µM apalutamide, or 0.5 µM ARCC-4 for 9 days (E) and 183-A PDX organoids treated with vehicle or 10 µM enzalutamide for 1 week (F).

(G) Representative immunofluorescence images of RFP- and DRP1^{S616E}-transduced LTenza 16D cells stained for TUFM (green) and DAPI (blue). Scale bars, 10 µm.

(H) Quantification of mitochondrial aspect ratio from TUFM stains from at least 28 cells per treatment group. Data represent the mean ± SEM.

(legend continued on next page)

Enzalutamide induces mitochondrial elongation via reduced DRP1 activity

As mitochondrial dynamics can change in response to cellular and environmental stresses,[26] we explored the effect of AR inhibition on mitochondrial morphology. Mitochondria were visualized by staining for the mitochondria-associated protein Tu translation elongation factor (TUFM). Immunofluorescence identified robustly elongated mitochondria in enzalutamide-treated 16D cells (Figure 4A). Quantification of mitochondrial elongation and branching was performed by calculating the mitochondrial aspect ratio, which is equal to the ratio of the major axis to the minor axis of an object, and form factor, a value that compensates for irregularity in the shape of an object, respectively[27] (Figure 4B). Enzalutamide-treated 16D cell mitochondria exhibited a higher aspect ratio (Figure 4C) and lower form factor (Figure 4D) compared with naive cell mitochondria, consistent with mitochondrial elongation and increased branching. Eccentricity, the ratio of the distance between the foci of an ellipse and its major axis length, was elevated in mitochondria from enzalutamide-treated 16D cells, confirming mitochondrial elongation (Figure S4A). Enzalutamide treatment did not alter mitochondrial size, subtly increased mitochondrial count, and did not alter mitochondrial volume (Figures S4B–S4D).

Mitochondrial morphology is determined by the relative amounts of mitochondrial fission and fusion.[28] Several reports provide evidence that AR may regulate expression of DRP1,[29] encoded by the *DNM1L* gene, which mediates mitochondrial fission. Analysis of LNCaP and 16D AR chromatin immunoprecipitation-sequencing (ChIP-seq) data[30] revealed binding to the *DNM1L* locus (Figure S4E). We therefore explored whether DRP1 levels are altered in 16D cells treated with various AR inhibitors. Surprisingly, DRP1 expression was only subtly reduced in enzalutamide-, apalutamide-, and ARCC-4-treated 16D cells (Figure 4E). We evaluated DRP1 phosphorylation at S616, which mediates DRP1 activity,[31] and found a dramatic reduction in enzalutamide-, apalutamide-, and ARCC-4-treated 16D cells (Figure 4E) and in enzalutamide-treated LAPC4 cells (Figure S4F). When enzalutamide was removed from enzalutamide-maintained 16D cells for 10 days, DRP1-S616 phosphorylation returned to levels present in naive cells (Figure S4G). In addition, in organoids derived from the MDA-PCa 183-A PDX model, which originated from a patient with metastatic treatment-naive prostate cancer, enzalutamide treatment results in decreased DRP1-S616 expression (Figure 4F). Enzalutamide-treated 16D tumors (Figures S4H and S4I), 180-30 PDX tumors (Figure S4J), and 173-2 PDX tumors (Figures S4K–S4L) contained both reduced total DRP1 expression and reduced DRP1-S616 phosphorylation, suggesting that the tumor microenvironment may influence the response of DRP1 expression to AR blockade. Interestingly, enzalutamide-resistant AR^+ 22Rv1 cells did not exhibit reduced DRP1-S616 expression in response to enzalutamide treatment (Figure S4M).

To evaluate the functional role of DRP1, we ectopically expressed RFP, or a constitutively active DRP1 phosphomimetic[31] $DRP1^{S616E}$, in enzalutamide-maintained 16D cells (Figure S4M). Expression of $DRP1^{S616E}$ was sufficient to reduce mitochondrial elongation and increase mitochondrial fission (Figures 4G and 4H). We evaluated IACS sensitivity using cell-cycle analysis and found that constitutive expression of DRP1 partially rescues enzalutamide-induced IACS sensitivity (Figures 4I and 4J). These data suggest that changes in mitochondrial morphology following AR blockade functionally contribute to metabolic dependencies.

Reduced glycolytic enzyme expression in cells that survive AR inhibition

We wondered what mechanisms induced by AR blockade may contribute to the reduction in glycolysis. Transcriptomic analysis identified a trend toward downregulation of glycolytic genes in enzalutamide-treated 16D cells, including *Hexokinase 2* (*HK2*) and *Lactate Dehydrogenase A* (*LDHA*) (Figure 5A). Western blot analysis confirmed reduced protein expression of HK2 and LDHA in enzalutamide-, apalutamide-, and ARCC-4-treated 16D cells (Figure 5B) and LAPC4 cells (Figure S4E), but not in enzalutamide-resistant AR^+ 22Rv1 cells (Figure S4L). Upon removal of enzalutamide, HK2 and LDHA abundance increased in 16D cells (Figure S4G). In addition, HK2 and LDHA were reduced in enzalutamide-treated 16D tumors, enzalutamide-treated 180-30 PDX tumors, and 173-2 PDX tumors grown in castrated mice (Figures 5C, 5D, S4J, S4K, and S5A). In LNCaP cells, glycolytic enzyme expression was similarly reduced as a result of enzalutamide treatment or DHT deprivation (Figures 5E and S5B). We also analyzed glycolytic enzyme expression in four clinical transcriptomic datasets: the Rajan et al. dataset[18] (seven locally advanced or metastatic prostate cancer tumors biopsied before and after ADT; Figure S5C), the Reiter trial (NCT01990196) (seven tumor-rich prostatic biopsies collected prior to and after ADT and enzalutamide treatment; Figure S5D), the Long et al. dataset[32] (six tumor-rich prostatic biopsies collected prior to and after ADT and bicalutamide treatment; Figure S5E), and the Wilkinson et al. dataset[33] (36 prostatic biopsies collected prior to and after ADT and enzalutamide treatment; Figure S5F). We found that *SLC16A1* was reduced in all datasets after AR inhibition, while *ENO1* and *TPI1* were reduced in three of the four datasets (Figures S5C–S5F). In the Rajan et al.[18] and Reiter trial (NCT01990196) *HK2* mRNA expression was reduced after AR blockade in all patients (Figures 5F and 5G). These data suggest that AR inhibition lowers expression of key glycolytic enzymes across various AR inhibition-responsive disease states.

Reduced MYC signaling regulates AR inhibition-induced metabolic phenotypes

We hypothesized that downregulation of HK2 following AR inhibition may mediate reduced glycolytic activity and sensitivity to complex I inhibition. Cells with HK2 overexpression maintained high levels of HK2 even in the presence of enzalutamide (Figure 5H) but still exhibit significant sensitivity to complex I inhibition

---

(I) Western blot indicating expression of DRP1-P616, DRP1, NSE, PSA, and actin (loading control) in RFP- and $DRP1^{S616E}$-transduced 16D cells maintained with or without 10 μM enzalutamide for 1 week.

(J) Cell-cycle analysis to quantify the relative sensitivity of RFP- and $DRP1^{S616E}$-transduced 16D cells maintained in 10 μM enzalutamide for 1 week to 30 nM IACS. Data represent the mean ± SEM of four technical replicates from a representative experiment (n = 2). The p values were calculated from an unpaired t test with Welch's correction; *p < 0.05, **p < 0.01, ***p < 0.001, ****p < 0.0001; n.s., not significant, p ≥ 0.05.

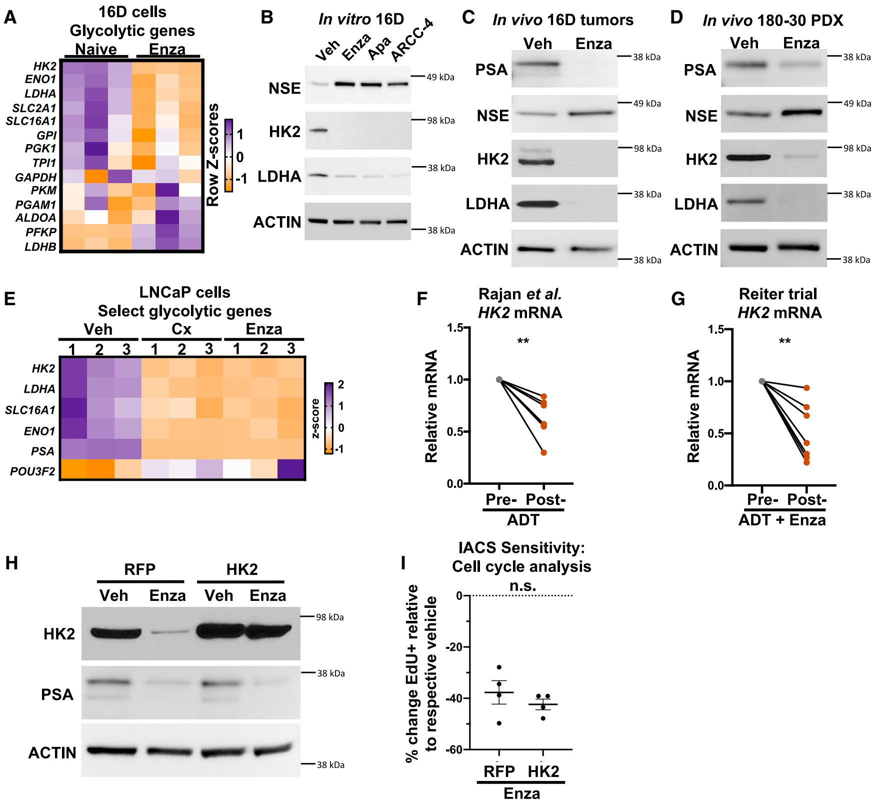

Figure 5. Downregulation of key glycolytic enzymes following AR inhibition

(A) Heatmap showing the mRNA expression of glycolytic genes from RNA sequencing of three technical replicates of naive and LTenza 16D cells.

(B–D) Western blots indicating the expression of PSA, NSE, HK2, LDHA, and actin (loading control) in lysates from 16D cells treated with vehicle, 10 µM enzalutamide, 10 µM apalutamide, or 0.5 µM ARCC-4 for 9 days (B), 16D tumors treated with vehicle (Veh) or enzalutamide (Enza) for 1 week *in vivo* (C), and 180-30 PDX tumors treated with Veh or Enza for 1 week *in vivo* (D).

(E) Heatmap showing the mRNA expression of select glycolytic genes from RNA sequencing of three technical replicates of Veh, 72 h castrated (Cx), and 72 h Enza-treated LNCaP cells.

(F and G) *HK2* mRNA expression in matched pre- and post-AR blockade biopsies from the Rajan et al.[18] (F) and Reiter trial (NCT01990196) (G) datasets.

(H) Western blot indicating expression of HK2, PSA, and actin (loading control) in RFP- and HK2-transduced 16D cells maintained with or without 10 µM Enza for 1 week.

(I) Cell-cycle analysis to quantify the relative sensitivity of RFP- and HK2-transduced 16D cells maintained in 10 µM Enza for 1 week to 30 nM IACS. Data represent the mean ± SEM of four technical replicates from a representative experiment (n = 2). The p values were calculated from a ratio-paired t test (F and G) and an unpaired t test with Welch's correction (I); $**p < 0.01$, $***p < 0.001$; n.s., not significant, $p \geq 0.05$.

(Figure 5I). These data suggest that expression of HK2 does not mediate sensitivity to complex I inhibition following AR inhibition. Since several glycolytic enzymes and transporters are downregulated after AR inhibition, we investigated whether AR blockade alters transcriptional signatures of MYC, a key regulator of glycolysis[34] and an AR target gene.[35] GSEA revealed negative enrichment of Hallmark_Myc_targets in the Rajan et al.,[18] Reiter trial (NCT01990196), Long et al.,[32] and Wilkinson et al.[33] patient samples after AR blockade (Figures 6A and S6A–S6C). In addition, negative enrichment of Hallmark_Myc_targets was observed after castration in the AR-positive LTL331 PDX model[36] (Figure 6B). Consistent with these data, Hallmark_Myc_targets is negatively enriched in enzalutamide-treated 16D cells (Figure 6C) and in LNCaP cells deprived of DHT (Figure S6D).

To determine whether reduced MYC activity mediates reduced glycolytic enzyme expression in AR-inhibited cells, we attempted to rescue MYC transcriptional activity via ectopic MYC expression. GSEA revealed positive enrichment of Hallmark_Myc_targets in

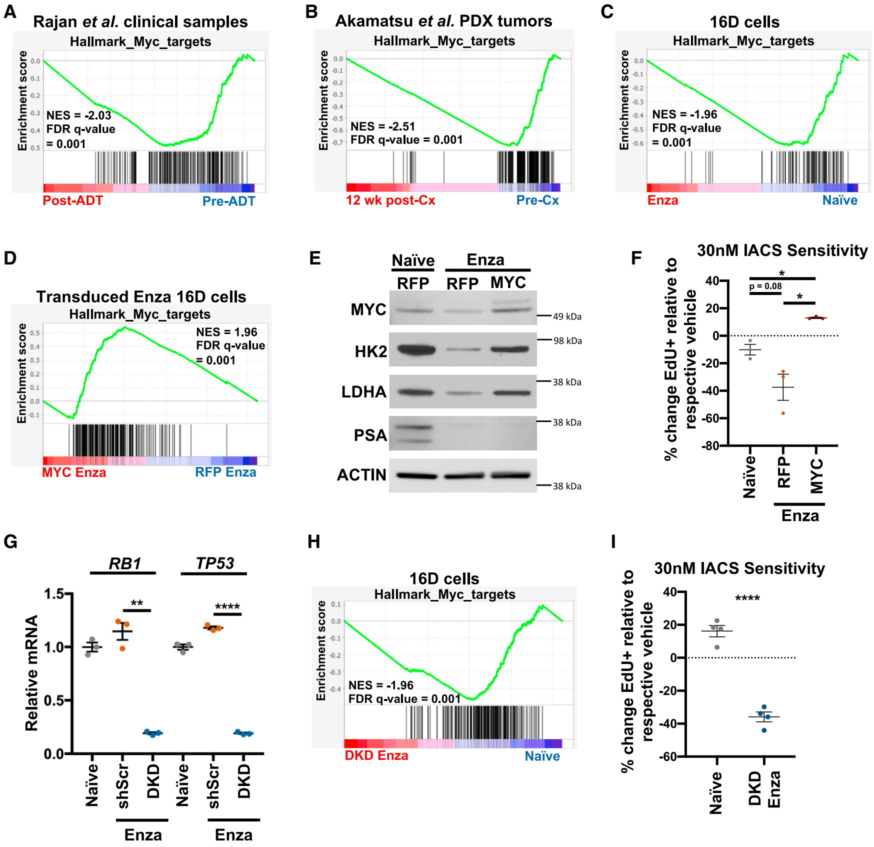

Figure 6. Decreased Myc signaling following AR inhibition mediates complex I inhibition sensitivity

(A–D) GSEA of Hallmark_Myc_targets in Rajan et al.[18] pre-ADT and post-ADT samples (A), Akamatsu et al.[36] pre-castration (pre-Cx) and 12 weeks post-castration (post-Cx) (B), naive and LTenza 16D cells (C), and RFP- and MYC-transduced LTenza cells (D) showing normalized enrichment scores (NESs) and FDRs.

(E) Western blot indicating expression of MYC, HK2, LDHA, PSA, and actin (loading control) in naive, RFP-transduced LTenza, and MYC-transduced LTenza 16D lysates.

(F) Cell-cycle analysis to quantify the relative sensitivity of naive and RFP- and MYC-transduced LTenza 16D cells to 30 nM IACS. Data represent the mean ± SEM of four technical replicates from a representative experiment (n = 3).

(G) mRNA expression of *RB1* and *TP53* in naive, shScr-transduced (shScr) LTenza, and shRB1_shTP53-transduced (DKD) LTenza 16D cells. Data represent the mean ± SEM of three technical replicates.

(H) GSEA of Hallmark_Myc_targets in naive and DKD LTenza cells.

(I) Cell-cycle analysis to quantify the relative sensitivity of naive and DKD LTenza 16D cells to 30 nM IACS. Data represent the mean ± SEM of four technical replicates from a representative experiment (n = 2). The p values were calculated from an unpaired t test with Welch's correction; *p < 0.05, **p < 0.01, ****p < 0.0001; n.s., not significant, p ≥ 0.05.

MYC-transduced enzalutamide-treated cells compared with RFP-transduced enzalutamide-treated 16D cells (Figure 6D). Furthermore, there was no significant negative enrichment of Hallmark_Myc_targets in MYC-transduced enzalutamide-treated cells relative to naive 16D cells, indicating successful restoration of MYC transcriptional activity (Figure S6E). Western blot analysis revealed increased expression of HK2 and LDHA in MYC-transduced enzalutamide-treated cells compared with RFP-transduced enzalutamide-treated 16D cells (Figure 6E). While ectopic MYC effectively rescued LDHA expression to levels observed in naive 16D cells, HK2 expression remained roughly 50% lower in MYC-transduced enzalutamide-treated cells compared with naive 16D cells

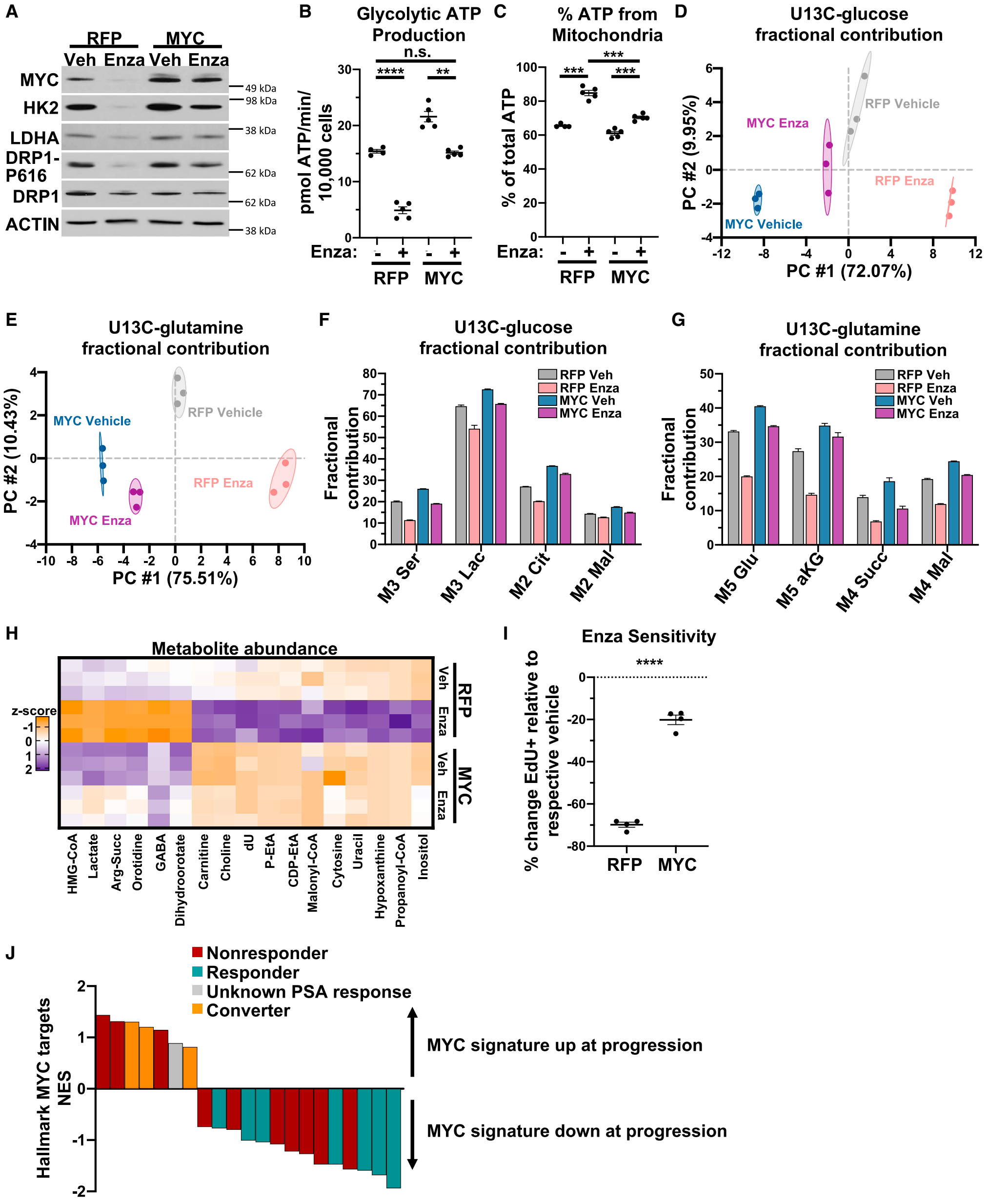

(legend on next page)

(Figure 6E). Similarly, removal of enzalutamide resulted in a complete rebound in LDHA but only a partial increase in HK2 expression (Figure S4G). Targeted bisulfite sequencing identified a statistically significant increase in the mean percentage of methylated CpGs within the transcriptional start site of *HK2* in enzalutamide-treated 16D cells, suggesting that epigenetic alterations may cooperate with reduced MYC activity to antagonize HK2 expression (Figure S6F). We used cell-cycle analysis (Figure S6G) to explore whether rescuing MYC activity influences the response to complex I inhibition and found that MYC restoration in enzalutamide-treated cells eliminates sensitivity to IACS (Figure 6F). These results suggest that MYC activity regulates reliance on mitochondrial oxidative metabolism in cells that survive AR inhibition.

To evaluate whether genetic alterations associated with prostate cancer progression alter AR inhibition-induced metabolic phenotypes, we knocked down *RB1* and *TP53*, two tumor suppressors that are commonly dysregulated in aggressive disease variants, including neuroendocrine prostate cancer.[37] Knockdown of *RB1* and *TP53* in enzalutamide-treated 16D cells (Figure 6G) increased neuroendocrine signatures[38–40] (Figures S6H–S6J) but did not rescue MYC transcriptional activity (Figures 6H and S6K), glycolytic enzyme expression (Figure S6L), glycolysis (Figures S6M–S6P), or sensitivity to complex I inhibition (Figure 6I). These data suggest that modulating lineage identity without restoring MYC activity is not sufficient to resolve AR inhibition-induced reliance on mitochondrial oxidative metabolism.

Sustained MYC expression promotes antiandrogen resistance

We hypothesized that maintenance of MYC activity during enzalutamide treatment may enable cells to better survive AR inhibition due to maintenance of glycolysis. We found that ectopic MYC expression in 16D cells was sufficient to mitigate the enzalutamide-mediated reduction in HK2, LDHA, and DRP1-P616 expression (Figure 7A); restore glycolytic ATP production to levels observed in vehicle-treated cells (Figure 7B); and partially rescue the enzalutamide-mediated increase in the percentage of ATP produced by mitochondrial oxidative metabolism (Figure 7C). We also performed [U-^{13}C]glucose tracing, [U-^{13}C]glutamine tracing, and metabolic profiling on RFP- and MYC-transduced 16D cells cultured with or without enzalutamide. Sustained MYC expression reverses enzalutamide-induced changes to glucose and glutamine utilization (Figures 7D–7H) but does not rescue enzalutamide-mediated reduction in neutral lipid content (Figure S7A).

Ectopic MYC expression significantly increased enzalutamide resistance in 16D cells (Figure 7I). To investigate if there is evidence of MYC-associated resistance to AR blockade in clinical samples, we analyzed the Westbrook et al. dataset,[41] which contains RNA-sequencing data of 21 mCRPC tumors before and after enzalutamide treatment. We found that seven patients had positive enrichment of Hallmark_Myc_targets with enzalutamide treatment. Of these seven patients, three were characterized as nonresponders to enzalutamide, three were characterized as having lineage plasticity with conversion to a double-negative phenotype, and one was characterized as having an unknown response to enzalutamide (Figure 7J). In contrast, 7 of the 14 patients exhibiting negative enrichment of Hallmark_Myc_targets with enzalutamide treatment exhibited a clinical response. These data correlate upregulation of MYC activity with clinical enzalutamide resistance. In addition, in the LTL331 PDX model,[36] which relapses as terminally differentiated neuroendocrine prostate cancer after castration, relapsed tumors contain robust enrichment of Hallmark_Myc_targets compared with castrated tumors (Figures S7B and S7C) despite maintenance of low AR activity (Figures S7D and S7E). These data suggest that rescue of AR activity is not necessary to restore MYC signaling and support our hypothesis that MYC reactivation may promote resistance to AR blockade.

DISCUSSION

Therapy-induced metabolic reprogramming has been reported in various cancers where standard-of-care therapy can synergize with targeting of reprogrammed metabolism to impair treatment resistance.[42–44] In this study, we comprehensively characterized the effects of AR blockade on prostate cancer metabolism. Transcriptomic and metabolomic analyses revealed AR-inhibition-induced changes to metabolic gene expression and metabolite abundance, respectively. Using bioenergetic assays, we identified sustained oxidative mitochondrial metabolism, including increased maximal respiration, and reduced basal and oligomycin-stimulated glycolysis, after AR inhibition. These AR-blockade-induced metabolic alterations confer sensitivity to complex I inhibition. Mechanistically, reduced phosphorylation of DRP1-S616 and MYC signaling

Figure 7. Sustained MYC expression promotes antiandrogen resistance

(A) Western blot indicating expression of MYC, HK2, LDHA, DRP1-P616, DRP1, and actin (loading control) in RFP- and MYC-transduced 16D cells maintained with or without 10 μM enzalutamide for 1 week.

(B and C) Glycolytic ATP production (B) and percentage of total ATP production from mitochondrial ATP production (% ATP from Mitochondria) (C) of RFP- and MYC-transduced 16D cells maintained with or without 10 μM enzalutamide for 1 week. Data represent the mean ± SEM of four technical replicates.

(D and E) Principal-component analysis (PCA) of [U-^{13}C]glucose (D) or [U-^{13}C]glutamine (E) fractional contribution data from RFP- and MYC-transduced 16D cells maintained with or without 10 μM enzalutamide for 6 days prior to addition of [U-^{13}C]glucose or [U-^{13}C]glutamine for 24 h.

(F and G) Fractional contribution for M3 serine, M3 lactate, M2 citrate, and M2 malate from [U-^{13}C]glucose (F) or M5 glutamate, M5 α-ketoglutarate, M4 succinate, and M4 malate (G) in RFP- and MYC-transduced 16D cells maintained with or without 10 μM enzalutamide for 6 days prior to addition of [U-^{13}C]glucose or [U-^{13}C]glutamine for 24 h.

(H) Heatmap of differentially abundant metabolites (fold change $\geq$1.5, $p < 0.05$) in RFP- and MYC-transduced 16D cells maintained with or without 10 μM enzalutamide for 7 days.

(I) Cell-cycle analysis to quantify the relative sensitivity of RFP- and Myc-transduced 16D cells to 10 μM enzalutamide. Data represent the mean ± SEM of four technical replicates from a representative experiment (n = 2).

(J) GSEA of Hallmark_Myc_targets in 21 mCRPC tumors before and after enzalutamide treatment from the Westbrook et al.[41] dataset. The p values were calculated from an unpaired t test with Welch's correction; $^{**}p < 0.01$, $^{***}p < 0.001$, $^{****}p < 0.0001$; n.s., not significant, $p \geq 0.05$.

both play key roles in mediating AR-inhibition-induced metabolic rewiring and dictating vulnerability to metabolic inhibitors.

Our study identifies altered mitochondrial dynamics following AR inhibition. Mitochondrial elongation has been shown to protect cells during nutrient starvation[26,45] and enable survival after chemotherapy.[46,47] The functional impact of mitochondrial morphology on metabolic output has proven to be highly context dependent.[48–51] Future work is needed to understand how AR inhibition alters DRP1 phosphorylation and how the subsequent mitochondrial elongation influences other metabolic phenotypes.

Previous studies have demonstrated that MYC overexpression accelerates prostate cancer progression toward a metastatic, castration-resistant state by antagonizing the canonical AR transcriptional program.[52] MYC has also been shown to promote androgen-independent prostate cancer growth.[53] We show that reactivation of MYC rescues AR-inhibition-mediated reduction in glycolysis and phosphorylation of DRP1-S616. Future studies will be required to determine if MYCN (N-MYC) overexpression, which has been shown to promote lineage plasticity in prostate cancer,[54,55] has an effect on metabolism similar to that of MYC reactivation.

Consistent with prior studies, our results suggest that mitochondrial oxidative metabolism contributes to prostate cancer growth and survival. Our findings also suggest there may be a therapeutic window after AR inhibition to target mitochondrial metabolism. Tumor location must also be considered, as metabolic dependencies can differ based on site of implantation.[56] Trials to determine the efficacy of combined metformin treatment and AR blockade have been inconclusive.[57,58] Importantly, the concentration of metformin required to inhibit complex I activity *in vitro* (1 mM) is more than 10 times higher than the maximally achievable therapeutic concentration (70 μM) found in patients.[24,59] Metformin has been shown to reduce AR and cyclin D1 levels.[60,61] These effects may explain why naive 16D cells exhibit sensitivity to metformin, despite lacking sensitivity to IACS, which reduces mitochondrial respiration by greater than 95%. In addition, metformin has been shown to synergize with bicalutamide in mouse models by preventing AR-blockade-induced hyperinsulinemia.[62] Furthermore, IACS-010759 has recently been shown to have dose-limiting toxicities in patients.[63] Therefore, it will be critical to identify tumor-specific regulators of mitochondrial metabolism in order to target cancer cell growth and limit toxicity in patients.

Limitations of the study

In the present study, we demonstrate that AR inhibition results in reduced glycolysis, reduced glutaminolysis, and increased reliance on mitochondrial oxidative metabolism. While metabolic profiling was performed both *in vitro* and *in vivo*, the technical challenges of performing *in vivo* metabolic assays limited our capacity to fully define the *in vivo* metabolic response to AR inhibition. While our findings were relatively consistent across a range of AR$^+$ models, the heterogeneity of clinical prostate cancer is likely to increase the complexity of metabolic phenotypes and vulnerabilities. We evaluated metabolic gene expression before and after AR inhibition in four clinical datasets representative of localized and locally advanced or metastatic prostate cancer, but we lack sufficient clinical data to define treatment-induced metabolic changes in a larger cohort of advanced metastatic prostate cancer. Finally, we showed that MYC activity regulates DRP1 phosphorylation, but we were not able to define the precise mechanism by which S616 is phosphorylated in prostate cancer cells.

STAR★METHODS

Detailed methods are provided in the online version of this paper and include the following:

- KEY RESOURCES TABLE
- RESOURCE AVAILABILITY
  - Lead contact
  - Materials availability
  - Data and code availability
- EXPERIMENTAL MODEL AND SUBJECT DETAILS
  - Animal work
- METHOD DETAILS
  - *In vitro* metabolic profiling and 13C isotope tracing
  - *In vitro* metabolic profiling and 13C isotope tracing
  - Apoptosis analysis
  - *Bioenergetic* assays
  - Cell cycle *analysis*
  - Cell lines, *lentiviral* transductions, and cloning of knockdown vectors
  - ChIP *sequencing*
  - DNA methylation *analysis*
  - Immunohistochemistry
  - *In vivo* metabolomics
  - Neutral lipid analysis
  - Organoid culture
  - RNA sequencing
  - Reiter clinical trial: patient cohort
  - Reiter clinical trial: tumor RNA sequencing
  - Clinical data: RNA data processing
  - Clinical data: Differential abundance and gene set enrichment
  - Clinical data: Statistical analysis
  - Visualization of mitochondria and lipid droplets
  - Western blot
- QUANTIFICATION AND STATISTICAL ANALYSIS
  - Ki67 immunohistochemistry quantification
  - Metabolomics analysis
  - Mitochondrial content and morphology, and lipid droplets
  - RNA sequencing analysis
  - Western blot quantification

SUPPLEMENTAL INFORMATION

Supplemental information can be found online at https://doi.org/10.1016/j.celrep.2023.113221.

ACKNOWLEDGMENTS

P.D.C. and J.M.G. acknowledge the support of the Ruth L. Kirschstein National Research Service Award (GM007185) and the UCLA Eli and Edythe Broad Center of Regenerative Medicine and Stem Cell Research Training Program. P.D.C. is also supported by NIH grants TL1 DK132768 and U2C DK129496. A.E.J. is supported by a UCLA Tumor Cell Biology Training grant (NIHT32CA009056). A.S.G. is supported by the National Cancer

Institute of the National Institutes of Health under award no. R01CA237191. The content is solely the responsibility of the authors and does not necessarily represent the official views of the National Institutes of Health. A.M.L.D. is supported by an NCI/NIH supplement related to R01CA237191. A.S.G. is also supported by Department of Defense PCRP award HT94252310379, American Cancer Society award RSG-17-068-01-TBG, a UCLA Eli and Edythe Broad Center of Regenerative Medicine and Stem Cell Research Rose Hills Foundation Innovator grant, the UCLA Jonsson Comprehensive Cancer Center and Eli and Edythe Broad Center of Regenerative Medicine and Stem Cell Research Ablon Scholars Program, the National Center for Advancing Translational Sciences UCLA CTSI grant UL1TR001881, Stop Cancer, and the UCLA Institute of Urologic Oncology. A.S.G., A.S.D., O.S.S., R.E.R., M.B.R., and P.C.B are supported by the UCLA Prostate Cancer Specialized Programs of Research Excellence (SPORE) (NCIP50 CA092131). M.C.H. is supported by the US Department of Defense Prostate Cancer Research Program (W81XWH-20-1-0111 and W81XWH-21-1-0229) and grant 2021184 from the Doris Duke Charitable Foundation. N.M. Navone is supported by NCIU01 CA224044-03. We acknowledge the support of the Hutton FamilyFoundation. We thank the UCLA Technology Center for Genomics & Bioinformatics, UCLA Metabolomics Center, and UCLA MCDB/BSCRC Microscopy Core. The UCLA Integrated Technologies Core is supported by CURE/P30 DK041301. The NIH Common Fund's National Metabolomics Data Repository (NMDR) website, the Metabolomics Workbench, is supported by NIH grants U2C-DK119886 and OT2-OD030544. We thank Michaela Veliova, Thomas Graeber, Linsey Stiles, Brigitte Gomperts, and other collaborators who provided intellectual support and critical feedback during the course of this project.

AUTHOR CONTRIBUTIONS

P.D.C., J.M.G., A.E.J., N.M. Nunley, T.H., A.M.L.D., M.J.B., J.A.D., and K.Y.H. conducted the experiments. P.D.C., J.M.G., A.E.J., A.S.D., and A.S.G. designed the experiments and wrote and edited the manuscript. R.R.H. and H.Y. performed immunohistochemistry and provided pathology expertise and wrote the related methods section. A.P. and O.S.S. performed mitochondrial morphology quantification, provided metabolism expertise, and wrote the related methods section. R.A. and P.C.B. analyzed clinical datasets and wrote the related methods section. J.-Y.L. and M.C.H. performed the DNA methylation analysis and wrote the related methods section. N.M. and H.R.C. performed mass spectrometry on *in vivo* tumor metabolites, provided metabolism expertise, and wrote the related methods section. N.M. Navone provided PDX models. A.Z. provided ChIP-sequencing data and key cell lines and wrote the related methods section. M.B.R. and R.E.R. provided clinical RNA-sequencing data. A.S.G. procured funding and supervised the experiments.

DECLARATION OF INTERESTS

P.C.B. sits on the scientific advisory boards of Sage Bionetworks, BioSymetrics, Inc., and Intersect Diagnostics, Inc.

INCLUSION AND DIVERSITY

One or more of the authors of this paper self-identifies as an underrepresented ethnic minority in their field of research or within their geographical location. One or more of the authors of this paper self-identifies as a gender minority in their field of research. One or more of the authors of this paper self-identifies as a member of the LGBTQIA+ community. One or more of the authors of this paper received support from a program designed to increase minority representation in their field of research.

Received: February 13, 2023
Revised: August 17, 2023
Accepted: September 20, 2023

REFERENCES

1. Siegel, R.L., Miller, K.D., Wagle, N.S., and Jemal, A. (2023). Cancer statistics, 2023. CA A Cancer J. Clin. *73*, 17–48. https://doi.org/10.3322/caac.21763.
2. Sayegh, N., Swami, U., and Agarwal, N. (2022). Recent Advances in the Management of Metastatic Prostate Cancer. JCO Oncol. Pract. *18*, 45–55. https://doi.org/10.1200/OP.21.00206.
3. Nakazawa, M., Paller, C., and Kyprianou, N. (2017). Mechanisms of Therapeutic Resistance in Prostate Cancer. Curr. Oncol. Rep. *19*, 13. https://doi.org/10.1007/s11912-017-0568-7.
4. Tran, C., Ouk, S., Clegg, N.J., Chen, Y., Watson, P.A., Arora, V., Wongvipat, J., Smith-Jones, P.M., Yoo, D., Kwon, A., et al. (2009). Development of a second-generation antiandrogen for treatment of advanced prostate cancer. Science *324*, 787–790. https://doi.org/10.1126/science.1168175.
5. Beer, T.M., Armstrong, A.J., Rathkopf, D.E., Loriot, Y., Sternberg, C.N., Higano, C.S., Iversen, P., Bhattacharya, S., Carles, J., Chowdhury, S., et al. (2014). Enzalutamide in metastatic prostate cancer before chemotherapy. N. Engl. J. Med. *371*, 424–433. https://doi.org/10.1056/NEJMoa1405095.
6. Alumkal, J.J., Sun, D., Lu, E., Beer, T.M., Thomas, G.V., Latour, E., Aggarwal, R., Cetnar, J., Ryan, C.J., Tabatabaei, S., et al. (2020). Transcriptional profiling identifies an androgen receptor activity-low, stemness program associated with enzalutamide resistance. Proc. Natl. Acad. Sci. USA *117*, 12315–12323. https://doi.org/10.1073/pnas.1922207117.
7. Schmidt, K.T., Huitema, A.D.R., Chau, C.H., and Figg, W.D. (2021). Resistance to second-generation androgen receptor antagonists in prostate cancer. Nat. Rev. Urol. *18*, 209–226. https://doi.org/10.1038/s41585-021-00438-4.
8. Faubert, B., Solmonson, A., and DeBerardinis, R.J. (2020). Metabolic reprogramming and cancer progression. Science *368*, eaaw5473. https://doi.org/10.1126/science.aaw5473.
9. Bader, D.A., Hartig, S.M., Putluri, V., Foley, C., Hamilton, M.P., Smith, E.A., Saha, P.K., Panigrahi, A., Walker, C., Zong, L., et al. (2019). Mitochondrial pyruvate import is a metabolic vulnerability in androgen receptor-driven prostate cancer. Nat. Metab. *1*, 70–85. https://doi.org/10.1038/s42255-018-0002-y.
10. Choi, S.Y.C., Ettinger, S.L., Lin, D., Xue, H., Ci, X., Nabavi, N., Bell, R.H., Mo, F., Gout, P.W., Fleshner, N.E., et al. (2018). Targeting MCT4 to reduce lactic acid secretion and glycolysis for treatment of neuroendocrine prostate cancer. Cancer Med. *7*, 3385–3392. https://doi.org/10.1002/cam4.1587.
11. Lin, C., Blessing, A.M., Pulliam, T.L., Shi, Y., Wilkenfeld, S.R., Han, J.J., Murray, M.M., Pham, A.H., Duong, K., Brun, S.N., et al. (2021). Inhibition of CAMKK2 impairs autophagy and castration-resistant prostate cancer via suppression of AMPK-ULK1 signaling. Oncogene *40*, 1690–1705. https://doi.org/10.1038/s41388-021-01658-z.
12. Massie, C.E., Lynch, A., Ramos-Montoya, A., Boren, J., Stark, R., Fazli, L., Warren, A., Scott, H., Madhu, B., Sharma, N., et al. (2011). The androgen receptor fuels prostate cancer by regulating central metabolism and biosynthesis. EMBO J. *30*, 2719–2733. https://doi.org/10.1038/emboj.2011.158.
13. Priolo, C., Pyne, S., Rose, J., Regan, E.R., Zadra, G., Photopoulos, C., Cacciatore, S., Schultz, D., Scaglia, N., McDunn, J., et al. (2014). AKT1 and MYC induce distinctive metabolic fingerprints in human prostate cancer. Cancer Res. *74*, 7198–7204. https://doi.org/10.1158/0008-5472.CAN-14-1490.
14. Reina-Campos, M., Linares, J.F., Duran, A., Cordes, T., L'Hermitte, A., Badur, M.G., Bhangoo, M.S., Thorson, P.K., Richards, A., Rooslid, T., et al. (2019). Increased Serine and One-Carbon Pathway Metabolism by PKClambda/iota Deficiency Promotes Neuroendocrine Prostate Cancer. Cancer Cell *35*, 385–400.e9. https://doi.org/10.1016/j.ccell.2019.01.018.
15. Xu, L., Yin, Y., Li, Y., Chen, X., Chang, Y., Zhang, H., Liu, J., Beasley, J., McCaw, P., Zhang, H., et al. (2021). A glutaminase isoform switch drives therapeutic resistance and disease progression of prostate cancer.

Proc. Natl. Acad. Sci. USA *118*, e2012748118. https://doi.org/10.1073/pnas.2012748118.

16. Zadra, G., Ribeiro, C.F., Chetta, P., Ho, Y., Cacciatore, S., Gao, X., Syamala, S., Bango, C., Photopoulos, C., Huang, Y., et al. (2019). Inhibition of de novo lipogenesis targets androgen receptor signaling in castration-resistant prostate cancer. Proc. Natl. Acad. Sci. USA *116*, 631–640. https://doi.org/10.1073/pnas.1808834116.
17. Basu, H.S., Wilganowski, N., Robertson, S., Reuben, J.M., Cohen, E.N., Zurita, A., Ramachandran, S., Xiao, L.C., Titus, M., and Wilding, G. (2021). Prostate cancer cells survive anti-androgen and mitochondrial metabolic inhibitors by modulating glycolysis and mitochondrial metabolic activities. Prostate *81*, 799–811. https://doi.org/10.1002/pros.24146.
18. Rajan, P., Sudbery, I.M., Villasevil, M.E.M., Mui, E., Fleming, J., Davis, M., Ahmad, I., Edwards, J., Sansom, O.J., Sims, D., et al. (2014). Next-generation sequencing of advanced prostate cancer treated with androgen-deprivation therapy. Eur. Urol. *66*, 32–39. https://doi.org/10.1016/j.eururo.2013.08.011.
19. Bishop, J.L., Thaper, D., Vahid, S., Davies, A., Ketola, K., Kuruma, H., Jama, R., Nip, K.M., Angeles, A., Johnson, F., et al. (2017). The Master Neural Transcription Factor BRN2 Is an Androgen Receptor-Suppressed Driver of Neuroendocrine Differentiation in Prostate Cancer. Cancer Discov. *7*, 54–71. https://doi.org/10.1158/2159-8290.CD-15-1263.
20. Divakaruni, A.S., Paradyse, A., Ferrick, D.A., Murphy, A.N., and Jastroch, M. (2014). Analysis and interpretation of microplate-based oxygen consumption and pH data. Methods Enzymol. *547*, 309–354. https://doi.org/10.1016/B978-0-12-801415-8.00016-3.
21. Jones, A.E., Sheng, L., Acevedo, A., Veliova, M., Shirihai, O.S., Stiles, L., and Divakaruni, A.S. (2021). Forces, fluxes, and fuels: tracking mitochondrial metabolism by integrating measurements of membrane potential, respiration, and metabolites. Am. J. Physiol. Cell Physiol. *320*, C80–C91. https://doi.org/10.1152/ajpcell.00235.2020.
22. Desousa, B.R., Kim, K.K., Jones, A.E., Ball, A.B., Hsieh, W.Y., Swain, P., Morrow, D.H., Brownstein, A.J., Ferrick, D.A., Shirihai, O.S., et al. (2023). Calculation of ATP production rates using the Seahorse XF Analyzer. EMBO Rep.e56380 https://doi.org/10.15252/embr.202256380.
23. Molina, J.R., Sun, Y., Protopopova, M., Gera, S., Bandi, M., Bristow, C., McAfoos, T., Morlacchi, P., Ackroyd, J., Agip, A.N.A., et al. (2018). An inhibitor of oxidative phosphorylation exploits cancer vulnerability. Nat. Med. *24*, 1036–1046. https://doi.org/10.1038/s41591-018-0052-4.
24. He, L., and Wondisford, F.E. (2015). Metformin action: concentrations matter. Cell Metab. *21*, 159–162. https://doi.org/10.1016/j.cmet.2015.01.003.
25. Palanisamy, N., Yang, J., Shepherd, P.D.A., Li-Ning-Tapia, E.M., Labanca, E., Manyam, G.C., Ravoori, M.K., Kundra, V., Araujo, J.C., Efstathiou, E., et al. (2020). The MD Anderson Prostate Cancer Patient-derived Xenograft Series (MDA PCa PDX) Captures the Molecular Landscape of Prostate Cancer and Facilitates Marker-driven Therapy Development. Clin. Cancer Res. *26*, 4933–4946. https://doi.org/10.1158/1078-0432.CCR-20-0479.
26. Gomes, L.C., Di Benedetto, G., and Scorrano, L. (2011). During autophagy mitochondria elongate, are spared from degradation and sustain cell viability. Nat. Cell Biol. *13*, 589–598. https://doi.org/10.1038/ncb2220.
27. Petcherski, A., Trudeau, K.M., Wolf, D.M., Segawa, M., Lee, J., Taddeo, E.P., Deeney, J.T., and Liesa, M. (2018). Elamipretide Promotes Mitophagosome Formation and Prevents Its Reduction Induced by Nutrient Excess in INS1 beta-cells. J. Mol. Biol. *430*, 4823–4833. https://doi.org/10.1016/j.jmb.2018.10.020.
28. Mishra, P., and Chan, D.C. (2016). Metabolic regulation of mitochondrial dynamics. J. Cell Biol. *212*, 379–387. https://doi.org/10.1083/jcb.201511036.
29. Lee, Y.G., Nam, Y., Shin, K.J., Yoon, S., Park, W.S., Joung, J.Y., Seo, J.K., Jang, J., Lee, S., Nam, D., et al. (2020). Androgen-induced expression of DRP1 regulates mitochondrial metabolic reprogramming in prostate cancer. Cancer Lett. *471*, 72–87. https://doi.org/10.1016/j.canlet.2019.12.017.
30. Davies, A., Nouruzi, S., Ganguli, D., Namekawa, T., Thaper, D., Linder, S., Karaoğlanoğlu, F., Omur, M.E., Kim, S., Kobelev, M., et al. (2021). An androgen receptor switch underlies lineage infidelity in treatment-resistant prostate cancer. Nat. Cell Biol. *23*, 1023–1034. https://doi.org/10.1038/s41556-021-00743-5.
31. Rambold, A.S., Kostelecky, B., Elia, N., and Lippincott-Schwartz, J. (2011). Tubular network formation protects mitochondria from autophagosomal degradation during nutrient starvation. Proc. Natl. Acad. Sci. USA *108*, 10190–10195. https://doi.org/10.1073/pnas.1107402108.
32. Long, X., Hou, H., Wang, X., Liu, S., Diao, T., Lai, S., Hu, M., Zhang, S., Liu, M., and Zhang, H. (2020). Immune signature driven by ADT-induced immune microenvironment remodeling in prostate cancer is correlated with recurrence-free survival and immune infiltration. Cell Death Dis. *11*, 779. https://doi.org/10.1038/s41419-020-02973-1.
33. Wilkinson, S., Ye, H., Karzai, F., Harmon, S.A., Terrigino, N.T., VanderWeele, D.J., Bright, J.R., Atway, R., Trostel, S.Y., Carrabba, N.V., et al. (2021). Nascent Prostate Cancer Heterogeneity Drives Evolution and Resistance to Intense Hormonal Therapy. Eur. Urol. *80*, 746–757. https://doi.org/10.1016/j.eururo.2021.03.009.
34. Stine, Z.E., Walton, Z.E., Altman, B.J., Hsieh, A.L., and Dang, C.V. (2015). MYC, Metabolism, and Cancer. Cancer Discov. *5*, 1024–1039. https://doi.org/10.1158/2159-8290.CD-15-0507.
35. Gao, L., Schwartzman, J., Gibbs, A., Lisac, R., Kleinschmidt, R., Wilmot, B., Bottomly, D., Coleman, I., Nelson, P., McWeeney, S., and Alumkal, J. (2013). Androgen receptor promotes ligand-independent prostate cancer progression through c-Myc upregulation. PLoS One *8*, e63563. https://doi.org/10.1371/journal.pone.0063563.
36. Akamatsu, S., Wyatt, A.W., Lin, D., Lysakowski, S., Zhang, F., Kim, S., Tse, C., Wang, K., Mo, F., Haegert, A., et al. (2015). The Placental Gene PEG10 Promotes Progression of Neuroendocrine Prostate Cancer. Cell Rep. *12*, 922–936. https://doi.org/10.1016/j.celrep.2015.07.012.
37. Ku, S.Y., Rosario, S., Wang, Y., Mu, P., Seshadri, M., Goodrich, Z.W., Goodrich, M.M., Labbé, D.P., Gomez, E.C., Wang, J., et al. (2017). Rb1 and Trp53 cooperate to suppress prostate cancer lineage plasticity, metastasis, and antiandrogen resistance. Science *355*, 78–83. https://doi.org/10.1126/science.aah4199.
38. Guo, H., Ci, X., Ahmed, M., Hua, J.T., Soares, F., Lin, D., Puca, L., Vosoughi, A., Xue, H., Li, E., et al. (2019). ONECUT2 is a driver of neuroendocrine prostate cancer. Nat. Commun. *10*, 278. https://doi.org/10.1038/s41467-018-08133-6.
39. Aggarwal, R., Huang, J., Alumkal, J.J., Zhang, L., Feng, F.Y., Thomas, G.V., Weinstein, A.S., Friedl, V., Zhang, C., Witte, O.N., et al. (2018). Clinical and Genomic Characterization of Treatment-Emergent Small-Cell Neuroendocrine Prostate Cancer: A Multi-institutional Prospective Study. J. Clin. Oncol. *36*, 2492–2503. https://doi.org/10.1200/JCO.2017.77.6880.
40. Beltran, H., Prandi, D., Mosquera, J.M., Benelli, M., Puca, L., Cyrta, J., Marotz, C., Giannopoulou, E., Chakravarthi, B.V.S.K., Varambally, S., et al. (2016). Divergent clonal evolution of castration-resistant neuroendocrine prostate cancer. Nat. Med. *22*, 298–305. https://doi.org/10.1038/nm.4045.
41. Westbrook, T.C., Guan, X., Rodansky, E., Flores, D., Liu, C.J., Udager, A.M., Patel, R.A., Haffner, M.C., Hu, Y.M., Sun, D., et al. (2022). Transcriptional profiling of matched patient biopsies clarifies molecular determinants of enzalutamide-induced lineage plasticity. Nat. Commun. *13*, 5345. https://doi.org/10.1038/s41467-022-32701-6.
42. Mukhopadhyay, S., Goswami, D., Adiseshaiah, P.P., Burgan, W., Yi, M., Guerin, T.M., Kozlov, S.V., Nissley, D.V., and McCormick, F. (2020). Undermining Glutaminolysis Bolsters Chemotherapy While NRF2 Promotes Chemoresistance in KRAS-Driven Pancreatic Cancers. Cancer Res. *80*, 1630–1643. https://doi.org/10.1158/0008-5472.CAN-19-1363.
43. Evans, K.W., Yuca, E., Scott, S.S., Zhao, M., Paez Arango, N., Cruz Pico, C.X., Saridogan, T., Shariati, M., Class, C.A., Bristow, C.A., et al. (2021). Oxidative Phosphorylation Is a Metabolic Vulnerability

in Chemotherapy-Resistant Triple-Negative Breast Cancer. Cancer Res. *81*, 5572–5581. https://doi.org/10.1158/0008-5472.CAN-20-3242.

44. Zhou, W., Yao, Y., Scott, A.J., Wilder-Romans, K., Dresser, J.J., Werner, C.K., Sun, H., Pratt, D., Sajjakulnukit, P., Zhao, S.G., et al. (2020). Purine metabolism regulates DNA repair and therapy resistance in glioblastoma. Nat. Commun. *11*, 3811. https://doi.org/10.1038/s41467-020-17512-x.
45. Li, J., Huang, Q., Long, X., Guo, X., Sun, X., Jin, X., Li, Z., Ren, T., Yuan, P., Huang, X., et al. (2017). Mitochondrial elongation-mediated glucose metabolism reprogramming is essential for tumour cell survival during energy stress. Oncogene *36*, 4901–4912. https://doi.org/10.1038/onc.2017.98.
46. Baek, M.L., Lee, J., Pendleton, K.E., Berner, M.J., Goff, E.B., Tan, L., Martinez, S.A., Wang, T., Meyer, M.D., Lim, B., et al. (2022). Mitochondrial structure and function adaptation in residual triple negative breast cancer cells surviving chemotherapy treatment. Preprint at bioRxiv. https://doi.org/10.1101/2022.02.25.481996.
47. Kong, B., Tsuyoshi, H., Orisaka, M., Shieh, D.B., Yoshida, Y., and Tsang, B.K. (2015). Mitochondrial dynamics regulating chemoresistance in gynecological cancers. Ann. N. Y. Acad. Sci. *1350*, 1–16. https://doi.org/10.1111/nyas.12883.
48. Courtois, S., de Luxán-Delgado, B., Penin-Peyta, L., Royo-García, A., Parejo-Alonso, B., Jagust, P., Alcalá, S., Rubiolo, J.A., Sánchez, L., Sainz, B., Jr., et al. (2021). Inhibition of Mitochondrial Dynamics Preferentially Targets Pancreatic Cancer Cells with Enhanced Tumorigenic and Invasive Potential. Cancers *13*, 698. https://doi.org/10.3390/cancers13040698.
49. Yu, M., Nguyen, N.D., Huang, Y., Lin, D., Fujimoto, T.N., Molkentine, J.M., Deorukhkar, A., Kang, Y., San Lucas, F.A., Fernandes, C.J., et al. (2019). Mitochondrial fusion exploits a therapeutic vulnerability of pancreatic cancer. JCI Insight *5*, e126915. https://doi.org/10.1172/jci.insight.126915.
50. Hagenbuchner, J., Kuznetsov, A.V., Obexer, P., and Ausserlechner, M.J. (2013). BIRC5/Survivin enhances aerobic glycolysis and drug resistance by altered regulation of the mitochondrial fusion/fission machinery. Oncogene *32*, 4748–4757. https://doi.org/10.1038/onc.2012.500.
51. Kumar, R., Bhat, T.A., Walsh, E.M., Chaudhary, A.K., O'Malley, J., Rhim, J.S., Wang, J., Morrison, C.D., Attwood, K., Bshara, W., et al. (2019). Cytochrome c Deficiency Confers Apoptosome and Mitochondrial Dysfunction in African-American Men with Prostate Cancer. Cancer Res. *79*, 1353–1368. https://doi.org/10.1158/0008-5472.CAN-18-2383.
52. Qiu, X., Boufaied, N., Hallal, T., Feit, A., de Polo, A., Luoma, A.M., Alahmadi, W., Larocque, J., Zadra, G., Xie, Y., et al. (2022). MYC drives aggressive prostate cancer by disrupting transcriptional pause release at androgen receptor targets. Nat. Commun. *13*, 2559. https://doi.org/10.1038/s41467-022-30257-z.
53. Bernard, D., Pourtier-Manzanedo, A., Gil, J., and Beach, D.H. (2003). Myc confers androgen-independent prostate cancer cell growth. J. Clin. Invest. *112*, 1724–1731. https://doi.org/10.1172/JCI19035.
54. Berger, A., Brady, N.J., Bareja, R., Robinson, B., Conteduca, V., Augello, M.A., Puca, L., Ahmed, A., Dardenne, E., Lu, X., et al. (2019). N-Myc-mediated epigenetic reprogramming drives lineage plasticity in advanced prostate cancer. J. Clin. Invest. *129*, 3924–3940. https://doi.org/10.1172/JCI127961.
55. Dardenne, E., Beltran, H., Benelli, M., Gayvert, K., Berger, A., Puca, L., Cyrta, J., Sboner, A., Noorzad, Z., MacDonald, T., et al. (2016). N-Myc Induces an EZH2-Mediated Transcriptional Program Driving Neuroendocrine Prostate Cancer. Cancer Cell *30*, 563–577. https://doi.org/10.1016/j.ccell.2016.09.005.
56. Mossa, F., Robesti, D., Sumankalai, R., Corey, E., Titus, M., Kang, Y., Zhang, J., Briganti, A., Montorsi, F., Vellano, C.P., et al. (2023). Subtype and Site Specific-Induced Metabolic Vulnerabilities in Prostate Cancer. Mol. Cancer Res. *21*, 51–61. https://doi.org/10.1158/1541-7786.MCR-22-0250.
57. Nobes, J.P., Langley, S.E.M., Klopper, T., Russell-Jones, D., and Laing, R.W. (2012). A prospective, randomized pilot study evaluating the effects of metformin and lifestyle intervention on patients with prostate cancer receiving androgen deprivation therapy. BJU Int. *109*, 1495–1502. https://doi.org/10.1111/j.1464-410X.2011.10555.x.
58. Ahn, H.K., Lee, Y.H., and Koo, K.C. (2020). Current Status and Application of Metformin for Prostate Cancer: A Comprehensive Review. Int. J. Mol. Sci. *21*, 8540. https://doi.org/10.3390/ijms21228540.
59. Hess, C., Unger, M., Madea, B., Stratmann, B., and Tschoepe, D. (2018). Range of therapeutic metformin concentrations in clinical blood samples and comparison to a forensic case with death due to lactic acidosis. Forensic Sci. Int. *286*, 106–112. https://doi.org/10.1016/j.forsciint.2018.03.003.
60. Demir, U., Koehler, A., Schneider, R., Schweiger, S., and Klocker, H. (2014). Metformin anti-tumor effect via disruption of the MID1 translational regulator complex and AR downregulation in prostate cancer cells. BMC Cancer *14*, 52. https://doi.org/10.1186/1471-2407-14-52.
61. Ben Sahra, I., Laurent, K., Loubat, A., Giorgetti-Peraldi, S., Colosetti, P., Auberger, P., Tanti, J.F., Le Marchand-Brustel, Y., and Bost, F. (2008). The antidiabetic drug metformin exerts an antitumoral effect in vitro and in vivo through a decrease of cyclin D1 level. Oncogene *27*, 3576–3586. https://doi.org/10.1038/sj.onc.1211024.
62. Colquhoun, A.J., Venier, N.A., Vandersluis, A.D., Besla, R., Sugar, L.M., Kiss, A., Fleshner, N.E., Pollak, M., Klotz, L.H., and Venkateswaran, V. (2012). Metformin enhances the antiproliferative and apoptotic effect of bicalutamide in prostate cancer. Prostate Cancer Prostatic Dis. *15*, 346–352. https://doi.org/10.1038/pcan.2012.16.
63. Yap, T.A., Daver, N., Mahendra, M., Zhang, J., Kamiya-Matsuoka, C., Meric-Bernstam, F., Kantarjian, H.M., Ravandi, F., Collins, M.E., Francesco, M.E.D., et al. (2023). Complex I inhibitor of oxidative phosphorylation in advanced solid tumors and acute myeloid leukemia: phase I trials. Nat. Med. *29*, 115–126. https://doi.org/10.1038/s41591-022-02103-8.
64. Stoyanova, T., Cooper, A.R., Drake, J.M., Liu, X., Armstrong, A.J., Pienta, K.J., Zhang, H., Kohn, D.B., Huang, J., Witte, O.N., and Goldstein, A.S. (2013). Prostate cancer originating in basal cells progresses to adenocarcinoma propagated by luminal-like cells. Proc. Natl. Acad. Sci. USA *110*, 20111–20116. https://doi.org/10.1073/pnas.1320565110.
65. Klein, K.A., Reiter, R.E., Redula, J., Moradi, H., Zhu, X.L., Brothman, A.R., Lamb, D.J., Marcelli, M., Belldegrun, A., Witte, O.N., and Sawyers, C.L. (1997). Progression of metastatic human prostate cancer to androgen independence in immunodeficient SCID mice. Nat. Med. *3*, 402–408. https://doi.org/10.1038/nm0497-402.
66. Godar, S., Ince, T.A., Bell, G.W., Feldser, D., Donaher, J.L., Bergh, J., Liu, A., Miu, K., Watnick, R.S., Reinhardt, F., et al. (2008). Growth-inhibitory and tumor- suppressive functions of p53 depend on its repression of CD44 expression. Cell *134*, 62–73. https://doi.org/10.1016/j.cell.2008.06.006.
67. Ramírez, F., Ryan, D.P., Grüning, B., Bhardwaj, V., Kilpert, F., Richter, A.S., Heyne, S., Dündar, F., and Manke, T. (2016). deepTools2: a next generation web server for deep-sequencing data analysis. Nucleic Acids Res. *44*, W160–W165. https://doi.org/10.1093/nar/gkw257.
68. Krueger, F., and Andrews, S.R. (2011). Bismark: a flexible aligner and methylation caller for Bisulfite-Seq applications. Bioinformatics *27*, 1571–1572. https://doi.org/10.1093/bioinformatics/btr167.
69. Pang, Z., Chong, J., Zhou, G., de Lima Morais, D.A., Chang, L., Barrette, M., Gauthier, C., Jacques, P.É., Li, S., and Xia, J. (2021). MetaboAnalyst 5.0: narrowing the gap between raw spectra and functional insights. Nucleic Acids Res. *49*, W388–W396. https://doi.org/10.1093/nar/gkab382.
70. Kamentsky, L., Jones, T.R., Fraser, A., Bray, M.A., Logan, D.J., Madden, K.L., Ljosa, V., Rueden, C., Eliceiri, K.W., and Carpenter, A.E. (2011). Improved structure, function and compatibility for CellProfiler: modular high-throughput image analysis software. Bioinformatics *27*, 1179–1180. https://doi.org/10.1093/bioinformatics/btr095.
71. Huang, D.W., Sherman, B.T., and Lempicki, R.A. (2009). Systematic and integrative analysis of large gene lists using DAVID bioinformatics resources. Nat. Protoc. *4*, 44–57. https://doi.org/10.1038/nprot.2008.211.

72. Huang, D.W., Sherman, B.T., and Lempicki, R.A. (2009). Bioinformatics enrichment tools: paths toward the comprehensive functional analysis of large gene lists. Nucleic Acids Res. *37*, 1–13. https://doi.org/10.1093/nar/gkn923.

73. Subramanian, A., Tamayo, P., Mootha, V.K., Mukherjee, S., Ebert, B.L., Gillette, M.A., Paulovich, A., Pomeroy, S.L., Golub, T.R., Lander, E.S., and Mesirov, J.P. (2005). Gene set enrichment analysis: a knowledge-based approach for interpreting genome-wide expression profiles. Proc. Natl. Acad. Sci. USA *102*, 15545–15550. https://doi.org/10.1073/pnas.0506580102.

74. Mootha, V.K., Lindgren, C.M., Eriksson, K.F., Subramanian, A., Sihag, S., Lehar, J., Puigserver, P., Carlsson, E., Ridderstråle, M., Laurila, E., et al. (2003). PGC-1alpha-responsive genes involved in oxidative phosphorylation are coordinately downregulated in human diabetes. Nat. Genet. *34*, 267–273. https://doi.org/10.1038/ng1180.

75. Dobin, A., Davis, C.A., Schlesinger, F., Drenkow, J., Zaleski, C., Jha, S., Batut, P., Chaisson, M., and Gingeras, T.R. (2013). STAR: ultrafast universal RNA-seq aligner. Bioinformatics *29*, 15–21. https://doi.org/10.1093/bioinformatics/bts635.

76. Cordes, T., and Metallo, C.M. (2019). Quantifying Intermediary Metabolism and Lipogenesis in Cultured Mammalian Cells Using Stable Isotope Tracing and Mass Spectrometry. Methods Mol. Biol. *1978*, 219–241. https://doi.org/10.1007/978-1-4939-9236-2_14.

77. Trefely, S., Ashwell, P., and Snyder, N.W. (2016). FluxFix: automatic isotopologue normalization for metabolic tracer analysis. BMC Bioinf. *17*, 485. https://doi.org/10.1186/s12859-016-1360-7.

78. Desousa, B.R., Kim, K.K.O., Hsieh, W.Y., Jones, A.E., Swain, P., Morrow, D.H., Ferrick, D.A., Shirihai, O.S., Neilson, A., Nathanson, D.A., et al. (2022). Calculating ATP production rates from oxidative phosphorylation and glycolysis during cell activation. Preprint at bioRxiv. https://doi.org/10.1101/2022.04.16.488523.

79. Zhang, A., Zhao, J.C., Kim, J., Fong, K.W., Yang, Y.A., Chakravarti, D., Mo, Y.Y., and Yu, J. (2015). LncRNA HOTAIR Enhances the Androgen-Receptor-Mediated Transcriptional Program and Drives Castration-Resistant Prostate Cancer. Cell Rep. *13*, 209–221. https://doi.org/10.1016/j.celrep.2015.08.069.

80. Robinson, J.T., Thorvaldsdóttir, H., Winckler, W., Guttman, M., Lander, E.S., Getz, G., and Mesirov, J.P. (2011). Integrative genomics viewer. Nat. Biotechnol. *29*, 24–26. https://doi.org/10.1038/nbt.1754.

81. Yegnasubramanian, S., Lin, X., Haffner, M.C., DeMarzo, A.M., and Nelson, W.G. (2006). Combination of methylated-DNA precipitation and methylation-sensitive restriction enzymes (COMPARE-MS) for the rapid, sensitive and quantitative detection of DNA methylation. Nucleic Acids Res. *34*, e19. https://doi.org/10.1093/nar/gnj022.

82. Chambers, M.C., Maclean, B., Burke, R., Amodei, D., Ruderman, D.L., Neumann, S., Gatto, L., Fischer, B., Pratt, B., Egertson, J., et al. (2012). A cross-platform toolkit for mass spectrometry and proteomics. Nat. Biotechnol. *30*, 918–920. https://doi.org/10.1038/nbt.2377.

83. Pluskal, T., Castillo, S., Villar-Briones, A., and Oresic, M. (2010). MZmine 2: modular framework for processing, visualizing, and analyzing mass spectrometry-based molecular profile data. BMC Bioinf. *11*, 395. https://doi.org/10.1186/1471-2105-11-395.

84. Myers, O.D., Sumner, S.J., Li, S., Barnes, S., and Du, X. (2017). One Step Forward for Reducing False Positive and False Negative Compound Identifications from Mass Spectrometry Metabolomics Data: New Algorithms for Constructing Extracted Ion Chromatograms and Detecting Chromatographic Peaks. Anal. Chem. *89*, 8696–8703. https://doi.org/10.1021/acs.analchem.7b00947.

85. Su, X., Lu, W., and Rabinowitz, J.D. (2017). Metabolite Spectral Accuracy on Orbitraps. Anal. Chem. *89*, 5940–5948. https://doi.org/10.1021/acs.analchem.7b00396.

86. Drost, J., Karthaus, W.R., Gao, D., Driehuis, E., Sawyers, C.L., Chen, Y., and Clevers, H. (2016). Organoid culture systems for prostate epithelial and cancer tissue. Nat. Protoc. *11*, 347–358. https://doi.org/10.1038/nprot.2016.006.

87. Chen, S., Zhou, Y., Chen, Y., and Gu, J. (2018). fastp: an ultra-fast all-in-one FASTQ preprocessor. Bioinformatics *34*, i884–i890. https://doi.org/10.1093/bioinformatics/bty560.

88. Ewels, P., Magnusson, M., Lundin, S., and Käller, M. (2016). MultiQC: summarize analysis results for multiple tools and samples in a single report. Bioinformatics *32*, 3047–3048. https://doi.org/10.1093/bioinformatics/btw354.

89. Bray, N.L., Pimentel, H., Melsted, P., and Pachter, L. (2016). Near-optimal probabilistic RNA-seq quantification. Nat. Biotechnol. *34*, 525–527. https://doi.org/10.1038/nbt.3519.

90. Love, M.I., Huber, W., and Anders, S. (2014). Moderated estimation of fold change and dispersion for RNA-seq data with DESeq2. Genome Biol. *15*, 550. https://doi.org/10.1186/s13059-014-0550-8.

91. P'ng, C., Green, J., Chong, L.C., Waggott, D., Prokopec, S.D., Shamsi, M., Nguyen, F., Mak, D.Y.F., Lam, F., Albuquerque, M.A., et al. (2019). BPG: Seamless, automated and interactive visualization of scientific data. BMC Bioinf. *20*, 42. https://doi.org/10.1186/s12859-019-2610-2.

92. Quigley, D.A., Dang, H.X., Zhao, S.G., Lloyd, P., Aggarwal, R., Alumkal, J.J., Foye, A., Kothari, V., Perry, M.D., Bailey, A.M., et al. (2018). Genomic Hallmarks and Structural Variation in Metastatic Prostate Cancer. Cell *174*, 758–769.e9. https://doi.org/10.1016/j.cell.2018.06.039.

93. Sud, M., Fahy, E., Cotter, D., Azam, K., Vadivelu, I., Burant, C., Edison, A., Fiehn, O., Higashi, R., Nair, K.S., et al. (2016). Metabolomics Workbench: An international repository for metabolomics data and metadata, metabolite standards, protocols, tutorials and training, and analysis tools. Nucleic Acids Res. *44*, D463–D470. https://doi.org/10.1093/nar/gkv1042.

STAR★METHODS

KEY RESOURCES TABLE

REAGENT or RESOURCE	SOURCE	IDENTIFIER
Antibodies		
Mouse anti-TUFM	Atlas Antibodies	Cat#AMAb90966; RRID: AB_2665738
Rabbit anti-phospho DRP1 (S616)	Cell Signaling	Cat#3455S; RRID: AB_2085352
Rabbit anti-DRP1	Cell Signaling	Cat#5391S; RRID: AB_11178938
Rabbit anti-PSA	Cell Signaling	Cat#5877; RRID: AB_2797624
Mouse anti-beta Actin	Thermo Fisher Scientific	Cat#MA1-140; RRID: AB_2536844
Mouse anti-NSE	Proteintech	Cat#66150-1-Ig; RRID: AB_2881546
Rabbit anti-Hexokinase II	Cell Signaling	Cat#2867, clone C64G5; RRID: AB_2232946
Mouse anti-Ki67	Dako	Cat#IR62661-2, clone MIB-1
Mouse anti-LDHA	Millipore Sigma	Cat#MABC150
Mouse anti-cMYC	Abcam	Cat#Ab32072; RRID: AB_731658
Rabbit anti-Androgen receptor	Cell Signaling	Cat#5153S; RRID: AB_10691711
Alexa Fluor 488-conugated goat anti-mouse IgG (H+L)	Thermo Fisher Scientific	Cat#A11001; RRID: AB_2534069
Alexa Fluor 647-conjugated goat anti-mouse IgG (H+L)	Thermo Fisher Scientific	Cat#A21235; RRID: AB_2535804
Alexa Fluor 647-conjugated goat anti-rabbit IgG (H+L)	Thermo Fisher Scientific	Cat#A21244; RRID: AB_2535812
HRP-conjugated goat anti-mouse IgG (H+L)	Thermo Fisher Scientific	Cat#31430; RRID: AB_228307
HRP-conjugated goat anti-rabbit IgG (H+L)	Thermo Fisher Scientific	Cat#31463; RRID: AB_228333
Bacterial and virus strains		
FU-MYC-CRW lentivirus	Stoyanova et al.[64]	N/A
DRP1-S616E lentivirus	VectorBuilder	VB211024-1031mfm
HK2-overexpression lentivirus	VectorBuilder	VB211024-1030wt
FU-shScramble-CRW lentivirus	This study	N/A
FU-shTP35-shRB1-CRW lentivirus	This study	N/A
Biological samples		
MDA-PCa 180-30 patient-derived xenograft	Palanisamy et al.[25]	N/A
MDA-PCa 173-2 patient-derived xenograft	Palanisamy et al.[25]	N/A
MDA-PCa 183-A patient-derived xenograft	Palanisamy et al.[25]	N/A
Chemicals, peptides, and recombinant proteins		
Trypsin-EDTA	GIBCO	Cat#25300-054
Poly-L-Lysine 0.01% (v/v)	Sigma	Cat#P4832
5α-Androstan-17β-ol-3-one (DHT)	Sigma	Cat#A8380-1G
Fetal bovine serum, charcoal stripped	Sigma	Cat#F6765
cOmplete protease inhibitor cocktail tablet	Roche	Cat#11697498001
Phosphatase inhibitor cocktail	Halt	Cat#78428

(*Continued on next page*)

Continued

REAGENT or RESOURCE	SOURCE	IDENTIFIER
Polybrene	Thermo Fisher Scientific	Cat#NC0663391
4’,6-diamidino-2-phenylindole (DAPI)	Thermo Fisher Scientific	Cat#D1306
Hoechst 33342	Thermo Fisher Scientific	Cat#62249
BODIPY 493/503	Thermo Fisher Scientific	Cat#D3922
U-13C_6-glucose	Cambridge Isotope Laboratories	Cat#CLM-1396-5
Enzalutamide	Selleck Chemicals	Cat#S1250
Apalutamide	Cayman Chemicals	Cat#17132
ARCC4	Tocris	Cat#7254
IACS-010759	ChemieTek	Cat#CT-IACS107
Metformin	Selleck Chemicals	Cat#S1950
Oligomycin	Sigma-Aldrich	Cat#75351
Carbonyl cyanide 4-(trifluoromethoxy) phenylhydrazone (FCCP)	Sigma-Aldrich	Cat#C2920
Rotenone	Sigma-Aldrich	Cat#R8875
Antimycin A	Sigma-Aldrich	Cat#A8674
Matrigel growth factor-reduced membrane matrix	Corning	Cat#CB-40230C
Matrigel membrane matrix	Corning	Cat#CB-40234
DNase I from bovine pancreas	Sigma-Aldrich	Cat#D5025
Dispase II	Gibco	Cat#17-105-041
Collagenase, Type I	Gibco	Cat#17-100-017
Y-27632 dihydrochloride (ROCK inhibitor)	Selleck Chemicals	Cat#S1049
B27 supplement, 50x	Life Technologies	Cat#17504-044
GlutaMAX, 100x	Life Technologies	Cat#35050-068
Nicotinamide	Sigma-Aldrich	Cat#N0636
N-acetyl-L-cysteine	Sigma-Aldrich	Cat#A9165
Normocin	Thermo Fisher Scientific	Cat#ant-nr-1
Recombinant human Noggin	PeproTech	Cat#120-10C
SB202190	Sigma-Aldrich	Cat#S7076
A83-01	Tocris Bioscience	Cat#2939
Human FGF-2	PeproTech	Cat#100-18B
Prostaglandin E2	Tocris Bioscience	Cat#2296
Human fibroblast growth factor (FGF)-10	PeproTech	Cat#100-26
Human epidermal growth factor (EGF)	PeproTech	Cat#AF-100-15
Critical commercial assays		
RNeasy Mini Kit	QIAGEN	Cat#74104
KAPA Stranded mRNA-Seq Kit	Roche	Cat#07962193001
Apoptosis Detection Kit (FITC Annexin V with 7-AAD)	Biolegend	Cat#640922
Click-iT^{TM} Plus EdU Alexa Fluor^{TM} 647 Flow Cytometry Assay Kit	Thermo Fisher Scientific	Cat#C10635
EZ DNA methylation kit	Zymo Research	Cat#D5001
Deposited data		
Raw and processed RNAseq (16D Enzalutamide timecourse)	This paper	GEO: GSE202885

(*Continued on next page*)

Continued

REAGENT or RESOURCE	SOURCE	IDENTIFIER
Raw and processed RNAseq (LNCaP Castration vs Enzalutamide)	This paper	GEO: GSE202755
Raw and processed RNAseq (16D Enzalutamide-treated cells transduced with cMyc, shRb1, shTp53, or shRb1_shTp53)	This paper	GEO: GSE202897
Raw and processed ChIP-seq (16D AR ChIP)	Davies et al.[30]	GEO: GSE138460
Raw metabolomics data (*In vivo* 16D vehicle and Enzalutamide tumors)	This paper	NMDR: ST002852
Raw metabolomics data (*In vitro* 16D vehicle and Enzalutamide replicate 1 for Figure 2I)	This paper	NMDR: ST002859
Raw metabolomics data (*In vitro* 16D vehicle and Enzalutamide replicates 2 and 3 for Figure 2I)	This paper	NMDR: ST002860
Raw metabolomics data (*In vitro* 16D validation of IACS-010759)	This paper	NMDR: ST002856
Raw metabolomics data (*In vitro* 16D vehicle and Enzalutamide for Figures S1FS-H)	This paper	NMDR: ST002863
Raw metabolomics data (*In vitro* 16D Enzalutamide, Apalutamide, ARCC-4)	This paper	NMDR: ST002865
Raw metabolomics data (*In vitro* 16D -/+ MYC -/+ Enza)	This paper	NMDR: ST002864
Experimental models: Cell lines		
LNCaP	ATCC	CRL-1740
V16D	Bishop et al.[19]	N/A
LAPC4	Klein et al.[65]	N/A
22Rv1	ATCC	CRL-2505
Experimental models: Organisms/strains		
Mouse: NSG	Jackson Laboratories and the UCLA Department of Radiation Oncology Animal Core Facility	Cat#005557
Oligonucleotides		
5’-AATTCTTTAATTAAAG-3’	This paper	N/A
5’-CCTTAATTAAGCGATC GCACTGGGTACCTGGGCC-3’	This paper	N/A
5’-CAGGTACCCAGTG CGATCGCTTAATTAAGGGTAC-3’	This paper	N/A
5’-CTTAATTAAACTGGGGAGC TCCGC-3’	This paper	N/A
5’-GGAGCTCCCCAGTTTAATT AAGAGCT-3’	This paper	N/A
5’-GACGATGATTAATTAA-3’	This paper	N/A
5’-CACCGAATTCTTCC ATAGAGCTCGTCAAGAGCGA GCTCTATGGAAGAATTC-3’	This paper	N/A

(*Continued on next page*)

Continued

REAGENT or RESOURCE	SOURCE	IDENTIFIER
5'-AAAAGAATTCTTCC ATAGAGCTCGCTCTTGACGAG CTCTATGGAAGAATTC-3'	This paper	N/A
F-5′- AGTTGAGTTTTAGTGATT TTGTGGT -3′	This paper	N/A
R-5′- AACTTACCTTCTACACTT AATCATAATTAA -3′	This paper	N/A
Recombinant DNA		
pBluescript II KS(+)	Stratagene	Cat#212207
shp53 pLO1 pure	Godar et al.[66]	Addgene Cat#19119
pENTR/U6 vector	Thermo Fisher Scientific	Cat#K4945-00
Software and algorithms		
DeepTools program suite	Ramirez et al.[67]	https://deeptools.readthedocs.io/en/develop/index.html
Trim Galore version 0.6.6	N/A	https://github.com/FelixKrueger/TrimGalore
Bismark version 0.23.0	Krueger et al.[68]	https://www.bioinformatics.babraham.ac.uk/projects/bismark/
Principal component analysis projection plots	This paper	https://github.com/Nick-Nunley/PCA-for-AR-induced-metabolic-reprogramming-in-CRPCa
Metaboanalyst 5.0	Pang et al.[69]	https://www.metaboanalyst.ca/MetaboAnalyst/home.xhtml
ImageJ v1.53c	ImageJ	https://imagej.nih.gov/ij/download.html
CellProfiler v2.0	Kamentsky et al.[70]	https://cellprofiler.org/
Imaris software	Oxford Instruments	https://imaris.oxinst.com/
DAVID Bioinformatics	Huang et al.,[71] Huang et al.[72]	https://david.ncifcrf.gov/
GSEA_4.0.3	Subramanian et al.,[73] Mootha et al.[74]	https://www.gsea-msigdb.org/gsea/index.jsp
STAR aligner version 2.5.0b	Dobin et al.[75]	N/A
Prism v8	GraphPad	https://www.graphpad.com/scientific-software/prism/
Other		
Sonic dismembrator	Thermo Fisher Scientific	Cat#FB120

RESOURCE AVAILABILITY

Lead contact

Further information and requests for resources and reagents should be directed to and will be fulfilled by the lead contact, Andrew Goldstein (agoldstein@mednet.ucla.edu).

Materials availability

This study did not generate new unique reagents.

Data and code availability

- RNA sequencing data that support the findings of this study have been deposited in NCBI's Gene Expression Omnibus and are accessible through GEO Series accession numbers GSE202885, GSE202755, and GSE202897. Metabolomics data that support the findings of this study have been deposited in the National Metabolomics Data Repository[93] and are accessible through Study IDs ST002852, ST002859, ST002860, ST002856, ST002863, ST002864, and ST002865. Previously published ChIP sequencing data that was reanalyzed here is available under accession number GSE138460.
- Code for generating PCA projection plots can be found at https://github.com/Nick-Nunley/PCA-for-AR-induced-metabolic-reprogramming-in-CRPCa

- Any additional information required to reanalyze the data reported in this work paper is available from the lead contact upon request.

EXPERIMENTAL MODEL AND SUBJECT DETAILS

Animal work

All animal work was performed using IACUC approved protocols under the supervision of veterinarians from the Division of Laboratory Animal Medicine at UCLA.

7 million 16D cells were implanted subcutaneously with 100 µl Matrigel (Corning) into male NSG mice to form primary tumors. Primary tumors were harvested, minced, and re-implanted (20 - 80 mg of minced tumor tissue with 100 µl Matrigel per mouse) into NSG mice. 16D tumor-bearing mice were treated by oral gavage with 10 mg/kg/day of Enzalutamide in the vehicle (1% carboxymethyl cellulose, 0.5% Tween 80, and 5% dimethylsulfoxide) or the vehicle only, with a two-days-on/one-day-off schedule. Tumors were collected after 10 days of treatment and prepared for histology, protein extraction, and metabolite extraction.

MDA-PCa 180-30 PDX tumors were maintained by serial implantation of 20 – 80 mg of minced tumor tissue. Treatment with vehicle or Enzalutamide was initiated one week after implantation and performed using the approach described above. Tumors were collected after 7 days of treatment and prepared for protein extraction and *ex vivo* organoid culture.

MDA-PCa 173-2 PDX tumors were maintained by serial implantation of 20 – 80 mg of minced tumor tissue. Tumors pieces were implanted into intact or castrated mice. Nine days after implantation, tumors were treated by oral gavage with 7.5 mg/kg/day of IACS-010759 in the vehicle (10% dimethylsulfoxide, 0.5% methylcellulose) or the vehicle only for five days before collection for immunohistochemistry.

MDA-PCa 183-A PDX tumors were maintained by serial implantation of 20 – 80 mg of minced tumor tissue. Tumor tissue was harvested dissociated to plate into organoid culture as described in the "Organoid culture" section.

METHOD DETAILS

In vitro metabolic profiling and 13C isotope tracing

These methods refer to Figure 2I and Figures S2A–S2C. Naïve and LTenza 16D cells were plated in 6-well dishes at 225,000 and 350,000 cells/well respectively. After 24 hours, cells were washed and cultured in a base RPMI supplemented with 10mM U13C-glucose (Cambridge Isotope Laboratories), 10% (v/v) FBS, 2mM glutamine, 100 units/mL penicillin, and 100 µg/mL streptomycin.

24 hours after the addition of U13C-glucose, cells were harvested and extracted for GC/MS analysis using established methods[76]. Briefly, cell plates were placed on ice and quickly washed with ice-cold 0.9% (w/v) NaCl. Cells were immediately treated with 500 µL of ice-cold MeOH and 200 µL water containing 1 µg of the internal standard norvaline. Cells were then scraped and placed in 1.5 mL centrifuge tubes kept on ice. Next, 500 µL of chloroform was added, after which samples were vortexed for 1 minute and then spun at 10,000g for 5 minutes at 4°C. The aqueous layer was transferred to a GC/MS sample vial and dried overnight using a refrigerated CentriVap.

Once dry, samples were resuspended in 20 µL of 2% (w/v) methoxyamine in pyridine and incubated at 37°C for 45 minutes. This was followed by addition of 20 µL of MTBSTFA + 1% TBDMSCl (Ntert-Butyldimethylsilyl-N-methyltrifluoroacetamide with 1% tert-Butyldimethylchlorosilane), mixing, and incubation for an additional 45 minutes at 37°C. Samples were run as previously described[76], and analyzed using Agilent MassHunter software. Stable isotope tracing data was corrected for natural abundance of heavy isotopes with FluxFix software using a reference set of unlabeled metabolite standards[77].

In vitro metabolic profiling and 13C isotope tracing

These methods refer to Figures 1E–1H, 7D–7H and Figures S1F–S1H, Figures S1N, and S1O. Cells were seeded at 30 percent confluence and cultured in 6-well dishes for 48 hours. Cells were then washed and cultured in glucose-free RPMI 1640 plus 11mM U13C-glucose (Cambridge Isotope Laboratories), 10% (v/v) FBS, 100 units/mL penicillin, and 100 µg/mL streptomycin or glutamine-free RPMI 1640 plus 2mM U13C-glutamine (Cambridge Isotope Laboratories), 10% (v/v) FBS, 100 units/mL penicillin, and 100 µg/mL streptomycin for 24 hours prior to metabolite extraction.

For metabolite extraction, media was aspirated and cells were washed with cold 150mM ammonium acetate pH 7.3. Metabolite extractions were performed by adding 500µl of cold 80% methanol containing 2nM Norvaline (Sigma) as an internal standard per well. Cells were removed using a cell scraper before transferring cell suspensions to 1.5ml Eppendorf tubes. Samples were vortexed for 30 seconds and spun at 4°C for 5 minutes at maximum speed to pellet the insoluble fraction before 420 µl of the soluble fraction was transferred to ABC vials (Thermo Fisher Scientific). 80% MeOH was evaporated from the ABC vials using the EZ-2Elite evaporator (Genevac) and samples were stored at -80°C until analysis.

Dried metabolites were resuspended in 50% ACN:water and 1/10th was loaded onto a Luna 3um NH2 100A (150 × 2.0 mm) column (Phenomenex). The chromatographic separation was performed on a Vanquish Flex (Thermo Fisher Scientific) with mobile phases A (5 mM NH4AcO pH 9.9) and B (ACN) and a flow rate of 200 µl/minute. A linear gradient from 15% A to 95% A over 18 minutes was followed by 9 minutes isocratic flow at 95% A and reequilibration to 15% A. Metabolites were detection with a Thermo Fisher

Scientific Q Exactive mass spectrometer run with polarity switching (+3.5 kV/– 3.5 kV) in full scan mode with an m/z range of 70-975 and 70.000 resolution. TraceFinder 4.1 (Thermo Fisher Scientific) was used to quantify the targeted metabolites by area under the curve using expected retention time and accurate mass measurements (< 5 ppm).

Normalization was performed by resuspending the insoluble fraction in 300 μl of lysis solution (0.1M NaCl, 20mM Tris-HCl, 0.1% SDS, 5mM EDTA in distilled water) and proceeding with DNA measurement. Samples were syringed with a 25G needle to reduce viscosity and 50 μl of each sample was transferred to a 96-well black wall clear bottom tissue culture plate (Corning). 50 μl lysis solution was added to one well for a blank reading. 100 μl of 5μg/ml Hoechst 33342 (Thermo Fisher Scientific) in distilled water was added to each well and 96-well plates were incubated for 30 minutes in the dark at 37°C before measurement of DNA-based florescence using a Tecan Infinite M1000 plate reader with 355nm excitation and 465nm emission. The blank reading was subtracted from each absorbance value to calculate relative cell amount.

Apoptosis analysis

Cells were seeded at 40 percent confluence and cultured in 6-well dishes for 48 hours prior to apoptosis analysis. No media changes were performed to preserve all material. Cell culture media and wash media were collected and pooled with quenched trypsin-containing media containing cells and apoptosis analysis was performed using an apoptosis detection kit (BioLegend, 640922) according to the provided protocol. Flow cytometry was performed to quantify the percentage of annexin V^+ cells. In experiments using transduced lines, analysis was restricted to the transduced cells which were identified via flow cytometry by analyzing RFP florescence.

Bioenergetic assays

Oxygen consumption and extracellular acidification rates were measured using an Agilent Seahorse XF96 or XF^e96 Analyzer. Briefly, 16D prostate cancer cells were plated at 40,000 cells/well in XF96 plates for 24 hours. At the time of experiment, tissue culture growth medium was replaced with assay medium consisting of unbuffered DMEM (Sigma, 5030) supplemented with 10mM glucose, 2mM pyruvate, 2mM glutamine, and 5mM HEPES. Respiration was measured at baseline and in response to acute treatment with 2μM oligomycin, FCCP (two sequential pulses of 500nM), and 0.2μM rotenone with 1μM antimycin A. All respiratory parameters were calculated as previously described in[20].

Rates of ATP produced from oxidative phosphorylation and glycolysis were calculated as previously described[78]. Mitochondrial ATP production rates were determined by stoichiometric conversion of the ATP-linked respiration rate, and glycolytic ATP production rates were measured by correcting rates of extracellular acidification for the scaling factor of the microplate sensor coverage and confounding respiratory acidification. Where indicated, cells were treated with 2μM oligomycin 15 minutes prior to recording the initial measurements.

Cell cycle *analysis*

Cells were seeded at 30 percent confluence and cultured in 6-well dishes for 72 hours prior to cell cycle analysis. Media changes were performed 48 hours after plating. After 72 hours of culture, cell cycle analysis was performed using a 5-ethynyl-2'-deoxyuridine-based (EdU) kit (Thermo Fisher Scientific, C10635) according to the specified protocol. EdU labeling was performed for 2 hours in LNCaP and 16D cells, and for 5 hours in 180-30 PDX organoids. For experiments that contained small molecule inhibitors, fresh inhibitor(s) were adding during each media change. PDX 180-30 organoids were dissociated after EdU labeling prior to fixation for cell cycle analysis. In select experiments, the 1μg/ml Hoechst 33342 DNA stain (Thermo Fisher Scientific, 62249) was added prior to flow cytometry analysis to identify G2 and M phase cells. Flow cytometry analysis identified the percentage of EdU-positive and/or Hoechst-positive cells. For experiments with transduced lines, analysis was restricted to the RFP-positive transduced cells.

Cell lines, *lentiviral* transductions, and cloning of knockdown vectors

Cell lines were routinely tested for mycoplasma and authentication by short tandem repeat analysis (Laragen). Tissue culture plates were coated with 0.01% (v/v) Poly-L-Lysine (Sigma, P4832) diluted 1/20 in distilled water and washed with PBS to enhance cell attachment. 16D and LNCaP cells were cultured in RPMI base media (Gibco) + 10% FBS (v/v) + 100 units/mL penicillin, and 100μg/mL streptomycin. Enzalutamide treatment was performed by adding 10μM Enzalutamide (Selleck Chemicals, S1250) every 48 hours. For LNCaP castration experiments, LNCaP cells were grown in RPMI base media + 10% CSS (v/v) (Sigma, F6765) + 100 units/mL penicillin, and 100μg/mL streptomycin +/- 0.5nM DHT (Sigma) and fresh media was provided every 48 hours.

For lentiviral transductions, cells were seeded at 30-50% confluence. Transductions were performed 24-48 hours after seeding with 8μg/ml Polybrene (Thermo Fisher Scientific, NC0663391). Flow cytometry-based cell sorting was performed at least 72 hours after transduction to isolate color-tagged transduced cells.

MYC virus was produced using a plasmid vector FU-MYC-CRW[64]. Plasmid vectors for HK2-overexpression and DRP1-S616E were obtained from VectorBuilder. shScramble (FU-shScr-CRW) and shRB1-shTP53 (FU-shTP35-shRB1-CRW) vectors were cloned as follows. First, the pBSPacI shuttle vector was made by inserting an adaptor oligonucleotide AG220: 5'-AATTCTTTAAT TAAAG-3' at the EcoRI site of pBluescript II KS(+) (Stratagene). The pPass1 shuttle was cloned as follows. Annealed oligonucleotides AG232: 5'-CCTTAATTAAGCGATCGCACTGGGTACCTGGGCC-3' and AG233: 5'-CAGGTACCCAGTGCGATCGCTTAATTAAGGGT AC-3' were inserted between KpnI and ApaI sites of pBluescript II KS(+). Then, annealed oligonucleotides AG234: 5'-CTT

AATTAAACTGGGGAGCTCCGC-3’ and AG235: 5’-GGAGCTCCCCAGTTTAATTAAGAGCT-3’ were inserted between SacI and SacII sites. This creates a PacI-AsiSI-[Multiple cloning sites]-PacI cassette. Annealed oligonucleotides AG218: 5’-GACGATGATTAATTAA-3’, and AG220 (above) were ligated with KflI-EcoRI fragment of shp53 pLO1 pure (Addgene) and inserted into PacI site in pBSPacI (pBSPacI-shTP53). PacI fragment of pBSPacI-shTP53 was then inserted into the AsiSI site in pPassI (pPass1-shTP53). The PacI-PacI fragment of FU-shRB1-AR-CGW was blunted and digested with HindIII creating a HindIII-blunt fragment of H1-shRB1 cassette. This cassette was inserted between HindIII and EcoRV sites in pPass1-shTP53 (pPass1-shTP53-shRB1). PacI fragment of pPass1-shTP53-shRB1 was then inserted into the PacI site of FU-CRW (FU-shTP53-shRB1-CRW). The U6-Scramble cassette was made by ligating annealed oligonucleotides AG227: 5’-CACCGAATTCTTCCATAGAGCTCGTCAAGAGCGAGCTCTATGGAAGAATTC-3’ and AG228: 5’-AAAAGAATTCTTCCATAGAGCTCGCTCTTGACGAGCTCTATGGAAGAATTC-3’ in pENTR/U6 vector (Thermo Fisher Scientific). Then, the BamHI-XbaI fragment was purified and inserted between BamHI and XbaI sites in pBSPacI (pBSPacI-shScr21A). The PacI fragment from pBSPacI-shScr21A was inserted at the PacI site in FU-CRW (FU-shScr-CRW). Concentrated viral aliquots were produced either by VectorBuilder or UCLA Integrated Molecular Technologies Core.

ChIP *sequencing*

AR ChIP-seq bigwig files were generated using DeepTools program suite[67]. AR binding profiles of LNCaP-Ctrl, LNCaP-R1881[79], 16D[30] samples at genomic loci (namely LDHA, HK2 and DNM1L) were analyzed by visualizing AR ChIP-seq bigwig tracks using IGV[80].

DNA methylation *analysis*

Bisulfite sequencing was carried out as described previously[81]. In brief, genomic DNA was bisulfite converted using the EZ DNA methylation kit (Zymo Research, Orange, CA, USA) and amplified using primers specific to the promoter of HK2 (F-5′- AGTTGAGTTTTAGTGATTTTGTGGT -3′, R-5′- AACTTACCTTCTACACTTAATCATAATTAA -3′). All PCR reactions were carried out in 40 μl volume containing 20 ng of bisulfite converted DNA, 1 × Platinum Taqbuffer (Thermo Fisher Scientific), 1.5 U Platinum Taq (Life Technologies), 250 μM each dNTPs, 1.5mM MgCl2, 0.25 μg/μl bovine serum albumin, 2 μl dimethyl sulfoxide, 400nM forward primer, and 400nM reverse primer. Cycling conditions were 95°C for 3 minutes, 36 cycles of 95°C for 30 seconds, 55°C for 30 seconds, and 72°C for 30 seconds, followed by a 7 min extension step at 72°C. PCR products were gel purified after electrophoresis on a 2% agarose gel. Amplicons were sequenced to an average coverage of 27,380x using established amplicon sequencing protocols (Azenta). Raw bisulfite amplicon sequencing fastq reads were first trimmed using Trim Galore version 0.6.6 and then aligned to UCSC hg19 reference genome using Bismark version 0.23.0[68]. Bismark was further used to deduplicate the alignments and extract methylation call files which report the percentage of methylated cytosines for each CpG dinucleotide.

Immunohistochemistry

Tumor tissue was fixed with 4% paraformaldehyde in PBS for 6-8 hours and processed for paraffin sections. Tumor samples were color inked and formalin-fixed paraffin embedded. 3- to 4-μm thick sections were placed on charged slides for immunohistochemical staining that was carried out on Dako’s Automated AS48Link Autostainer in SPORE Pathology Core laboratory at UCLA. Positive and negative control slides were pretreated with Heat Induced Epitope Retrieval (HIER) in Dako PT Link using the Envision FLEX Target Retrieval solution at low pH (6.0), and incubated at 97°C for 15 minutes. Primary rabbit anti-Human HK2 monoclonal antibody (Cell Signaling, 2867; clone, C64G5) or primary mouse anti-Ki67 antibody (Dako, IR62661-2; clone, MIB-1) was added at a 1:600 or 1:100 dilution, respectively, and incubated for 60 minutes at room temperature. Sections were then incubated for 5 minutes with the EnVision Flex+ Rabbit linker (Agilent, SM805) prior to a 5-minute treatment with the Polymer Flex/HRP (Agilent, SM802) reagent. Negative control slides received the Flex Rabbit Negative Control Immunoglobulin fraction (Agilent, IR600) instead of primary antibody. Slides were developed in Envision Flex DAB+Chromogen and counterstained with Mayer’s hematoxylin.

In vivo metabolomics

After tumor dissection, a maximum of 30mg of tissue was weighed, snap frozen, and stored at -80°C until metabolite extraction. To extract metabolites, weighed tumor tissue was added to a bead tube (Thermo Fisher Scientific) containing 1ml 80% methanol plus 10mM potassium trifluoromethanesulfonate (TMSO) internal standard on ice. Samples were homogenized for 1 minute at max speed on a bead homogenizer (Thermo Fisher Scientific). Bead tubes were spun at 17000g at 4°C for 10 minutes. The supernatant was transferred to an Eppendorf tube and spun at 17000g at 4°C for 10 minutes. A volume of extraction equivalent to 3mg of tumor tissue was transferred to an ABC vial (Thermo Fisher Scientific). All volumes were normalized to 500 μl with 80% methanol containing TMSO internal standard. 80% MeOH was evaporated from the ABC vials using the EZ-2Elite evaporator (Genevac) and samples were stored at -80°C until analysis.

Dried metabolites were reconstituted in 100 μL of a 50% acetonitrile (ACN) 50% dH20 solution. Samples were vortexed and spun down for 10 minutes at 17,000g. 70 μL of the supernatant was then transferred to HPLC glass vials. 10 μL of these metabolite solutions were injected per analysis. Samples were run on a Vanquish (Thermo Fisher Scientific) UHPLC system with mobile phase A (20mM ammonium carbonate, pH 9.7) and mobile phase B (100% ACN) at a flow rate of 150 μL/min on a SeQuant ZIC-pHILIC Polymeric column (2.1 × 150 mm 5 μm, EMD Millipore) at 35°C. Separation was achieved with a linear gradient from 20% A to 80% A in 20 minutes followed by a linear gradient from 80% A to 20% A from 20 minutes to 20.5 minutes. 20% A was then held from

20.5 minutes to 28 minutes. The UHPLC was coupled to a Q-Exactive (Thermo Fisher Scientific) mass analyzer running in polarity switching mode with spray-voltage=3.2kV, sheath-gas=40, aux-gas=15, sweep-gas=1, aux-gas-temp=350°C, and capillary-temp=275°C. For both polarities mass scan settings were kept at full-scan-range=(70-1000), ms1-resolution=70,000, max-injection-time=250ms, and AGC-target=1E6. MS2 data was also collected from the top three most abundant singly-charged ions in each scan with normalized-collision-energy=35. Each of the resulting ".RAW" files was then centroided and converted into two ".mzXML" files (one for positive scans and one for negative scans) using msconvert from ProteoWizard[82]. These ".mzXML" files were imported into the MZmine 2 software package[83]. Ion chromatograms were generated from MS1 spectra via the built-in Automated Data Analysis Pipeline (ADAP) chromatogram module[84] and peaks were detected via the ADAP wavelets algorithm. Peaks were aligned across all samples via the Random sample consensus aligner module, gap-filled, and assigned identities using an exact mass MS1(+/-15ppm) and retention time RT (+/-0.5min) search of our in-house MS1-RT database. Peak boundaries and identifications were then further refined by manual curation. Peaks were quantified by area under the curve integration and exported as CSV files. If stable isotope tracing was used in the experiment, the peak areas were additionally processed via the R package AccuCor[85] to correct for natural isotope abundance. Peak areas for each sample were normalized by the measured area of the internal standard trifluoromethanesulfonate (present in the extraction buffer) and by the number of cells present in the extracted well.

Neutral lipid analysis

Cells were trypsinized, washed with PBS, and stained with 2μM BODIPY 493/503 for 15 minutes at 37°C in the dark. Cells were then washed and resuspended in PBS prior to flow cytometry analysis.

Organoid culture

Using a razor blade, individual tumors were mechanically dissociated in dissociation media comprised of RPMI-1640 containing 10% (v/v) fetal bovine serum, 100 units/mL penicillin, and 100μg/mL streptomycin, 1mg/mL collagenase type I, 1mg/ml dispase, 0.1mg/mL deoxyribonuclease, and 10μM of the p160ROCK inhibitor Y-27632 dihydrochloride (Tocris Bioscience). When chunks were no longer visible, the samples were incubated at 37°C on a nutating platform for 45 minutes in 10 mL of dissociation media. After centrifugation at 800g for 5 minutes, the pellet was washed with 1x phosphate buffered saline. The cell pellet was resuspended in human organoid media[86] and passed through a 100μm cell strainer. Growth factor reduced Matrigel (Corning) was added to the cell suspension at a final concentration of 75% before plating into rings in 24-well plates. After Matrigel rings solidified at 37°C for 1 hour, 500 μl human organoid media was added to each well. Each vehicle- and Enzalutamide-treated sample was cultured +/- 30nM IACS-010759 (ChemieTek) for 72 hours.

RNA sequencing

RNA was extracted from samples using the RNeasy Mini Kit (QIAGEN). Library preparation was performed using the KAPA Stranded mRNA-Seq Kit (Roche). The workflow consists of mRNA enrichment, cDNA generation, and end repair to generate blunt ends, A-tailing, adaptor ligation, and PCR amplification. Different adaptors were used for multiplexing samples in one lane. The Illumina HiSeq 3000 was used to perform sequencing for 1x50 run.

Reiter clinical trial: patient cohort

All patients provided informed consent to join study NCI-2015-01448 (NCT01990196).

Men with prostate adenocarcinoma with planned radical prostatectomy with curative intent were randomized to three treatment groups: patients treated with Enzalutamide and either Degarelix, Trametinib, or Dasatinib. Each patient underwent a targeted biopsy prior to neo-adjuvant treatment, and a subsequent radical prostatectomy. RNA was extracted from both FFPE pre-treatment needle biopsy and post-treatment surgical specimens from each patient.

Pre-ADT samples from all treatment arms were used in this study. Only post-ADT samples treated with Enzalutamide and Degarelix were included. Enzalutamide was delivered 160mg orally daily. Degarelix was administered with a 240mg subcutaneous loading dose in the first month, and then 80mg subcutaneously every four weeks.

Reiter clinical trial: tumor RNA sequencing

Libraries for RNA-Seq were prepared with Clonetech SMARTer Stranded Total RNA-Seq (Pico) Kit. The workflow consists of converting total RNA to cDNA, and then adapters for Illumina sequencing are added through PCR. The PCR products are purified, and then ribosomal cDNA is depleted. The cDNA fragments are further amplified with primers universal to all libraries. Lastly, the PCR products are purified once more to yield the final cDNA library. Different adaptors were used for multiplexing samples in one lane. Sequencing was performed on Illumina Novaseq 6000 for a paired-end read 50 bp run. Data quality check was done on Illumina SAV. Demultiplexing was performed with Illumina Bcl2fastq2 (v2.17) program.

Clinical data: RNA data processing

RNA data processing steps were common to all datasets. RNA sequencing reads were aligned to GRCh38.13 using STAR (v2.7.6a)[75]. fastqc (v0.11.8) was used for file-level per base sequence quality, GC content and other metrics (Babraham Bioinformatics - FastQC A Quality Control tool for High Throughput Sequence Data https://www.bioinformatics.babraham.ac.uk/projects/fastqc/.). We used fastp (v0.20.1) to trim adaptor sequences[87]. multiqc (v1.15) was used to summarize fastqc metrics for all samples and collate into summary plots[88]. RNA quantification was performed using RSEM (v1.3.3)[89].

Clinical data: Differential abundance and gene set enrichment

We used DESeq2 (v1.40.2) for differential mRNA abundance analysis[90]. RSEM's gene-level expected counts were used for model fitting. For pre vs. post treatment comparisons across all datasets, batch effects were captured in the model design:

$$Count \sim ADT\ Status + Dataset$$

'ADT Status' is either "Pre-ADT" or "Post-ADT" and 'Dataset' is one of the four datasets included in this study. When estimating differential abundance within a dataset, we did not include a Dataset term in our model.

Gene set enrichment analysis was performed using the hallmark gene set from the Molecular Signatures Database (MSigDB) using GSEA (v4.3.2)[73]. Normalized TPM counts were used as input for GSEA. All hallmark gene sets were tested against the complete expression set output from DESeq2. ADT (Pre/Post) was used as the phenotype for the GSEA analysis. Gene set permutation was used to calculate the p-value for each gene set, and 1000 permutations were performed. Gene sets with an FDR q-value < 0.05 were considered significant.

Clinical data: Statistical analysis

We performed all statistical analysis using R (v4.2.2) (R Core Team (2016). R: A Language and Environment for Statistical Computing (R Foundation for Statistical Computing)). Data visualization was performed using the BPG package (v7.0.5)[91].

Visualization of mitochondria and lipid droplets

Cells were cultured in μ-Slide Well (Ibidi) and fixed with 4% Paraformaldehyde/PBS for 2 minutes. After washing with PBS, cells were stained with anti-TUFM (Atlas Antibodies, AMAb90966) followed by Alexa Fluor 488-conjugated anti-mouse IgG (H+L) (Thermo Fisher Scientific, A11001) to visualize mitochondria, or 1 μg/ml BODIPY 493/503 for 15 minutes to visualize lipid droplets, and 4',6-diamidino-2-phenylindole (DAPI) (Sigma, D8417). Signals were visualized using Zeiss LSM 880 confocal scanning microscope with Airyscan with 100x oil immersion objectives.

Western blot

Cells were lysed in RIPA buffer (50mM Tris-HCL pH8.0, 150nM NaCl, 1% NP-40, 0.5% Sodium Deoxycholate, 0.1% SDS) containing a phosphatase inhibitor cocktail (Halt, 78428) and a protease inhibitor cocktail (Millipore Sigma, 11697498001). Sonication was performed with a sonic dismembrator (Thermo Fisher Scientific, FB120) to improve membranous and nuclear protein yield. For extraction of protein lysate from tumor samples, tumors were minced with a razor blade prior to transfer to pre-filled bead mill tubes (Thermo Fisher Scientific, 15-340-153) and resuspension in the lysis solution described above. Homogenization was performed for 2 minutes at max intensity using a Bead Mill 4 homogenizer (Thermo Fisher Scientific, 15-340-164). Samples were run on NuPAGE 4%-12% Bis-Tris Gels (Thermo Fisher Scientific, NP0335) and protein was transferred to PVDF transfer membranes (Thermo Fisher Scientific, IPV00010). Total protein was visualized using the SYPRO RUBY protein blot stain (Thermo Fisher Scientific, S11791) and membranes were blocked in PBS + 0.1% Tween-20 (Thermo Fisher Scientific, BP337-500) + 5% milk (Thermo Fisher Scientific, BC9121673). Proteins were probed with primary antibodies followed by chromophore-conjugated anti-mouse (Thermo Fisher Scientific, A21235) or anti-rabbit secondary antibodies (Thermo Fisher Scientific, A21244) or HRP-conjugated anti-mouse (Thermo Fisher Scientific, 31430) or anti-rabbit secondary antibodies (Thermo Fisher Scientific, 31463) and detected via florescence or HRP chemiluminescence respectively. Primary antibodies used were beta-Actin (Thermo Fisher Scientific, MA1-140), Androgen Receptor (Cell Signaling, 5153S), Hexokinase II (Cell Signaling, 2867), DRP1 (Cell Signaling, 5391S), Phospho-DRP1 (Ser616) (Cell Signaling, 3455S), Anti-LDH-A (MilliporeSigma, MABC150), Recombinant-Anti-c-MYC (Abcam, ab32072), NSE (Proteintech, 66150-1-Ig), and PSA/KLK3 (Cell Signaling, 5877).

QUANTIFICATION AND STATISTICAL ANALYSIS

Ki67 immunohistochemistry quantification

Ki67-stained images were opened into ImageJ and converted into 8 bit files. The threshold was set to identify positive staining and applied across all images, and mean grey value was measured for each image to reflect the average intensity over all pixels in the image. Relative staining was calculated based on the average for the control (intact/vehicle) samples.

Metabolomics analysis

For projection plots, principal component analysis (PCA) was performed with the scikit-learn, NumPy, pandas, and Matplotlib libraries in Python. Feature selection was done based on shared features between differing datasets. Count/abundance matrices were sorted along their respective feature-axis to ensure features were listed in the same order. After performing z-score scaling, the coordinates from the *in vitro* samples were merged onto a PCA plot with the values from *in vivo* samples. 95% confidence ellipses were generated from PCA-transformed coordinates using a script from Matplotlib (https://github.com/Nick-Nunley/PCA-for-AR-induced-metabolic-reprogramming-in-CRPCa). Heatmaps were generated by plotting row z-scores in GraphPad Prism

Version 7. To generate the average z-score plot, an *in vivo* Enzalutamide-enriched metabolite signature was defined. Row z-scores of *in vivo* Enzalutamide-enriched metabolites were calculated from *the in vitro* metabolomics dataset. Row z-scores from three technical replicates from a representative experiment (n=3) were averaged and represented on a dot plot. MSEA was generated using Metaboanalyst 5.0[69] (https://www.metaboanalyst.ca/MetaboAnalyst/home.xhtml).

Mitochondrial content and morphology, and lipid droplets

Mitochondrial elongation was expressed as aspect ratio (long axis/short axis ratio) and eccentricity, calculated as the ratio of the distance between the foci of an ellipse and its major axis length. Branching was expressed as form factor ((4π(area))/Perimeter[2]). Mitochondrial parameters were determined from mitochondrial TUFM staining. Image analysis was performed using ImageJ v1.53c and CellProfiler v2.0[70]. For mitochondrial volume quantification, z-stack images were processed with Imaris software (Oxford Instruments) to identify TUFM-positive regions and calculate TUFM-positive volume. The number of lipid droplets per cell were quantified with Imaris software (Oxford instruments).

RNA sequencing analysis

KEGG pathway analysis was performed using DAVID Bioinformatics[71,72]. GSEA was performed as described previously using GSEA_4.0.3 software[73,74]. Projection plots were generated as described for metabolomics analysis. After performing z-score scaling, the coordinates from the *in vitro* 16D Enzalutamide time-course RNA-sequencing data were merged onto a PCA plot with the values from the *Rajan et al* dataset. 95% confidence ellipses were generated as described for metabolomics analysis. Average z-score plots and heatmaps were generated as described for metabolomics analysis.

In the *Quigley et al* dataset, there were 63 Enzalutamide-naive and 36 Enzalutamide-resistant patients whose tumor underwent RNA-seq[92]. Alignment to hg38-decoy reference was performed using STAR aligner (version 2.5.0b) with per-gene counts quantification on the basis of Illumina RNA-seq alignment app Version 1.1.0[75].

Western blot quantification

Western blots were quantified using ImageJ software. Background values were subtracted from the mean gray value for each band. Each band was normalized to its respective loading control.

Cell Reports, Volume *42*

Supplemental information

MYC is a regulator of androgen receptor inhibition-induced metabolic requirements in prostate cancer

Preston D. Crowell, Jenna M. Giafaglione, Anthony E. Jones, Nicholas M. Nunley, Takao Hashimoto, Amelie M.L. Delcourt, Anton Petcherski, Raag Agrawal, Matthew J. Bernard, Johnny A. Diaz, Kylie Y. Heering, Rong Rong Huang, Jin-Yih Low, Nedas Matulionis, Nora M. Navone, Huihui Ye, Amina Zoubeidi, Heather R. Christofk, Matthew B. Rettig, Robert E. Reiter, Michael C. Haffner, Paul C. Boutros, Orian S. Shirihai, Ajit S. Divakaruni, and Andrew S. Goldstein

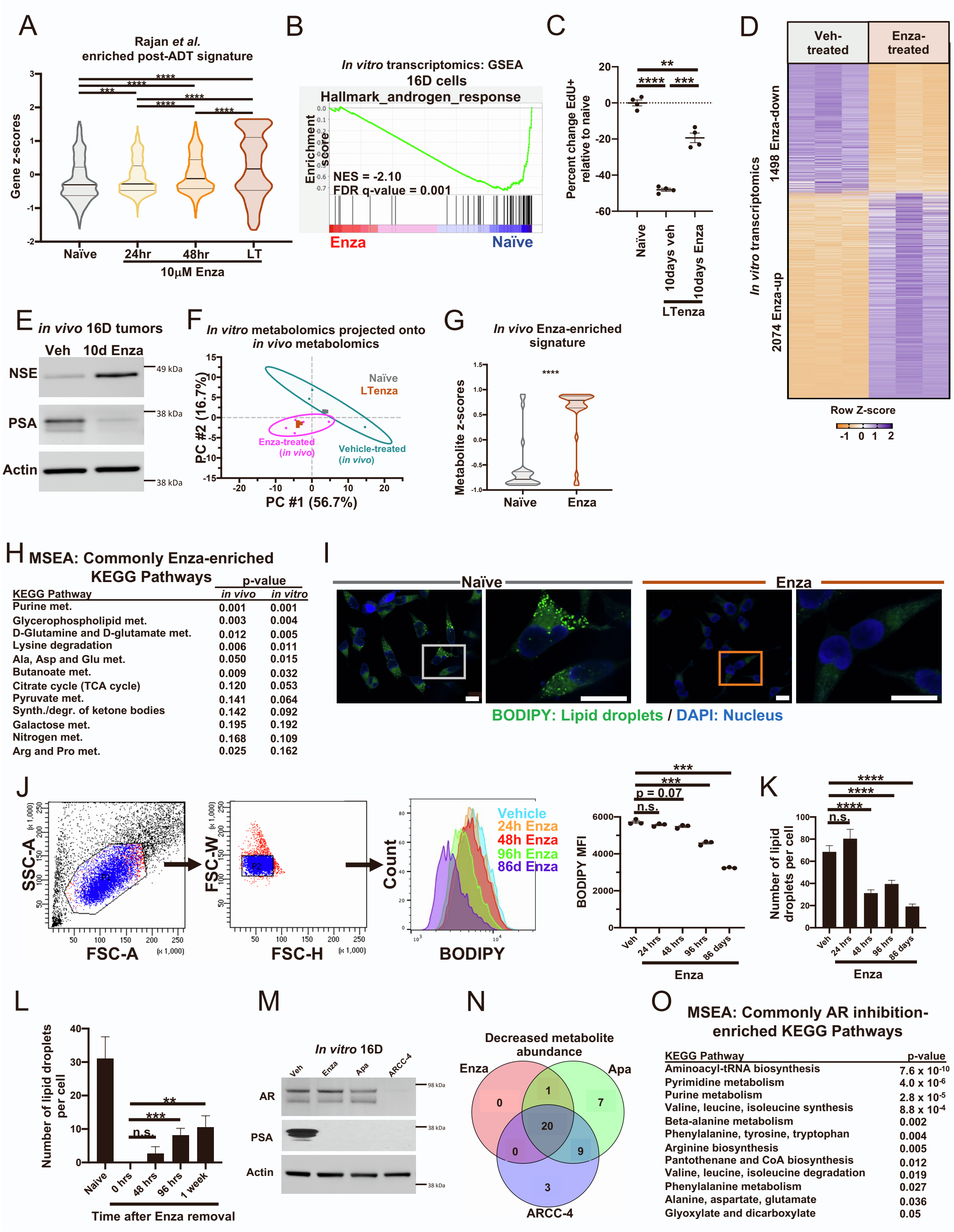

H MSEA: Commonly Enza-enriched KEGG Pathways

KEGG Pathway	p-value *in vivo*	p-value *in vitro*
Purine met.	0.001	0.001
Glycerophospholipid met.	0.003	0.004
D-Glutamine and D-glutamate met.	0.012	0.005
Lysine degradation	0.006	0.011
Ala, Asp and Glu met.	0.050	0.015
Butanoate met.	0.009	0.032
Citrate cycle (TCA cycle)	0.120	0.053
Pyruvate met.	0.141	0.064
Synth./degr. of ketone bodies	0.142	0.092
Galactose met.	0.195	0.192
Nitrogen met.	0.168	0.109
Arg and Pro met.	0.025	0.162

O MSEA: Commonly AR inhibition-enriched KEGG Pathways

KEGG Pathway	p-value
Aminoacyl-tRNA biosynthesis	7.6×10^{-10}
Pyrimidine metabolism	4.0×10^{-6}
Purine metabolism	2.8×10^{-5}
Valine, leucine, isoleucine synthesis	8.8×10^{-4}
Beta-alanine metabolism	0.002
Phenylalanine, tyrosine, tryptophan	0.004
Arginine biosynthesis	0.005
Pantothenane and CoA biosynthesis	0.012
Valine, leucine, isoleucine degradation	0.019
Phenylalanine metabolism	0.027
Alanine, aspartate, glutamate	0.036
Glyoxylate and dicarboxylate	0.05

Supplementary Figure 1. Validation of *in vitro* 16D model, *in vivo* enzalutamide delivery and heatmap from *in vitro* metabolomics. (A) Violin plot indicating gene z-scores of 1023 Rajan *et al.* genes enriched post-ADT (fold change ≥ 2, FDR < 0.2) in naïve, 24hr Enzalutamide-treated (Enza), 48hr Enza, and LTenza 16D cells. Data represent mean +/- SEM. (B) Gene Set Enrichment Analysis (GSEA) of Hallmark_androgen_response genes in naïve and LTenza 16D cells showing normalized enrichment score (NES) and false discovery rate (FDR). (C) Cell cycle analysis performed on naïve 16D cells, LTenza 16D cells, and LTenza 16D cells grown in the absence of Enzalutamide for 10 days. Data represent the mean +/- SEM of 4 technical replicates. (D) Heatmap of differentially expressed genes (fold change ≥ 2, FDR < 0.05) in LTenza 16D cells (Enza-treated) compared to naïve (Veh-treated) 16D cells. (E) Western blot analysis of NSE, PSA, and Actin (loading control) in lysates from vehicle-treated (Veh) and 10-day (10d) enzalutamide-treated subcutaneous 16D tumors. (F) *In vitro* naïve and LTenza 16D metabolomics data projected onto PCA plot of vehicle-treated and Enza-treated samples from *in vivo 16D* metabolomics. 95% confidence eclipses for vehicle- and Enza-treated *in vivo* data are shown in cyan and pink respectively. (G) Violin plot indicating metabolite z-scores of 47 *in vivo* Enza-enriched metabolites (fold change ≥ 1.25, FDR < 0.2) in naïve and LTenza 16D cells. Data represent mean +/- SEM. (H) Metabolite Set Enrichment Analysis (MSEA) on *in vivo* Enzalutamide-enriched metabolites (fold change ≥ 1.25, FDR < 0.2) and *in vitro* Enzalutamide-enriched metabolites (fold change ≥ 1.25, FDR < 0.05) identifies commonly-enriched KEGG pathways (p < 0.2). (I) Representative fluorescent staining images of naïve and LTenza 16D cells stained for BODIPY (green) and DAPI (blue). Scale bars, 20μm. (J-K) Quantification of BODIPY mean fluorescence intensity (MFI) (J) or number of lipid droplets per cell (K) in 16D cells treated with vehicle or 10μM Enzalutamide for 24 hours, 48 hours, 96 hours, or 86 days. (L) Quantification of number of lipid droplets per cell in naïve 16D cells and LTenza 16D cells after removal of Enzalutamide for 48 hours, 96 hours, or 1 week. (M) Western blot analysis of AR, PSA, or ACTIN (loading control) in 16D cells treated with vehicle, 10μM Enzalutamide, 10μM Apalutamide, or 0.5μM ARCC-4 for nine days. (N) Venn diagram illustrating overlap in metabolites with decreased abundance (fold change ≥ 1.5) in Enzalutamide-, Apalutamide-, or ARCC-4-treated 16D cells relative to vehicle-treated 16D cells. (O) MSEA on metabolites commonly enriched with Enzalutamide, Apalutamide, or ARCC-4 treatment (fold change ≥ 1.5) identifies commonly-enriched KEGG pathways. P-values were calculated from an unpaired t-test with Welch's correction (C and G) and a Fisher's Exact Test (H). ***p < 0.001, ****p < 0.0001.

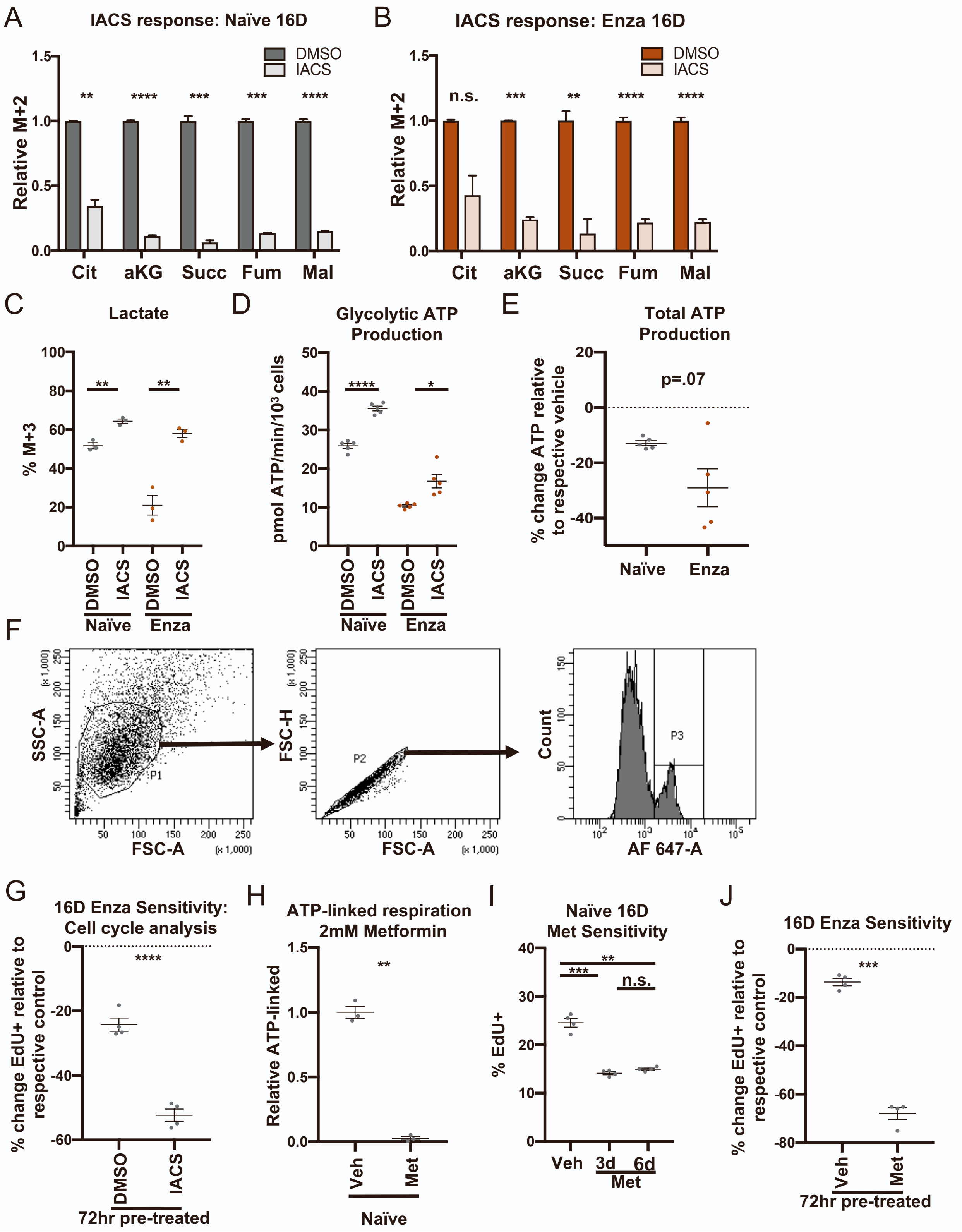
A
IACS response: Naïve 16D
Relative M+2
DMSO
IACS
** **** *** *** ****
Cit aKG Succ Fum Mal
B
IACS response: Enza 16D
Relative M+2
DMSO
IACS
n.s. *** ** **** ****
Cit aKG Succ Fum Mal
C
Lactate
% M+3
DMSO IACS DMSO IACS
Naïve Enza
D
Glycolytic ATP Production
pmol ATP/min/10^3 cells
**** *
DMSO IACS DMSO IACS
Naïve Enza
E
Total ATP Production
% change ATP relative to respective vehicle
p=.07
Naïve Enza
F
SSC-A
FSC-A
P1
FSC-H
P2
Count
P3
AF 647-A
G
16D Enza Sensitivity: Cell cycle analysis
% change EdU+ relative to respective control
****
DMSO IACS
72hr pre-treated
H
ATP-linked respiration 2mM Metformin
Relative ATP-linked
**
Veh Met
Naïve
I
Naïve 16D Met Sensitivity
% EdU+
*** ** n.s.
Veh 3d 6d
Met
J
16D Enza Sensitivity
% change EdU+ relative to respective control
***
Veh Met
72hr pre-treated

Supplementary Figure 2. Validation of complex I inhibitors and sensitivity of Enzalutamide-treated cells to complex I inhibition. (A-B) Relative M+2-labeling of citrate (cit), alpha-ketoglutarate (aKG), succinate (succ), fumarate (fum), and malate after 24hr U13C-glucose tracer analysis of DMSO- and 30nM IACS-010759-treated naïve (A) or LTenza 16D cells (B). Data represent the mean +/- SEM of 3 technical replicates. (C) Percentage of M+3-labeled lactate in naïve and LTenza 16D cells treated with DMSO or 30nM IACS for 24 hours. Data represent the mean +/- SEM of 3 technical replicates. (D) Glycolytic ATP production of naïve and LTenza 16D cells treated with DMSO or 30nM IACS for 24 hours. Data represent the mean +/- SEM of 5 technical replicates. (E) Relative sensitivity of the total ATP production of naïve and LTenza 16D cells to 30nM IACS. Data represent the mean +/- SEM of 5 technical replicates. (F) Representative flow cytometry plots illustrating gating scheme for cell cycle analysis. (G) Cell cycle analysis to quantify the relative sensitivity of DMSO- and 72hr 30nM IACS-treated naïve 16D cells to enzalutamide. Data represent the mean +/- SEM of 4 technical replicates. (H) ATP-linked respiration of naïve 16D cells treated with DMSO or 2mM Metformin (Met) for 24 hrs. Data represent the mean +/- SEM of 3 technical replicates. (I) Cell cycle analysis measuring the percentage of EdU$^+$ cells of vehicle-, 3d, and 6d 2mM Met-treated naïve 16D cells. Data represent the mean +/- SEM of 4 technical replicates. (J) Cell cycle analysis to quantify the relative sensitivity of DMSO- and 72hr 2mM Met-treated naïve 16D cells to Enzalutamide. Data represent the mean +/- SEM of 4 technical replicates. P-values were calculated from an unpaired t-test with Welch's correction. *p < 0.05, **p < 0.01, ***p < 0.001, ****p < 0.0001, n.s. = not significant, $p \geq 0.05$.

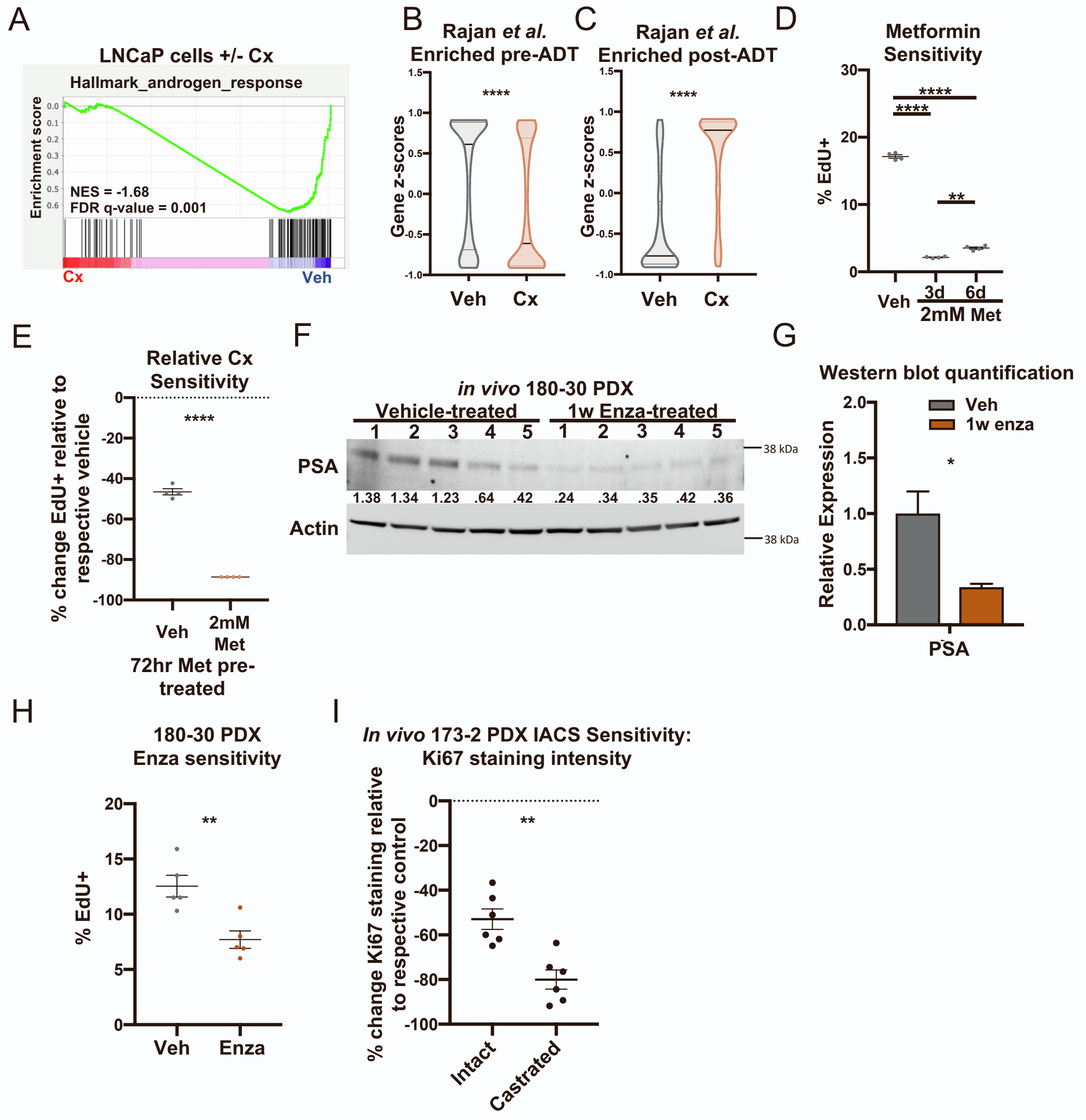
A
LNCaP cells +/- Cx
Hallmark_androgen_response
Enrichment score
0.0
0.1
0.2
0.3
0.4
0.5
0.6
NES = -1.68
FDR q-value = 0.001
Cx
Veh
B
Rajan et al.
Enriched pre-ADT
Gene z-scores
1.5
1.0
0.5
0.0
-0.5
-1.0
****
Veh
Cx
C
Rajan et al.
Enriched post-ADT
Gene z-scores
1.5
1.0
0.5
0.0
-0.5
-1.0
****
Veh
Cx
D
Metformin Sensitivity
% EdU+
30
20
10
0
****
****
**
Veh
3d
6d
2mM Met
E
Relative Cx Sensitivity
% change EdU+ relative to respective vehicle
0
-20
-40
-60
-80
-100
****
Veh
2mM Met
72hr Met pre-treated
F
in vivo 180-30 PDX
Vehicle-treated
1w Enza-treated
1 2 3 4 5 1 2 3 4 5
PSA
1.38 1.34 1.23 .64 .42 .24 .34 .35 .42 .36
Actin
38 kDa
38 kDa
G
Western blot quantification
Veh
1w enza
Relative Expression
2.0
1.5
1.0
0.5
0.0
*
PSA
H
180-30 PDX
Enza sensitivity
% EdU+
20
15
10
5
0
**
Veh
Enza
I
In vivo 173-2 PDX IACS Sensitivity:
Ki67 staining intensity
% change Ki67 staining relative to respective control
0
-20
-40
-60
-80
-100
**
Intact
Castrated

Supplementary Figure 3. AR inhibition-induced metabolic hallmarks are observed in LNCaP cells after castration. (A) GSEA of Hallmark_androgen_response genes in control (veh) and 72-hour castrated (Cx) LNCaP cells showing normalized enrichment score (NES) and false discovery rate (FDR). (B and C) Violin plots indicating gene z-scores of Rajan *et al.* genes enriched pre-ADT (fold change ≥ 2, FDR < 0.2, 911 genes) (B) or post-ADT (fold change ≥ 2, FDR < 0.2, 1023 genes) (C) in veh and 72-hour Cx LNCaP cells. Data represent mean +/- SEM. (D) Cell cycle analysis measuring the % EdU$^+$ cells of veh, 3-day (3d), and 6d 2mM Metformin-treated (Met) LNCaP cells. Data represent the mean +/- SEM of 4 technical replicates. (E) Cell cycle analysis to quantify the relative sensitivity of veh and 72hr Met LNCaP cells to castration. Data represent the mean +/- SEM of 4 technical replicates. (F and G) Western blot detecting HK2, LDHA, PSA, and Actin (loading control) expression in lysates from 5 vehicle-treated and 5 1-week Enzalutamide-treated 180-30 PDX tumors (F) and associated quantification (G). (H) Cell cycle analysis to quantify the proliferation (% EdU$^+$) of vehicle-treated (veh) and 1w Enza-treated 180-30 tumors after 3-day *ex vivo* culture in organoid conditions. Data represent the mean +/- SEM of 5 tumor samples per treatment group. (I) Percent change in Ki67 staining in 173-2 PDX tumors grown in intact or castrated mice treated with 7.5 mg/kg/day IACS for five days relative to vehicle. Data represent the mean +/- SEM. P-values were calculated from an unpaired t-test with Welch's correction. **p < 0.01, ****p < 0.0001.

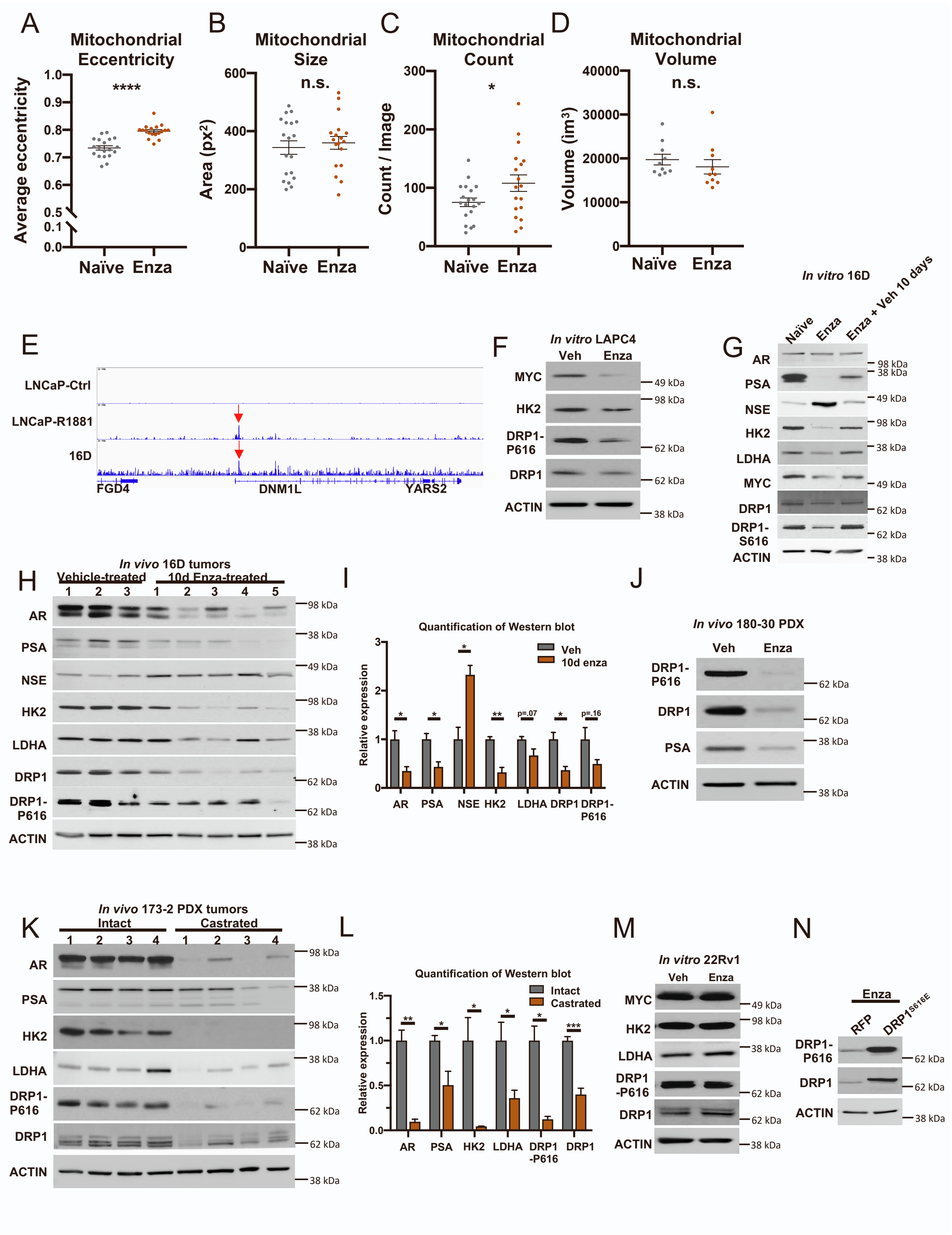
A
Mitochondrial Eccentricity
****
Average eccentricity
1.0
0.9
0.8
0.7
0.6
0.5
0.1
0.0
Naïve
Enza
B
Mitochondrial Size
n.s.
Area (px²)
600
400
200
0
Naïve
Enza
C
Mitochondrial Count
*
Count / Image
300
200
100
0
Naïve
Enza
D
Mitochondrial Volume
n.s.
Volume (im³)
40000
30000
20000
10000
0
Naïve
Enza
E
LNCaP-Ctrl
LNCaP-R1881
16D
FGD4
DNM1L
YARS2
F
In vitro LAPC4
Veh
Enza
MYC
HK2
DRP1-P616
DRP1
ACTIN
49 kDa
98 kDa
62 kDa
62 kDa
38 kDa
G
In vitro 16D
Naïve
Enza
Enza + Veh 10 days
AR
PSA
NSE
HK2
LDHA
MYC
DRP1
DRP1-S616
ACTIN
98 kDa
38 kDa
49 kDa
98 kDa
38 kDa
49 kDa
62 kDa
62 kDa
38 kDa
H
In vivo 16D tumors
Vehicle-treated
10d Enza-treated
1
2
3
1
2
3
4
5
AR
PSA
NSE
HK2
LDHA
DRP1
DRP1-P616
ACTIN
98 kDa
38 kDa
49 kDa
98 kDa
38 kDa
62 kDa
62 kDa
38 kDa
I
Quantification of Western blot
Veh
10d enza
Relative expression
3
2
1
0
*
*
*
**
p=.07
*
p=.16
AR
PSA
NSE
HK2
LDHA
DRP1
DRP1-P616
J
In vivo 180-30 PDX
Veh
Enza
DRP1-P616
DRP1
PSA
ACTIN
62 kDa
62 kDa
38 kDa
38 kDa
K
In vivo 173-2 PDX tumors
Intact
Castrated
1
2
3
4
1
2
3
4
AR
PSA
HK2
LDHA
DRP1-P616
DRP1
ACTIN
98 kDa
38 kDa
98 kDa
38 kDa
62 kDa
62 kDa
38 kDa
L
Quantification of Western blot
Intact
Castrated
Relative expression
1.5
1.0
0.5
0.0
**
*
*
*
*
***
AR
PSA
HK2
LDHA
DRP1-P616
DRP1
M
In vitro 22Rv1
Veh
Enza
MYC
HK2
LDHA
DRP1-P616
DRP1
ACTIN
49 kDa
98 kDa
38 kDa
62 kDa
62 kDa
38 kDa
N
Enza
RFP
DRP1S616E
DRP1-P616
DRP1
ACTIN
62 kDa
62 kDa
38 kDa

Supplementary Figure 4. Quantification of mitochondrial parameters in naïve and LTenza 16D cells and DRP1 expression in vehicle- and enzalutamide-treated 16D tumors. (A-C) Quantification of mitochondrial eccentricity (A), mitochondrial size (B), and mitochondrial count (C) from TUFM stains from 20 images of naïve or LTenza 16D cells. Data represent the mean +/- SEM. (D) Quantification of the mitochondrial volume of naïve and LTenza 16D cells from 3-dimensional reconstruction of 10 z-stack images per treatment group. Data represent the mean +/- SEM. (E) AR binding of LNCaP-Ctrl, LNCaP-R1881 and 16D at the DNM1L genomic locus was analyzed by visualizing AR ChIP-seq bigwig tracks. Red arrow indicates sharp peak called by macs to demonstrate binding of AR. (F) Western blot analysis of MYC, HK2, DRP1-P616, DRP1, and ACTIN (loading control) in LAPC4 cells treated with vehicle or 10μM Enzalutamide for one week. (G-H) Western blot indicating AR, PSA, NSE, HK2, LDHA, DRP1, DRP1 phosphorylation at S616 (DRP1-P616), and ACTIN (loading control) expression in lysates from three vehicle-treated and five 10-day Enzalutamide-treated (10d Enza-treated) 16D tumors (G) and associated quantification (H). Data represent the mean +/- SEM. (I) Western blot of DRP1-P616, DRP1, PSA, and ACTIN (loading control) in vehicle- and Enzalutamide-treated 180-30 PDX tumors. (J-K) Western blot indicating AR, PSA, HK2, LDHA, DRP1-P616, DRP1, and ACTIN (loading control) expression in lysates from 173-2 PDX tumors grown in intact or castrated mice (J) and associated quantification (K). (L) Western blot of MYC, HK2, LDHA, DRP1-P616, DRP1, and ACTIN (loading control in vehicle- or Enzalutamide-treated 22Rv1 cells. (M) Western blot indicating DRP1-P616, DRP1, PSA, and Actin (loading control) expression in lysates from RFP- or DRP1^{S616E}-transduced naïve and LTenza 16D cells. P-values were calculated from an unpaired t-test with Welch's correction. *p < 0.05, **p < 0.01, ****p < 0.0001, n.s. = not significant, p ≥ 0.05.

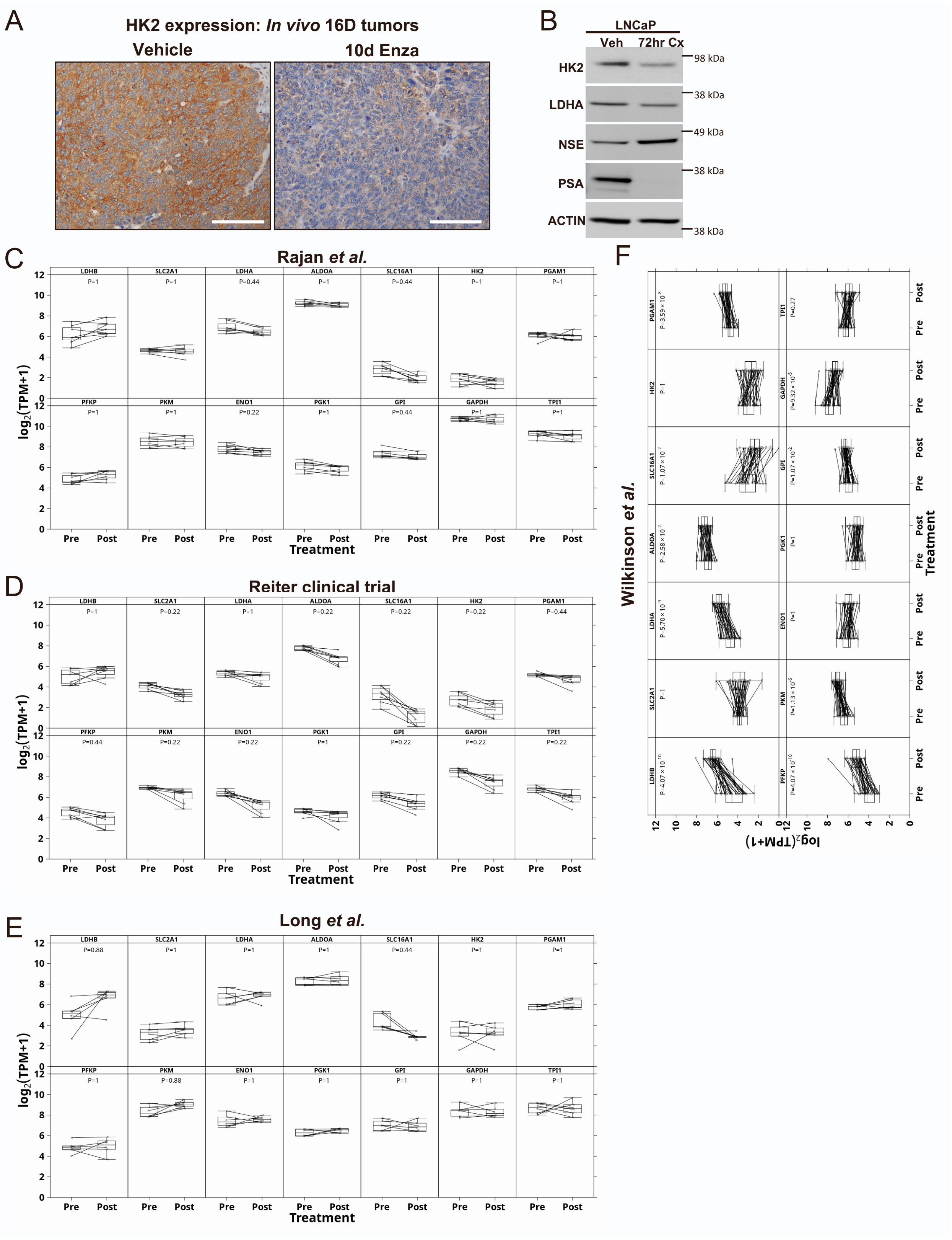
A
HK2 expression: In vivo 16D tumors
Vehicle
10d Enza
B
LNCaP
Veh
72hr Cx
HK2
LDHA
NSE
PSA
ACTIN
98 kDa
38 kDa
49 kDa
38 kDa
38 kDa
C
Rajan et al.
LDHB P=1
SLC2A1 P=1
LDHA P=0.44
ALDOA P=1
SLC16A1 P=0.44
HK2 P=1
PGAM1 P=1
PFKP P=1
PKM P=1
ENO1 P=0.22
PGK1 P=1
GPI P=0.44
GAPDH P=1
TPI1 P=1
log2(TPM+1)
Pre
Post
Treatment
D
Reiter clinical trial
LDHB P=1
SLC2A1 P=0.22
LDHA P=1
ALDOA P=0.22
SLC16A1 P=0.22
HK2 P=0.22
PGAM1 P=0.44
PFKP P=0.44
PKM P=0.22
ENO1 P=0.22
PGK1 P=1
GPI P=0.22
GAPDH P=0.22
TPI1 P=0.22
log2(TPM+1)
Pre
Post
Treatment
E
Long et al.
LDHB P=0.88
SLC2A1 P=1
LDHA P=1
ALDOA P=1
SLC16A1 P=0.44
HK2 P=1
PGAM1 P=1
PFKP P=1
PKM P=0.88
ENO1 P=1
PGK1 P=1
GPI P=1
GAPDH P=1
TPI1 P=1
log2(TPM+1)
Pre
Post
Treatment
F
Wilkinson et al.
PGAM1 P=3.59 × 10^-8
TPI1 P=0.27
HK2 P=1
GAPDH P=9.32 × 10^-3
SLC16A1 P=1.07 × 10^-2
GPI P=1.07 × 10^-2
ALDOA P=2.58 × 10^-2
PGK1 P=1
LDHA P=5.70 × 10^-9
ENO1 P=1
SLC2A1 P=1
PKM P=1.13 × 10^-6
LDHB P=4.07 × 10^-10
PFKP P=4.07 × 10^-10
Post
Pre
Treatment
log2(TPM+1)
0 2 4 6 8 10 12

Supplementary Figure 5. HK2 immunohistochemistry and evaluation of glycolytic enzymes in LNCaP cells. (A) Immunohistochemistry of HK2 in subcutaneous 16D tumors treated with vehicle or 10μM Enzalutamide for 10 days. (B) Western blot indicating HK2, LDHA, NSE, PSA, and Actin (loading control) in LNCaP cells +/- 72 hours castration (Cx). (C-F) RNA abundance of glycolytic enzymes in Rajan *et al.* (C), Reiter clinical trial (D), Long *et al.* (E), and Wilkinson *et al.* (F) clinical datasets. For C-F, statistical significance was determined using the Wilcoxon U test. P values were combined using Fisher's method and corrected for multiple comparisons using the Bonferroni method.

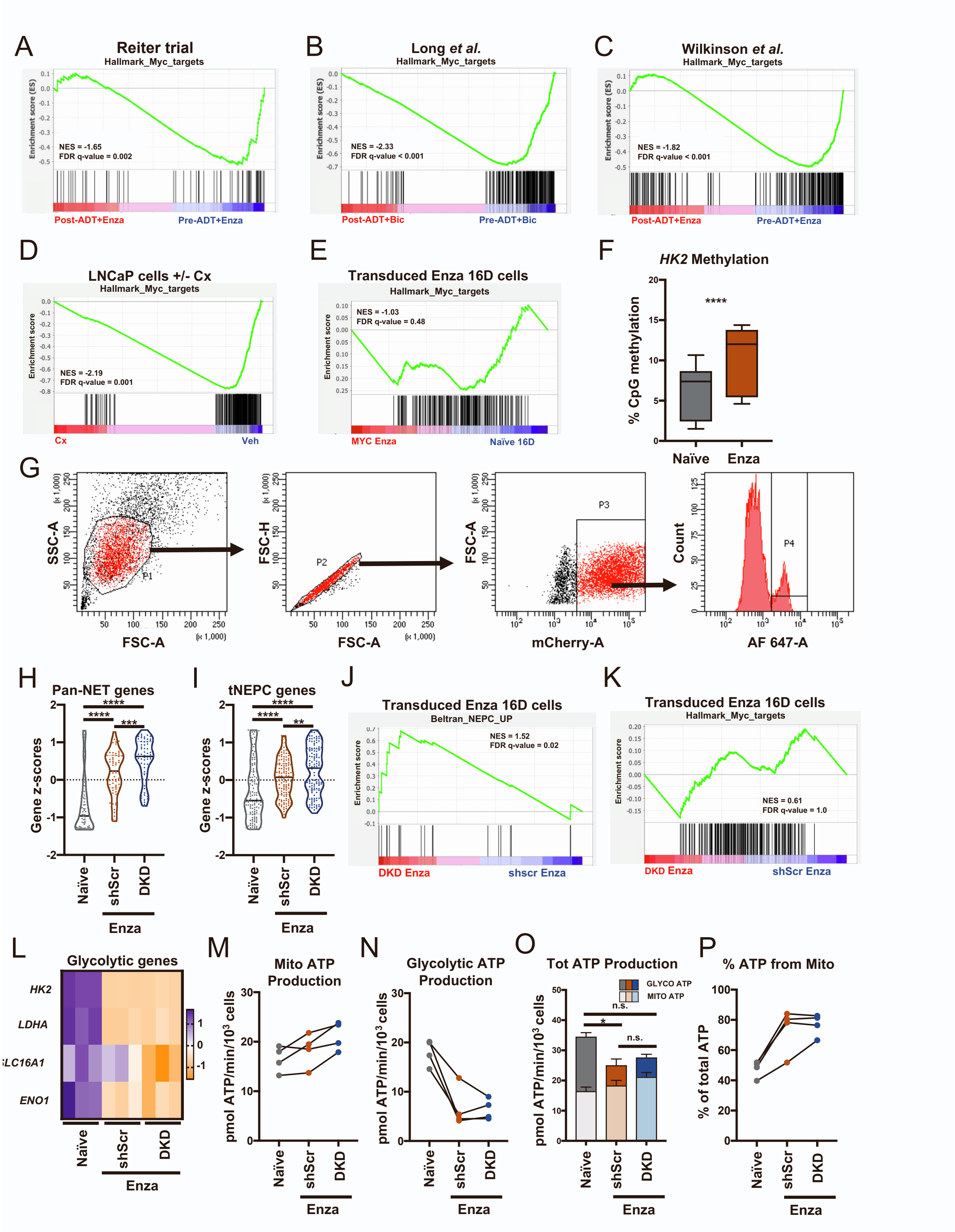
A
Reiter trial
Hallmark_Myc_targets
Enrichment score (ES)
NES = -1.65
FDR q-value = 0.002
Post-ADT+Enza
Pre-ADT+Enza
B
Long et al.
Hallmark_Myc_targets
Enrichment score (ES)
NES = -2.33
FDR q-value < 0.001
Post-ADT+Bic
Pre-ADT+Bic
C
Wilkinson et al.
Hallmark_Myc_targets
Enrichment score (ES)
NES = -1.82
FDR q-value < 0.001
Post-ADT+Enza
Pre-ADT+Enza
D
LNCaP cells +/- Cx
Hallmark_Myc_targets
Enrichment score
NES = -2.19
FDR q-value = 0.001
Cx
Veh
E
Transduced Enza 16D cells
Hallmark_Myc_targets
Enrichment score
NES = -1.03
FDR q-value = 0.48
MYC Enza
Naïve 16D
F
HK2 Methylation
% CpG methylation
****
Naïve
Enza
G
SSC-A
FSC-A
P1
FSC-H
P2
FSC-A
P3
mCherry-A
Count
P4
AF 647-A
H
Pan-NET genes
Gene z-scores
****
****
***
Naïve
shScr
DKD
Enza
I
tNEPC genes
Gene z-scores
****
****
**
Naïve
shScr
DKD
Enza
J
Transduced Enza 16D cells
Beltran_NEPC_UP
Enrichment score
NES = 1.52
FDR q-value = 0.02
DKD Enza
shscr Enza
K
Transduced Enza 16D cells
Hallmark_Myc_targets
Enrichment score
NES = 0.61
FDR q-value = 1.0
DKD Enza
shScr Enza
L
Glycolytic genes
HK2
LDHA
SLC16A1
ENO1
Naïve
shScr
DKD
Enza
M
Mito ATP Production
pmol ATP/min/10³ cells
Naïve
shScr
DKD
Enza
N
Glycolytic ATP Production
pmol ATP/min/10³ cells
Naïve
shScr
DKD
Enza
O
Tot ATP Production
pmol ATP/min/10³ cells
GLYCO ATP
MITO ATP
n.s.
*
n.s.
Naïve
shScr
DKD
Enza
P
% ATP from Mito
% of total ATP
Naïve
shScr
DKD
Enza

Supplementary Figure 6. AR inhibition-induced metabolic hallmarks are retained in enzalutamide-treated 16D cells after knockdown of *RB1* and *TP53*. (A-C) GSEA of Hallmark_Myc_targets in Reiter trial (A), Long *et al.* (B), and Wilkinson *et al.* (C) clinical datasets showing NES and FDR. (D-E) GSEA of Hallmark_Myc_targets genes in veh and 72-hour Cx LNCaP cells (D) and naïve and Myc-transduced LTEnza 16D cells (E) showing NES and FDR. (F) Mean percentage of methylated CpGs within the *HK2* locus of naïve and LTenza 16D cells. (G) Representative flow cytometry plots indicating gating strategy for cell cycle assays. (H-I) Violin plots indicating gene z-scores of Pan-neuroendocrine tumor (Pan-NET) associated genes defined by Guo *et al.* (H) and treatment-emergent small-cell neuroendocrine prostate cancer (tNEPC) associated genes (fold change ≥ 1.5, 330 genes) from the Aggarwal *et al.* dataset (I) in naïve, shScr LTenza, and DKD LTenza 16D cells. Data represent mean +/- SEM. (J) GSEA of Beltran_NEPC_UP genes in DKD LTenza and shScr LTenza 16D cells.(K) GSEA of Hallmark_Myc_targets in DKD LTenza and naïve 16D cells. (L) Heatmap of select glycolytic genes from 3 technical replicates per line. (M-N) Mitochondrial (Mito) ATP production (M) and glycolytic ATP production (N) in naïve, shScr LTenza, and DKD LTenza 16D cells from 4 biological replicate experiments. (O) Total ATP production, represented as the sum of mitochondrial ATP production (Mito ATP) and glycolytic ATP production (Glyco ATP), of naïve, shScr LTenza, and DKD LTenza 16D cells from 4 biological replicate experiments. Statistics refer to comparison of total ATP levels. Data represent mean +/- SEM. (P) Percentage of total ATP production from mitochondrial ATP production (% ATP from Mito) of naïve, shScr LTenza, and DKD LTenza 16D cells from 4 biological replicate experiments. P-values were calculated from an unpaired t-test with Welch's correction. *p < 0.05, **p < 0.01, ***p < 0.001, ****p < 0.0001, n.s. = not significant, p ≥ 0.05.

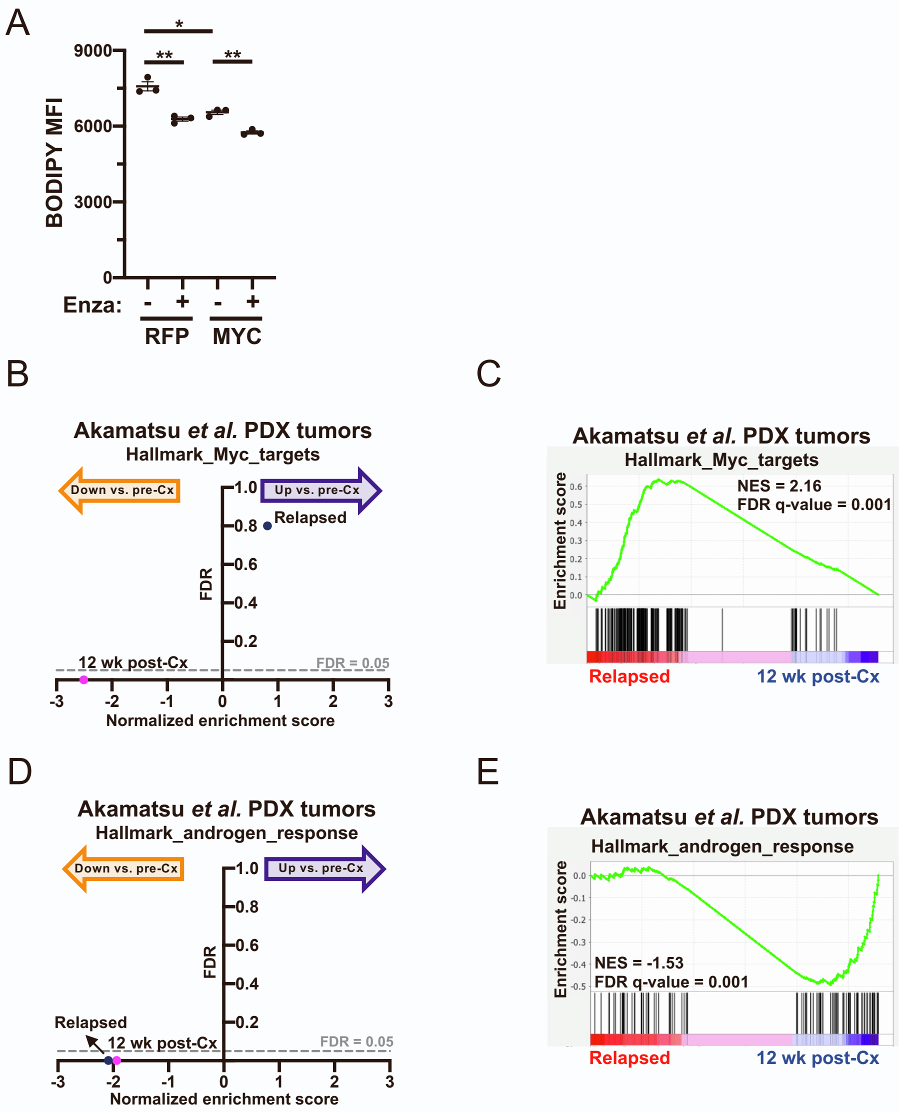
A
BODIPY MFI
9000
6000
3000
0
*
**
**
Enza:
-
+
-
+
RFP
MYC
B
Akamatsu *et al.* PDX tumors
Hallmark_Myc_targets
Down vs. pre-Cx
Up vs. pre-Cx
Relapsed
12 wk post-Cx
FDR = 0.05
FDR
1.0
0.8
0.6
0.4
0.2
-3
-2
-1
0
1
2
3
Normalized enrichment score
C
Akamatsu *et al.* PDX tumors
Hallmark_Myc_targets
Enrichment score
NES = 2.16
FDR q-value = 0.001
Relapsed
12 wk post-Cx
D
Akamatsu *et al.* PDX tumors
Hallmark_androgen_response
Down vs. pre-Cx
Up vs. pre-Cx
Relapsed
12 wk post-Cx
FDR = 0.05
FDR
1.0
0.8
0.6
0.4
0.2
-3
-2
-1
0
1
2
3
Normalized enrichment score
E
Akamatsu *et al.* PDX tumors
Hallmark_androgen_response
Enrichment score
NES = -1.53
FDR q-value = 0.001
Relapsed
12 wk post-Cx

Supplementary Figure 7. MYC target gene expression is restored in LTL331 model of relapsed castration-resistant prostate cancer despite maintenance of low AR activity. (A) BODIPY mean fluorescence intensity in RFP- and MYC-transduced 16D cells maintained +/- 10μM Enzalutamide for 1 week. (B-C) GSEA of Hallmark_Myc_targets in relapsed and 12-week post-castration (12 wk post-Cx) LTL331 tumor samples (B) and relapsed and pre-castration (Pre-Cx) samples (C) from the Akamatsu *et al.* dataset. (D-E) GSEA of Hallmark_androgen_response genes in relapsed and 12 wk post-Cx LTL331 tumor samples (D) and relapsed and pre-Cx samples (E) from the Akamatsu *et al.* dataset. Significance was evaluated using normalized enrichment scores (NES) and false discovery rates (FDR).

Supplementary Table 1. KEGG PATHWAY analysis: Rajan et al. Top 30 significantly enriched pathways

KEGG Pathway	**Fold enrichment**	**p-value**
Neuroactive ligand-receptor interaction	2.658	2.35E-07
Arginine and proline metabolism	-4.870	2.28E-05
Mineral absorption	-5.073	3.99E-05
Metabolic pathways	-1.482	5.79E-05
cAMP signaling pathway	2.444	1.56E-04
Protein digestion and absorption	3.347	2.30E-04
Pathways in cancer	1.873	4.24E-04
Dilated cardiomyopathy	3.256	5.45E-04
Renin-angiotensin system	-6.176	6.67E-04
Biosynthesis of antibiotics	-2.201	6.79E-04
Fructose and mannose metabolism	-5.073	7.53E-04
Basal cell carcinoma	3.896	8.68E-04
Calcium signaling pathway	2.233	1.96E-03
Amino sugar and nucleotide sugar metabolism	-3.805	2.10E-03
Fatty acid metabolism	-3.805	2.10E-03
Steroid biosynthesis	-6.088	2.34E-03
ECM-receptor interaction	2.902	2.53E-03
Glutamatergic synapse	2.583	2.74E-03
Renin secretion	3.287	2.97E-03
Hypertrophic cardiomyopathy (HCM)	2.967	3.55E-03
Arrhythmogenic right ventricular cardiomyopathy (ARVC)	3.140	4.07E-03
Protein export	-5.294	4.49E-03
Circadian entrainment	2.657	5.05E-03
PPAR signaling pathway	-3.029	5.15E-03
Serotonergic synapse	2.464	6.06E-03
Biosynthesis of amino acids	-2.818	8.28E-03
Focal adhesion	1.940	8.68E-03
Retinol metabolism	2.958	1.02E-02
Morphine addiction	2.543	1.05E-02
Glutathione metabolism	-3.183	1.17E-02

Supplementary Table 2. KEGG PATHWAY analysis: 16D cells Top 30 significantly enriched pathways

KEGG Pathway	Fold enrichment	p-value
Axon guidance	2.835	1.04E-06
Glutamatergic synapse	2.707	1.64E-05
Ras signaling pathway	1.991	1.24E-04
Cell adhesion molecules (CAMs)	2.264	2.11E-04
Cholinergic synapse	2.433	2.95E-04
Alcoholism	2.034	4.88E-04
Pathways in cancer	1.636	5.21E-04
Calcium signaling pathway	2.011	5.84E-04
Pentose and glucuronate interconversions	-4.446	6.57E-04
Steroid hormone biosynthesis	-3.373	6.58E-04
Basal cell carcinoma	3.095	7.07E-04
Neuroactive ligand-receptor interaction	1.764	7.11E-04
Drug metabolism - cytochrome P450	-3.116	7.48E-04
Circadian entrainment	2.436	8.94E-04
Ascorbate and aldarate metabolism	-4.830	9.30E-04
cGMP-PKG signaling pathway	2.034	1.05E-03
Focal adhesion	1.873	1.16E-03
Aldosterone synthesis and secretion	2.540	1.23E-03
ErbB signaling pathway	2.365	2.58E-03
Phenylalanine metabolism	-5.753	2.81E-03
Protein digestion and absorption	2.338	2.90E-03
Proteoglycans in cancer	1.800	3.12E-03
Chemical carcinogenesis	-2.649	3.18E-03
AMPK signaling pathway	-2.253	3.22E-03
Tyrosine metabolism	-3.726	4.61E-03
Serotonergic synapse	2.085	4.98E-03
Renin secretion	-2.802	5.10E-03
Retinol metabolism	-2.802	5.10E-03
Metabolic pathways	-1.284	5.28E-03
cAMP signaling pathway	1.753	5.36E-03

Chapter 5: Conclusion

Cellular metabolism is involved in energy production, biosynthesis of macromolecules, the regulation of signaling pathways, and epigenetic processes. Rewiring of metabolic pathways has been shown to alter lineage identity in several tissues and contribute to therapy resistance in many cancer types[1–5]. Furthermore, reprogrammed energy metabolism can often be exploited to impair cancer cell growth[6–8]. Prostate cancer is the leading cause of cancer-related death in non-smoking men with an estimated 34,700 deaths in 2023 in the United States alone[9]. In this dissertation, I explored the relationship between lineage identity, metabolism, and response to therapy in prostate cancer. In Chapter 2, I described our efforts to further optimize prostate organoid culture methods. In Chapter 3, I established that inhibition of mitochondrial pyruvate uptake results in large-scale chromatin remodeling, influencing both lineage-specific transcription factors and response to treatment. Finally in Chapter 4, I defined treatment-induced metabolic alterations and vulnerabilities in prostate cancer and identified molecular mechanisms that regulate these phenotypes. These discoveries yield insights into how manipulating metabolism can impact prostate cancer progression and inform novel strategies for treatment.

Regulation of prostate cell fate through a metabolic-epigenetic axis

Prostate epithelial lineage transitions occur during development[10, 11], tissue regeneration[12], inflammation[13], prostate cancer initiation[14, 15], and treatment resistance[16–20]. Recent studies have identified the epigenome as a regulator of prostate cell fate[16, 21–23], yet how upstream metabolic signaling contributes to the establishment and maintenance of lineage identity is poorly defined. In Chapter 3, I described our efforts to investigate the metabolic regulation of differentiation in the prostate and evaluate how the modulation of metabolism can impact response to treatment. To delineate prostate epithelial cell type-specific metabolic features, we developed an approach to perform metabolomics on primary basal and luminal cells. Using this approach, we discovered that basal and luminal cells of the prostate exhibit distinct metabolomes and nutrient utilization patterns. Furthermore, we establish that basal to luminal differentiation is accompanied by increased pyruvate oxidation. The mitochondrial pyruvate carrier (MPC) and subsequent lactate accumulation emerged as regulators of prostate luminal identity. Inhibition of the MPC or supplementation with exogenous lactate reprogram the chromatin landscape of key lineage-specific transcription factors and modulate response to antiandrogen treatment. These results establish reciprocal regulation of metabolism and prostate epithelial lineage identity.

Previous studies have demonstrated that modulation of pyruvate and lactate metabolism can mediate differentiation phenotypes through a metabolic-epigenetic axis. For example, deletion of the MPC drives CD8+ T cell differentiation toward a memory phenotype due to increased acetyl-coenzyme-A production and enhanced histone acetylation of pro-memory genes[24]. Lactate supplementation has been shown to promote a stem-like phenotype in CD8+ T cells through histone deacetylase (HDAC) inhibition[25]. In prostate organoids, we found that HDAC inhibition antagonizes luminal differentiation, that MPC inhibition and HDAC inhibition have similar effects on gene expression, and that the two treatments do not synergize to alter gene expression. Future studies will investigate if lactate is binding to HDACs and if this binding is required for the reduction in luminal differentiation. Additional ChIP sequencing and bisulfite sequencing is also necessary to further elucidate the epigenetic impact of MPC inhibition.

Metabolic manipulation of lineage identity to promote antiandrogen sensitivity

Resistance to androgen receptor (AR) inhibition is a major cause of disease progression and prostate cancer-associated lethality. The loss of luminal identity is associated with resistance to AR inhibition[18, 19]. We established that MPC inhibition and intracellular lactate accumulation antagonize luminal differentiation. However, it remains unclear whether metabolic regulation of lineage identity can be exploited to promote the reacquisition of luminal features and restore sensitivity to AR inhibition in prostate cancer. Future studies will explore whether MPC overexpression, lactate dehydrogenase inhibition, or increased pyruvate oxidation via pyruvate dehydrogenase kinase inhibition in non-luminal treatment-resistant prostate cancer organoids promotes the reacquisition of luminal features and enhances sensitivity to AR blockade. As treatment-resistant disease accounts for the vast majority of prostate cancer-related death, developing new strategies to target treatment-resistant prostate cancer is critical.

Metabolic heterogeneity in prostate cancer

Metabolic transformation during tumor progression plays a pivotal role in sustaining tumor growth and is influenced by a complex interplay between the tumor mutational landscape, epigenetic alterations, and microenvironmental factors. Elucidating the heterogeneity in tumor metabolic dependencies may provide novel biomarkers for personalized therapy or new strategies to improve cancer treatment efficacy. Using two independent cohorts, we found that prostate cancer patients who fail to respond to AR inhibition exhibit lower MPC expression than do exceptional responders[26, 27]. Future studies will be necessary to identify novel treatment strategies for patients that have tumors with low MPC expression. Furthermore, future studies will be required to identify additional metabolic determinants that can predict which patients are likely to respond and which patients are likely to develop resistance to AR inhibition. Additional work will also be required to define how prostate cancer driver mutations alter metabolic properties and whether they confer sensitivity to unique metabolic vulnerabilities.

Therapy-induced metabolic reprogramming and vulnerabilities in prostate cancer

Metabolic rewiring occurs in many tissues during cancer initiation and progression and can contribute to therapy resistance. In many cases, altered energy metabolism can be leveraged for the diagnosis, monitoring, and/or treatment of cancer. Several studies demonstrate that metabolic pathways can be targeted to impair prostate cancer cell growth[28–34]. Furthermore, AR inhibition has been shown to increase reliance on electron transport chain complex I activity and glutaminase activity[34]; however, the mechanisms that govern AR inhibition-induced metabolic reprogramming have not been elucidated. Defining the molecular mechanisms that regulate how prostate cancer cells respond to AR-targeted therapies is critical in order to develop approaches to prevent or delay disease progression. In Chapter 4, I describe our effort to determine how AR blockade alters prostate cancer metabolism and metabolic vulnerabilities. Using transcriptomic, metabolomics, and bioenergetic approaches, we comprehensively define how prostate cancer metabolism is altered by AR blockade. Following AR inhibition, cells reduce glycolytic activity and maintain oxidative phosphorylation, resulting in increased reliance on complex I of the electron transport chain. We establish DRP1 activity and MYC signaling as mediators of AR blockade-induced metabolic phenotypes. Our findings identify altered metabolic signaling as a resistance mechanism and provide an example of how therapy-induced metabolic rewiring can be targeted to eradicate the cells that survive AR inhibition.

Our results suggest that mitochondrial oxidative metabolism is required for prostate cancer growth and survival following AR blockade. Several observational and clinical trials have been performed to determine the efficacy of combined Metformin treatment and AR blockade but have thus far been inconclusive regarding recurrence-free and overall survival[35, 36]. Importantly, the maximally-achievable therapeutic concentration (70μM) found in patients is more than 10 times lower than the concentration (1mM) necessary to inhibit complex I activity[37, 38]. Furthermore, IACS-010759 has been shown to have dose-limiting toxicities in patients, limiting the potential of complex I inhibition as a therapeutic strategy[39]. Therefore, clinically-viable inhibitors of oxidative metabolism are needed to test whether AR blockade can synergize with inhibition of mitochondrial metabolism to improve patient outcomes. Alternatively, identifying tumor-specific regulators of oxidative metabolism may limit toxicity in patients and enable the impairment of prostate cancer cell growth.

Role of altered mitochondrial dynamics following AR inhibition

In Chapter 4, we identify increased maximal respiration, decreased DRP1 phosphorylation at S616, and mitochondrial elongation following AR blockade. Elongation has been shown to protect mitochondria from autophagosomal degradation during nutrient starvation[40]. In several contexts, including breast and gynecological cancers, hyperfused mitochondrial networks enable chemotherapy resistance[41, 42]. Importantly, the functional consequence of mitochondrial morphology on metabolic activity is highly context dependent. For example, mitochondrial fragmentation increases oxidative metabolism in pancreatic cancer models[43], whereas mitochondrial fragmentation reduces oxidative metabolism in neuroblastoma cells[44]. Future work is necessary to thoroughly evaluate how altered mitochondrial dynamics influence metabolic phenotypes and response to AR blockade in prostate cancer. It remains unknown if other proteins involved in the regulation of mitochondrial dynamics, such as PGC-1α, MFN2, and OPA1, influence metabolic characteristics in prostate cancer. Furthermore, additional experiments are necessary to elucidate how AR inhibition results in decreased DRP1 phosphorylation. It also remains unknown whether the increased maximal respiration observed following AR blockade has functional implications for therapy resistance and treatment-induced metabolic vulnerabilities.

Influence of genetic drivers of lineage plasticity on metabolism

Previous studies have demonstrated that increased MYC activity antagonizes the canonical AR transcriptional program, accelerates prostate cancer progression toward a castration-resistant state, and promotes androgen-independent growth[45, 46]. In Chapter 4, we demonstrate that maintenance of MYC activity prevents AR blockade-induced reduction in glycolysis, phosphorylation of DRP1-S616, and glutamine utilization. Future studies are necessary to investigate whether N-MYC overexpression, which has been shown to promote lineage plasticity in prostate cancer[16, 17], has a similar effect on metabolism as MYC reactivation. Furthermore, additional studies are required to elucidate whether distinct genetic drivers of lineage plasticity converge on similar metabolic phenotypes or if distinct genetic drivers impart unique metabolic phenotypes. Metabolic vulnerabilities may be dependent on tumor lineage phenotype. Alternatively, elucidating driver-specific metabolic vulnerabilities may enable a personalized medicine approach to treating prostate cancer.

References

1. Mews, P., Donahue, G., Drake, A.M., et al. Acetyl-CoA synthetase regulates histone acetylation and hippocampal memory. Nature. 546 (7658), 381–386, doi: 10.1038/nature22405 (2017).

2. Agathocleous, M., Meacham, C.E., Burgess, R.J., et al. Ascorbate regulates haematopoietic stem cell function and leukaemogenesis. Nature. 549 (7673), 476–481, doi: 10.1038/nature23876 (2017).

3. Baksh, S.C., Todorova, P.K., Gur-cohen, S., et al. Extracellular serine controls epidermal stem cell fate and tumour initiation. Nature Cell Biology. 22 (7), 779–790, doi: 10.1038/s41556-020-0525-9 (2020).

4. Yu, Y., Newman, H., Shen, L., et al. Glutamine Metabolism Regulates Proliferation and Lineage Allocation in Skeletal Stem Cells. Cell Metabolism. 29 (4), 966–978, doi: 10.1016/j.cmet.2019.01.016 (2019).

5. Mukhopadhyay, S., Goswami, D., Adiseshaiah, P.P., et al. Undermining glutaminolysis bolsters chemotherapy while NRF2 promotes chemoresistance in KRAS-driven pancreatic cancers. Cancer Research. 80 (8), 1630–1643, doi: 10.1158/0008-5472.CAN-19-1363 (2020).

6. Huang, F., Ni, M., Chalishazar, M.D., et al. Inosine monophosphate dehydrogenase dependence in a subset of small cell lung cancers. Cell Metabolism. 28 (3), 369–382, doi: 10.1016/j.cmet.2018.06.005 (2018).

7. Maddocks, O.D.K., Athineos, D., Cheung, E.C., et al. Modulating the therapeutic response of tumours to dietary serine and glycine starvation. Nature. 544 (7650), 372–376, doi: 10.1038/nature22056 (2017).

8. Gabra, M.B.I., Yang, Y., Li, H., et al. Dietary glutamine supplementation suppresses epigenetically-activated oncogenic pathways to inhibit melanoma tumour growth. Nature Communications. 11 (1), doi: 10.1038/s41467-020-17181-w (2020).

9. Siegel, R.L., Miller, K.D., Wagle, N.S., et al. Cancer statistics, 2023. CA: A Cancer Journal for Clinicians. 73, 17–48, doi: 10.3322/caac.21763 (2023).

10. Ousset, M., Keymeulen, A. Van, Bouvencourt, G., et al. Multipotent and unipotent progenitors contribute to prostate postnatal development. Nature Cell Biology. 14 (11), doi: 10.1038/ncb2600 (2012).

11. Wang, J., Zhu, H.H., Chu, M., et al. Symmetrical and asymmetrical division analysis provides evidence for a hierarchy of prostate epithelial cell lineages. Nature Communications. 5 (4758), doi: 10.1038/ncomms5758 (2014).

12. Toivanen, R., Mohan, A., Shen, M.M. Basal progenitors contribute to repair of the prostate epithelium following induced luminal anoikis. Stem Cell Reports. 6 (5), 660–667, doi: 10.1016/j.stemcr.2016.03.007 (2016).

13. Kwon, O., Zhang, L., Ittmann, M.M., et al. Prostatic inflammation enhances basal-to-luminal

differentiation and accelerates initiation of prostate cancer with a basal cell origin. PNAS. 5 (111), doi: 10.1073/pnas.1318157111 (2013).

14. Choi, N., Zhang, B., Zhang, L., et al. Adult murine prostate basal and luminal cells are self-sustained lineages that can both serve as targets for prostate cancer initiation. Cancer Cell. 21 (2), 253–265, doi: 10.1016/j.ccr.2012.01.005 (2012).

15. Stoyanova, T., Cooper, A.R., Drake, J.M., et al. Prostate cancer originating in basal cells progresses to adenocarcinoma propagated by luminal-like cells. PNAS. 110 (50), 20111–20116, doi: 10.1073/pnas.1320565110 (2013).

16. Dardenne, E., Beltran, H., Benelli, M., et al. N-Myc induces an EZH2-mediated transcriptional program driving neuroendocrine prostate cancer. Cancer Cell. 30 (4), 563–577, doi: 10.1016/j.ccell.2016.09.005 (2016).

17. Berger, A., Beltran, H., Rickman, D.S., et al. N-Myc –mediated epigenetic reprogramming drives lineage plasticity in advanced prostate cancer. Journal of Clinical Investigation. 129 (9), 3924–3940, doi: 10.1172/JCI127961 (2019).

18. Ku, S.Y., Rosario, S., Wang, Y., et al. Rb1 and Trp53 cooperate to suppress prostate cancer lineage plasticity, metastasis, and antiandrogen resistance. Science. 355 (6320), 78–83, doi: 10.1126/science.aah4199 (2017).

19. Beltran, H., Hruszkewycz, A., Scher, H.I., et al. The role of lineage plasticity in prostate cancer therapy resistance. Clinical Cancer Research. 25 (23), 6916–6924, doi: 10.1158/1078-0432.CCR-19-1423 (2019).

20. Davies, A.H., Beltran, H., Zoubeidi, A. Cellular plasticity and the neuroendocrine phenotype in prostate cancer. Nature Reviews Urology. 15 (5), 271–286, doi: 10.1038/nrurol.2018.22 (2018).

21. Zhang, B., Ci, X., Tao, R., et al. Klf5 acetylation regulates luminal differentiation of basal progenitors in prostate development and regeneration. Nature Communications. 11 (1), doi: 10.1038/s41467-020-14737-8 (2020).

22. Fraser, M., Livingstone, J., Wrana, J.L., et al. Somatic driver mutation prevalence in 1844 prostate cancers identifies ZNRF3 loss as a predictor of metastatic relapse. Nature Communications. 12 (6248), 1–15, doi: 10.1038/s41467-021-26489-0 (2021).

23. Parolia, A., Cieslik, M., Chu, S., et al. Distinct structural classes of activating FOXA1 alterations in advanced prostate cancer. Nature. 571 (7765), doi: 10.1038/s41586-019-1347-4 (2019).

24. Wenes, M., Jaccard, A., Wyss, T., et al. The mitochondrial pyruvate carrier regulates memory T cell differentiation and antitumor function. Cell Metabolism. 34 (5), 731–746, doi: 10.1016/j.cmet.2022.03.013 (2022).

25. Feng, Q., Liu, Z., Yu, X., et al. Lactate increases stemness of CD8+ T cells to augment anti-tumor immunity. Nature Communications. 13 (4981), doi: 10.1038/s41467-022-32521-8 (2022).

26. Tewari, A.K., Cheung, A.T.M., Crowdis, J., et al. Molecular features of exceptional response to neoadjuvant anti-androgen therapy in high-risk localized prostate cancer. Cell Reports. 36 (10), doi: 10.1016/j.celrep.2021.109665 (2021).

27. Alumkal, J.J., Sun, D., Lu, E., et al. Transcriptional profiling identifies an androgen receptor activity-low , stemness program associated with enzalutamide resistance. PNAS. 22 (117), 12315–12323, doi: 10.1073/pnas.1922207117 (2020).

28. Zadra, G., Ribeiro, C.F., Chetta, P., et al. Inhibition of de novo lipogenesis targets androgen receptor signaling in castration-resistant prostate cancer. PNAS. 116 (2), 631–640, doi: 10.1073/pnas.1808834116 (2019).

29. Xu, L., Yin, Y., Li, Y., et al. A glutaminase isoform switch drives therapeutic resistance and disease progression of prostate cancer. PNAS. 118 (13), 1–11, doi: 10.1073/pnas.2012748118 (2021).

30. Bader, D.A., Hartig, S.M., Putluri, V., et al. Mitochondrial pyruvate import is a metabolic vulnerability in androgen recptor-driven prostate cancer. Nature Metabolism. 1 (1), 70–85, doi: 10.1038/s42255-018-0002-y (2019).

31. Massie, C.E., Lynch, A., Ramos-montoya, A., et al. The androgen receptor fuels prostate cancer by regulating central metabolism and biosynthesis. EMBO. 30 (13), 2719–2733, doi: 10.1038/emboj.2011.158 (2011).

32. Frigo, D.E., Howe, M.K., Wittmann, B.M., et al. CaM kinase kinase beta-mediated activation of the growth regulatory kinase AMPK is required for androgen-dependentmigration of prostate cancer cells. Cancer Research. 71 (2), 528–537, doi: 10.1158/0008-5472.CAN-10-2581 (2011).

33. Reina-campos, M., Linares, J.F., Duran, A., et al. Increased serine and one-carbon pathway metabolism by PKC I / i deficiency promotes neuroendocrine prostate cancer. Cancer Cell. 35 (3), 385–400, doi: 10.1016/j.ccell.2019.01.018 (2019).

34. Basu, H.S., Wilganowski, N., Robertson, S., et al. Prostate cancer cells survive anti-androgen and mitochondrial metabolic inhibitors by modulating glycolysis and mitochondrial metabolic activities. The Prostate. 81 (12), 799–811, doi: 10.1002/pros.24146 (2021).

35. Nobes, J.P., Langley, S.E.M., Klopper, T., et al. A prospective, randomized pilot study evaluating the effects of metformin and lifestyle intervention on patients with prostate cancer receiving androgen deprivation therapy. BJU International. 109 (10), 1495–1502, doi: 10.1111/j.1464-410X.2011.10555.x (2011).

36. Ahn, H.K., Lee, Y.H., Koo, K.C. Current status and application of metformin for prostate cancer: A comprehensive review. International Journal of Molecular Sciences. 21 (22), doi: 10.3390/ijms21228540 (2020).

37. He, L., Wondisford, F.E. Metformin action: concentrations matter. Cell Metabolism. 21 (2), 159–162, doi: 10.1016/j.cmet.2015.01.003 (2015).

38. Hess, C., Unger, M., Madea, B., et al. Range of therapeutic metformin concentrations in

clinical blood samples and comparison to a forensic case with death due to lactic acidosis. Forensic Science International. 286, 106–112, doi: 10.1016/j.forsciint.2018.03.003 (2018).

39. Yap, T.A., Daver, N., Mahendra, M., et al. Complex I inhibitor of oxidative phosphorylation in advanced solid tumors and acute myeloid leukemia: phase I trials. Nature Medicine. 29 (1), 115–126, doi: 10.1038/s41591-022-02103-8 (2023).

40. Rambold, A.S., Kostelecky, B., Elia, N., et al. Tubular network formation protects mitochondria from autophagosomal degradation during nutrient starvation. PNAS. 108 (25), 10190–10195, doi: 10.1073/pnas.1107402108/-/DCSupplemental.www.pnas.org/cgi/doi/10.1073/pnas.1107402108 (2011).

41. Baek, M.L., Lee, J., Pendleton, K.E., et al. Mitochondrial structure and function adaptation in residual triple negative breast cancer cells surviving chemotherapy treatment. Oncogene. 42 (14), 1117–1131, doi: 10.1038/s41388-023-02596-8 (2023).

42. Kong, B., Tsuyoshi, H., Orisaka, M., et al. Mitochondrial dynamics regulating chemoresistance in gynecological cancers. Annals of the New York Academy of Sciences. (1350), 1–16, doi: 10.1111/nyas.12883 (2015).

43. Courtois, S., Lux, B. De, Penin-peyta, L., et al. Inhibition of mitochondrial dynamics preferentially targets pancreatic cancer cells with enhanced tumorigenic and invasive potential. Cancers. 13 (4), doi: 10.3390/cancers13040698 (2021).

44. Hagenbuchner, J., Kuznetsov, A. V, Obexer, P., et al. BIRC5/Survivin enhances aerobic glycolysis and drug resistance by altered regulation of the mitochondrial fusion/fission machinery. OncogeneOncogene. 32 (40), 4748–4757, doi: 10.1038/onc.2012.500 (2013).

45. Qiu, X., Boufaied, N., Hallal, T., et al. MYC drives aggressive prostate cancer by disrupting transcriptional pause release at androgen receptor targets. Nature Communications. 13 (1), doi: 10.1038/s41467-022-30257-z (2022).

46. Bernard, D., Gil, J., Beach, D.H., et al. Myc confers androgen-independent prostate cancer cell growth. Journal of Clinical Investigation. 112 (11), 1724–1731, doi: 10.1172/JCI200319035.Introduction (2003).